MULTI LENGTH SCALE FINITE ELEMENT DESIGN FRAMEWORK FOR ADVANCED WOVEN FABRICS

by

Galip Ozan Erol

A dissertation submitted to the Faculty of the University of Delaware in partial fulfillment of the requirements for the degree of Doctor of Philosophy in Mechanical Engineering

Summer 2017

MULTI LENGTH SCALE FINITE ELEMENT DESIGN FRAMEWORK FOR ADVANCED WOVEN FABRICS

by

Galip Ozan Erol

Approved: ____

Ajay K. Prasad, Ph.D.
Chair of the Department of Mechanical Engineering

Approved: ____

Babatunde A. Ogunnaike, Ph.D.
Dean of the College of Engineering

Approved: ____

Ann L. Ardis, Ph.D.
Senior Vice Provost for Graduate and Professional Education

I certify that I have read this dissertation and that in my opinion it meets the academic and professional standard required by the University as a dissertation for the degree of Doctor of Philosophy.

Signed: ____

Michael Keefe, Ph.D.
Professor in charge of dissertation

I certify that I have read this dissertation and that in my opinion it meets the academic and professional standard required by the University as a dissertation for the degree of Doctor of Philosophy.

Signed: ____

Brian Powers, Ph.D.
Member of dissertation committee

I certify that I have read this dissertation and that in my opinion it meets the academic and professional standard required by the University as a dissertation for the degree of Doctor of Philosophy.

Signed: ____

Michael H. Santare, Ph.D.
Member of dissertation committee

I certify that I have read this dissertation and that in my opinion it meets the academic and professional standard required by the University as a dissertation for the degree of Doctor of Philosophy.

Signed: ____

Shridhar Yarlagadda, Ph.D.
Member of dissertation committee

ACKNOWLEDGMENTS

Word crashed the 100th time as I started typing this but I cannot believe that this dissertation work is finally over. This would not be possible without the constant support of people around me.

I would like to express my sincere gratitude to my advisor, Dr. Keefe for his continuous support and guidance through my studies. I would not be able to complete this work without his help. I also would like to thank Dr. Powers for his support. It would not be possible to develop the models in this work without his knowledge and expertise in numerical modeling. I am grateful to have Dr. Santare and Dr. Yarlagadda as my committee members and for their advice and time. I also would like to acknowledge the help of Dr. Haque and Dr. Gillespie for providing the tools that I need for this research and allowing me to use Center for Composite Materials resources. I feel very fortunate to get to know Dr. Buckley during my studies. It was a great pleasure to work with her and experience student oriented teaching during the classes that I TA'ed. I am also grateful for her constant encouragement during some of the difficult times.

I would like to thank the Department of Mechanical Engineering staff (Lisa Katzmire, Lita Toto and Ann Connor), and Center for Composite Materials staff (Corinne Hamed, Robin Mack, Johnny Thiravong and Steve Durbano). I would like to thank my office mates Dr. Sockalingam, Raja Hariharan and Venkat Santhamam for their friendship and useful discussions in various aspects of research. I am also extremely grateful to spend my last year in the Spencer Test Lab with the most amazing crew: David Bucha, John Salyers, Connor McCarthy, Gene Wildonger and Erin Rezich. The last year would be really difficult without your friendship and our coffee runs every day. I would like to thank Dr. Hatice Sas, Dr. Sevil Buzcu, Dr. Furkan Cayci and Berk Gonenc for their help and support from day one. I am grateful that I got the chance to go through this journey with them.

I am extremely grateful to have my family's support, especially my parents Yuksel and Enis, and my brother Baris. Always knowing that I had their constant support and love helped me to motivate and go through tough times. I would also like to thank my second family here in the USA, Mr. and Mrs. Bucha, Kellie, Alan, Emily, Kim, Andy and David. I really appreciate that they allowed me to become a part of their family and supported me during graduate school.

I complained so many times about my PhD during my time at University of Delaware but I also got to meet my wife, Amy. I cannot thank her enough for bearing my craziness, her constant love and support. I would not able to complete this dissertation without you and I am excited to see what the life will bring with you.

TABLE OF CONTENTS

LIST OF TABLES

LIST OF FIGURES

ABSTRACT

Woven fabrics are integral parts of many engineering applications spanning from personal protective garments to surgical scaffolds. They provide a wide range of opportunities in designing advanced structures because of their high tenacity, flexibility, high strength-to-weight ratios and versatility. These advantages result from their inherent multi scale nature where the filaments are bundled together to create yarns while the yarns are arranged into different weave architectures. Their highly versatile nature opens up potential for a wide range of mechanical properties which can be adjusted based on the application. While woven fabrics are viable options for design of various engineering systems, being able to understand the underlying mechanisms of the deformation and associated highly nonlinear mechanical response is important and necessary. However, the multiscale nature and relationships between these scales make the design process involving woven fabrics a challenging task. The objective of this work is to develop a multiscale numerical design framework using experimentally validated mesoscopic and macroscopic length scale approaches by identifying important deformation mechanisms and recognizing the nonlinear mechanical response of woven fabrics.

This framework is exercised by developing mesoscopic length scale constitutive models to investigate plain weave fabric response under a wide range of loading conditions. A hyperelastic transversely isotropic yarn material model with transverse material nonlinearity is developed for woven yarns (commonly used in

personal protection garments). The material properties/parameters are determined through an inverse method where unit cell finite element simulations are coupled with experiments. The developed yarn material model is validated by simulating full scale uniaxial tensile, bias extension and indentation experiments, and comparing to experimentally observed mechanical response and deformation mechanisms. Moreover, mesoscopic unit cell finite elements are coupled with a design-of-experiments method to systematically identify the important yarn material properties for the macroscale response of various weave architectures.

To demonstrate the macroscopic length scale approach, two new material models for woven fabrics were developed. The Planar Material Model (PMM) utilizes two important deformation mechanisms in woven fabrics: (1) yarn elongation, and (2) relative yarn rotation due to shear loads. The yarns' uniaxial tensile response is modeled with a nonlinear spring using constitutive relations while a nonlinear rotational spring is implemented to define fabric's shear stiffness. The second material model, Sawtooth Material Model (SMM) adopts the sawtooth geometry while recognizing the biaxial nature of woven fabrics by implementing the interactions between the yarns. Material properties/parameters required by both PMM and SMM can be directly determined from standard experiments. Both macroscopic material models are implemented within an explicit finite element code and validated by comparing to the experiments. Then, the developed macroscopic material models are compared under various loading conditions to determine their accuracy.

Finally, the numerical models developed in the mesoscopic and macroscopic length scales are linked thus demonstrating the new systematic design framework involving linked mesoscopic and macroscopic length scale modeling approaches. The approach is demonstrated with both Planar and Sawtooth Material Models and the simulation results are verified by comparing the results obtained from meso and macro models.

Chapter 1

INTRODUCTION

1.1 Background

Technical fabrics are textile products manufactured to achieve certain functionality for a given application. They provide opportunities to create a variety of architectures and thus a wide range of mechanical properties. The weaving process is widely used for technical fabrics and typically involves yarns made from man-made fibers (Aramid, polyester, polypropylene, etc.) woven together in different weave patterns. This complex construction provides the wide range of options for designing engineering structures. Because of their high tenacity and flexibility, high strength-to-weight ratios and versatility, woven fabrics have been used in various applications including: personal protective clothing, airbags, functional rehabilitation garments, medical scaffolds, containment systems, inflatable decelerators and composite textile preforms (Figure 1.1) [1-8].

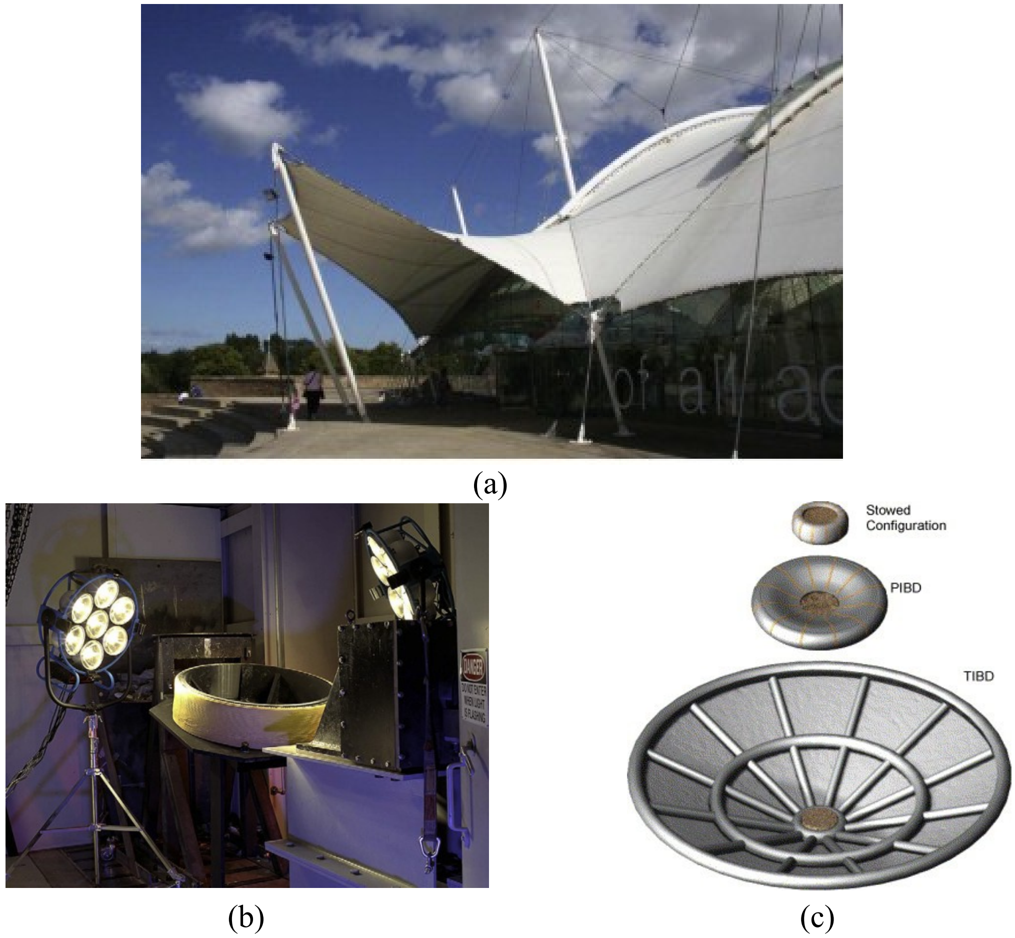

Figure 1.1 Application areas of woven fabrics: (a) Structural applications, (b) Ballistic protection, and (c) Inflatable decelerators.

The advantages of woven fabrics such flexibility and high strength over conventional materials such as steel result from their inherent multi-scale nature (Figure 1.2). These length scales can be classified based on the dimensions of the structural elements: (1) microscale (filaments), (2) mesoscale (yarns), and (3) macroscale (fabric). Each length scale contributes to the overall behavior of the fabric. Beside the multi-scale nature, the arrangement of the yarns (weave architecture) also plays an important role and affects the deformation of the woven fabrics.

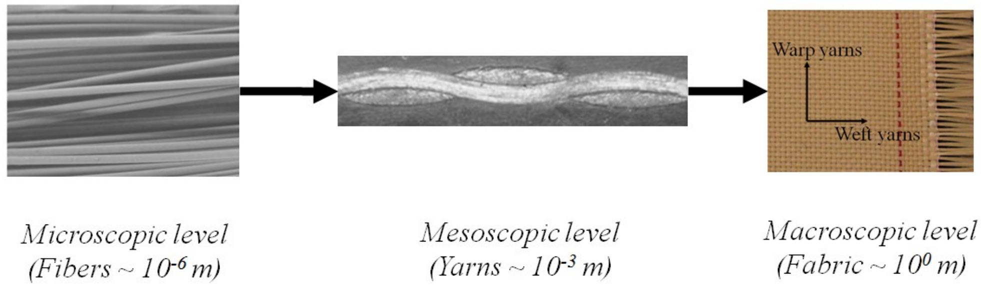

Figure 1.2 Length scales involved in woven fabrics.

Woven fabrics can undergo large deformations because of their multi-scale nature. The filaments/yarns are free to move, extend, rotate, bend and slide relative to each other. This behavior results in low resistance to deformation under various loading conditions making woven fabrics highly flexible. The mechanical response and deformation mechanisms involved in woven fabrics are determined by the fiber/yarn material and the weave architecture. The fiber/yarn material can be changed to adjust the mechanical response at both meso and macro length scales while the weave architecture can be used to change the overall macro mechanical response (Figure 1.3).

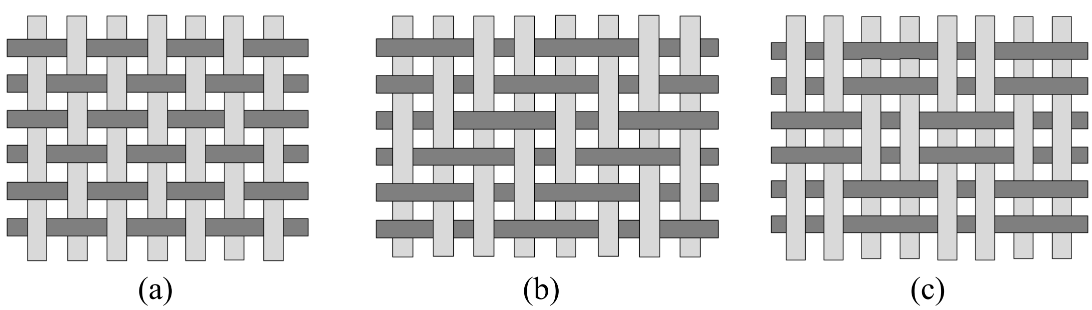

Figure 1.3 Commonly used weave architectures: (a) Plain weave, (b) Twill weave, and (c) Basket weave.

Woven fabrics have been widely used in composite manufacturing. They are an integral part of composite materials because of their ability to take any complex forms due to their flexibility. They are draped over molds during pre-forming step of composite manufacturing processes. The woven fabrics can take the complex shape of a mold since their resistance to deformation is fairly low. The weave architecture and fiber/yarn materials can be changed to adjust the material properties along with the flexibility thus allowing manufacturing of complex shapes based on the needs of the designer. Moreover, woven fabrics are also used in functional garments that are clothing systems designed to protect an individual from everyday work situations such as construction and manufacturing workers or from severe environments (astronauts and military). Hard and rigid protection systems are important but they are not feasible for the extremities of the body (such as legs and arms) since flexibility is an important factor for the mobility of the person. Woven fabrics can provide this flexibility to the wearer while protecting them from severe environments.

While the woven fabrics are viable options for various applications, their multi-scale construction also results in highly nonlinear mechanical response and complex deformation mechanisms. The highly nonlinear behavior and complex deformations make the design of structures involving woven fabrics a challenging task. Hence, it is important to understand these mechanisms to design better end results/products involving woven fabrics.

1.1.1 Experimental Characterization of Woven Fabrics

The woven fabrics exhibit highly nonlinear mechanical response due to their multiscale nature. Hence, several experimental characterization methods have been used to characterize the material response under various loads. Since there are two distinct yarn directions, the uniaxial and biaxial tensile tests are used to determine the tensile behavior. Moreover, bias extension and picture-frame tests are used to characterize the shear behavior.

1.1.1.1 Uniaxial tensile tests

In woven fabrics, initially straight yarns are woven into different weave architectures to obtain the final fabric structure. The weaving process results in permanent undulations (crimp) on the yarns and creates two distinct yarn directions [9]. These yarns exhibit different mechanical responses (based on the weave type, material and manufacturing methods used). Therefore, yarns extracted from a fabric and fabric itself are generally tested under uniaxial tensile loads. ASTM D3822-07 (Test method for tensile properties of single textile fibers) and ASTM D5035-95 (Test method for breaking force and elongation of textile fabrics - Strip method) are the mostly commonly adopted test methods for single yarns and fabrics, respectively [10–12]. For single yarn tests, the yarns are extracted from the fabric and clamped at both ends and subjected to tensile loading. As the deformation progresses, the yarns start to lose their undulations under tensile loading and become straight. This deformation mechanism is called decrimping and it results in initial compliant force response followed by a non-compliant mechanical response.

Woven fabrics are also tested in a similar manner to single yarns under uniaxial loading [9, 13–15]. Specimens are constructed such that either weft or warp yarns are clamped at both ends and aligned with the applied load direction (Figure 1.4a). During the test, the yarns subjected to uniaxial loading lose their crimp while the transverse yarns that are free to move (Figures 1.4b and 1.4c).

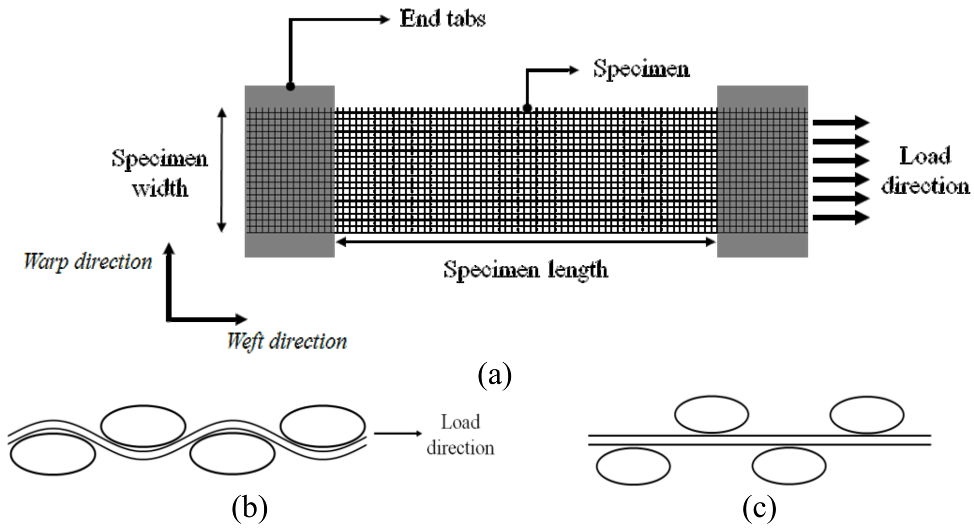

Figure 1.4 Uniaxial tensile characterization: (a) Fabric uniaxial tensile test, (b) Undeformed fabric, and (c) Deformed fabric.

The transverse yarns increase their crimp amplitudes due to the interactions between the yarns at the crossover points. This deformation mechanism is called crimp interchange. Since the yarns in the transverse direction increase their crimp amplitudes, they reduce their apparent length. This deformation also decreases the width of the specimen resulting in a Poisson's effect (Figure 1.5). Moreover, the force response for both yarns exhibit a bilinear mechanical response similar to single yarn uniaxial tests since the decrimping is the main deformation mechanism.

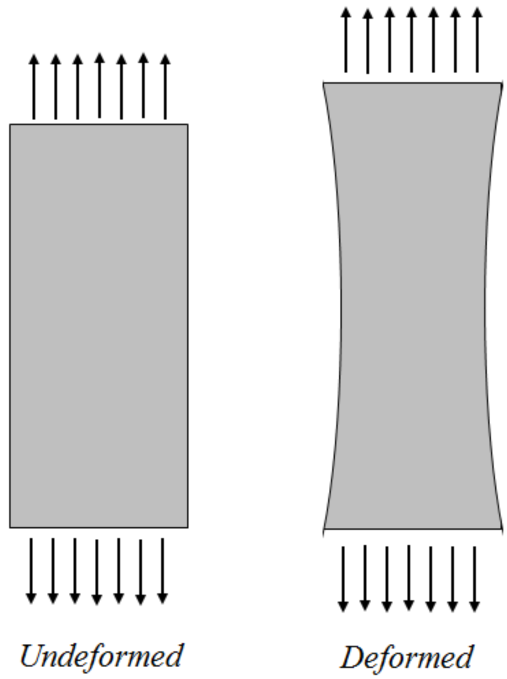

Figure 1.5 Fabric deformation under uniaxial tensile loading.

1.1.1.2 Biaxial tensile tests

The weft and warp yarns can interact at the crossover points where they contact with each other. When both yarn directions are subjected to tensile loads at the same time, they start to lose their undulations and start compressing each other at the crossover points. This deformation mechanism results in a stiffer response compared to uniaxial tensile loading. Hence, biaxial tensile tests are used to characterize the biaxial mechanical response of the woven fabrics (Figure 1.6) [16–19]. In this test, a cruciform shaped specimen is generally adopted to reduce the edge effects on the test results. Yarn directions are clamped on both ends and subjected to tensile loading. Different loading schemes can be applied to the specimen such as applying different displacements to the yarn directions based on the test setup used [3, 20, 21].

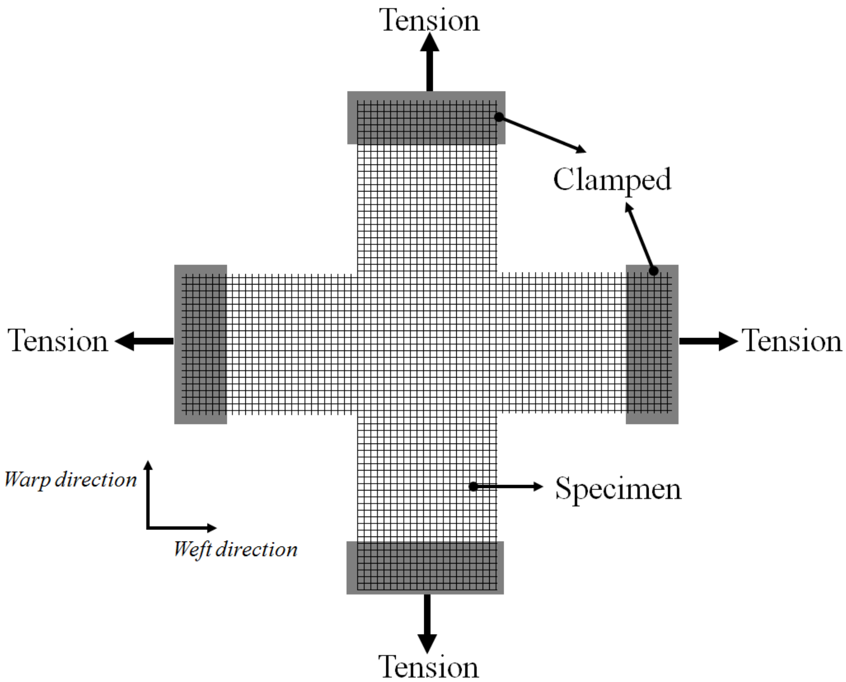

Figure 1.6 Biaxial tensile test setup.

1.1.1.3 Shear characterization tests

Among the different deformation mechanisms, shear deformation is the most prominent mechanism in woven fabrics due to initial yarn sliding/rotation and potential locking due to yarn contact in the transverse direction. The mechanical response of woven fabrics is highly nonlinear due to the complex deformations involved. Bias extension and picture frame are the two most commonly used experimental methods to characterize woven fabrics' mechanical response under shear [20, 22–26].

1.1.1.3.1 Bias extension test

In bias extension test, the woven fabric is cut into a rectangular shape and clamped on shorter edges such that the yarns are initially oriented at $\pm 45^{\circ}$ with respect to the loading direction (Figure 1.7a) [9]. The test requires a minimum of 2 aspect ratio (defined by the specimen's length and width) to obtain a proper shear region at the middle of the specimen [26–28]. The yarns initially slide and relatively rotate at the crossover points when the fabric is subjected to the loading. The yarns also compress each other in the transverse direction as the deformation progresses. During bias extension tests, the fabric specimens exhibit three distinct deformation zones (Figure 1.7b & 1.7c). Region "A" experiences simple shear while the region "B" experiences mixed deformation mode. Region "C" does not undergo any deformation due to the boundary conditions imposed at the clamped edges. Moreover, the amount of shear deformation observed in region "B" is half of the region "A" due to the boundary conditions imposed by both regions "A" and "C". The angle between the yarns decreases until it reaches a critical angle called "locking angle" where the yarns compress each other in the transverse direction. The specimen starts to buckle (out-of-plane deformation) resulting in a wrinkle along region "A" after this angle is reached. (Figure 1.7d). The mechanical response of the woven fabric under shear is highly dependent on the deformation mechanisms observed during the bias extension test. The force response exhibits a compliant response due to the initial yarn sliding and relative rotation. This compliant response is followed by a non-compliant response because of the yarn transverse compression.

Bias extension test is simple to conduct and does not require special clamps to carry out the test. However, it suffers from the heterogeneous deformation zones as shown in Figure 1.7c. Hence, it requires optical imaging to determine the angle between the yarns during the deformation to characterize the woven fabrics.

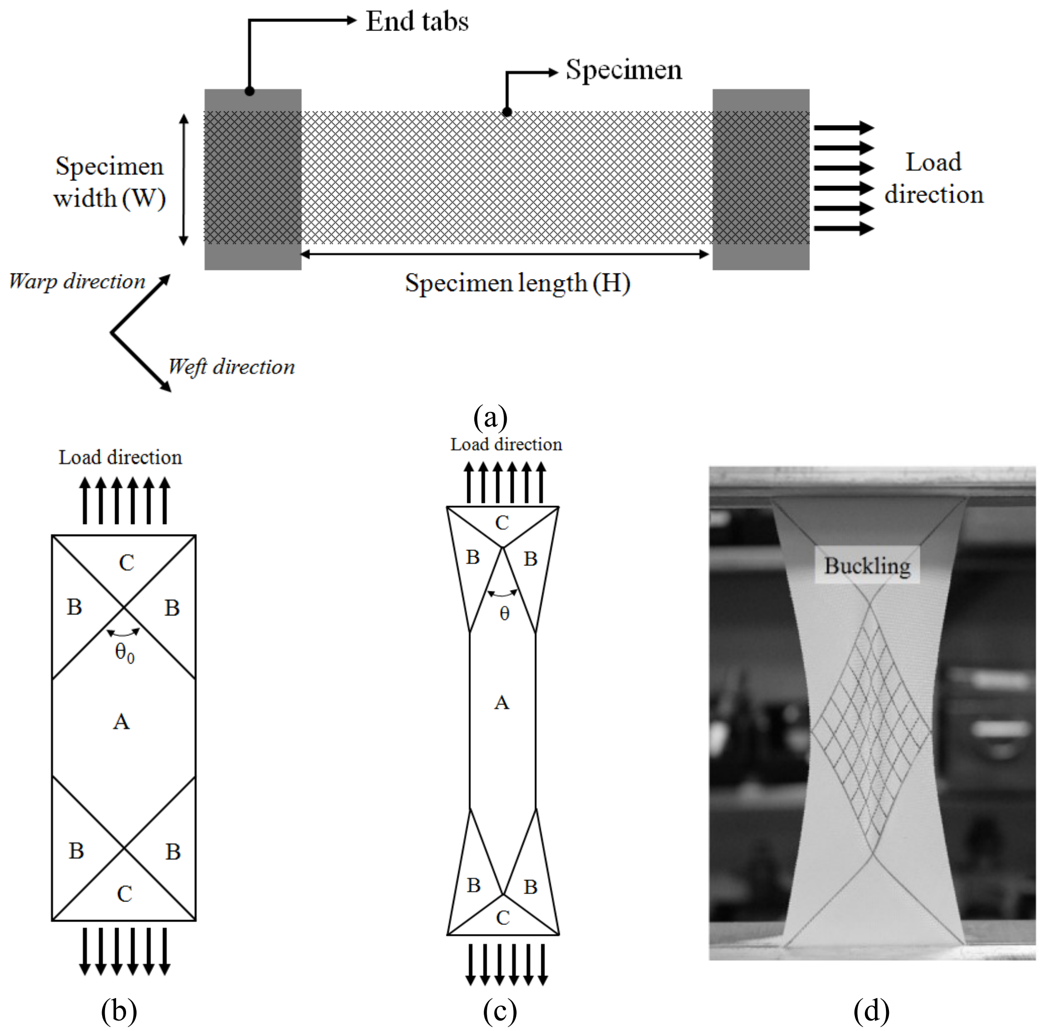

Figure 1.7 Bias extension test: (a) Test setup, (b) Undeformed specimen, (c) Deformed specimen, and (d) Out-of-plane buckling experienced during deformation.

1.1.1.3.2 Picture frame test

In picture frame tests, the fabric specimen is cut into a square shape and attached to specially designed four clamping plates (Figure 1.8a) [24, 26, 29, 30]. The force applied to the crosshead is transferred to the specimen through the clamps. As the deformation progresses, the initial square shape of the fabric start to take a rhomboid shape resulting in a homogeneous shear region across the specimen (Figures 1.8b & 1.8c). Yarns initially slide and rotate relatively in a similar manner to bias extension tests. Then, the yarn transverse compression becomes the dominant deformation mechanism resulting in an out-of-plane buckling deformation where a non-compliant mechanical response is observed.

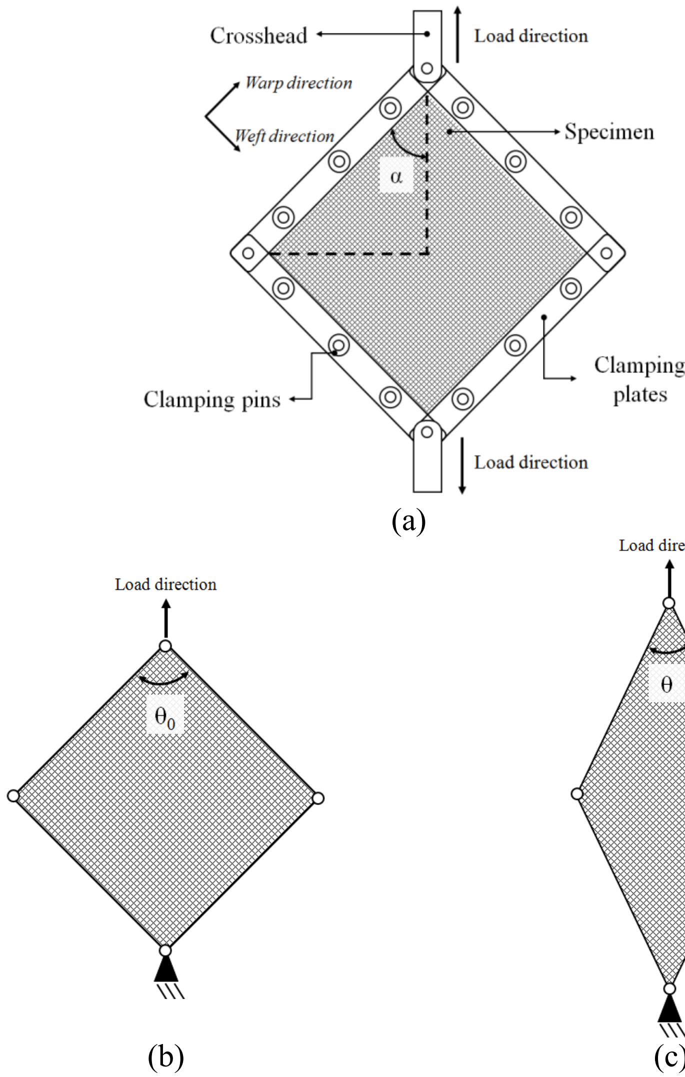

Figure 1.8 Picture frame test: (a) Test setup, (b) Undeformed specimen, (c) Deformed specimen.

The results are highly dependent on the clamp design since the misalignments and preloads imposed on the specimen by the clamps can result in an increased shear resistance and errors in the results. Hence, various modifications to the test have been proposed in the literature to overcome these difficulties [24]. In general, the test method is relatively easy to perform and does not require optical imaging to determine the angle between the yarns since the deformation is homogeneous across the fabric. The angle can be easily determined from the crosshead displacement and fabric dimensions. However, it requires custom-made clamps and special attention should be given to avoid imposing tensile force on yarn directions for correct characterization. Table 1.1 shows the summary of commonly adopted experimental methods used in the literature.

Table 1.1 Summary of commonly used experimental techniques used for woven fabrics.

Loading	Method	Deformation modes	Outputs
Tensile	Single yarn	Yarn decrimping	Yarn tensile modulus
	Uniaxial tensile	Yarn crimp interchange	Fabric tensile modulus
	Biaxial tensile	Decrimping & compression	Biaxial response
Shear	Bias extension Picture frame	Relative yarn rotation Yarn compaction Yarn locking	Normalized unit torque

1.1.2 Computational Modeling of Woven Fabrics

Finite element modeling is the most commonly adopted technique to model woven fabrics. The modeling efforts in the literature can be divided into three main categories based on the length scale modeled: (1) microscopic (filaments), (2) mesoscopic (yarns), and (3) macroscale (fabrics). The following sections will briefly introduce the woven fabric modeling approaches at different length scales.

1.1.2.1 Microscopic length scale modeling

In microscopic length scale modeling, the individual filaments within the yarns are explicitly modeled to study different deformation and energy dissipation mechanisms involved in this length scale (Figure 1.9) [31–35]. This length scale modeling can mechanistically capture actual yarn deformation mechanisms through modeling filament level contact mechanics.

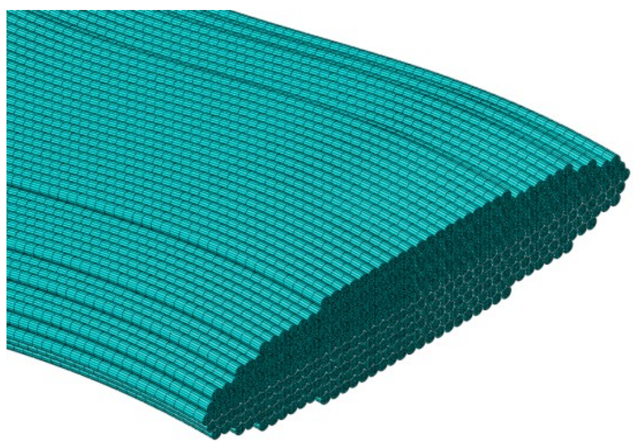

Figure 1.9 Microscopic length scale finite element model.

However, high computational resources are required for this length scale modeling approach. The simulations of structures involving woven fabrics are challenging using this level of modeling due to this requirement. To overcome the requirement of high computational resources, Wang et al. proposed a digital element method to represent and simulate woven fabrics under ballistic impact [35]. Each filament is modeled as digital rod elements connected by frictionless pins (Figure 1.10). A contact algorithm was implemented to detect collisions between the filaments.

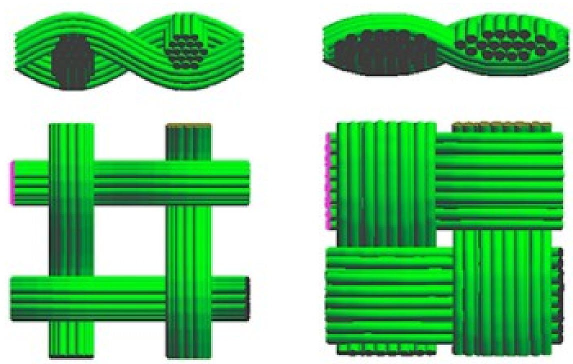

Figure 1.10 Digital element approach [35].

Dobrich et al. adopted a similar method where individual filaments are modeled with beam elements [31]. Fabric structures using the beam elements were obtained by simulating a weaving process using a finite element framework. The approach was able to reproduce the structure of different woven fabrics where the filaments were explicitly modeled. However, the digital element method does not take into account the Poisson's effects and transverse shear deformation of the filaments. Nilakantan and Sockalingam et al. developed finite element models where the individual filaments were modeled with solid elements (Figure 1.11) [33]. A transversely isotropic material model was adopted to investigate the ballistic response of Kevlar 706 yarns. The models were used to study the ballistic impact of Aramid filaments and yarns and limited to single yarn.

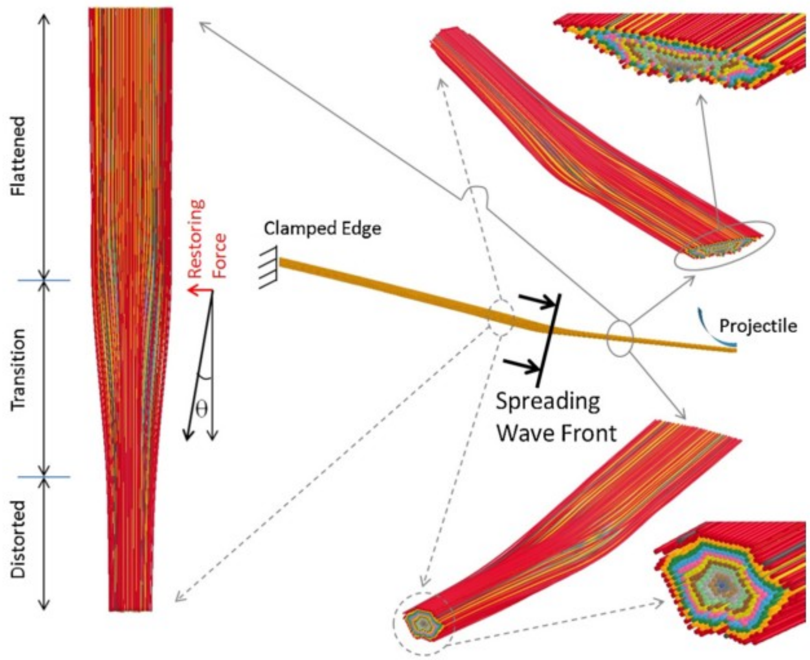

Figure 1.11 Microscopic length scale modeling with solid elements [33].

1.1.2.2 Mesoscopic length scale modeling

In mesoscopic length scale modeling, the yarns within a fabric are modeled as solid homogenized continuums (Figure 1.12). These models allow investigation of certain deformation mechanisms involved in mesoscopic length scale that are important to woven fabric overall mechanical response. Yarn-to-yarn relative rotation, frictional dissipation due to yarns' contact and yarn transverse compression are some of these important deformation mechanisms involved in the fabric response.

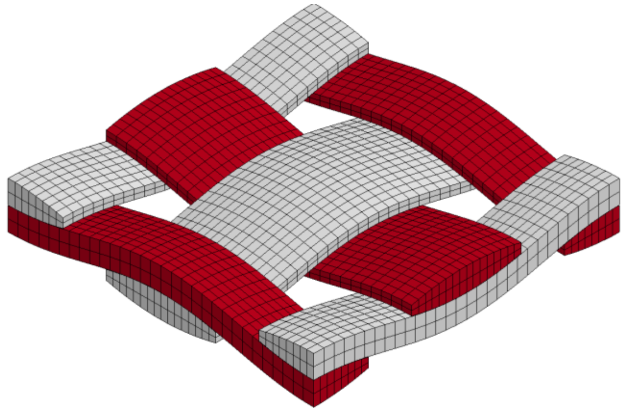

Figure 1.12 Mesoscopic length scale finite element model.

There are several different approaches to model yarns as solid continuums and the choice of the material model used for yarns depends on the application. For ballistic impact applications, the yarns are generally assumed to be transversely isotropic with linear material properties [4, 5, 36–39]. Duan et al. developed mesoscopic woven fabrics to study the role of friction during ballistic impact [4, 5]. They used 8-noded hexahedron elements to model yarns with a trigonometric yarn path definition. The yarns were modeled with LS-DYNA's built-in orthotropic material model with small yarn transverse and shear moduli values compared to yarn longitudinal modulus. The model behavior was not experimentally validated. Rao et al. and Nilakantan et al. extended this modeling approach using shell elements for yarns and combined with numerical models where yarns were modeled with solid elements [40, 41].

Though yarns were modeled with linear models for ballistic applications, their fibrous nature can be taken into account to obtain the highly non-linear mechanical behavior of the yarns. For example, an orthotropic hypoelastic constitutive equation (orthotropic elastic rate constitutive equation) with transverse non-linear behavior was developed to model yarns' mechanical response [1, 13, 42, 43]. The Cauchy stress ($\underline{\sigma}$) was defined as a function of the strain rate ($\underline{D}$) and constitutive tensor ($\underline{C}$):

$$\underline{\sigma}^{\nabla} = \underline{C} : \underline{D} \tag{1.1}$$

where $\underline{\sigma}^{\nabla}$ is the objective time derivate of the Cauchy stress. Eq. 1.1 can be implemented in the incremental form as:

$$\left[\sigma^{n+1}\right]_{f^{n+1}} = \left[\sigma^{n}\right]_{f^{n}} + \left[\sigma^{n+\frac{1}{2}}\right]_{f^{n+1}} \left[\Delta\varepsilon^{n+\frac{1}{2}}\right]_{f^{n+1}} \tag{1.2}$$

where σ^n, C^n and $\Delta\varepsilon^n$ are stress, stiffness matrix and strain increment at a given time step in the current coordinate frame.

Badel et al., Boisse et al. and Gasser et al. modeled yarns using the previously explained hypoleastic formulation. The yarns were assumed to be transversely isotropic [1, 3, 44]. The yarn direction modulus was also assumed to be constant and obtained from a tensile test on a single yarn. Poisson's ratios were assumed to zero and very low shear moduli was chosen due to the fibrous nature of the yarns. Moreover, the nonlinear transverse behavior was implemented with a crushing law. Transverse modulus (E_t) was defined as a function of the transverse strain (ε_{33}) and longitudinal strain (ε_{11}):

$$E_t = E_{in} + E_0 \left|\varepsilon_{33}^{n}\right| \varepsilon_{11}^{m} \tag{1.3}$$

where E_{in} is the initial transverse modulus in the undeformed state. E_0, n and m are material parameters that were determined from the experiments. The material properties and parameters were determined through an inverse method where the biaxial tensile test experiments were used. An error function was defined using the finite element and experimental results of a biaxial tensile test. The Levenberg-

Marquardt method was used to minimize this error function to obtain these material parameters. Woven fabrics were only simulated at the unit cell level with periodic boundary conditions due to the high computational resources required by the models. The simulations were validated with uniaxial, biaxial and picture frame tests. Komeili et al. used the same approach to study the uncertainties involved in woven fabrics but the longitudinal modulus was defined as a function of longitudinal strain in [45].

Lin et al. adopted the hypoelastic approach to model the yarn behavior [46]. The yarn material behavior was implemented as a function of the fiber volume fraction. Longitudinal modulus was defined such that it had a linear relation with the fiber volume fraction. Moreover, the non-linear transverse modulus was implemented by using power law which is based on the relationship between the pressure applied to a tow and change in the fiber volume fraction during compaction experiments. The nonlinear transverse modulus was defined as:

$$E_t = \frac{-a\left(V_f^0 \big/ \exp(\varepsilon_t) \right)^b + a\left(V_f^0\right)^b}{\varepsilon_t} \tag{1.4}$$

where V_f^0 and ε_t are initial fiber volume fraction and total transverse strain, and a and b are the material parameters that are obtained from compaction experiments, respectively. The material model was used to simulate fabric shear behavior and compaction behavior.

Badel et al. developed a nonlinear yarn material model using the hypoelastic approach [47]. They distinguished the two transverse deformation modes that were observed in tomography scans. These deformation modes were identified as fiber density changes (Spherical part) and shape changes (Deviatoric part). It was assumed that these two modes were decoupled from each other and total transverse strain (ε_t) was expressed as:

$$
\begin{gathered}
[\varepsilon_t] = \begin{bmatrix} \varepsilon_s & 0 \\ 0 & \varepsilon_s \end{bmatrix} + \begin{bmatrix} \varepsilon_d & \varepsilon_{23} \\ \varepsilon_{23} & -\varepsilon_d \end{bmatrix} \\
\varepsilon_s = \frac{\varepsilon_{22} + \varepsilon_{33}}{2}, \varepsilon_d = \frac{\varepsilon_{22} - \varepsilon_{33}}{2}
\end{gathered} \tag{1.5}
$$

where ε_s and ε_d are the spherical and deviatoric strains. Moreover, ε_{22}, ε_{33} and ε_{23} are the strain components in the local yarn coordinate frame. Then, the following relations were developed to obtain the nonlinear yarn behavior in the transverse direction:

$$
\begin{aligned}
\Delta\sigma_s &= A\Delta\varepsilon_s \\
\Delta\sigma_d &= B\Delta\varepsilon_d \\
\Delta\sigma_{23} &= B\Delta\varepsilon_{23}
\end{aligned}
\qquad
\begin{aligned}
A &= A_0 e^{-p\varepsilon_s} e^{n\varepsilon_{11}} \\
B &= B_0 e^{-p\varepsilon_d}
\end{aligned} \tag{1.6}
$$

where σ_s and σ_d are spherical and deviatoric stresses, respectively. A_0, B_0, p and n are the material properties that are determined from the experiments. These material parameters were obtained from uniaxial and biaxial tensile tests using an inverse approach in Badel et al.'s work [1, 42, 47]. The material model was validated with compression and shear experiments coupled with tomography scans.

A hyperelastic approach was developed by Charmetant et al. [48]. Four deformation modes were identified: (1) Elongation, (2) Compaction, (3) Cross sectional distortion, and (4) Longitudinal shear. Strain energy functions were developed for each of the deformation modes. The model requires 4 parameters for elongation part, 2 for compaction, 1 for distortion and 1 for longitudinal shear. Tensile tests on the yarns, biaxial tensile and tensile tests on the fabric were used to determine these material parameters. The material model was used to simulate a unit cell and validated with uniaxial tensile, biaxial and picture frame tests.

The comparison of the available mesoscale material models in the literature in terms of formulation, implemented mechanical responses and experimental validation is given in Table 1.2.

Table 1.2 Comparison of mesoscopic length scale material models in the literature.

Work	Formulation	Material Model	Validation
Duan et al. [4], [5] Rao et al. [38], [41]	Hyperelastic Solid & shell elements	Transversely isotropic Constant material properties	N/A
Badel et al. [1], [42] Gasser et al. [44] Gatouillat et al. [13]	Hypoelastic Solid elements	Transversely isotropic Constant longitudinal modulus Constant shear moduli	Uniaxial Biaxial Picture frame
Lin et al. [46]	Hypoelastic Solid elements	Nonlinear transverse modulus Transversely isotropic Nonlinear longitudinal modulus Constant shear moduli Nonlinear transverse modulus	Picture frame Compression
Charmetant et al. [48]	Hyperelastic Solid elemernts	Transversely isotropic Linear longitudinal modulus Constant shear moduli Nonlinear transverse modulus	Uniaxial Biaxial Picture frame

1.1.2.3 Macroscopic length scale modeling

Different length scales are involved in woven fabric mechanical response because of their multi-scale nature. This multi-scale nature creates a highly heterogeneous structure resulting in nonlinear behavior as stated before. In macroscale length scale modeling, the woven fabrics are assumed to have a structure of homogeneous material and the nonlinear behavior is obtained with special constitutive relations defining the mechanical response of woven fabrics. Most of the material models in this length scale are developed for shell or membrane elements since the thickness of the fabric is fairly small compared to other in-plane dimensions and stays almost constant during deformation.

Dong et al. and Manimala et al. developed an incremental macroscale material model for plain weave Kevlar fabrics [9, 49]. The woven fabric was assumed to have two layers representing each yarn direction. The fabric uniaxial behavior was implemented with a bilinear modulus obtained from uniaxial tensile tests on fabrics. The shear modulus was assumed to be constant while the non-linear shear behavior was obtained by using a non-dimensional yarn spacing parameter. This parameter was used as a fitting parameter to change the transverse modulus of the each layer. The value of the non-dimensional parameter for each layer was determined using a trial-error procedure to match the numerical simulations to experimental results. The material model was validated with uniaxial tensile, bias extension, 30^{o} off-axis tension and indentation tests.

A non-orthogonal constitutive material model was proposed by Peng et al. and Xue et al. [14, 23, 50, 51]. A convected coordinate system was adopted to implement large deformations. Covariant strains and contravariant stresses were introduced and transformed between local and global coordinate systems. The uniaxial tension and shear behaviors were decoupled while the biaxial response was not included in the model. The uniaxial response was implemented with a nonlinear tensile modulus while the shear response was obtained by using a polynomial curve fit for the shear modulus. The uniaxial tensile modulus was obtained from uniaxial tensile tests on the fabrics while the polynomial coefficients used for the shear modulus were obtained by running simulations to achieve experimental force results of bias extension tests. The model was validated using picture frame tests and a hemispherical stamping simulation.

Hyperelastic constitutive models were proposed by Aimene et al., Dridi et al. and Peng et al. [23, 52, 53]. The hyperelastic approach aimed to define strain energy functions for woven fabrics where the uniaxial and shear behaviors are decoupled. The strain energy function (*W*) with invariants was defined as:

$$W = W_1(L_1) + W_2(L_2) + W_{12}(L_{12}) \tag{1.7}$$

where the first two terms are strain energies due to yarn deformation and the third term is the shear energy due to the yarn interaction. Then, the second Piola Kirchoff stress tensor ($\underline{S}$) was obtained from the strain energy function:

$$\underline{S} = 2\frac{\partial W}{\partial \underline{C}} \tag{1.8}$$

where $\underline{C}$ is Green-Lagrange strain tensor. The hyperelastic models available in the literature do not consider the biaxial nature due to the yarn compression and interactions at the crossover point. Hence, Eq. 1.7 does not include the strain energy function related to this deformation. The model behavior was obtained by matching the experimental data from uniaxial tensile test and the corresponding strain energy functions (first two terms in Eq. 1.7). In a similar manner, the shear response was determined by using either bias extension or picture frame tests. Peng et al. validated their model using uniaxial tensile, bias extension, picture frame experiments and double dome forming [23].

Yarns in woven fabrics are arranged such that they repeat a certain pattern called a repeating unit cell. There are several material models that employ this repeating unit cell to obtain woven fabric mechanical response [20, 22, 36, 39, 54–60]. Hamila et al. called this modeling approach semi-discrete since it considered the mesoscale structure of the fabric within a macroscale formulation [55]. In this model, the virtual work theorem was adopted to relate the internal, exterior and acceleration virtual work. The internal virtual work (W_{int}) within a virtual displacement field (η) was divided into three components: (1) Tension, (2) Shear, and (3) Bending as:

$$W_{\text{int}}(\underline{\eta}) = W_{\text{int}}^{tension} + W_{\text{int}}^{shear} + W_{\text{int}}^{bending} \tag{1.9}$$

The tension virtual work depends on the tensions developed as a function of both yarn deformations along the yarn directions while the virtual work due to shear is a function of the virtual angle between the yarn directions and shear moment generated due to yarn interactions. Moreover, the virtual work due to bending was related to the curvatures of the yarns as well as the bending moments generated. Relating the interior, exterior and acceleration virtual work allows calculation of nodal interior loads within a specially developed finite element. Boisse et al. developed a four-node finite element made of several woven cells while Hamila et al. extended formulation of the finite element to three-node triangular elements [20, 56]. The tension (Uniaxial and biaxial) and shear response of the fabric were calibrated by experimental testing and discrete models where the yarns are modeled explicitly.

Jauffres et al., Dangora et al. and Harrison et al. developed a method combining 1-D and 2-D finite elements to simulate woven fabric mechanical response [22, 54, 61]. 1-D elements (beam and truss elements) were used to implement the fabric's uniaxial behavior while 2-D elements (Shell and membrane elements) were employed to account for the shear resistance of the fabric. Since the models require a combination of beam/truss and shell/membrane elements, a custom code was developed to create the mesh for the woven fabric. This disadvantage limits the usage of model with available finite element pre-processors. Tangent modulus of the beam/truss elements was obtained from the experimental uniaxial tensile stress-strain curves while the shear modulus of the shell/membrane elements was determined by curve fitting a polynomial to the experimental shear stress-strain curve and then differentiating it.

Another modeling approach that is based on unit cell representation aims to model the 3D structure of woven fabric unit cell within a membrane/shell element formulation. These models are generally based on Kawabata's unit cell where the single yarn cross-over point was idealized with linear yarns (Figure 1.13) [36, 39, 57, 59, 60, 62].

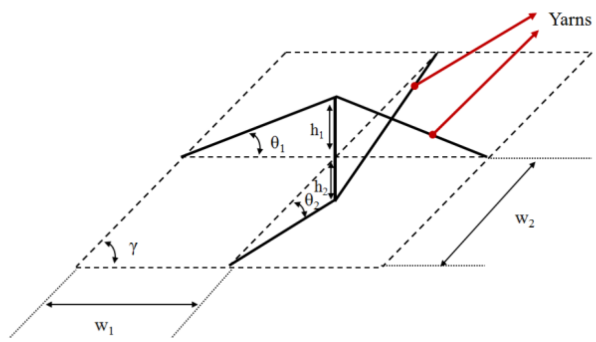

Figure 1.13 Idealized crossover geometry by Kawabata et al. [58].

Several researchers adopted this unit cell to model woven fabrics. King et al. developed a model using this cell and implemented several deformation mechanisms involved [58]. They used truss elements for yarn behavior, bending springs for decrimping response, an interference spring for biaxial response and locking trusses for the shear response. The deformation gradient was employed to determine the fabric configuration within a shell element formulation. An energy minimization technique was adopted to determine the geometric parameters that can't be computed from the deformation gradient. The yarn behavior and bending spring parameters were obtained from single yarn experiments while sandwich tests were employed to obtain the interference spring behavior. Moreover, a trial and error approach was adopted using picture frame tests to determine the parameters of the crossover spring and locking trusses. The model was validated with uniaxial tensile and picture frame tests. Shahkarami et al. adopted a similar approach to King et al. [39]. They used a mesoscale finite element model for a single crossover point and carried out compression tests to determine the interference spring's behavior. For shear behavior, they assumed a stepwise function for the shear modulus as a function of shear strain. The material model was only validated with impact experiments.

The comparison of most of the available macroscale material models in the literature in terms of model/formulation type, implemented mechanical responses and experimental validation is given in Table 1.3.

Table 1.3 Comparison of macroscale woven fabric models in the literature.

Work	Model type	Uniaxial	Biaxial	Shear	Validation
Dong et al. [9]	Planar Hypoelastic	Yes[1]	No	Yes[3]	Uniaxial tensile Bias extension 30° off-axis Indentation
Peng et al. [14]	Planar Hypoelastic	Yes[1]	No	Yes[3]	Bias extension Picture frame
Peng et al. [23]	Planar Hyperelastic	Yes[1]	No	Yes[1]	Uniaxial tensile Bias extension Picture frame
Boisse et al. [20] Hamila et al. [55]	Planar Hypoelastic	Yes[1]	Yes[2]	Yes[2]	Hemispherical forming Bias extension Picture frame
Jauffres et al. [22]	Planar Hypoelastic	Yes[1]	No	Yes[1]	Bias extension Picture frame
King et al. [58]	Sawtooth Hyperelastic	Yes[1]	Yes[1]	Yes[3]	Uniaxial tensile Bias extension
Shahkarami et al. [39]	Sawtooth Hypoelastic	Yes	Yes[3]	Yes[2]	Impact

[1] *Experimentally determined*
[2] *Numerically determined*
[3] *Trial and error (Both experimental and numerical)*

1.2 Problem Statement

Woven fabrics offer various possibilities in terms of design because of their high versatility and adjustable properties. However, their hierarchical construction involving different length scales separates them from the conventional materials and makes them a challenging choice in terms of design. Even though there are various computational modeling techniques at each length scale, there is no widely accepted modeling technique due to the complex length scale interactions. Therefore, there is still a need for experimentally validated robust, accurate and fast design framework for woven fabrics to expand their usage to other applications. The available computational models in the literature have their own advantages and disadvantages/limitations. Most of these models rely on rigorous, costly and time consuming experimental work to calibrate the material properties and parameters to obtain realistic fabric response without considering length scale effects. Most of these efforts are focused on macroscopic length scale since it is more computationally efficient. Moreover, the current approaches are fundamentally phenomenological and there is not a clear physically-based link between modeling the length scales thus rendering the use of a design framework approach almost impossible for new woven fabric materials limiting their application.

1.3 Research Objectives, Approach and Contributions

The main goal of the current work is to develop an experimentally validated robust and efficient multi length scale (meso and macro length scales) computational modeling framework for woven fabrics that is physically based providing valuable insight into key deformation mechanisms and associated nonlinear mechanical response (Figure 1.14). To achieve this goal, this dissertation has four distinct objectives:

i. To experimentally characterize woven fabrics (Plain weave Kevlar fabrics) under various loads while focusing on shear characterization and investigating important deformation mechanisms and extracting important material properties,

ii. To develop a mesoscale numerical modeling approach that can model meso length scale deformation mechanisms and mechanical response. The mesoscale approach's main goal is to reproduce the woven fabric behavior by carrying out virtual experiments. Another objective of mesoscale modeling is to parametrically study the effects of the material properties and architectural parameters on the overall fabric behavior,

iii. To develop macroscale numerical models based on the mesoscopic structure of woven fabrics to investigate the effects of important deformation mechanisms while studying the experimentally observed mechanical responses under various loads,

iv. To establish a systematic link between numerical modeling methods at mesoscopic and macroscopic length scales thus developing a robust design methodology for woven fabrics capable of identifying important parameters required by the framework.

To achieve these goals, the current work employs both experimental and numerical modeling approaches (Figure 1.14). The experimental approach aims to determine and investigate complex deformation mechanisms and associated nonlinear mechanical response necessary to validate the numerical work. Hence, both single yarns and woven fabric are experimentally characterized under various loadings. In the mesoscale modeling approach, mesoscale numerical models are developed and again validated using the results of the experimental approach. Then, macroscale numerical models are implemented and also validated using the experimental results in the macroscale approach. Finally, the mesoscopic and macroscopic modeling approaches are linked together to develop a design framework for woven fabrics.

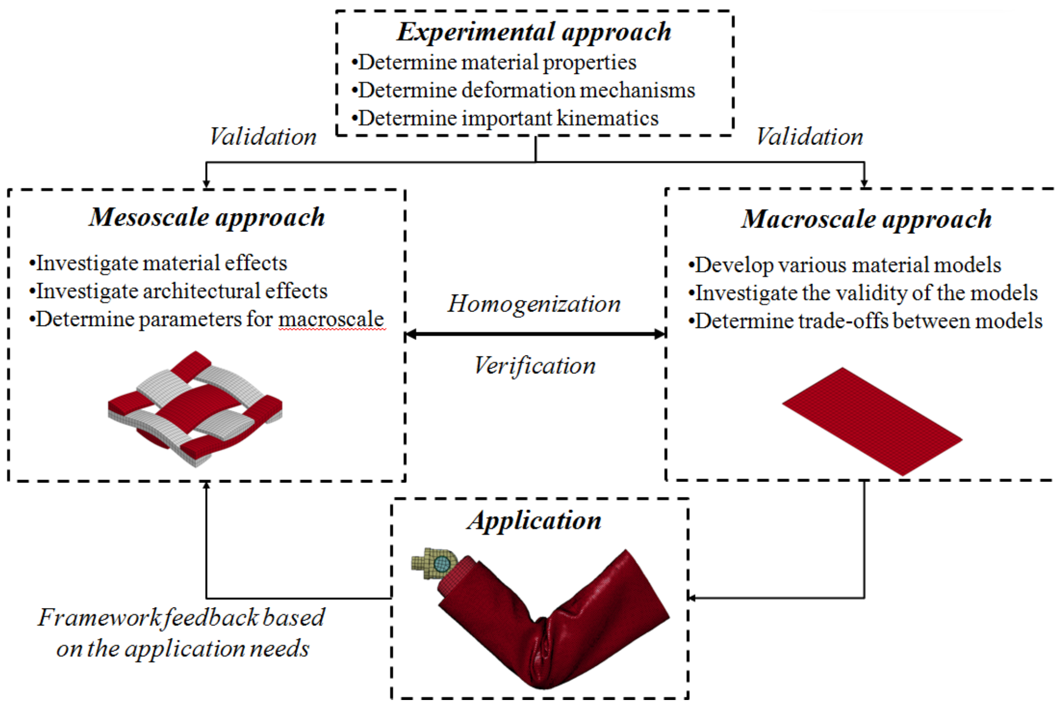

Figure 1.14 Research approach.

Furthermore, the current research work aims to make the following contributions to the state-of-the art:

i. Development of a new transversely isotropic yarn material model with transverse nonlinearity using a hyperelastic formulation, and identification of relative effects of yarn material properties on the macroscopic response of woven fabrics using design-of-experiments under various loading conditions.

ii. Development of an efficient macroscale constitutive material model assuming yarns lie on the same plane where material properties/parameters can be obtained directly from experiments.
iii. Development of a macroscale constitutive material model based on a sawtooth mesoscopic unit cell of woven fabrics thus considering the biaxial response where material properties/parameters can be obtained directly from experiments..
iv. Determination of domain and accuracy of the macroscopic material models developed through parametric variation of loads.
v. Development of a systematic link between the mesoscopic and macroscopic length scales to develop a design framework for woven fabrics considering different length scales; determination of material properties/parameters required by the macroscopic material models from mesoscopic level unit cell simulations.
vi. Determination of validity, computational efficiency as well as the trade-offs between the mesoscopic and macroscopic length scale modeling approaches.

To achieve the research objectives of the current work, the dissertation is organized as follows: the second chapter introduces the experimental methods used/adopted to characterize woven fabrics. The third chapter introduces the mesoscopic length scale numerical approach while the fourth chapter outlines the work carried out for macroscopic numerical approach. Moreover, the link between the numerical modeling approaches developed is detailed in chapter five. Finally, the chapter six concludes the dissertation with conclusions and future work.

Chapter 2

EXPERIMENTAL WOVEN FABRIC CHARACTERIZATION

2.1 Introduction

The mechanical response of woven fabrics depends on various parameters such as the materials used, yarn structure and the weave architecture. These factors play important roles in the large scale deformation mechanisms and macroscale mechanical response. This complex mechanical behavior also arises from woven fabrics' multiscale nature where smaller length scale effects are transferred to larger scales. Hence, experimental characterization coupled with computational simulations are required to study these complex material systems. This chapter focuses on the experimental characterization of woven fabrics under various loads including uniaxial, biaxial, shear and compression. Several experimental tests are carried out on plain weave Kevlar fabrics to determine important material properties and nonlinear mechanical response.

2.2 Woven Fabrics Characterized

Kevlar filaments belong to aromatic polyamide family of organic fibers and they are manufactured with polymerization of para-phenylene diamine and terephthaloyl [9]. The filaments are manufactured with a spinning process where chains form between the molecules. These chains result in higher strength and several other desirable material properties which make Kevlar fabrics advantageous materials for various engineering applications.

In this work, two different ballistic grade Kevlar fabrics are characterized under uniaxial and shear loads. Both woven fabrics have plain weave architecture since this weave is the most commonly adopted weave type in the ballistic applications. The woven fabrics studied exhibit different tightness and fiber materials. The first fabric (K706) is made out of Kevlar KM2 filaments while the second fabric (K745) uses Kevlar-29 filaments. Both fabrics have the distinct yellow color specific to Kevlar filaments (Figure 2.1). K706 fabric has smaller yarns compared to K745 and it is more tightly woven. On the other hand, K745 has larger and thicker yarns and it is a heavier weave. Some of the specifications of the woven fabrics from manufacturer's product datasheet are presented in Table 2.1 [63].

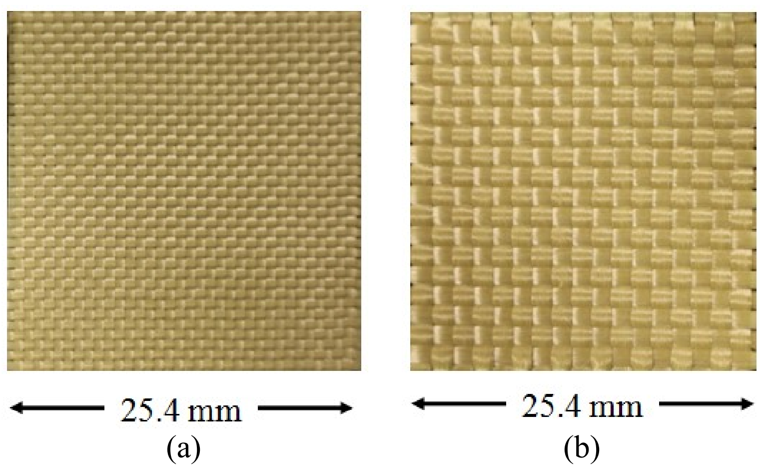

Figure 2.1 Kevlar woven fabrics characterized: (a) K706, and (b) K745.

Table 2.1 Specification of the selected fabrics.

Fabric type	Fiber type	Fiber density (g/cm^3)	Yarn size (denier)	Warp/weft count (yarns/in)
K706	KM2	1.44	600	34
K745	Kevlar-29	1.44	3000	17

The weaving process creates two distinct yarn directions called weft and warp. Since the yarns are subjected to multi-axial loads during the weaving process, they exhibit a permanent crimp (wavy structure). The amount of the crimp is based on the weave type as well as the yarn direction. For both fabrics studied, the weft yarns exhibit lower crimp amounts when compared to warp yarns due to the loads induced on the yarns during manufacturing.

2.3 Uniaxial Tensile Tests

Since the plain weave Kevlar fabrics studied have two distinct yarn directions, both fabrics and yarns extracted from the fabrics are characterized under uniaxial tensile loading. For single yarn experiments, the weft and warp yarns are carefully extracted from both fabric types to minimize any damage to the yarns. Test specimens are prepared based on the ASTM D7269 standard (standard test methods for tensile testing of Aramid yarns) with a specimen length 101.6 mm. Glass/epoxy end tabs are attached to the yarns with a high strength epoxy. The specimens are loaded into mechanical clamps and the crosshead displacement rate is set to 10 mm/min on a standard load test frame (Instron 5567). A 5kN load cell is used with a sampling rate of 50 Hz to collect displacement and force data. Five different specimens are tested for each yarn direction. Stress-strain curves are determined from force - displacement data obtained from the tensile machine. Since there is no direct way to measure the strain on the yarns due to the crimp, crosshead displacement and the initial specimen length are used to determine the strain (Apparent strain). The yarn cross section is assumed to be elliptical and constant to calculate the stresses [10]. Figure 2.2 shows the stress - strain curves for both Kevlar fabrics studied.

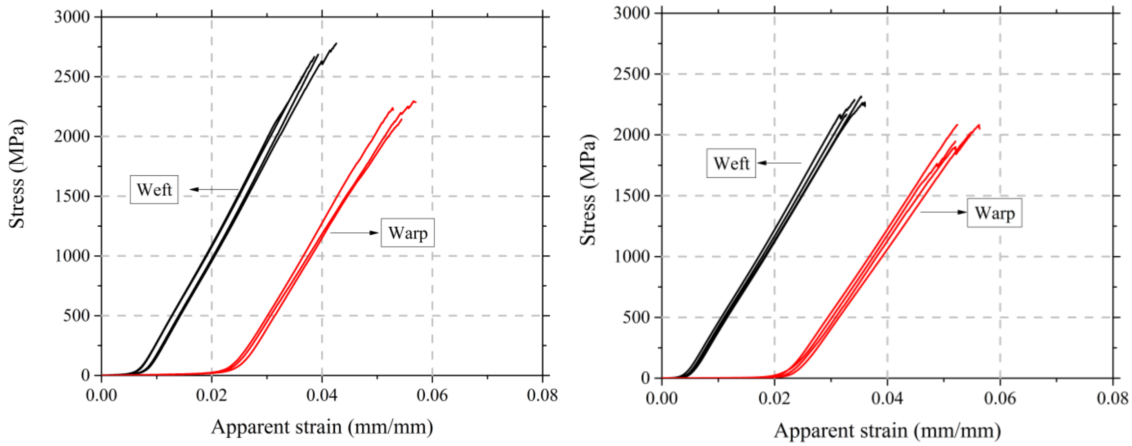

Figure 2.2 Representative single yarn uniaxial tensile tests results: (a) K706 yarns, and (b) K745 yarns.

Since both yarn directions for each fabric type have permanent crimp, the initial portions of the stress-strain curves exhibit a compliant response. The compliant mechanical response observed is mainly due to the yarns' initial crimped structure. The loaded yarns start to straighten and lose their crimp when they are subjected uniaxial loads. Once the yarns are fully straightened, the yarns' longitudinal direction aligns with the loading direction and a non-compliant response is observed. The yarns' moduli were calculated from this linear non-compliant region of stress-strain curves presented in Figure 2.2 (Table 2.2). The difference between the modulus of the weft and warp directions can be attributed to the weaving process and the resulting cross-sectional areas of each yarn direction.

Table 2.2 Yarns' modulus obtained from single yarn tensile tests (4 specimens with average and one standard deviation).

Fabric type	Weft modulus (GPa)	Warp modulus (GPa)
K706	79.83 ± 1.16	69.84 ± 2.15
K745	75.39 ± 1.11	65.59 ± 1.66

K706 fiber modulus: 82.6 GPa

The fabrics' mechanical response under uniaxial loading can also be investigated through uniaxial tensile test experiments. In these experiments, one of the yarn directions is aligned with the loading direction while the other direction is free to move (Figure 2.3).

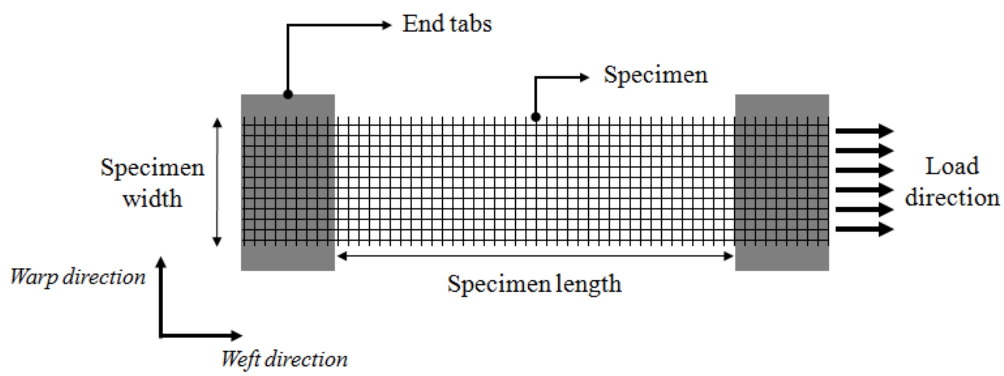

Figure 2.3 Uniaxial tensile test setup.

In the current work, the uniaxial tensile experimental results were taken from Dong et al.'s work [9]. The test specimens had a length of 101.6 mm and a width of 25.4 mm. Aluminum end tabs were bonded to the fabric specimens and attached to the tensile test machine with hydraulic grips. The experiments were carried out with 0.1 mm/second crosshead speed. The experimental results of K706 and K745 fabric styles are shown in Figure 2.4 for both yarn directions. Both fabric types exhibit bilinear mechanical response under uniaxial loading for weft and warp yarn directions. Since warp yarns have higher crimp amounts, higher deformations (strains) are required to fully straighten these yarns. The results presented in Figure 2.4 are used to validate the numerical models developed in the current work.

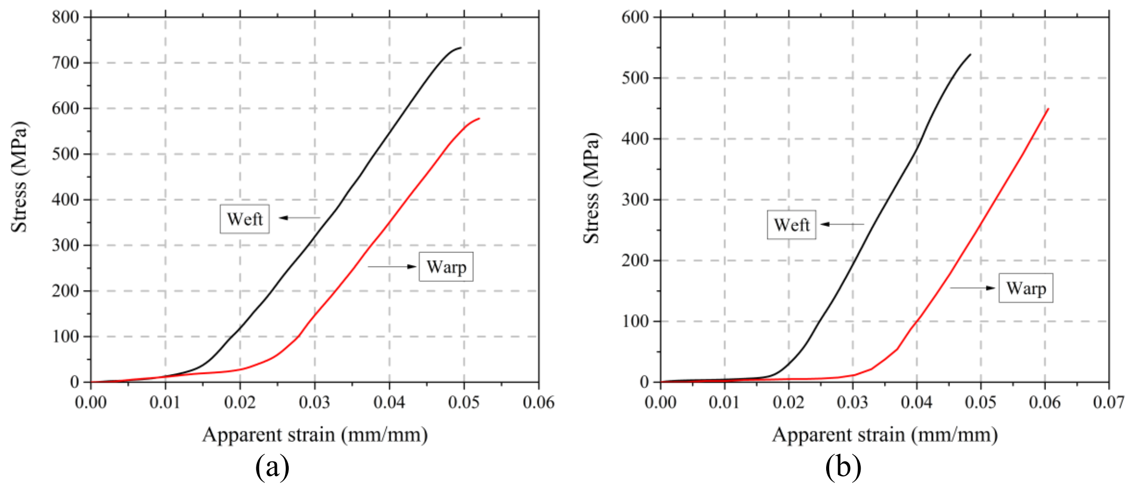

Figure 2.4 Fabric uniaxial tensile test results taken from Dong et al. [9].

2.4 Bias Extension Tests

Shear characterization of woven fabrics is more complicated due to the different mechanisms involved during the deformation. These mechanisms involve initial relative rotations of the yarns and potential locking of the yarns due to the transverse compression. Hence, woven fabrics exhibit highly nonlinear mechanical response under shear loads. Due to the highly complex nature of shear deformation, various experimental shear characterization methods have been proposed for woven fabrics. The most commonly adopted test methods are (1) Bias extension, and (2) Picture frame tests [24, 26, 30, 64].

In bias extension tests, a rectangular specimen is used where the yarns are initially oriented at $\pm 45^{o}$ with respect to the loading direction. The fabric specimen can be easily attached to a tensile test machine for shear characterization. This experimental method is fairly easy to conduct. However, the test suffers from heterogeneous deformation zones due to the boundary conditions imposed on the fabric. Hence, optical imaging and special formulations are required to determine the shear behavior [24]. The picture frame is another common test used for shear characterization of woven fabrics. In this test, a square shaped specimen is attached to a special clamping system. Then, a tensile test machine is used to impose shear loading through the clamping system. The picture frame provides a homogeneous deformation zones for shear characterization. However, the results are highly dependent on the boundary conditions due to the possibility of imposing preloads on the test specimen during clamping [65].

Bias extension tests are adopted in this dissertation to characterize woven fabrics' shear response since these tests do not require any special clamps and the results are not influenced due to preloads imposed during clamping of the specimens. The overall test setup adopted is shown in Figure 2.5.

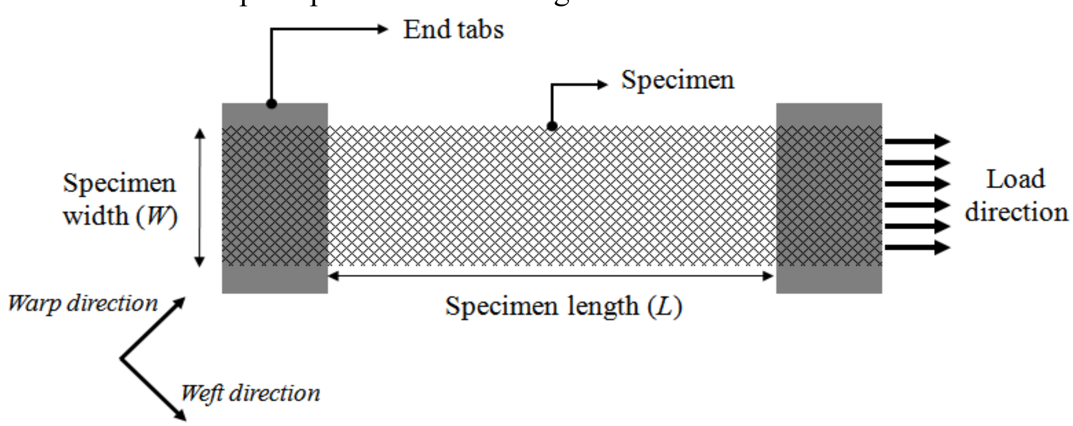

Figure 2.5 Bias extension test setup.

The woven fabric specimens are cut into rectangular shapes where the yarns are oriented at ±45^o with respect to the loading direction. During the tests, the shorter edges of the specimens are clamped while the longer edges were free to move. The specimens can be easily attached to a tensile test machine to impose shear deformation on the fabric. During the tests, the yarns initially rotate relative to each other and then start transversely compressing each other. Since the yarns at the clamped boundaries have one edge clamped while other edge is free, three distinct heterogeneous deformation zones are observed during these experiments. These zones are shown in Figure 2.6.

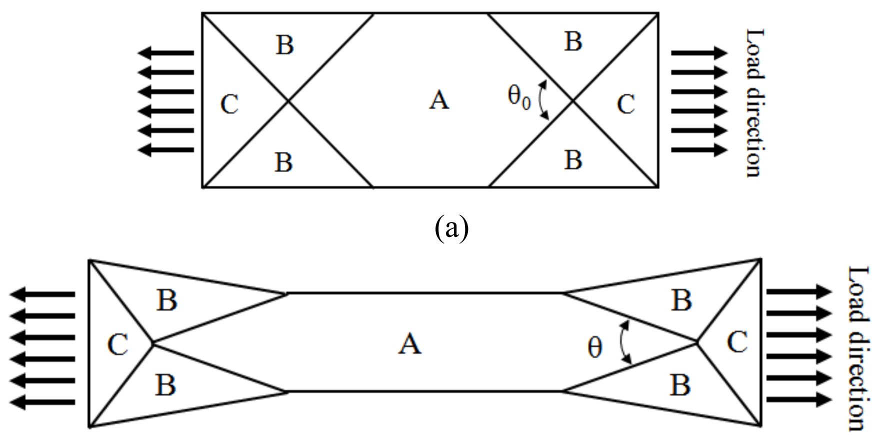

(b)

Figure 2.6 Heterogeneous deformation zones observed during bias extension tests: (a) Undeformed specimen, and (b) Deformed specimen.

As the crosshead displacement of the tensile test machine increases, the region "A" experiences full shear while other regions (B and C) undergo mixed deformation modes. In region "C', the specimen does not go through any shear deformation since the yarns in these regions do not rotate relative to each other. On the other hand, region "B" undergoes half shear since it is a transition zone between regions "A" and "C". Hence, the aspect ratio of the fabric specimen becomes important to avoid the effects of the heterogeneous deformation zones on the results. The specimens' aspect ratio is defined as the ratio of the specimen length (*L*) to the specimen width (*W*). An aspect ratio of 2 or higher is desired to obtain a homogeneous shear region in the middle of the specimen [24].

Since different materials and specimen sizes can be tested with bias extension tests, a normalization method based on energy arguments has been proposed to obtain normalized shear moment as a function of shear angle for comparison purposes [66]. During bias extension tests, force - displacement data can be extracted from the tensile test machine. The shear angle (γ) in region "A" can also be determined with the kinematic assumptions of inextensible and pin-jointed yarns as [24, 26, 66]:

$$\theta = 2\cos^{-1}\left[\cos\left(\theta_0/2\right) + \frac{\delta}{2(L-W)\cos\left(\theta_0/2\right)}\right]$$
$$\gamma = \frac{\pi}{2} - \theta \tag{2.1}$$

where L, W, θ_0, θ and δ are the specimen length and width, initial and current angles between the yarns, and the crosshead displacement measured from the tensile test machine, respectively (Figure 2.6). To calculate the normalized shear moment, the power generated by the tensile test machine can be related to the power dissipated in the regions "A" and "B" as:

$$F\dot{\delta} = M_s(\gamma)A_A\dot{\gamma} + M_s\left(\frac{\gamma}{2}\right)A_B\frac{\dot{\gamma}}{2} \tag{2.2}$$

where F, A_A, A_B and M_s are the force measured from the tensile machine, initial area of regions "A" and "B", unit moment per initial area to deform fabric, respectively. Eq. 2.2 does not include a term for region "C" since this region does not go through any shear deformation during the tests. On the other hand, the shear angle in region "B" is half of the region "A" since it undergoes half shear deformation due to the boundary conditions. Moreover, the areas of regions "A" and "B" can be determined from the specimen dimensions as:

$$A_A = \frac{2LW - 3W^2}{2}$$
$$A_B = W^2 \tag{2.3}$$

Then, the unit moment required to deform the fabric under shear loading can be determined by combining Eqs. 2.1-2.3 as:

$$M_s(\gamma) = \frac{1}{2L - 3W}\left\{\left(\frac{L}{W} - 1\right)F\left(\cos\frac{\gamma}{2}\right) - WM_s\left(\frac{\gamma}{2}\right)\cos\frac{\gamma}{2}\right\} \tag{2.4}$$

The unit moment defined by Eq. 2.4 is a function of force measured from the tensile machine and the shear angle. It also has a recursive form and values can be determined in an iterative manner. Moreover, Eq. 2.4 can also be used to compare shear response of various fabrics with different materials and architectures.

The shear characterization of K706 and K745 plain weave fabrics were carried out with bias extension tests. The specimens were initially cut into rectangular pieces with a width of 25. 4 mm and a length of 150.8 mm. Then, the glass/epoxy end tabs were attached to the fabric specimens using a high strength epoxy adhesive giving a final gauge length of 101.6 mm between the end tabs. 5 specimens for each fabric type were prepared. The specimens were marked without damaging the specimens along the yarn directions with a black marker (Figure 2.7) to determine the shear angles with an optical camera (Canon EOS T2i).

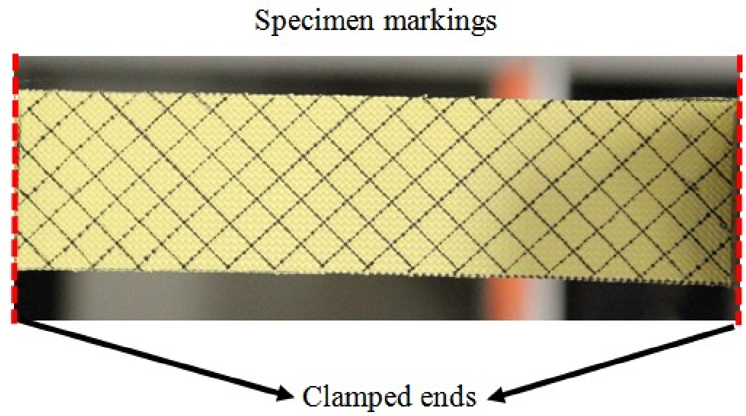

Figure 2.7 K706 specimen markings for bias extension tests.

The tests were carried out on a standard load test frame (Instron 5567) with a 5kN load cell and 10 mm/min cross head displacement rate for quasi-static loading. Force - displacement data was recorded at 50 Hz while images were taken at an interval of 1 image/mm for further processing. To determine the shear angle at a given crosshead displacement, a custom MATLAB code was developed that can calculate the angles between the marked yarns.

Figure 2.8 shows the force - displacement and shear angle-displacement curves (Including the ideal shear angle given by Eq. 2.1) for K706 and K745 woven fabrics. Error bars represent ±1 standard deviation (SD) of the experiments (4 specimens tested for each fabric type). Force - displacement curves exhibit a highly nonlinear nature for both fabric types (Figures 2.8a and 2.8c).

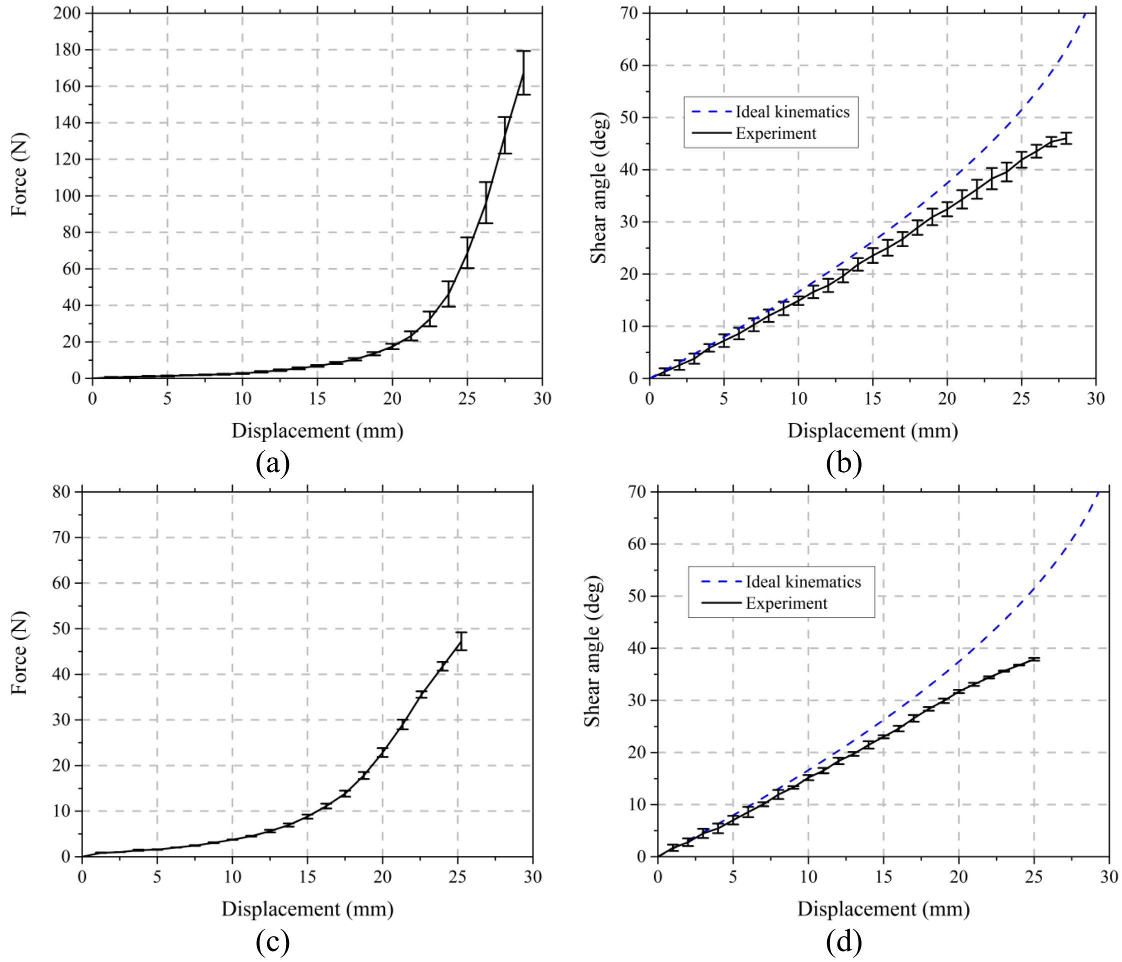

Figure 2.8 Bias extension test results; K706: (a) Force - displacement, (b) Shear angle - displacement, and K745: (c) Force - displacement, (d) Shear angle - displacement.

For both fabric types, an initial compliant force response followed by a steep rise was observed. The highly nonlinear mechanical response can be attributed to the deformation mechanisms involved at the yarn level (mesoscale). The yarns within the woven fabric are initially free to rotate. When the fabric is subjected to shear loading, the yarns start rotating relative to each other. During this stage, the resistance to deformation is mainly due to the frictional resistance to the yarns' rotation. After a certain deformation, the filaments within the yarns rearrange themselves and start compressing themselves in the transverse direction resulting in an increased resistance to the shear deformation. Hence, very highly nonlinear force responses were observed for both fabrics. Figures 2.8b and 2.8d show the shear angle change with the crosshead displacement as well as the shear angle change assuming ideal kinematics given in Eq. 2.1. It can be seen that K706 follows the ideal kinematics up to ~15 mm (25^o) crosshead displacement while K745 follows it up until ~10 mm (18^o) displacement. After these crosshead displacements, both fabric types start deviating from the ideal kinematics (inextensible and pin-jointed yarns). This deviation can be attributed to a yarn slippage mechanism involved during bias extension. The yarns at the boundaries are clamped only at one end while other is free to move. Because of these boundary conditions, the boundary yarns can slip causing specimen to extend without increasing the shear angle. This deformation mechanism is governed by the yarns' bending stiffness and frictional resistance at the crossover points. Due to this mechanism, experimental shear angle - displacement curves for both fabrics deviate from the ideal kinematics curve. Figure 2.9 shows the shear angle distribution across the woven fabrics at the 20 mm crosshead displacement as well as the progression of deformation up until the failure of the specimens. It can be seen that the specimen shape is similar to Figure 2.6 where three deformation regions (A, B and C) are visible.

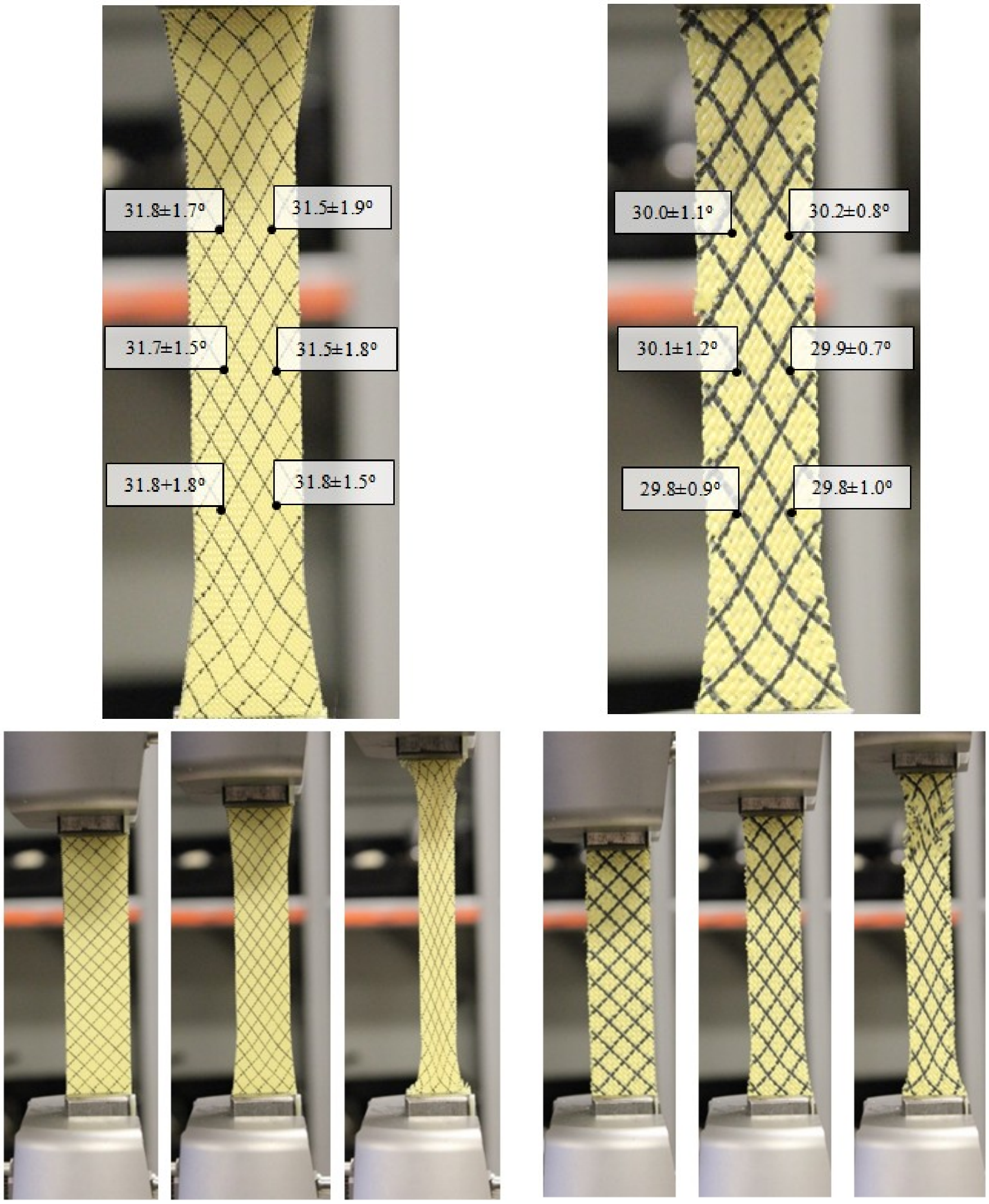

(a) (b)

Figure 2.9 Shear angle distribution at 20 mm crosshead displacement and deformation of the woven fabric specimens under shear loading: (a) K706, and (b) K745.

Since two different plain weave fabrics were characterized under shear loading, the energy based normalization method given in Eq. 2.4 was used to normalize the results for comparison purposes. A custom MATLAB code was developed to obtain the normalized unit moment - shear angle curves for each fabric characterized in a recursive manner. Figure 2.10 shows the normalized unit moment - shear angle curves for both K706 and K745 woven fabrics. It should be noted that K745 fabric exhibits a stiffer shear response compared to the K706 fabric style.

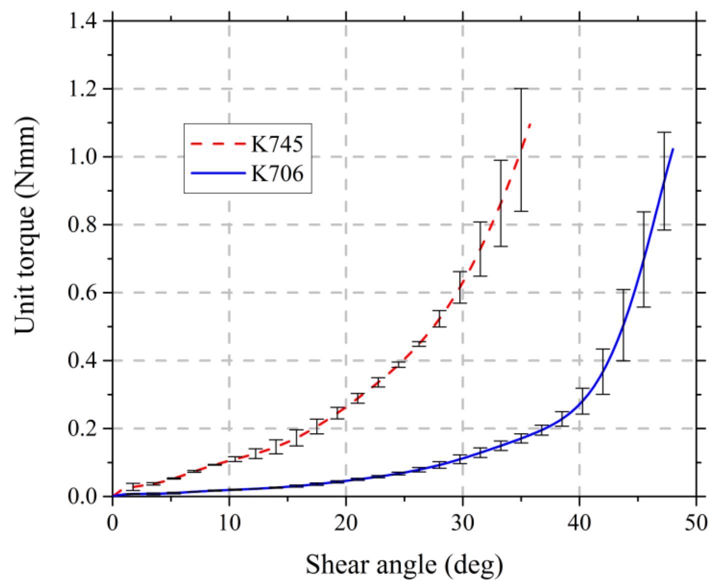

Figure 2.10 Normalized unit moment for K706 and K745 woven fabrics (Error bars represent ±1 SD).

This difference can be attributed to the yarn dimensions and materials of the fabrics even though they have the same plain weave architecture. The locking phenomenon was observed at an earlier shear angle for K745. Hence, K745 fabric can resist shear loads at the earlier stages of the deformation. To characterize this locking phenomenon, the shear angle corresponding to this deformation was determined both analytically and experimentally. The analytical locking angle can be determined by assuming the yarns lie on the same plane. Since the yarns start to compress each other in the transverse direction during locking, the yarns should have contact in this direction as shown in Figure 2.11. Hence, the locking angle (γ_{lock}) where the yarns contact each other in the transverse direction can be determined from fabric geometry and the assumption of inextensible/pin-jointed yarns as [22]:

$$\gamma_{lock} = \frac{\pi}{2} - \sin^{-1}\left(\frac{w}{s}\right) \tag{2.5}$$

where w and s are the yarn width and the span of the fabric.

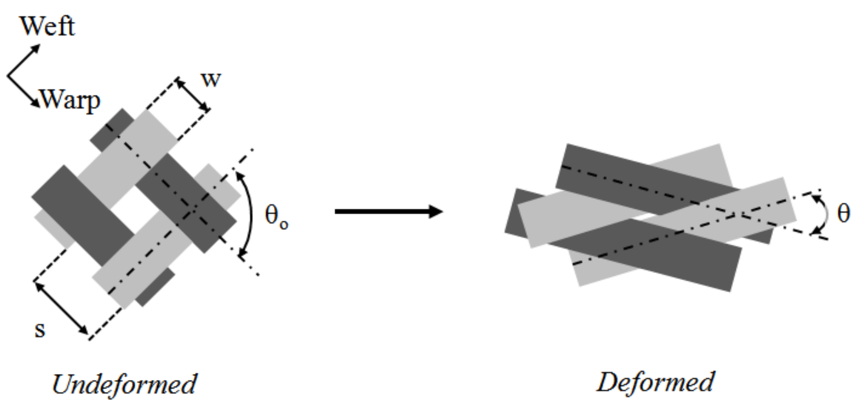

Figure 2.11 Determination of locking angle based on geometry.

The analytical locking angles for K706 and K745 fabrics were calculated using Eq. 2.5. The values of yarn width and thickness, and fabric span were taken from the literature for this purpose [40]. These values used in the calculations are presented in Table 2.3.

Table 2.3 Yarn and fabric dimensions for K706 and K745 [40].

Fabric type	Yarn width (mm)	Yarn thickness (mm)	Span (mm)
K706	0.536	0.115	0.747
K745	1.32	0.305	1.49

Beside the analytical locking angle, the experimental locking angle was also calculated from force - shear angle curves [30]. Two straight lines were fitted for the compliant and non-compliant regions of the force-shear angle curves and the intersection point of lines were assumed to be the experimental locking angle as shown in Figure 2.12.

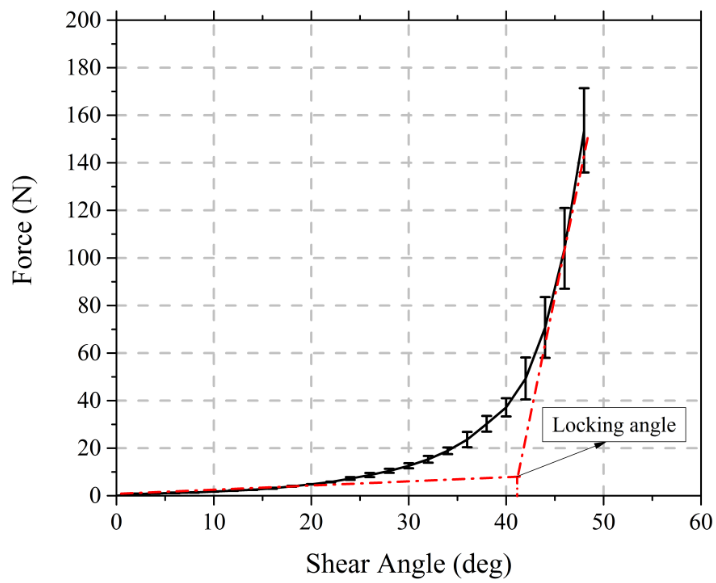

Figure 2.12 Determination of locking angle for K706 from experimental force - shear angle curves.

The values for both analytical and experimental locking angles are presented in Table 2.4 for both fabric types (K706 and K745). The theoretical locking angles are slightly higher than the experimental values. This difference can be attributed to the assumptions made in the calculation of analytical locking angle. The analytical model is solely based on the geometry. However, the yarn locking is a 3D phenomenon where yarn-to-yarn interactions and frictional effects are important. Hence, the locking happens at lower angles compared to the analytical one.

Table 2.4 Locking angles for K706 and K745 woven fabrics.

Fabric type	Analytical	Experimental
K706	43.7^o	$40.9^o \pm 1.7^o$
K745	28.8^o	$26.7^o \pm 0.7^o$

2.5 Indentation Tests

Although characterization using uniaxial and bias extension tests are necessary, the woven fabrics undergo more complex distortions involving both in-plane and out-of-plane deformations in actual use. In the current work, indentation tests are used to study the out-of-plane deformation and mechanical response (Figure 2.13). Dong et al. and Manimala et al.'s experimental work and results are adopted for the validation of the mesoscopic and macroscopic length scale finite element simulations [9, 49]. Figure 2.13 shows the setup used by Dong et al. and Manimala et al. to characterize the out-of-plane deformation and mechanical response for K706 fabric style. Two different indentation cases are studied based on the yarns' orientations with respect to the clamped edges of the fabric: (1) $\varphi=0^o/90^o$, and (2) $\varphi=\pm45^o$ (Figure 2.13). The $0^o/90^o$ degree specimens had dimensions of 51 mm x 40 mm where the shorter edges were bonded to aluminum end tabs with epoxy. An indenter with a 12 mm diameter was used to deform the fabric and the indenter displacement rate was set to 0.14 mm/s. The $\pm45^o$ tests had a specimen size of 52 mm x 25 mm while a 14 mm indenter was used. In both tests, the shorter edges were clamped and constrained while the longer edges were kept free.

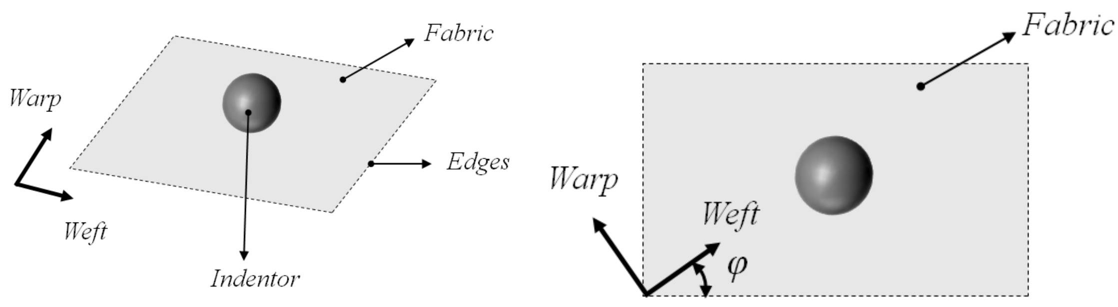

(a) (b)

Figure 2.13 Indentation test setup used in the experiments[9, 49].

The experimental results for $0^o/90^o$ yarn angle orientation are shown in Figure 2.14. Since only experimental averages were presented in Dong et al. and Manimala et al.'s work, Figure 2.14 shows only the average force response recorded during the experiments [9, 49]. 0^o and 90^o yarn directions correspond to warp and weft yarns, respectively. In the experiments, either weft or warp yarn directions were constrained while the other yarn direction was free to move. Both experiments ($0^o/90^o$) exhibit a nonlinear mechanical response. An initial compliant force response followed by a steep increase was observed for both experiments. The mechanical response is highly influenced by the yarns located underneath the indenter. Since one of the yarn directions underneath the indenter is clamped at both edges, these yarns undergo decrimping resulting in a nonlinear mechanical response. The difference between the force responses observed would be attributed to the amount of crimp of the yarns in the fabric. Since warp yarns exhibit higher crimp, it takes more deformation (larger indenter displacement) to straighten these yarns. Therefore, warp yarn direction is shifted towards higher indenter displacements as shown in Figure 2.14.

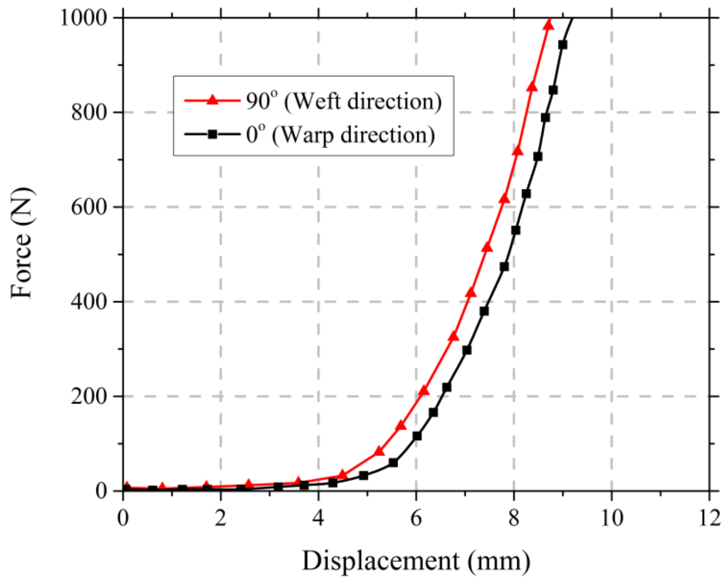

Figure 2.14 0°/90° yarn orientation indentation tests adopted from Manimala et al.'s work [49].

Figure 2.15 shows the mechanical response observed during the indentation tests with ±45° yarn orientation. The force response is compliant up until ~13 mm indenter displacement followed by a sudden increase. Since the aspect ratio of the fabric is ~2, the yarns underneath the indenter are free to rotate relatively. Hence, the force response of K706 fabric is softer compared to 0°/90° yarn orientation tests. As the deformation progresses, the yarns rotate freely until they are locked in a similar manner to the bias extension tests.

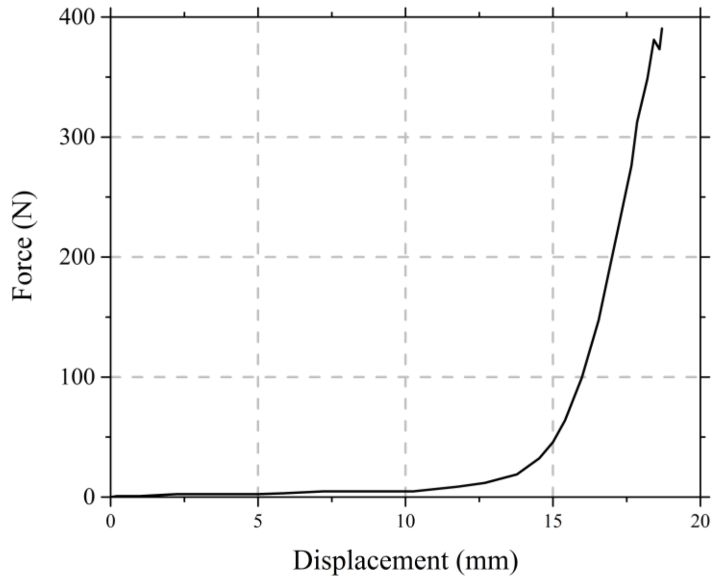

Figure 2.15 ±45° yarn orientation indentation tests adopted from Dong et al.'s work [9].

2.6 Summary and Contributions

Woven fabrics exhibit highly nonlinear mechanical response under various loading conditions. Hence, experimental characterization is important to capture and then analyze the complex deformation mechanisms and resulting nonlinear mechanical responses. In the current work, the single yarn tensile response and shear behavior of two commonly used plain weave Kevlar fabrics are characterized (K706 and K745). Single yarns extracted from woven fabrics are tested under uniaxial tensile loads to determine the Young's modulus of the yarns. Since the shear behavior of the woven fabrics are fairly complex due to the mesoscopic deformation mechanisms, bias extension tests were carried out on K706 and K745 fabrics. During the experiments, shear angle at different crosshead displacements were tracked and recorded for further analysis. The experimental results for both fabric types showed highly nonlinear mechanical response. Moreover, it was shown that the deformation kinematics observed during bias extension tests are not ideal and inherent yarn slippage becomes significant at certain shear angles. To compare the shear resistance of the two fabrics studied, an energy based normalization method was adopted to determine the normalized unit torque/moment required to deform a repeating unit cell of the woven fabric. The results revealed that K745 exhibit higher resistance to the shear deformation compared to the K706. The locking angle of the fabrics, which is a commonly used variable in numerical models, was also determined both analytically and experimentally. It was shown that experimental values are slightly lower than the analytical values.

On the other hand, Dong et al.'s uniaxial tensile tests on K706 and K745 fabric specimens are adopted to validate the numerical models presented in the following chapters. These tests are briefly explained and the experimental results are presented in this chapter. Furthermore, indentation tests carried out by Dong et al. and Manimala et al. are also adopted to validate the numerical models developed in this dissertation.

Chapter 3

MESOSCOPIC LENGTH SCALE COMPUTATIONAL MODELING

3.1 Introduction

In mesoscopic length scale modeling, the yarns are modeled explicitly and assumed to behave as continuums. This length scale modeling provides the ability to parametrically vary yarn-to-yarn interactions thus allowing one to develop physics based insights into the nonlinear mechanical response of woven fabrics. This chapter focuses on the modeling of woven fabrics at the mesoscopic length scale. Mesoscale computational models are developed and used to study the effects of material properties and architectures on the macroscale mechanical response of woven fabrics under various loading conditions.

3.2 Computational Modeling of Woven Fabrics

3.2.1 Numerical modeling of crimped single yarns using finite elements

Uncrimped (Straight) yarns are woven into different weave architectures to obtain the final woven structure. Due to the weaving process, the yarns are deformed with crimp. Even if the yarns are removed from the woven fabric, they still retain their crimped shape. To model the yarns and their geometric nonlinearity, 8-noded brick elements are the most commonly adopted element types as shown in Figure 3.1 [4, 5, 38, 41]. Therefore, solid elements are adopted to model yarns in the mesoscopic length scale modeling approach in this work.

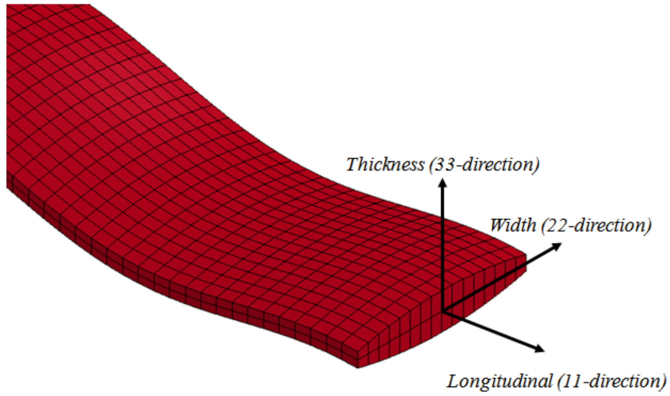

Figure 3.1 Crimped single yarn model with 8-noded brick elements.

The crimp of a yarn based on the weave architecture can be modeled with a trigonometric centerline equation defined as [4]:

$$z = \left(\frac{a}{2}\right)\cos\left(\frac{\pi x}{2}\right) \tag{3.1}$$

where x and a are the longitudinal distance and the yarn thickness in 33-direction, respectively. Furthermore, the yarn cross section is assumed to be fundamentally an ellipse given by the following equation:

$$\frac{z^2}{a^2} + \frac{y^2}{b^2} = 0.25 \tag{3.2}$$

where a and b are the yarn thickness (33-direction) and width (22-direction), respectively (11, 22 and 33 directions are defined as shown in Figure 3.1 since they are necessary for modeling the yarn material). To model the yarns with solid elements, 2 elements are used in the thickness direction based on previous studies to accurately capture the bending behavior of the yarns while the other mesh densities are determined based on a mesh sensitivity study [40].

The yarns are initially modeled with a hyperelastic orthotropic material model (Type 2 in LS-DYNA) relating the second Piola-Kirchhoff Stress ($\underline{S}$) to Green strain ($\underline{E}$) [67]. The model then relates the Piola-Kirchhoff stress to the Cauchy stress ($\underline{\sigma}$) using the deformation gradient. The constitutive relations used in the material model to obtain the yarn material behavior are given as (Prime denotes transpose):

$$\underline{S} = \underline{C}\,\underline{E} \tag{3.3}$$

$$\underline{E} = \frac{1}{2}\left(\underline{F}'\,\underline{F} - \underline{I}\right) \tag{3.4}$$

$$\underline{C} = \underline{T}'\,\underline{C_L}\,\underline{T} \tag{3.5}$$

$$\underline{C_L^{-1}} = \begin{bmatrix} 1/E_{11} & -\nu_{21}/E_{22} & -\nu_{31}/E_{33} & 0 & 0 & 0 \\ -\nu_{12}/E_{11} & 1/E_{22} & -\nu_{32}/E_{33} & 0 & 0 & 0 \\ -\nu_{13}/E_{11} & -\nu_{23}/E_{22} & 1/E_{33} & 0 & 0 & 0 \\ 0 & 0 & 0 & 1/G_{12} & 0 & 0 \\ 0 & 0 & 0 & 0 & 1/G_{23} & 0 \\ 0 & 0 & 0 & 0 & 0 & 1/G_{31} \end{bmatrix} \tag{3.6}$$

$$\underline{\sigma} = \frac{1}{J}\underline{F}\,\underline{S}\,\underline{F}' \tag{3.7}$$

where $\underline{C}$, $\underline{C_L}$, $\underline{F}$ and $\underline{T}$ are the global compliance matrix, the material compliance matrix, the deformation gradient and the transformation matrix between the global and material coordinate systems, respectively. The subscript 11 given in Eq. 3.6 corresponds to the longitudinal direction while 22 and 33 correspond to the width and thickness directions, respectively (Figure 3.1). The yarns are assumed to behave as transversely isotropic continuum where 22 and 33 directional properties are assumed to be the same. The material model requires 4 material properties based on the assumption: E_{11}, E_{22}=E_{33}, G_{12}=G_{31} and G_{23}. Moreover, the filament level interactions are assumed to be weak during deformation since the filaments are free to move within the yarns. Hence, all Poisson's ratios are assumed to be zero [4, 48]. However, it should be noted that the yarns might exhibit Poisson's effects when the filaments are closely packed together.

An initial mesh convergence analysis is carried out to determine the acceptable number of elements to accurately model the individual yarns. The number of elements along the longitudinal direction (11-direction in Figure 3.1) is determined through a mesh sensitivity analysis while the width (22-direction) and thickness directions' (33-direction) mesh densities are kept constant based on a previous study [40]. Hence, 2 elements across the yarn thickness and 6 elements across the width are used for the mesh convergence analysis. Single yarn uniaxial tensile test simulations are carried out for this purpose. The single yarn model has a length of 25.4 mm with a width of 0.536 mm and a thickness of 0.115 mm. Table 3.1 shows the material properties used for the yarn [40]. One of the ends of the models is fixed by constraining all of the translational degree-of-freedoms while a displacement boundary condition is prescribed to the other end.

Table 3.1 Material properties used for the initial mesh density study.

ρ (g/cm^3)	**E_{11} (MPa)**	**E_{22} (E_{33}) (MPa)**	**G_{12} (G_{31}) (MPa)**	**G_{23} (MPa)**
1.31	69000	620	3200	3200

The Grid Convergence Index (GCI), a common technique used in Computational Fluid Dynamics (CFD), is adopted to determine the number of elements required to accurately model the yarns [68]. The GCI method assumes a relation between the exact solution (f_{exact}) and the approximate solution ($f(h)$):

$$f_{exact} = f(h) + Ah^p + Higher \quad Order \quad Terms \tag{3.8}$$

where h is the discretization amount, A is a constant and p is the order of convergence. Then, the error is described by neglecting higher order terms as:

$$E = f(h) - f_{exact} = Ah^p \tag{3.9}$$

Eq. 3.9 can be used to investigate the order of convergence. Using 3 different mesh densities denoted as h_1, h_2 and h_3, where $h_1<h_2<h_3$ and assuming constant mesh refinement ratio ($r=(h_3/h_2)=(h_2/h_1)$), the following relation is defined:

$$p = \log\left(\frac{f_3 f_2}{f_2 - f_1}\right) \Big/ \log(r) \tag{3.10}$$

where p is the order of convergence and f is the outcome of the simulation. To quantify the amount of discretization error, the GCI method defines the following relations:

$$\begin{aligned} GCI_{12} &= \frac{F_s\left|e_{12}\right|}{\left(r^p - 1\right)} \\ GCI_{23} &= \frac{F_s\left|e_{23}\right|}{\left(r^p - 1\right)} \end{aligned} \tag{3.11}$$

where F_s is defined as a safety factor and has a value of 1.25 for comparison of three different mesh densities. Hence, GCI is a measure of percent deviation of the numerical solution from the asymptotic value. The asymptotic range of convergence can be checked using:

$$GCI_{23} = r^p GCI_{12} \tag{3.12}$$

Moreover, the unknown exact solution can be estimated through the following equation:

$$f_{exact} \approx f_1 - \frac{f_2 - f_1}{r^p - 1} \tag{3.13}$$

To determined the appropriate mesh density for single yarns, three different mesh densities were used for the mesh refinement study: 108, 216 and 432 elements per yarn period with a mesh refinement ratio of 2. Then, uniaxial tensile tests on single yarns were simulated by constraining the nodes at one of the yarns ends while applying a displacement boundary condition to the other yarn end. Force-strain curves obtained from simulations with specific mesh densities are shown in Figure 3.2.

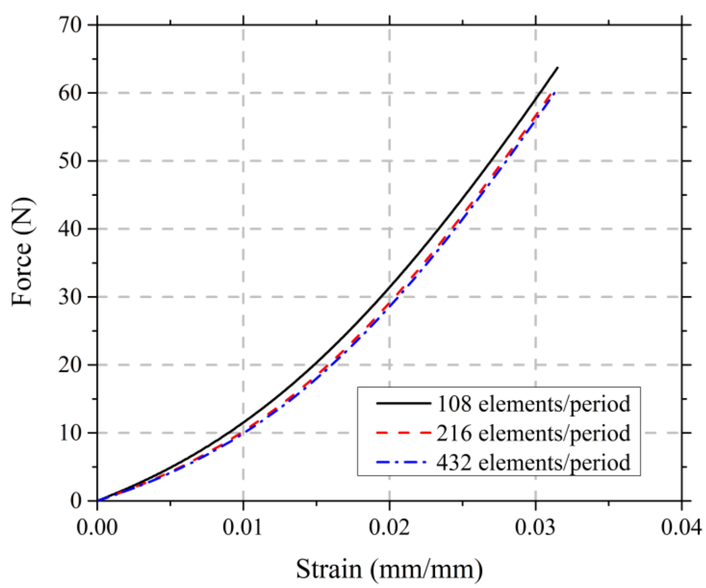

Figure 3.2 Mesh sensitivity analysis for single yarn simulations under uniaxial loading.

A strong convergence was observed in the force-strain curves of the simulations. The GCI analysis was carried out using the maximum force reached at the end of the simulations, corresponding to 3.15% strain as the outcome. The results of the analysis for the single yarn simulations is shown in Table 3.2. The convergence asymptotic check is close to 1 indicating that the solutions are within the asymptotic range of convergence. Based on the GCI analysis and Figure 3.2, mesh density of 216 elements per yarn period was determined to be adequate to obtain accurate results while keeping the computational resources low. It should be noted that different number of elements might be required for different loading types and the results presented in Table 3.2 is valid for only tensile loading.

Table 3.2 GCI analysis for the mesh sensitivity of single yarn uniaxial tensile test simulations.

Parameter	Value
Refinement ratio (r)	2
Order of convergence (p)	1.996
Estimate of exact force value (f_{exact}) (N)	60.858
Analytical force value (N)	60.306
Grid convergence index (G_{12}) (%)	0.422
Grid covergence index (G_{23}) (%)	1.669
Asymptotic range of convergence check	0.989

To determine the effects of the yarn material properties on the uniaxial tensile response, an initial parametric study is carried out by varying the yarn material properties. Each yarn material property is varied between levels 1 and 4 while the other material properties are kept constant by using the values presented in Table 3.1. The levels used in this study are presented in Table 3.3. The highest values (Level-4) used in this study were based on previous studies and provide an upper bound for this initial study [4, 5, 8, 37, 38, 40, 41]. The lower values are chosen to be significantly lower (but large enough to avoid any numerical instabilities) to investigate a large range of material properties and their effects.

Table 3.3 Yarn material properties used for single yarn tensile test simulations.

Parameter (MPa)	Level-1	Level-2	Level-3	Level-4
E_{11}	10000	20000	40000	80000
E_{22} (E_{33})	100	500	1000	3000
G_{12} (G_{31})	0.5	5	50	500
G_{23}	0.5	5	50	500

The results of the parametric study are compared with an analytical model of a single yarn. In this analytical model, the yarn is idealized such that there is no resistance to the deformation until they lose their crimp (decrimping) after which they act as linear springs with constant stiffness. The strain value corresponding to decrimping can be determined by dividing the apparent length of the yarn before any deformation to the physical straight length as shown in Figure 3.3. Using the trigonometric relation provided in Eq. 3.1., the physical length of the yarn (L) when they are fully straightened can be determined from:

$$L = \int_0^{L_0} \sqrt{1 + \left[\frac{d}{dx} \left(\frac{a}{2} \cos\left(\pi x / 2 \right) \right) \right]^2} \tag{3.14}$$

where L_0 is the crimped length of the yarn. Hence, the decrimping strain for the yarn with a width of 0.536 mm and a thickness of 0.115 mm is calculated as 1.45%.

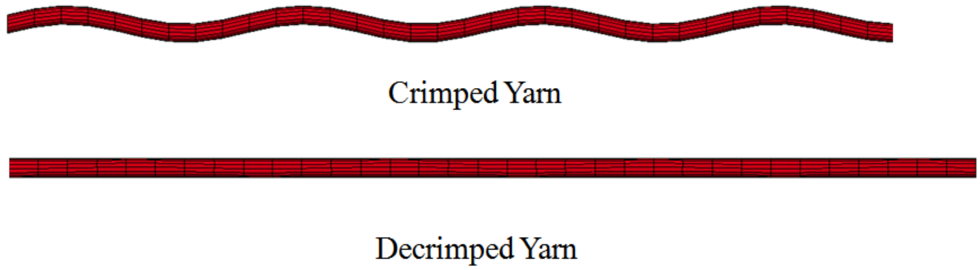

Figure 3.3 Deformation of a single yarn under uniaxial tensile loading.

Based on the results of parametric study on yarn material properties, the single yarns' force response under uniaxial loading was not affected by E_{22} (E_{33}) and G_{23}. On the other hand, E_{11} and G_{31} (G_{12}) had significant effects on the mechanical response of the yarns. The results of the variation of these two material properties are shown in Figure 3.4 along with the experimental results of King et al. for comparison purposes [58]. It is observed that G_{12} (G_{31}) had an influence on the force response before decrimping. This effect can be attributed to the change in the yarn geometry due to decrimping. When the yarns are subjected to uniaxial loading, they initially undergo transverse shear deformation which leads to a decrease in their crimp amount. Hence, the increased transverse shear modulus results in an increased resistance to uniaxial tensile deformation. Moreover, E_{11} had a similar influence on the mechanical response after decrimping. After decrimping, the longitudinal direction of the yarn aligns with the loading direction. Hence, the longitudinal modulus had a significant effect after decrimping.

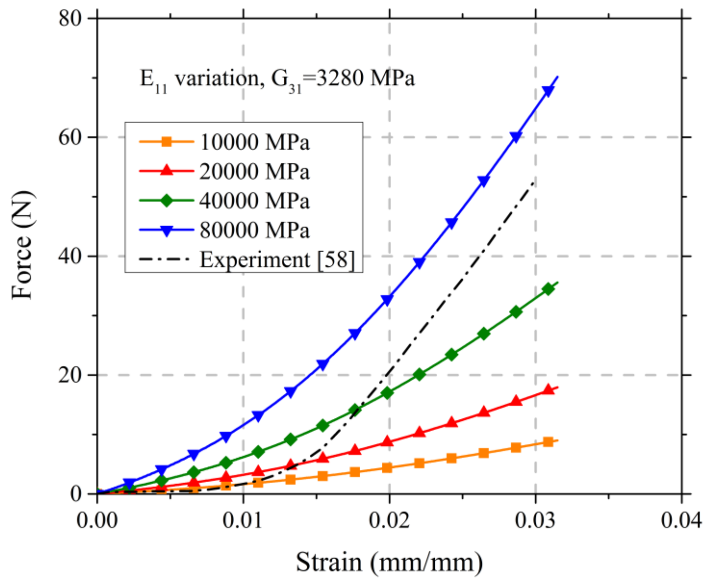

(a)

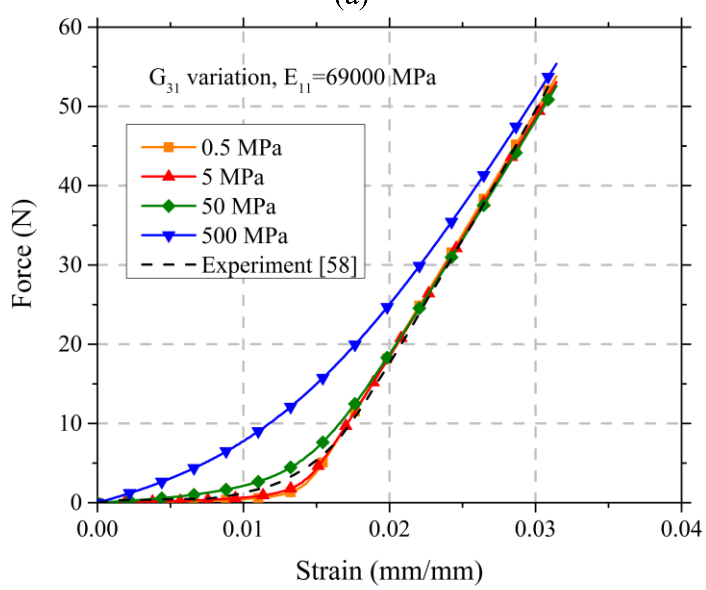

(b)

Figure 3.4 (a) Effect of E_{11} with a fixed G_{31} value, and (b) Effect of G_{12} (G_{31}) with a fixed E_{11} value [58].

3.2.2 Transversely Isotropic Nonlinear Material Model for Woven Yarns

The yarns within woven fabrics are constructed from several hundreds of fibers/filaments. Since they are weakly connected to each other, several deformation mechanisms are possible such as filament sliding and bending within the yarns. This weak connection between the filaments and associated deformation mechanisms result in a nonlinear mechanical response when the yarns are subjected to loads in the transverse direction (22 and 33 directions in Figure 3.1). The filaments within the yarns are free to move initially when they are not subjected to loads. They start to slide and move around filling the gaps within the yarns. This deformation mechanism results in an initial compliant mechanical response followed by a stiffer non-compliant response once the filaments can no longer simply move around and start to compress themselves when there are no gaps left within the yarn [3]. This mesoscopic length scale deformation of the yarns highly influences the mechanical response of the woven fabrics in the macroscopic length scale. Hence, the fibrous nature of the woven yarns should be taken into account in mesoscopic length scale to accurately model yarns. Several yarn material models taking into account the fibrous nature of the yarns have been proposed in the literature [1, 16, 20, 42, 43, 45, 46, 48, 69]. However, there is not any widely accepted material model due to the difficulty of determining material properties/parameters from experiments done on the individual yarns.

In the current work (which uses man-made filaments), the tensile and compression behavior of the yarns in the longitudinal direction (11-direction in Figure 3.1) are assumed to be same and the stiffness of this direction is determined by E_{11}. Moreover, the woven yarns are assumed to be transversely isotropic with a transverse nonlinear behavior. Hence, the material behavior is defined by the Eq. 3.6. The yarns within the fabric exhibit a highly nonlinear mechanical response when they are subjected to compressive loads in transverse direction. This behavior is mainly due to the filaments ability to move freely within a yarn. The filaments start to move and slide relative to each other when the yarn is subjected to transverse loading. During this deformation, a compliant response is observed. As the deformation progresses, the filaments start to pack and compress each other resulting in a highly non-compliant response. Moreover, the yarns do not resist deformation when they are subjected to tensile loads in the transverse direction since the interactions between the filaments are weak. Hence, the transverse moduli (E_{22} and E_{33}) are implemented using the following nonlinear form to take into account yarns' fibrous nature and provide a large and continuous change in stiffness as a function of applied strain:

$$E_{ii} = \begin{cases} E_{in} + E_0 e^{(-m\varepsilon_{ii})} & ,\varepsilon_{ii} < 0 \\ E_{in} & ,\varepsilon_{ii} \geq 0 \end{cases} \quad i = 2,3 \tag{3.15}$$

where ε_{ii} E_{in}, E_0, and m are the transverse strain at a given material direction, initial transverse modulus and material parameters required to define the nonlinear portion of the transverse yarn modulus. It should be noted that Eq. 3.15 has a nonlinear form for negative strains (compressive) while it is constant for positive strains (tensile). A small value is used for E_{in} to ensure the numerical stability of the finite element code. Figure 3.5 shows the transverse modulus variation defined by Eq. 3.15 as a function of compressive strain (Strain values shown in Figure 3.5 are the compressive strain applied to the yarns in the transverse direction). It should be noted that the models defining the yarns' transverse behavior (modulus as a function of transverse strain) in the literature are generally based on the high order polynomial functions and use incremental formulations. This can introduce oscillations, making explicit finite element simulations unstable. The current model adopts an exponential function to define yarns' behavior coupled with a hyperelastic formulation. Since the yarns are assumed to be transversely isotropic, the same values for E_{in}, E_0 and m are used for 22 and 33 directions. Moreover, all the Poisson's ratios are again assumed to be zero due to the weak interactions between the filaments. Hence, the material model requires a total of 6 material properties/parameters to define the yarn material behavior. These material properties/parameters are presented in Table 3.4. It should be noted that the yarn material response is assumed to be hyperelastic in all directions material directions and plastic deformations are not taken into account in the material model.

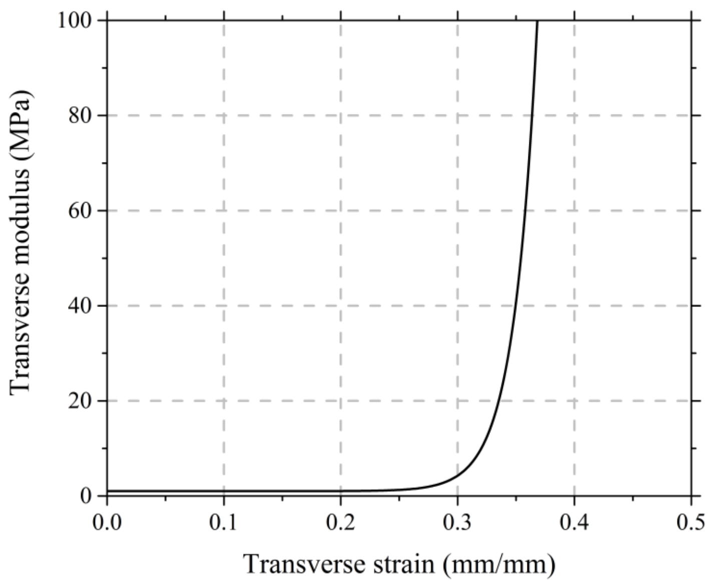

Figure 3.5 Nonlinear yarn transverse modulus change as a function of compressive transverse strain.

Table 3.4 Material properties/parameters required by the yarn material model.

Material property/parameter	Explanation
E_{11}	Longitudinal modulus
E_{ii} (i=2,3) & E_{in}, E_0, m	Transverse modulus
G_{12} (G_{31})	Transverse shear modulus
G_{23}	Shear modulus

The mesoscopic material model is implemented within an explicit finite element code through the user-defined-material (UMAT) subroutines. An incremental approach was initially adopted where incremental strains were used to determined Cauchy stresses. However, the material model was not able to reproduce the uniaxial tensile response due to inability of the finite element code to handle large displacements/rotations experienced during decrimping. Hence, the hyperelastic approach used by the LS-DYNA built-in linear orthotropic material model is adopted [67]. In this approach, the deformation gradient within the material coordinate frame is used to determine the Green-St. Venant strain tensors and stiffness matrix is assembled using the material model given by Eqs. 3.6 and 3.15. Then, 2nd Piola-Kirchoff stress tensor is determined. Since the finite element code used requires Cauchy stresses, 2nd Piola-Kirchoff stress tensor is transformed into Cauchy stresses and returned to the finite element code. Figure 3.6 shows the flowchart of the UMAT developed for the yarns.

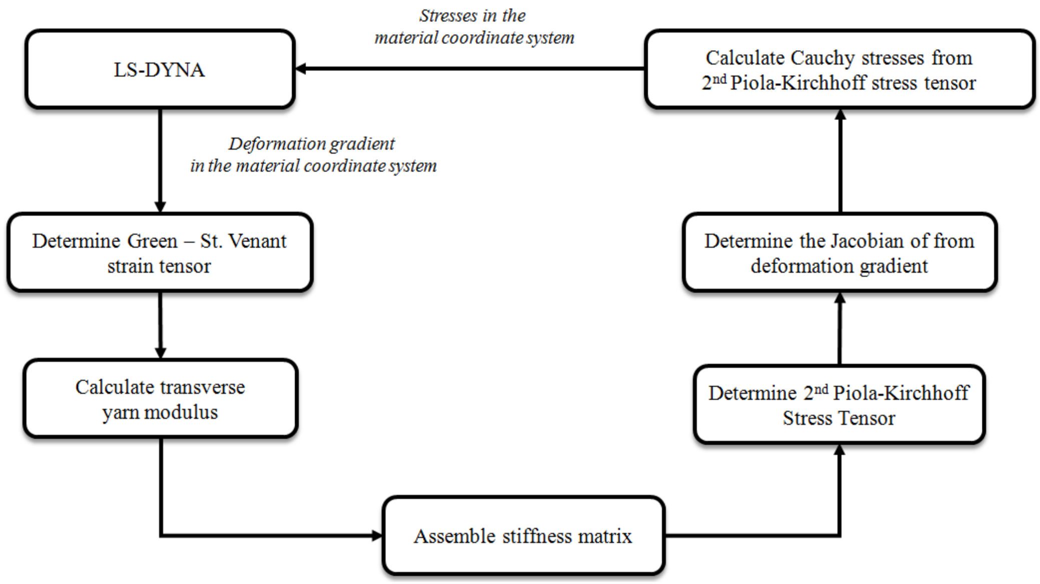

Figure 3.6 Flowchart of the nonlinear yarn material model within LS-DYNA.

3.2.3 Determination of material properties/parameters and validation of the material model

The yarn material model implemented requires a total of 6 material properties/parameters per yarn direction (weft and warp yarn directions). The values of these material properties/parameters are determined through an inverse method combining unit cell level numerical simulations and experimental tests. Therefore, unit cell level finite element modeling of woven fabrics is introduced initially and then that method will be used to determine the yarn material model properties/parameters is presented in this section.

Although real woven fabrics exhibit variations, for design studies, they can be considered as periodic materials since the yarns are woven into architectures that result in repeating unit cells [47]. The periodic structure of woven fabrics can be constructed by the translation of this unit cell (Figure 3.7). The periodicity of the woven fabrics can be assumed to be in-plane since they are considered as 2D materials. Hence, the periodicity can be expressed with two planar vectors defined as (Figure 3.7) [47]:

$$\underline{P} = \sum_{n=1}^{2} m_n \underline{P}_n \qquad n = 1,2 \tag{3.16}$$

where $\underline{P}_n$, m and $\underline{P}$ are directional translational vectors, scale factor and total translational vector, respectively. These vectors in both undeformed and deformed configurations of the periodic structure are shown in Figure 3.7.

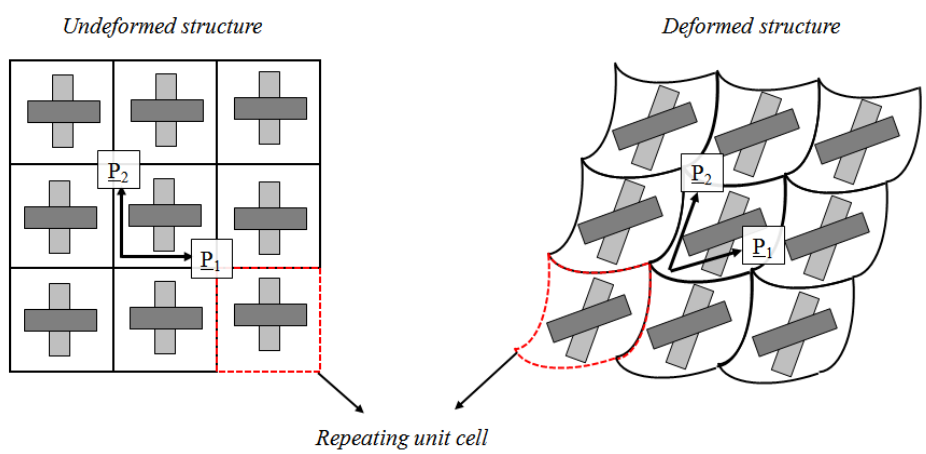

Figure 3.7 Repeating unit cells within a periodic structure in undeformed and deformed configurations.

For a given unit cell which can be translated with the vectors ($\underline{P}_n$ where n= 1, 2), the boundaries can be divided into two pairs (∂V_n^+ and ∂V_n^-) with undeformed boundary point locations ($\underline{X}_n^+$ and $\underline{X}_n^-$) and deformed boundary point locations ($\underline{x}_n^+$ and $\underline{x}_n^-$) as shown in Figure 3.8. These boundary points can be superimposed with the translational vectors ($\underline{P}_n$) assuming homogeneous deformation across the unit cell due to the periodic structure of the unit cell:

$$\underline{X}_n^+ - \underline{X}_n^- = \underline{P}_n \quad \underline{X}_n^+ \in \partial V_n^+ \quad \underline{X}_n^- \in \partial V_n^- \tag{3.17}$$

The function ($\underline{\varphi}(\underline{X})$) that transforms the initial undeformed unit cell to a deformed configuration can be separated into two parts: (1) Average displacement field ($\underline{\varphi}_l(\underline{X})$), and (2) Periodic fluctuation ($\underline{\varphi}_p(\underline{X})$) as shown in Figure 3.8. This function is given as:

$$\underline{\varphi}(\underline{X}) = \underline{\varphi}_l(\underline{X}) + \underline{\varphi}_p(\underline{X}) \tag{3.18}$$

In Eq. 3.17, the average displacement field is known while the periodic fluctuation is unknown and depends on the average displacement field imposed on the unit cell boundaries. Periodicity imposes that the points in the paired boundaries should have the same periodic fluctuations given as:

$$\underline{\varphi}_p(\underline{X}_n^+) = \underline{\varphi}_p(\underline{X}_n^-) \tag{3.19}$$

Moreover, the boundary point locations in the deformed configuration can be written in the following form due to the periodicity:

$$\underline{x}_n^+ - \underline{x}_n^- = \underline{\varphi}(\underline{X}_n^+) - \underline{\varphi}(\underline{X}_n^-) \tag{3.20}$$

By combining Eqs. 3.18-20, the following expression for the boundary point locations in the deformed configuration in terms of average displacement field can be obtained as:

$$\underline{x}_n^+ - \underline{x}_n^- = \underline{\varphi}_l(\underline{X}_n^+) - \underline{\varphi}_l(\underline{X}_n^-) \tag{3.21}$$

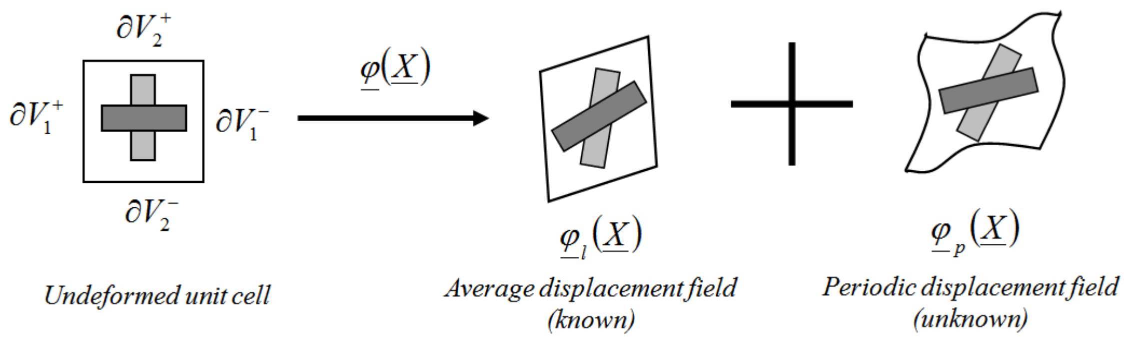

Figure 3.8 Periodic boundary conditions.

Eq. 3.21 can be easily implemented in a finite element code using nodal displacement constraint equations. A custom MATLAB code is developed to generate the woven fabric unit cell (Figure 3.9) and determine the node locations and numbers that are located at the unit cell boundaries. Then, the constraints defined by Eq. 3.21 are implemented in LS-DYNA using global constraint keyword cards (CONSTRAINT_MULTIPLE_GLOBAL). Moreover, the average displacement field shown in Figure 3.8 is imposed on the unit cell boundary nodes through control nodes.

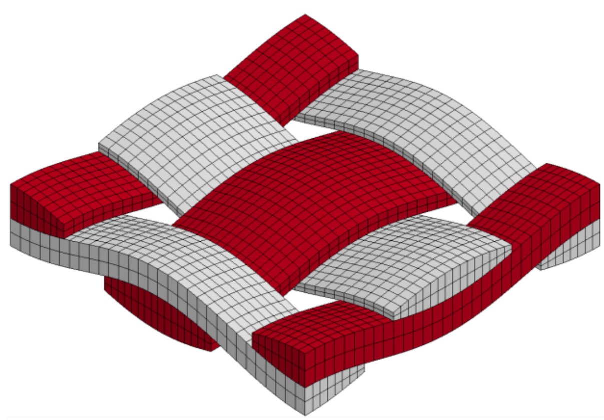

Figure 3.9 Plain weave repeating unit cell structure.

The unit cell modeling coupled with periodic boundary conditions allows the simulation of woven fabric behavior at different loading conditions such as uniaxial tensile and shear while keeping the computational resources low. As mentioned, the yarn material model implemented requires 6 yarn material properties/parameters for each yarn direction. The yarn longitudinal modulus (E_{11}) can be determined directly from single crimped yarn experiments. On the other hand, the determination of transverse modulus and transverse shear modulus require other approaches since there are no established experimental methods to determine these material properties from single yarns. Hence, an inverse method is adopted to determine the these material properties/parameters. To demonstrate and validate the material model, K706 plain weave fabric is modeled using the developed approach. The yarn and fabric dimensions are taken from a previously published study to create the unit cell finite element model of the fabric studied [4, 40]. Figure 3.9 shows the unit cell model of K706 plain weave fabric.

The transverse shear moduli of the yarns (G_{12}=G_{31} & G_{23}) are generally assumed to be low due to fibrous nature of the yarns. Since there is no experimental method to determine the values of the yarn transverse shear moduli, smaller values compared to longitudinal modulus have been used in the literature [40, 43, 45]. In Section 3.2.1, it was shown that the yarn transverse shear modulus had a significant effect on yarn mechanical response under uniaxial loading before decrimping. It was assumed that shear moduli of the yarns are constant during deformation and unit cell simulations were carried out under uniaxial tensile loading while varying transverse shear moduli. Moreover, no plastic deformation of yarns in shear was considered in the simulations. For this purpose, a displacement boundary condition is applied to a control node and this boundary condition is transferred to the unit cell boundary nodes through the constraint equations defined by Eq. 3.20. Moreover, yarn-to-yarn contact is defined with a single surface contact algorithm (AUTOMATIC SINGLE SURFACE) with Coulomb friction. The coefficient of friction is taken as 0.23 based on a previous study [4, 40]. The other material properties are kept constant during the study with the aim of minimization of root mean square error (RMSE) between the experimental average and simulations. Based on the study, the transverse shear modulus for weft and warp yarns were determined as 40 MPa and 35 MPa, respectively. Figure 3.10 shows the stress - strain curves obtained from the unit cell simulations with the determined transverse shear moduli. The material model is able to capture the experimental mechanical response of the woven fabric under uniaxial loading [9]. Figure 3.10b shows the von Mises Stress distribution at 3.5% strain in each yarn direction. It can be seen that weft direction yarns have higher stresses compared to warp yarns. This difference can be attributed to the amount of yarn crimp. Since warp yarns have higher crimp than weft yarns, larger strains are needed to decrimp warp yarns. Hence, weft yarns are fully straightened at lower strains which leads to higher stresses within the yarns.

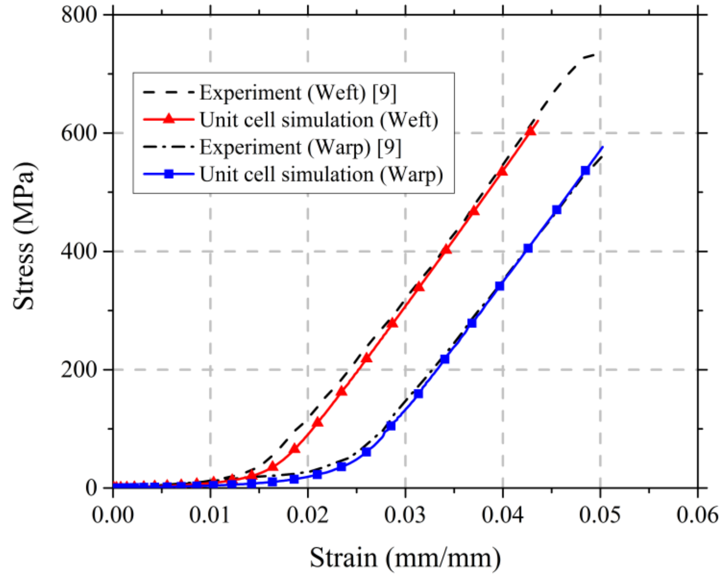

(a)

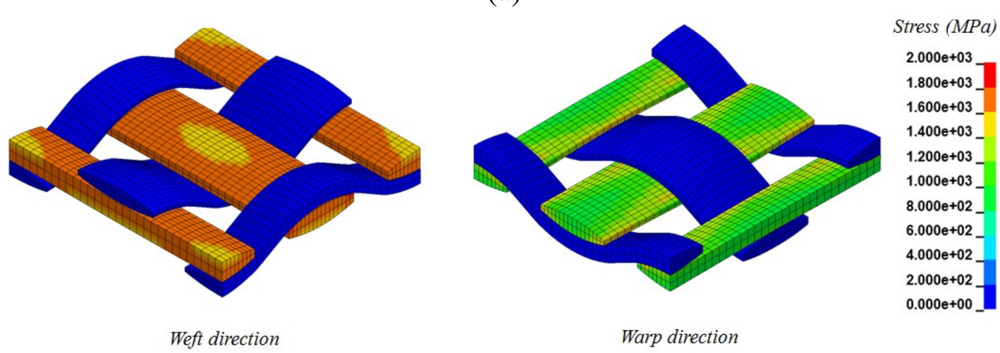

(b)

Figure 3.10 Unit cell finite element simulation results for K706 with the determined transverse shear modulus values: (a) Woven fabric stress-strain curves, and (b) Stress distribution at 3.5% strain [9].

To validate the material response under uniaxial loading, uniaxial tensile test experiments are also simulated using the mesoscopic length scale models. The fabric specimens with 101.6 mm x 25.4 mm were generated using the custom code developed. To simulate the experiments, one of the short ends was clamped by constraining all of the translational degree-of-freedoms while a displacement boundary condition was applied to the other short end. Figure 3.11a shows the stress-strain curves obtained for both weft and warp yarn directions. The numerical model is able to capture the mechanical response observed in the experiments as shown in Figure 3.11a. The simulated deformation of the fabric specimen at 0.03 strain is shown in Figure 3.11b.

The characterization of the yarns' transverse mechanical behavior is highly complex due to the fibrous nature of the yarns. Several single yarn experimental methods have been proposed in the literature to characterize the yarns in the transverse direction. However, the yarns do not exhibit the same mechanical response within the fabric when they are extracted from the fabric. This difference is mainly due to the weak interactions between the filaments and the boundary conditions imposed by the adjacent yarns within the fabric. Because of this reason, the yarns are easier to deform when they are extracted from the fabric. Hence, the single yarn experiments used to determine the transverse response of the yarns cannot reproduce the same yarn mechanical response observed in the fabric. In the current work, another inverse method is developed to determine the material properties/parameters required by the yarns' transverse moduli as defined by Eq. 3.15. Since the yarns undergo significant transverse deformation during shear deformation, unit cell models under shear loading are used to determine the parameters required by Eq. 3.15.

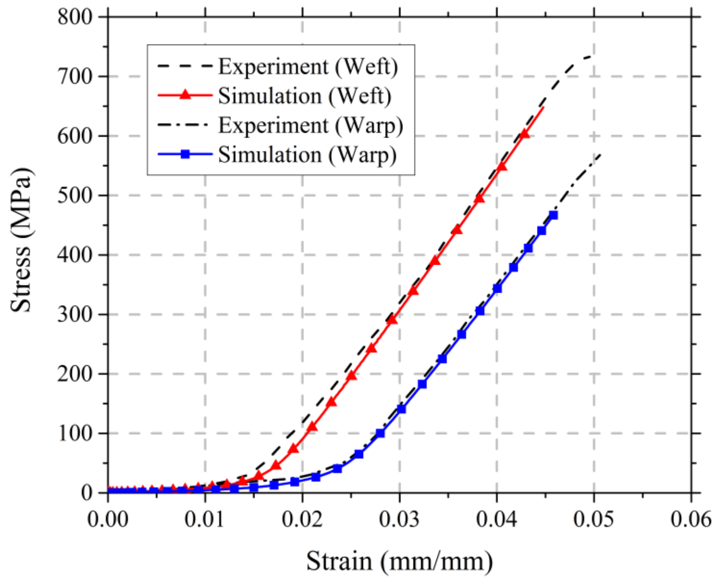

(a)

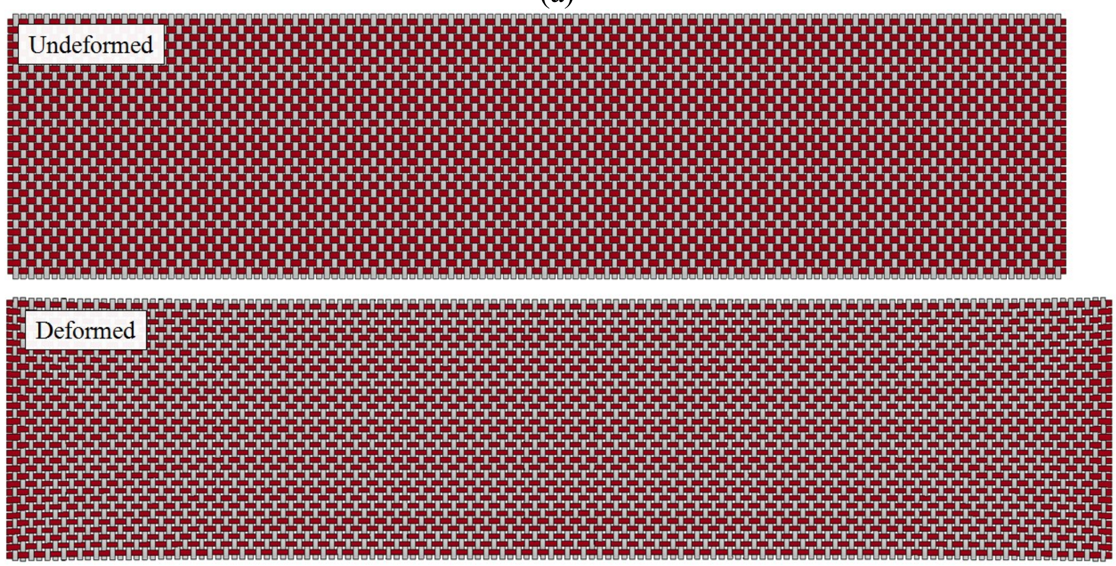

(b)

Figure 3.11 Uniaxial tensile test simulations for K706 to validate the tensile behavior of the material model: (a) Stress - strain curves, (b) Deformation of the fabric at 3% strain [9].

The shear loading is applied to the boundaries of the unit cell through four control nodes. It is assumed the average displacement field during shear is similar to picture frame test where the boundaries act as rigid rods. Hence, Eq. 3.20 can be rewritten in the following 2D form to implement the motion of the boundary nodes:

$$\underline{x}_n^+ - \underline{x}_n^- = \begin{bmatrix} L_x \sin\gamma \\ L_y(\cos\gamma - 1) \end{bmatrix} \tag{3.22}$$

where L_x and L_y are the unit cell boundary dimensions in x and y directions, respectively. Eq. 3.22 is implemented using global constraint cards within LS-DYNA.

To determine the properties/parameters required by the yarn transverse modulus defined in Eq. 3.15, the properties/parameters of the transverse yarn modulus (E_{in}, E_0, and m) are varied and the RMSE between the experimental and simulated unit torque/moment at a given shear angle is minimized. The simulated unit torque/moment at various shear angles is determined by using the external work done on the unit cell as follows [47]:

$$T(\gamma) = \frac{\dot{W}}{S\dot{\gamma}} \tag{3.23}$$

T, W, S and γ are unit torque, external work done on the unit cell, initial area of the unit cell and shear angle, respectively (The dot represents the time derivative in Eq. 3.23). Since in this weave the material is the same, both weft and warp yarns have the same transverse yarn modulus and simulations with varied yarn transverse properties/parameters were carried out to minimize the RMSE between the experimental average and simulations. The same contact definition (COF=0.23) used for the unit cell uniaxial loading simulations was also adopted in these simulations to implement yarn-to-yarn interactions.

Table 3.5 shows the yarn transverse material properties/parameters determined based on the shear loading case and the inverse method used as well as the tensile properties used for both yarn directions. It should be noted that E_{11} is the material property obtained from single yarn experiments. Other material properties listed in Table 3.5 are the yarn material properties within the fabric since an inverse method with fabric simulations was adopted to determine their values. These material properties might be different from the single yarn (extracted from fabric) material properties due to the weak interactions between the filaments and boundary conditions imposed by the fabric itself on the yarns.

Table 3.5 Yarn material properties/parameters determined using the inverse method.

Material Property/Parameter	Weft direction	Warp direction
E_{11} (MPa)	79000	69000
G_{12} (G_{31}) (MPa)	35	40
G_{23} (MPa)	35	40
E_{ii} (i=2 & 3)	E_{in}= 1 MPa E_0= 0.000001 MPa m= 50	
Coefficient of friction	0.23	

Figure 3.12a shows the simulated unit torque/moment with the material properties/parameters presented in Table 3.5. It can be seen that the yarn material model developed can capture the experimentally observed nonlinear mechanical response under shear loading. The initial resistance to shear deformation is mainly due to the yarn-to-yarn relative motion and associated frictional effects. As the deformation progresses, the yarns start to compress themselves resulting in rearrangement and compression of the filaments within the fabrics. This phenomenon results in increased resistance to deformation leading to a highly non-compliant

mechanical response as the deformation progresses as shown in Figure 3.12a. Figure 3.12b shows the stress distribution at various shear angles obtained from the simulations. It can be seen that the stresses at the yarn transverse contact areas increase as the shear angle increases. The simulations were able to capture the nonlinear mechanical response due the compression at these contact locations with the implemented yarn nonlinear transverse modulus.

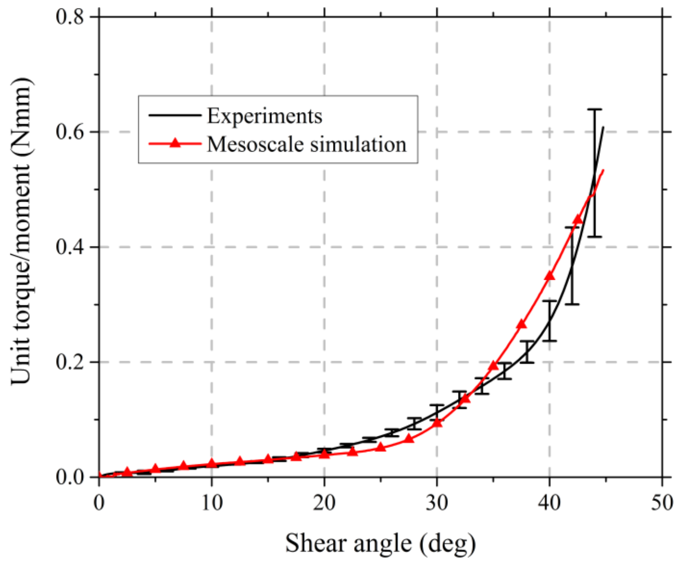

(a)

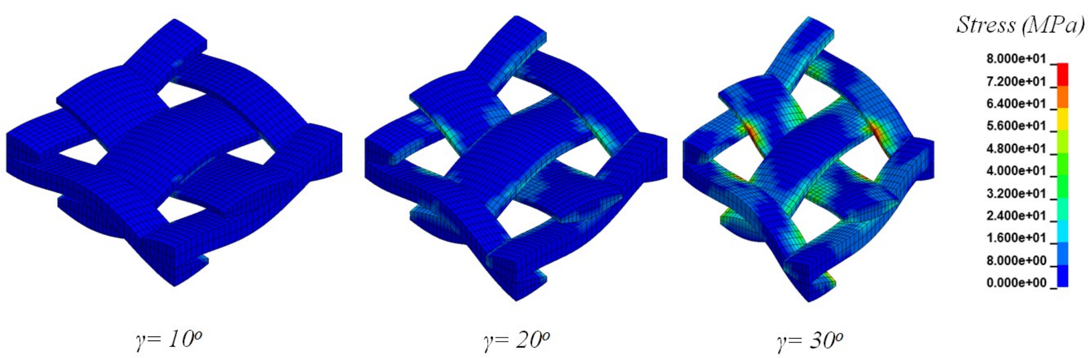

(b)

Figure 3.12 Unit cell finite element simulation under shear loading: (a) Unit torque/moment with respect to shear angle after calibrating the transverse modulus of the yarns, and (b) Stress distribution at 40^{o} shear angle.

The implemented material model was further validated with bias extension and indentation test simulations. The bias extension test numerical models were created by rotating the weft and warp yarns ±45° with respect to the loading direction. The numerical model had a width of 25.4 mm and a length of 101.6 mm corresponding to the experimental fabric dimensions used. The developed numerical model for bias extension test is shown in Figure 3.13. One of the shorter edges of the fabric was clamped by constraining all of the translational DOFs while a displacement boundary condition was applied to the other short end.

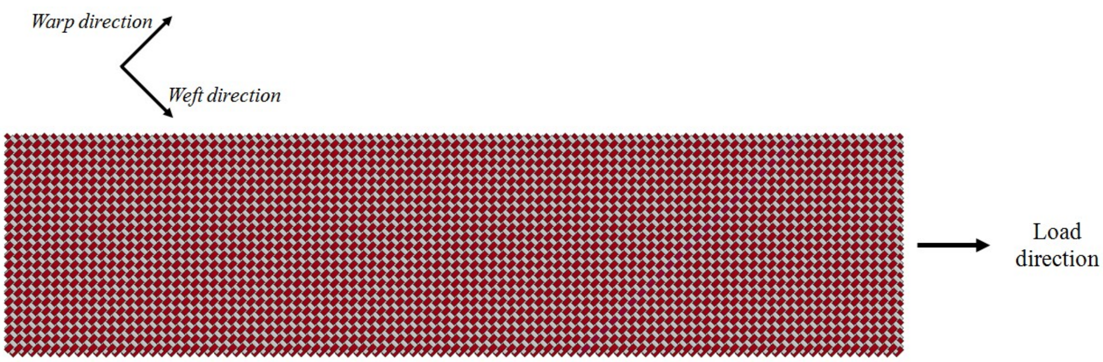

Figure 3.13 Bias extension test numerical model setup.

Figure 3.14 shows the results obtained from the simulated bias extension test and their comparison to the experimental results. It can be seen that the bias extension test numerical model with the developed nonlinear yarn material model can capture the nonlinear mechanical response observed in the experiments as shown in Figure 3.14a. Figure 3.14b shows the shear angle change at the middle of the fabric specimen as a function of the crosshead displacement. The simulated shear angle closely follows the experimental average. Since the yarns are explicitly modeled in the mesoscopic length scale, several mesoscopic deformation mechanisms observed in the bias extension experiments can be studied. Figure 3.14c shows some of these experimentally observed deformations (Figure 2.9) such as the heterogeneous deformation zones, yarn raveling at the specimen edges as well as the deformation of the yarns between Regions B and C which are subjected to tensile loads.

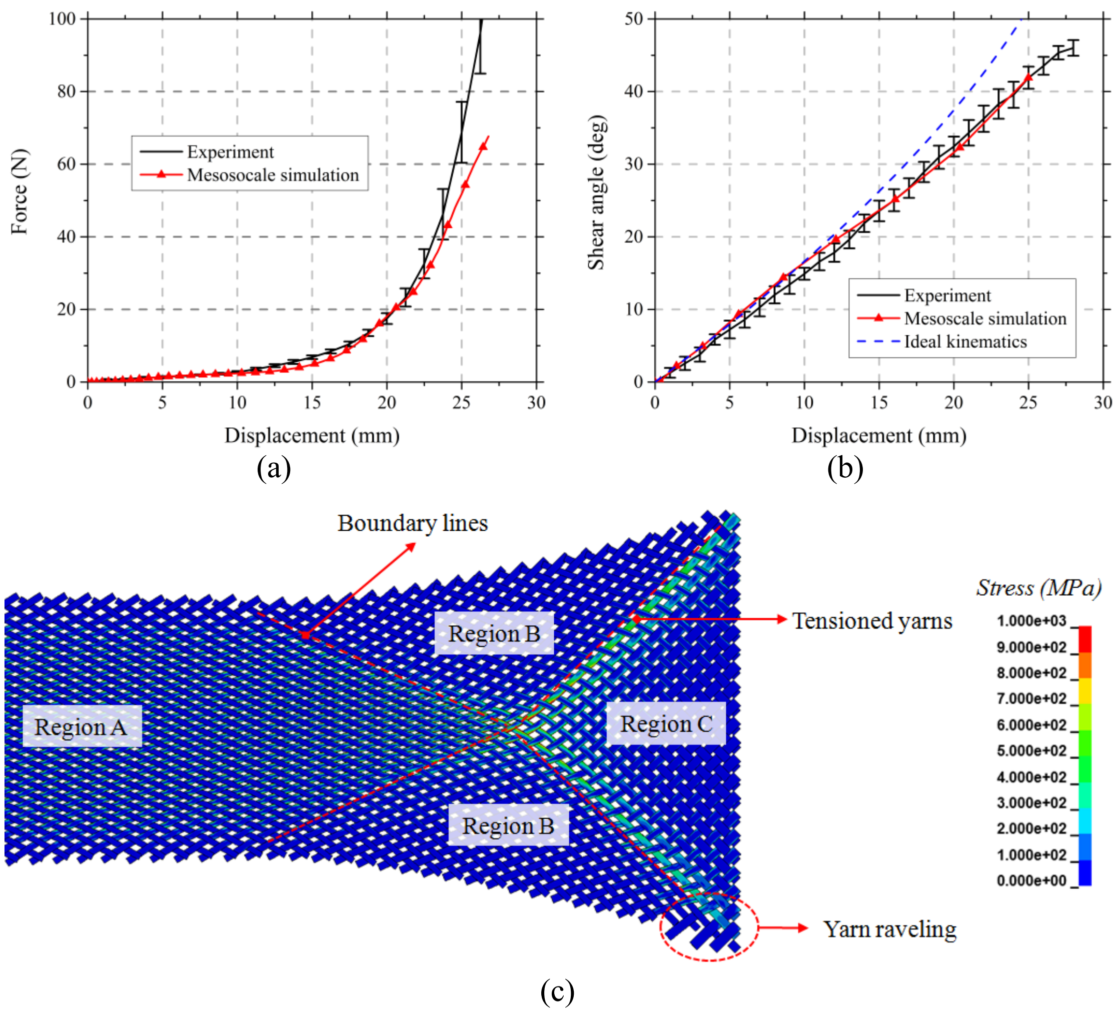

Figure 3.14 Bias extension test simulations: (a) Force - displacement, (b) Displacement - Shear angle, and (c) Stress distribution at 25 mm crosshead displacement.

The implemented yarn material model is further validated under more complex loading by simulating woven fabric under indentation loading. For this purpose, two different cases were simulated with different yarn orientation angles (ψ): (1) $0^o/90^o$, (2) $\pm 45^o$. The simulated woven fabric had dimensions of 51 mm x 40 mm for $0^o/90^o$ yarn orientation where the experimental results of Manimala et al. were adopted to validate the simulations [49]. Figure 3.15 shows the mesoscopic finite element model developed for the $0^o/90^o$ yarn orientation case. The short edges of the fabric were clamped while the longer edges were free to move. An indenter with a 12 mm diameter was modeled as a halved sphere with shell elements and an isotropic material model with steel material properties. The contact between the indenter and the yarns within the fabric was modeled with a single surface contact algorithm where the coefficient of friction between the yarns and the indenter was assigned as 0.2.

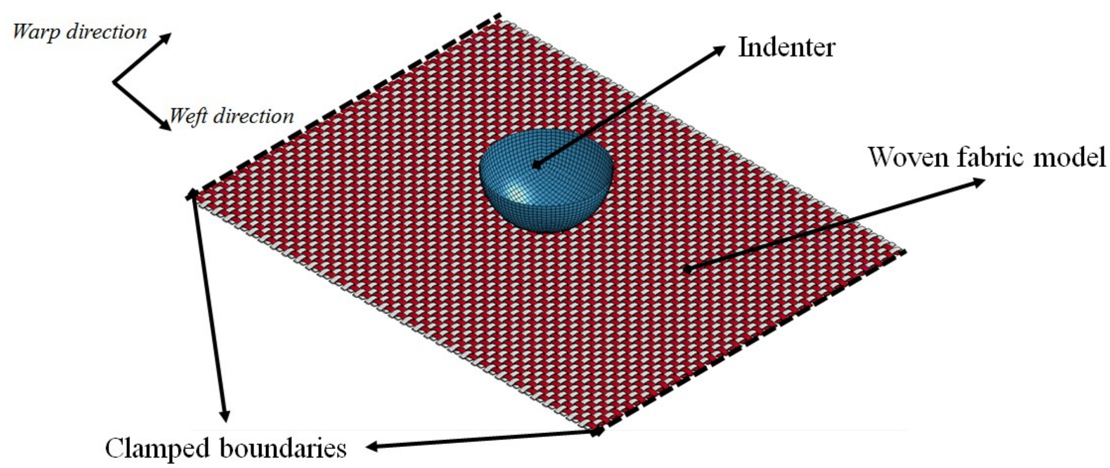

Figure 3.15 Mesoscopic finite element model for indentation loading simulations with yarn orientation angles: 0^o and 90^o.

Figure 3.16 shows the simulation results with yarn orientation angles of 0^{o} and 90^{o}. Both ends of the warp yarns were clamped in the 0^{o} yarn orientation simulation while the weft yarns were constrained at both ends for 90^{o}. Figure 3.16a shows force-displacement results of the simulations and their comparison to the experimental results [49]. The simulations were capable of reproducing the experimental nonlinear mechanical response observed for 0^{o} and 90^{o} yarn orientations. The mechanical response is governed by the interactions between the indenter and the yarns underneath it. The yarns that are clamped at both ends and underneath of the indenter undergo decrimping which results in an initial compliant response followed by a non-compliant force response (Figure 3.16a). It can be seen from Figure 3.16a that there is a difference between the yarn orientation angles studied. This difference can be attributed to the crimp amount of the weft and warp yarns. Since weft yarns have less crimp compared to the warp yarns, their force response becomes stiffer at lower indenter displacements. The mesocopic modeling approach adopted is able to capture this difference since both yarn directions are explicitly modeled. Figure 3.16b shows the stress distribution at 5 mm indenter displacement. The highest stresses were observed where the indenter contacts with the woven fabric model. Moreover, the yarns that are underneath the indenter and clamped at both ends are deformed more compared to the other yarns. Hence, these yarns exhibit higher stresses compared to other yarns. It should also be noted that the stresses observed for 90^{o} yarn orientation (weft yarns clamped) are higher than the 0^{o} yarn orientation (warp yarns clamped). This difference can again be attributed to the crimp amount of the weft yarns where lower strains are needed to fully straightened the yarns.

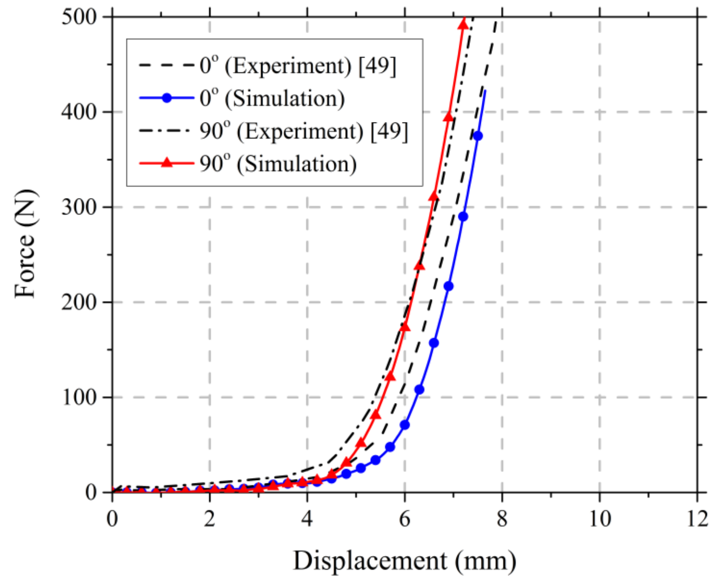

(a)

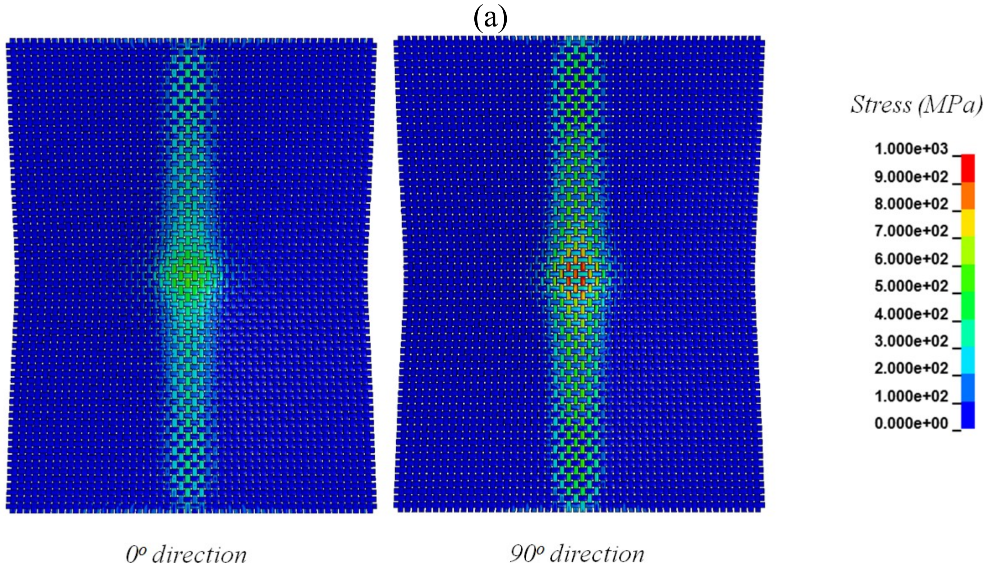

(b)

Figure 3.16 Indentation test simulations with 0° and 90° yarn orientations: (a) 0° indentation results, (b) 90° indentation results, and (c) Stress distribution at 5 mm indenter displacement [49].

The yarns were then oriented ±45° in the second indentation case studied using the mesoscopic length scale woven fabric models. Figure 3.17a shows the finite element model developed to study this indentation case. The woven fabric finite element model had dimensions of 52 mm x 25 mm with a 14 mm diameter indenter. Both short edges of the fabric model was clamped in a similar manner to $0^o/90^o$ indentation case. The same contact definition and indenter material used for $0^o/90^o$ simulations were also adopted for this simulation case. Moreover, the simulation results were validated by adopting the experimental results of Dong et al. [9]. Figure 3.17b shows the force-displacement results of the simulated fabric and its comparison to the experimental results.

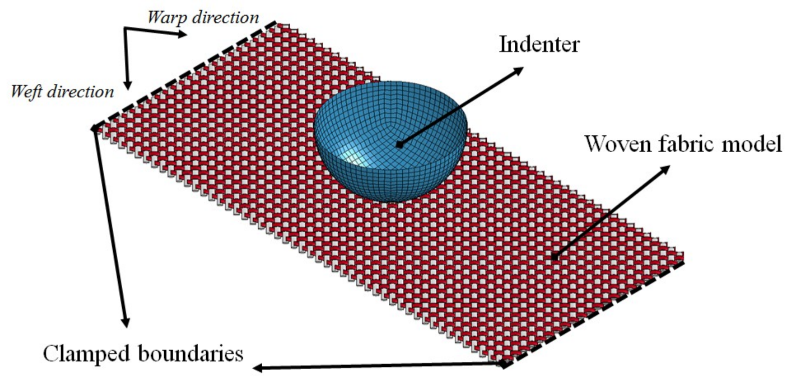

(a)

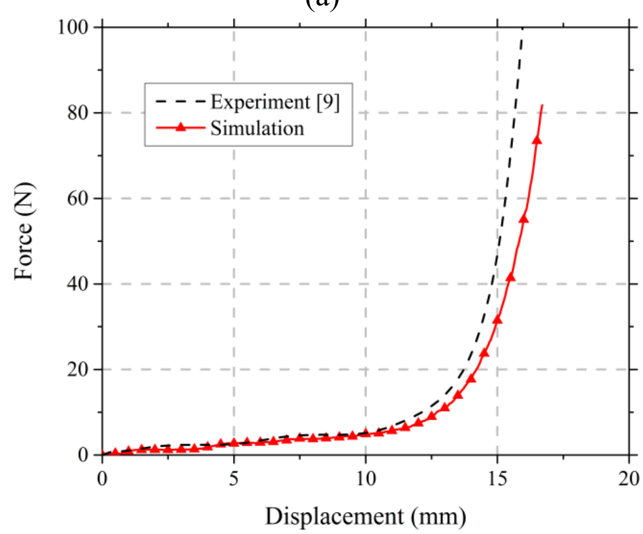

(b)

Figure 3.17 Indentation test simulations with ±45^o yarn orientation: (a) Finite element model developed, and (b) Force - displacement results [9].

As shown in Figure 3.17, the mesoscopic finite element model of K706 developed is able to capture the force response observed during the experiments. Both experimental and simulation force responses are highly nonlinear. Since the yarns are oriented in ±45°, the yarns within the fabric are able to rotate relative to each other in a similar manner to bias extension tests. Hence, an initial compliant response up until the ~13 mm indenter displacement is observed. The force displacement exhibits a stiffer response after this indenter displacement due to the possible yarn locking. Figure 3.18 shows the stress distribution across the woven fabric model at 5 mm and 15 mm indenter displacements. It can be seen that the yarns that are underneath the indenter rotate relative to each other as the indenter moves. Hence, the stresses at the middle of the fabric model increase due to the yarn-to-yarn interactions (transverse compression) and the indenter-yarn interactions.

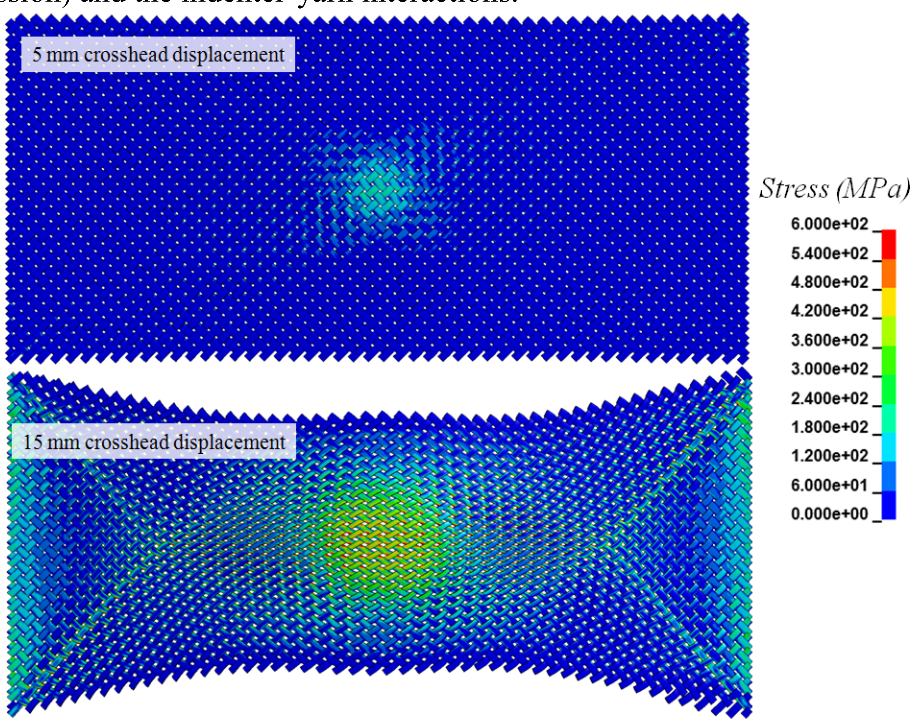

Figure 3.18 Stress distribution across the woven fabric at various indenter displacements.

3.3 Investigation of Mesoscopic Length Scale Material Properties and Weave Architectures on Macroscopic Mechanical Response

Mesoscopic length scale simulations provide unique opportunities to study the macroscale mechanical response of the woven fabrics considering yarn level interactions. This allows studying the effects of mesoscale properties in a systematic manner while providing insight into how to design a woven structure to produce a desired mechanical response. In Section 3.2, it was shown that the mesoscopic length scale simulations are capable of this task. Hence, one of the goals of the current work is to identify important mesoscale (yarn) material properties on resulting macroscale mechanical response of woven fabrics thus gaining potential insight into how these material properties can be tailored to obtain a specific material response. For this purpose, a systematic approach combining unit cell finite element and a design-of-experiments technique (Taguchi methodology) is developed. Several different weave architectures under various loads are studied to determine the effects of the yarn material properties and architectures on the macroscopic response of woven fabrics.

3.3.1 Design-of-Experiments Coupled with Finite Element Simulations

The design-of-experiments (DOE) approach is a widely used method to investigate and determine the effects of the parameters involved in a process (or design) on the desired outcome [70–73]. DOE techniques allow studying nonlinear parameter effects on specific outcomes in an efficient manner for problems involving large number of parameters. Hence, they have been adopted to investigate the cause-and-effect relationships in various fields. Full and fractional factorial methods are the two most commonly used DOE techniques among others. These methods' main goal is to try various number of possible combinations of parameters involved in a problem to investigate the effect and significance of each parameter on the selected outcome.

However, the number of possible combinations can become prohibitive if large number of parameters are involved in a problem. If a problem with 5 parameters at 3 different values is to be investigated, then 243 (3^5) different combinations are needed to be investigated to determine the main effects of the parameters in a full factorial DOE. In 1987, Taguchi introduced a DOE method designed to investigate and optimize product development and processes involving large number of parameters [73]. The method uses specialized tables called Orthogonal arrays (OAs) to significantly reduce the number of possible combinations required in a regular DOE approach. These arrays are pre-defined arrays and they are based on the number of parameters and levels to be studied. Table 3.6 shows the twenty-seven level (L_{27}) OA defined for 5 parameters at 3 different levels. Each row corresponds to the level to be used for each experiment. The method allows the investigation of parameter effects with only 27 experiments, considerably reducing the number required by the full factorial design (243 possible combinations for the same problem). The Taguchi method uses analysis of variance (ANOVA) calculations to determine whether a given parameter is statistically significant, its percent contribution to the outcome and parameter's relative effect on the outcome.

In this research work, the Taguchi DOE method is coupled with unit cell level finite element simulations to study the effects of the yarn material properties and weave architecture on the macroscale mechanical response of woven fabrics (Figure 3.19). The adopted approach requires inputs for Taguchi method as well as the finite element inputs. Then, simulations are carried out with the selected orthogonal array which is based on the number of parameters and levels used. Then, pre-defined outcomes are determined for simulation results and ANOVA calculations are carried out to determine parameters' significance and their relative effects on the selected outcome.

Table 3.6 L_{27} Orthogonal array.

Experiment	Parameters				
	P1	**P2**	**P3**	**P4**	**P5**
1	1	1	1	1	1
2	1	1	1	1	2
3	1	1	1	1	3
4	1	2	2	2	1
5	1	2	2	2	2
6	1	2	2	2	3
7	1	3	3	3	1
8	1	3	3	3	2
9	1	3	3	3	3
10	2	1	2	3	1
11	2	1	2	3	2
12	2	1	2	3	3
13	2	2	3	1	1
14	2	2	3	1	2
15	2	2	3	1	3
16	2	3	1	2	1
17	2	3	1	2	2
18	2	3	1	2	3
19	3	1	3	2	1
20	3	1	3	2	2
21	3	1	3	2	3
22	3	2	1	3	1
23	3	2	1	3	2
24	3	2	1	3	3
25	3	3	2	1	1
26	3	3	2	1	2
27	3	3	2	1	3

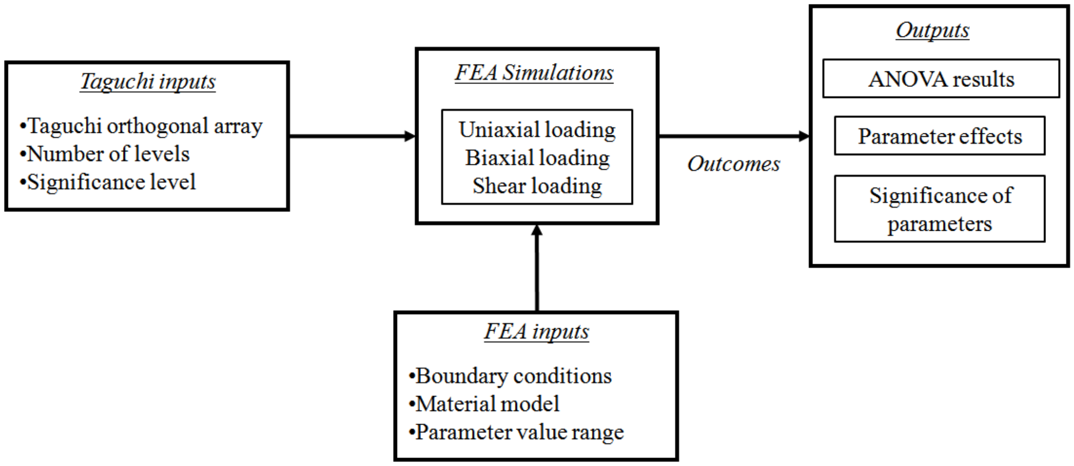

Figure 3.19 Taguchi method coupled with unit cell finite element simulations.

3.3.2 Application of the method to various weave architectures to investigate mesoscopic length material effects

To investigate the effects of the yarn material properties on the macroscale mechanical response of woven fabrics, four different weave architectures are studied using unit cell level modeling: (1) Plain weave, (2) Twill weave (2x2), (3) Basket weave (2x2), and (4) 5-harness satin weave.

Different mechanical responses and properties can be obtained from the various weave architectures due to their construction. In plain weave architecture, each yarn direction passes under and over the other yarn direction. The construction of basket weave is similar to plain weave but two (or more) yarns are alternated over and under the other yarn direction. On the other hand, one or more yarns are alternatively woven over and under two or more yarns in the other direction in twill weaves. Satin weave is also similar to Twill weaves with fewer crossover points. The custom MATLAB code to create plain weave unit cell finite element models is modified to generate unit cell models of the twill, basket and satin weaves. Figure 3.20 shows the unit cell finite element models of the weave architectures studied in the current work.

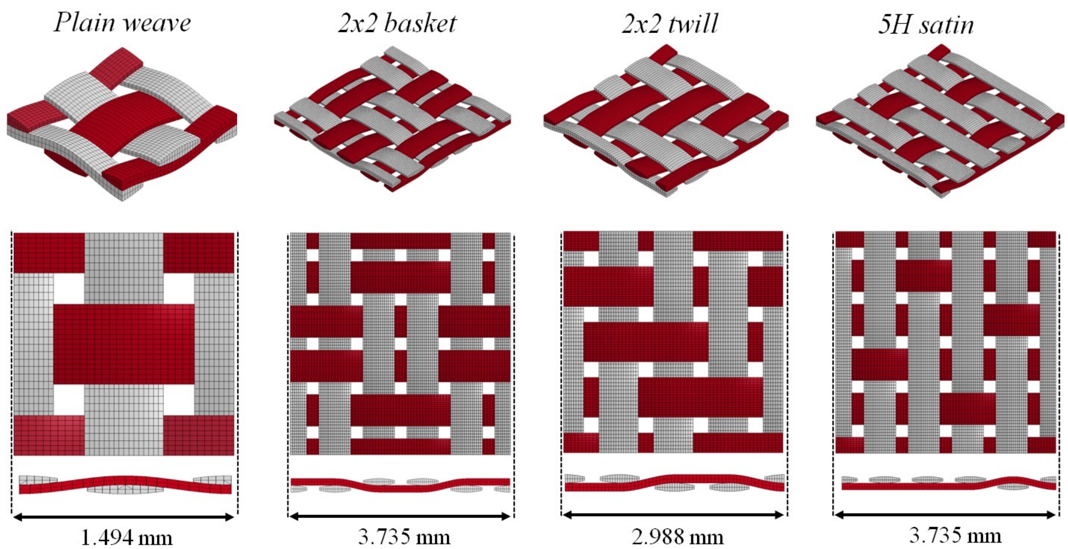

Figure 3.20 Weave architectures used in the current work.

For all the unit cells shown in Figure 3.20, the material boundaries and the geometric boundaries correspond to each other with paired nodes at each boundary. This is desirable since the kinematic conditions defining the average displacement field can only be applied on the material boundary [47]. Hence, it is convenient to apply kinematic boundary conditions, especially for shear loading, on a unit cell where material and geometric boundaries are the same. Because of this reason, the material and geometric boundaries are selected to be the same for all the unit cell weave architectures shown in Figure 3.20.

To study the effects of the weave architecture and yarn material properties, all the weave architectures are modeled with the same yarn geometric dimensions (0.536

mm width and 0.115 mm thickness) and fabric span based on K706 woven fabric. Since the weave architectures are different from each other, the unit cell sizes have to be different to obtain the same material and geometric boundaries as shown in Figure 3.20. Moreover, the amount of the yarn crimp varies between the architectures since the yarns are deformed in different amounts for certain weaves. The yarn decrimping strain for each weave can be determined by using Eq. 3.14. Comparison of the weave architectures studied with the developed approach in terms of geometric dimensions is given in Table 3.7.

Table 3.7 Comparison of the weaves studied in terms of dimensions.

Weave	Unit cell size (mm x mm)	Yarn count (yarns/mm)	Decrimping strain (%)
Plain	1.494 x 1.494	1.34	1.45
Basket	2.988 x 2.988	1.34	0.58
Twill	3.735 x 3.735	1.34	0.72
Satin	3.735 x 3.735	1.34	0.55

For all weave architectures studied, 3 main loading cases experienced by woven fabrics are investigated: (1) Uniaxial, (2) Biaxial, and (3) Shear. In the uniaxial loading case, a displacement boundary condition is applied to the control node and this boundary conditions is transferred to the unit cell boundary nodes through the constraint equations defined within the finite element. Biaxial loading is implemented in a similar way. Two control nodes with displacement boundary conditions are used to impose biaxial loading on the unit cells. Since the edge nodes belong to two unit cell surfaces, the known displacement field is directly applied to these nodes rather than using the constraint equations. In the shear loading case, pure shear displacement field is applied to the boundaries through four control nodes. Hence, Eq. 3.22 is adopted to implement the shear loading.

The effects of the yarn material properties under uniaxial, biaxial and shear loads are investigated through unit cell finite element models coupled with Taguchi method for all weave architectures. For this purpose, the yarns are modeled as commonly used transversely isotropic continuums with a hyperelastic linear orthotropic material model [67]. This material model is chosen to reduce the number of parameters required by the design-of-experiments technique used. Yarn-to-yarn contact for all simulations is defined with a single surface contact algorithm (AUTOMATIC SINGLE SURFACE) with Coulomb friction.

Five mesoscopic (yarn) material properties are chosen to investigate their effects on the macroscale woven fabric response. These properties include yarn longitudinal modulus (E_{11}), transverse modulus (E_{22}=E_{33}), transverse shear moduli (G_{12}=G_{31} and G_{23}) and coefficient of friction (COF) between the yarns. To investigate the nonlinear effects, 3 levels are assigned to each yarn material property investigated. The base values of the material properties (Level - 2) are taken from a previous study [4, 40]. Other levels (Levels 1 & 3) are determined to cover the values used for these material properties in previously published studies [4, 5, 7, 8, 37, 38, 40, 41]. All the levels used for the yarn material properties are presented in Table 3.8.

Table 3.8 Material property levels used in the study.

Material property	Level - 1	Level - 2	Level - 3
E_{11} (MPa)	50000	70000	90000
E_{22} (E_{33}) (MPa)	100	500	2500
G_{12} (G_{31}) (MPa)	50	250	1250
G_{23} (MPa)	50	250	1250
COF	0.1	0.25	0.5

Based on the number of parameters (material properties) and levels studied, an L_{27} orthogonal array (Table 3.6) is used for all loading types and weave architectures. Specific macroscale outcomes are chosen for each loading case to determine the effects of yarn material properties on these outcomes (Table 3.9). For each architecture and loading condition studied, the simulations defined by the L_{27} orthogonal array with parameter levels in Table 3.6 are carried out and the outcomes are recorded. The results are analyzed through ANOVA calculations with 95% (α=0.05) significance level by using a statistical analysis package (JMP Pro v12; Cary, NC). Then, the relative effects of the parameters (yarn material properties), their contributions to a specific outcome and statistical significances are determined for a given loading case.

Table 3.9 Outcomes chosen based on the loading type.

Loading type	Outcomes
Uniaxial tensile	Fabric modulus before decrimping (FMBD) Fabric modulus after decrimping (FMAD) Maximum Poisson's ratio
Biaxial tensile	External work
Shear	Frictional energy dissipated Total shear resistance

These outcomes are based on the overall mechanical response of woven fabrics experienced at the macroscale which can also be used as inputs to a macroscopic material models. For example, the woven fabrics exhibit a bilinear force response under uniaxial loading due to the crimp interchange deformation mechanism. Hence, two different moduli are defined based on this bilinear response under uniaxial loading: (1) Fabric modulus before decrimping (FMBD), and (2) Fabric modulus after decrimping (FMAD). Moreover, the crimp interchange during uniaxial loading also results in non-linear deformation kinematics such as varying Poisson's ratio [19]. Hence, the maximum Poisson's ratio attained during the uniaxial loading is also chosen as one of the outcomes along with FMBD and FMAD. To calculate the fabric modulus before and after decrimping, nodal forces at the loaded boundary (F_{nodal}) are summed up and divided by the effective cross-sectional area of the fabric for stresses (σ):

$$\sigma = \frac{F_{nodal}}{2L_{unit}t} \tag{3.24}$$

where L_{unit} and t are the unit cell length and the fabric thickness. The theoretical decrimping strains (Table 3.7) are used to determine the strain range for FMBD and FMAD values. Furthermore, the Poisson's ratio at a given strain value is calculated by assuming the woven fabric behaves as a continuum:

$$\nu = -\frac{\varepsilon_{xx}}{\varepsilon_{yy}} \tag{3.25}$$

where υ, ε_{xx} and ε_{yy} are Poisson's ratio, transverse strain and strain in the loading direction, respectively.

Figure 3.21 shows the stress-strain curves and stress distribution as well as the Poisson's ratio change with the applied strain of 17th simulation of L_{27} array for all the weave types. It can be seen from Figure 3.21a that the mechanical response of the woven fabrics are different than each other. Since the plain weave has the highest crimp amount due to its architecture, the mechanical response is more compliant over a larger strain range compared to other weave types (Figure 3.21a). There are less number of crossover points in twill, basket and satin weaves which result in less crimp and lower decrimping strains. The amount of crimp also affects the Poisson's ratio as shown in Figure 3.21b. Poisson's ratio can reach higher values in plain weave architecture since the crimp amount is higher compared to other weave types. This difference can be attributed to the yarns' ability to move during crimp interchange deformation. During crimp interchange, the yarns aligned with the loading direction loses their crimp while the yarn in the transverse direction increases theirs. Since the yarns in plain weave fabrics have higher crimps, the yarns aligned with the loading direction have to undergo larger deformations to lose their crimp while transverse yarns increase their crimp. Hence, the crimp amount directly affects the kinematics observed under uniaxial loading in different weave architectures.

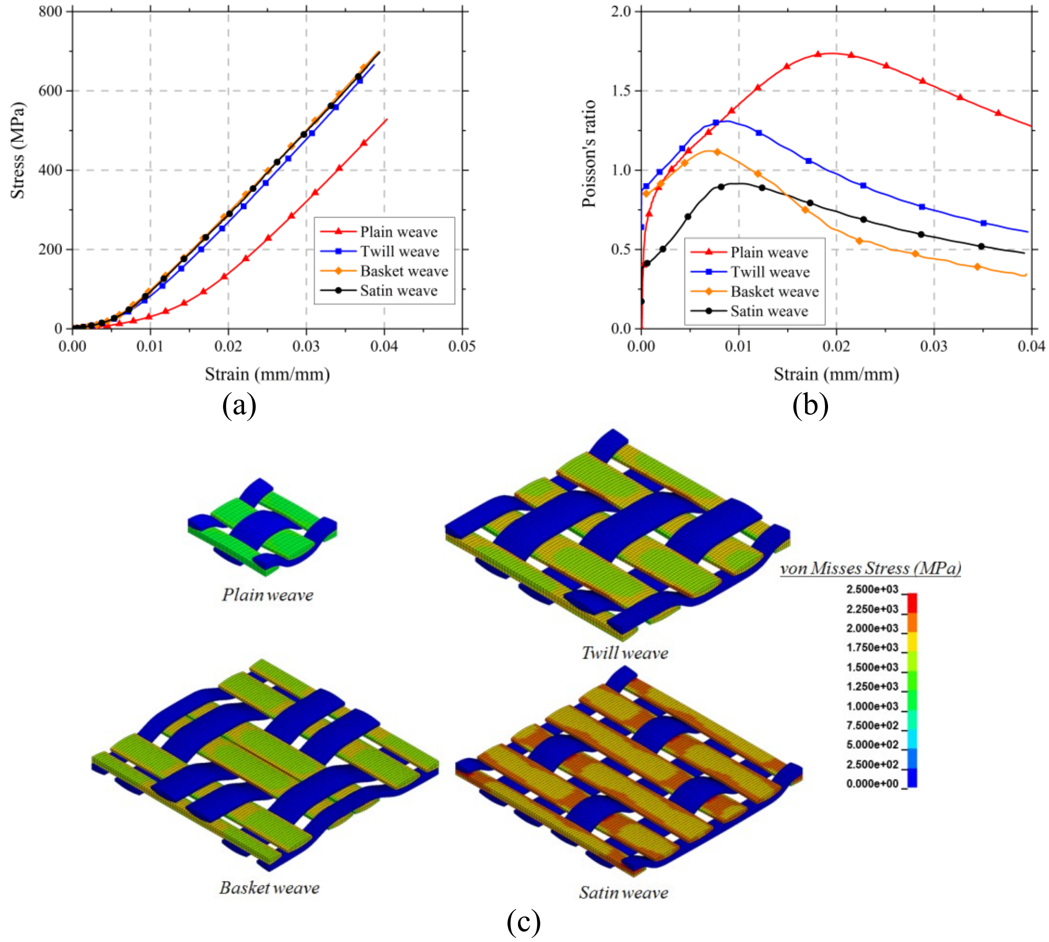

Figure 3.21 Uniaxial tensile test simulation results for the 17th simulation of L_{27} orthogonal array: (a) Stress-strain curves, (b) Poisson's ratio-strain curves, and (c) Stress distribution at 3% strain.

The ANOVA results of the FMBD outcome for all weave types are presented in Table 3.10. Table 3.10 shows the significance of each yarn material property and their contribution to the outcome. For the FMBD, all the material properties were found to be significant for all weave architectures. Moreover, G_{12} (G_{31}) had the highest contribution followed by E_{11} for all weaves. The results indicate G_{12} (G_{31}) had the highest influence on the FMBD. This effect can be attributed to the decrimping deformation where the yarns undergo transverse deformation until they are fully straightened. Figure 3.22 shows the relative effects of each yarn material property on the FMBD. Both G_{12} (G_{31}) and E_{11} resulted in a major increase in FMBD values as the levels (values assigned) increased for all weave types. On the other hand, other material properties had minimal effects on the FMBD which was also reflected with low percent contributions in Table 3.10.

Table 3.11 shows the results for the FMAD under uniaxial loading. E_{11} and G_{12} (G_{31}) were found to be significant while coefficient of friction (COF) was determined to be insignificant for all of the weaves. Moreover, E_{11} had the highest contribution among all the yarn material properties for the FMAD outcome. Figure 3.23 shows the influence of the parameters studied on FMAD. E_{11} had a positive effect on the FMAD outcome. FMAD increases with the increased E_{11} values for all weave architectures as shown in Figure 3.23. On the other hand, the other yarn material properties had minimal effect on the studied outcome since their percent contributions were determined to be relatively small compared to E_{11} (Table 3.11). It should be noted that the significances presented in Table 3.10 are individual significances of the material properties studied on the macroscale outcomes chosen.

Table 3.10 Significance and percent contributions of yarn material properties on fabric modulus before decrimping (FMBD) outcome under uniaxial loading.

Parameter	Plain	Twill	Satin	Basket
E_{11}	3.7^{+}	27.8^{+}	20.6^{+}	25.2^{+}
E_{22} (E_{33})	0.7^{+}	1.2^{+}	1.2^{+}	1.5^{+}
G_{12} (G_{31})	94.9^{+}	69^{+}	76.1^{+}	69.7^{+}
G_{23}	1.3^{+}	1.9^{+}	2.0^{+}	2.2^{+}
COF (μ)	0.001^{+}	0.09^{+}	0.002^{+}	1.3^{+}

$^{+}$*Significant parameter ($p<0.05$),* **Insignificant parameter ($p>0.05$)*

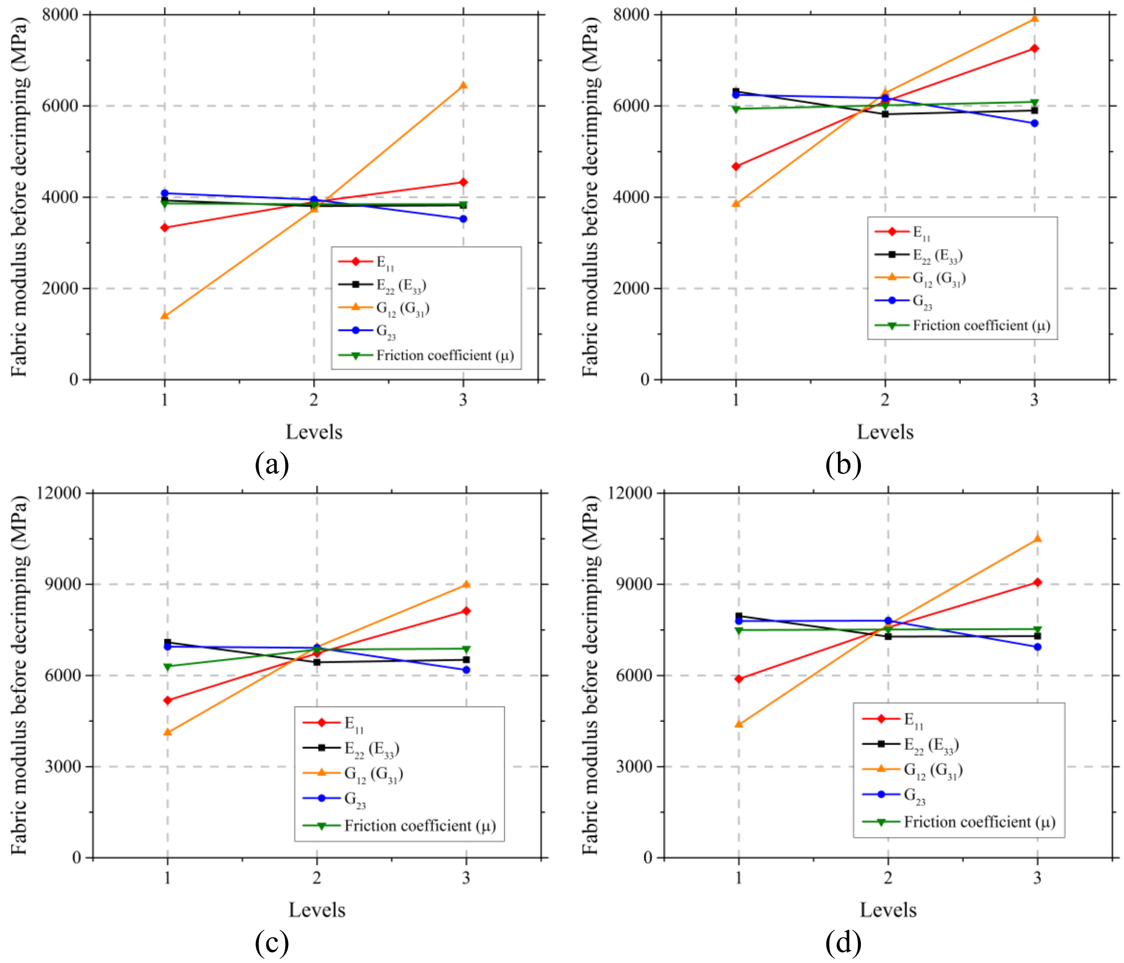

Figure 3.22 Main effects of yarn material parameters on Fabric modulus before decrimping (FMBD): (a) Plain weave, (b) Twill weave, (c) Basket weave, and (d) Satin weave.

Table 3.11 Significance and percent contributions of yarn material properties on fabric modulus after decrimping (FMAD) under uniaxial loading.

Parameter	Plain	Twill	Satin	Basket
E_{11}	97.8^{+}	99.6^{+}	99.8^{+}	99.8^{+}
E_{22} (E_{33})	0.03*	0.012^{+}	0.0003^{+}	0.05^{+}
G_{12} (G_{31})	1.76^{+}	0.34^{+}	0.21^{+}	0.08^{+}
G_{23}	0.16^{+}	0.014^{+}	0.006^{+}	0.002*
COF (μ)	0.027*	0.038*	2.10^{-5*}	0.03*

$^{+}$*Significant parameter ($p<0.05$),* **Insignificant parameter ($p>0.05$)*

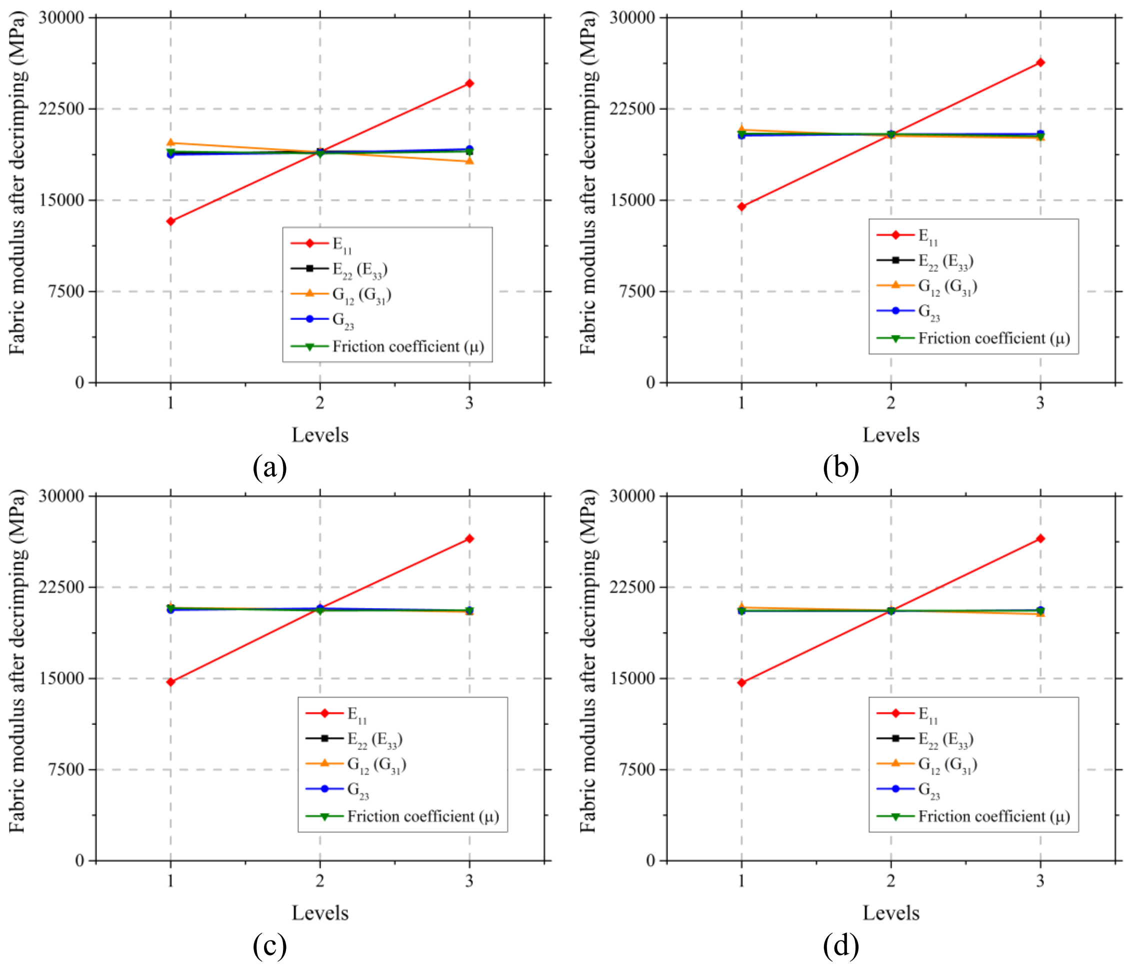

Figure 3.23 Main effects of yarn material parameters on fabric modulus after decrimping (FMAD): (a) Plain weave, (b) Twill weave, (c) Basket weave, and (d) Satin weave.

As shown in Figure 3.21b, Poisson's ratio for all weave types exhibited a nonlinear behavior. Hence, the effects of the yarn material properties on the maximum Poisson's ratio attained during uniaxial loading was studied with the proposed method. Table 3.12 shows the significance and percent contribution of the parameters studied. The transverse shear modulus (G_{12} & G_{31}) and longitudinal modulus (E_{11}) of the yarns were found to be significant for all weave architectures. G_{12} (G_{31}) had the highest contribution followed by E_{11} as shown in Table 3.12. Figure 3.24 shows the influence of the yarn material properties on the maximum Poisson's ratio. G_{12} (G_{31}) exhibited a negative influence where the maximum Poisson's ratio attained decreases with the increased G_{12} (G_{31}). On the other hand, E_{11} had a positive influence on the outcome with a relatively small contribution. The influence of G_{12} (G_{31}) on this outcome can be attributed to yarns' transverse shear deformation during crimp interchange. During uniaxial loading, the yarns aligned with the loading direction undergo decrimping where they are straightened (losing their crimp). As shown in Figure 3.22 and Table 3.10, the transverse shear moduli (G_{12} & G_{31}) directly affects the mechanical response during this deformation. While these yarns are straightened, the yarns in the transverse direction increases their crimp amount due to the contact of the yarn directions at the crossover points (Figure 3.21c). These yarns also undergo transverse shear deformation while shortening their effective lengths resulting in a decrease in the overall transverse dimension of the woven fabric. Hence, higher values of G_{12} (G_{31}) result in an increased resistance to shear deformation in the transverse yarns, leading to a negative influence on the outcome (maximum Poisson's ratio).

Table 3.12 Significance and percent contributions of yarn material properties on Maximum Poisson's ratio under uniaxial loading.

Parameter	Plain	Twill	Satin	Basket
E_{11}	3.57^{+}	2.64^{+}	4.3^{+}	2.6^{+}
E_{22} (E_{33})	1.24^{+}	0.68^{+}	0.33^{+}	0.92^{*}
G_{12} (G_{31})	94.8^{+}	95.5^{+}	94.7^{+}	89.4^{+}
G_{23}	0.35^{+}	0.83^{+}	0.51^{+}	0.96^{*}
COF (μ)	0.001^{*}	0.14^{*}	0.08^{*}	3.8^{+}

$^{+}$*Significant parameter ($p<0.05$),* **Insignificant parameter ($p>0.05$)*

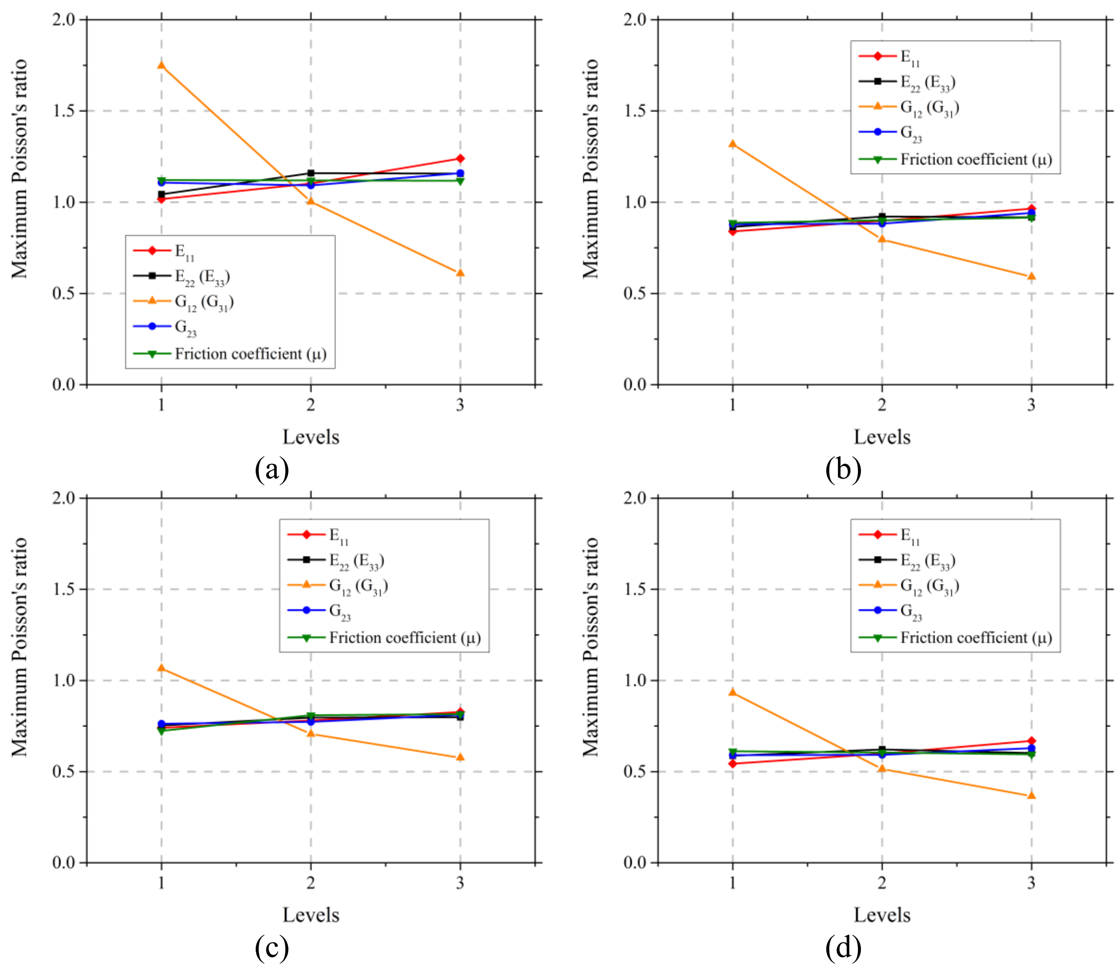

Figure 3.24 Main effects of yarn material properties on maximum Poisson's ratio: (a) Plain weave, (b) Twill weave, (c) Basket weave, and (d) Satin weave.

Both yarn directions within the woven fabric are subjected to tensile forces during biaxial loading. To impose a biaxial loading on the unit cell, the same displacement boundary condition is applied to the two control nodes resulting in the same strain values for both yarn directions. To quantify the effects of the yarn material properties on the mechanical response during biaxial loading, external work done on an unit cell is extracted from the simulations and normalized with the effective unit cell area to take into account different unit cell sizes adopted:

$$W_{norm} = \frac{W_{ext}}{L_{unit}^2} \tag{3.26}$$

where W_{norm}, W_{ext} and L_{unit} are the normalized external work, total external work and the unit cell side length of the unit cell, respectively. The normalized external work is then used as an outcome in the ANOVA calculations to determine the effects of the parameters studied. Figure 3.25a shows the comparison of the normalized external work done on the unit cells with different architectures at different strain values for the 17th simulation defined by the L_{27} orthogonal array. It can be seen that the external work done on the weave architectures are fairly close to each other. Plain weave exhibits the highest normalized external work while satin weave has the lowest values for the strain range studied. Figure 3.25b shows the stress distribution at 1% strain for both yarn directions for the 17th simulation. Since the same material properties and geometric dimensions are used for all the weaves, the stress distributions for both yarn directions are close to each other for all weave types studied.

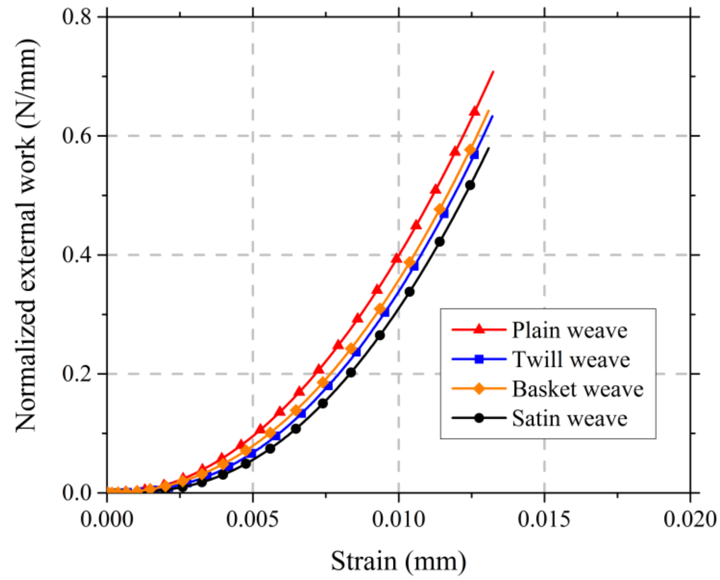

(a)

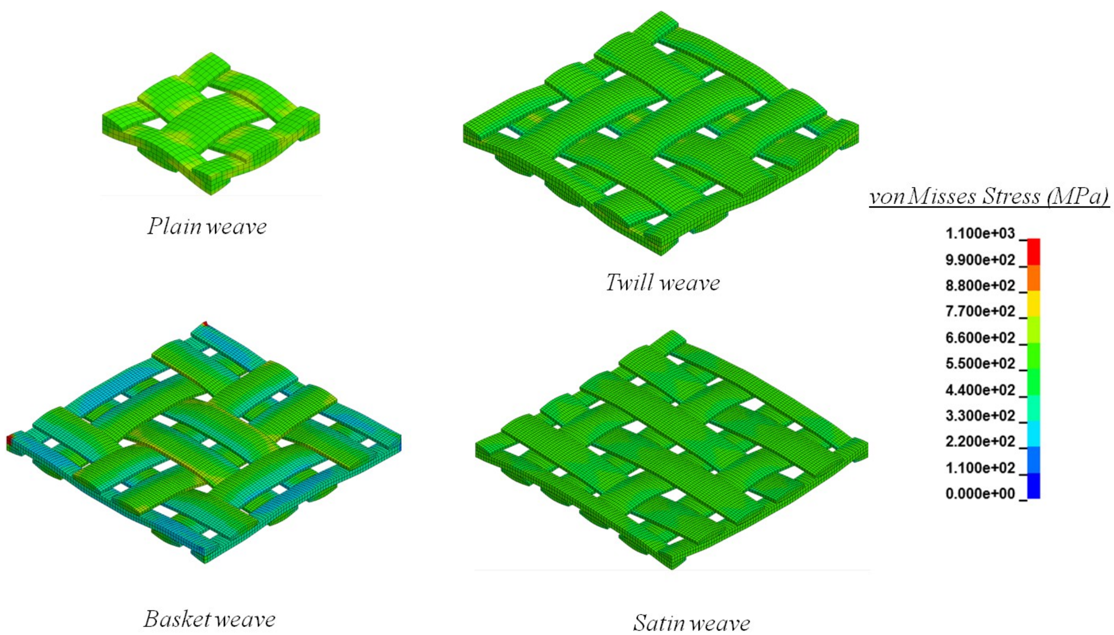

(b)

Figure 3.25 Biaxial tensile test simulations for 17th simulation of L_{27} orthogonal array: (a) Stress - strain curves, and (b) Stress distribution at 1% strain.

The ANOVA results for the normalized external work outcome are shown in Table 3.13. All yarn materials properties studied (expect G_{23} for basket weave) were found to be significant. For all the weave architectures, the yarn longitudinal modulus (E_{11}) had the highest contribution followed by transverse moduli (E_{22} & E_{33}) and transverse shear moduli of the yarns (G_{12} & G_{31}). The difference between the plain weave and other weave architectures could be attributed to the construction of the plain weave where the yarns have higher crimp and more cross-over points where they can interact with each other in the transverse direction compared to other weave types.

Both yarn directions are under tensile loads during biaxial loading. As the deformation progresses, the yarns undergo decrimping while compressing each other at the crossover points. Hence, yarn longitudinal, transverse and transverse shear moduli had influences on the external work done on an unit cell for all weave architectures studied. Figure 3.26 shows the relative effects of the yarn material properties studied on the selected outcome for biaxial loading case (Normalized external work done on the unit cell). E_{11}, E_{22} (E_{33}) and G_{12} (G_{31}) had positive influence on the outcome. As the values of these material properties increase, the normalized external work also increases for all the weave types as shown in Figure 3.26.

Table 3.13 Significance and percent contributions of yarn material properties on the external work done on the fabric under biaxial loading

Parameter	Plain	Twill	Satin	Basket
E_{11}	69.6^{+}	94.5^{+}	90.8^{+}	93.1^{+}
E_{22} (E_{33})	29.2^{+}	3.2^{+}	0.25^{+}	1.22^{+}
G_{12} (G_{31})	1.0^{+}	2.3^{+}	8.8^{+}	4.3^{+}
G_{23}	0.1^{+}	0.01^{+}	0.22^{+}	0.04^{*}
COF (μ)	0.14^{+}	0.02^{+}	0.01^{+}	0.74^{+}

$^{+}$*Significant parameter* ($p<0.05$), **Insignificant parameter* ($p>0.05$)

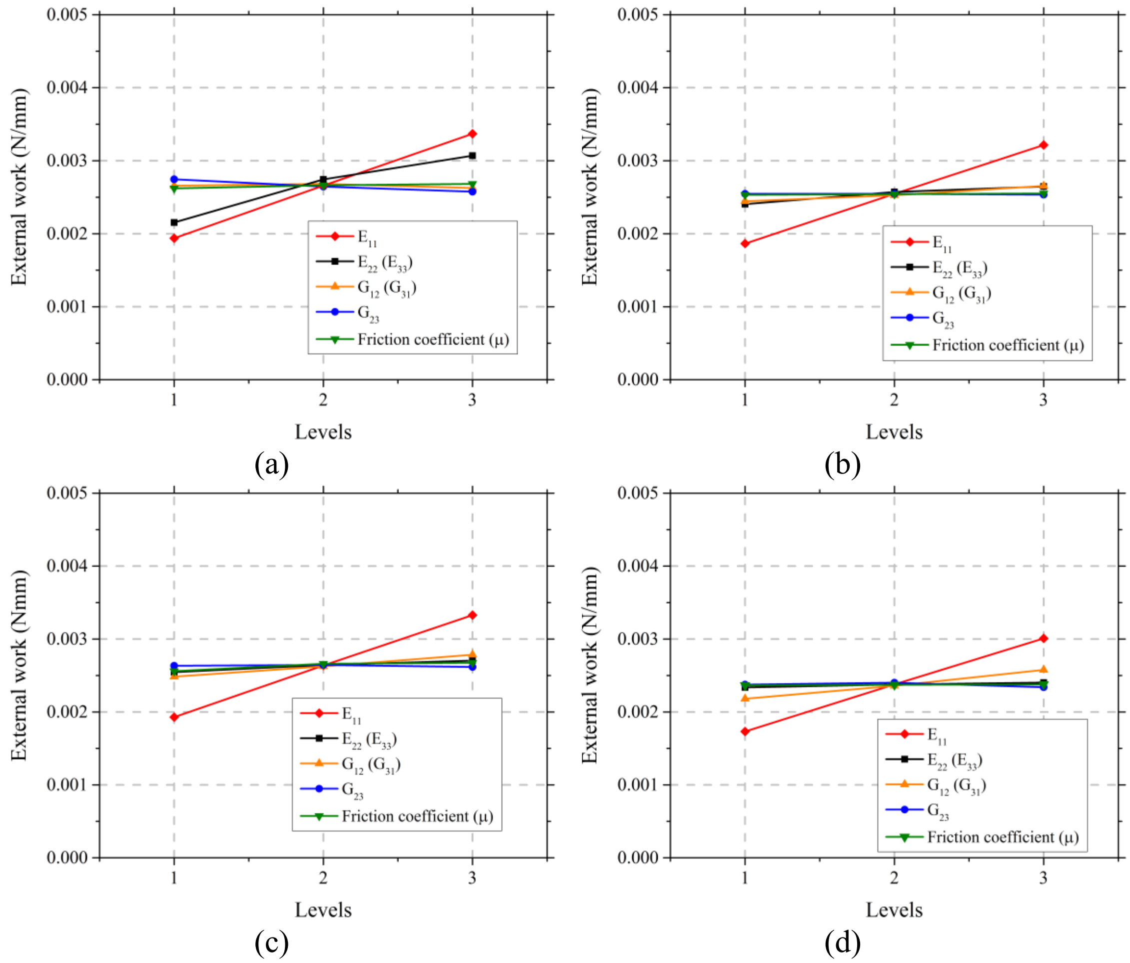

Figure 3.26 Main effects of the yarn material properties on the external work done under biaxial loading: (a) Plain weave, (b) Twill weave, (c) Basket weave, and (d) Satin weave.

The woven fabrics can undergo large deformations when they are subjected to shear loads. Since there are different deformations mechanisms involved during shear loading, the mechanical response observed is highly nonlinear. Hence, the effects of the yarn material properties on mechanical response under shear loading are investigated using the developed approach. Two outcomes are defined: (1) Frictional resistance (Area under the frictional energy - shear angle curve), and (2) Shear resistance (Area under the unit torque - shear angle curve). Frictional resistance is determined by extracting frictional energy dissipated due to the contact between the yarns at different shear angles. The area under this curve is calculated and then normalized with the unit cell area. Moreover, the shear resistance is determined from the unit torque - shear angle curves. For each simulation, the unit torque/moment required to deform a unit cell is determined from Eq. 3.23.

Figure 3.27 shows the comparison of normalized frictional energy and unit torque as well as the von Mises stress distribution on the yarns at 45^o shear angle for all weave types studied (The 17^{th} simulation based on L_{27} orthogonal array). Both frictional energy and unit torque profiles were different for each weave type studied. Plain weave architecture exhibited a higher energy dissipation compared to other weaves. This was followed by the other weave types, twill and satin weaves. On the other hand, basket weave exhibited different characteristics where an initial compliant response was followed by a non-compliant response for both frictional energy and unit torque (Figure 3.27a and 3.27b). The difference between basket and other weaves can be attributed to the construction of the basket weave where the initial yarn mobility is higher than the other weaves since the two yarns that are adjacent to each other are free to move and slide more compared to other weaves.

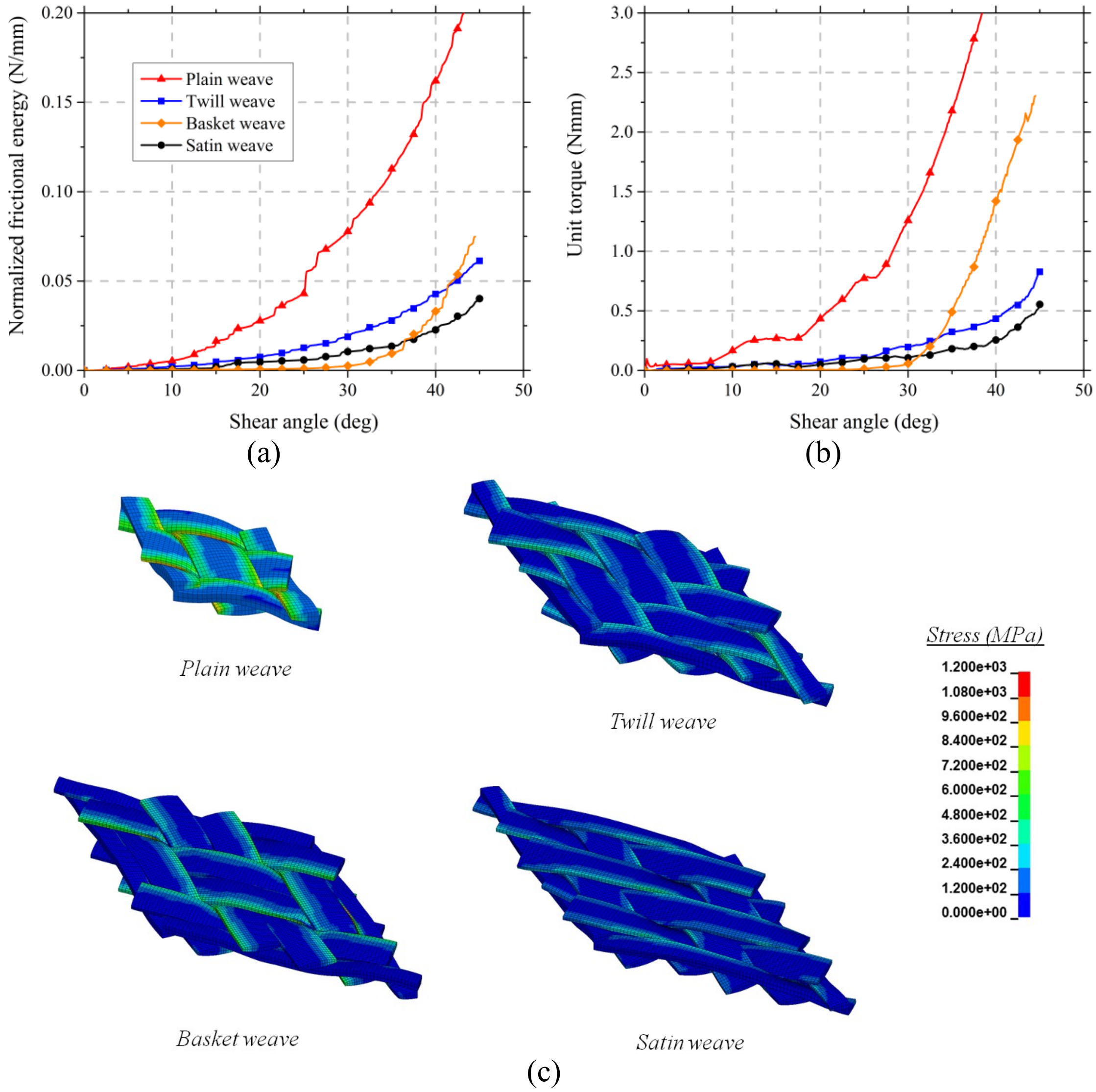

Figure 3.27 Shear loading simulation results for the 17th simulation defined by L_{27} orthogonal array: (a) Frictional energy - shear angle, (b) Unit torque - shear angle, and (c) Stress distribution at 45° shear angle.

The ANOVA results for the frictional energy outcome (The area under the frictional energy - shear angle curve) are presented in Table 3.14. For all the weave types, E_{22} (E_{33}), G_{12} (G_{31}) and COF were found to be significant while E_{11} and G_{23}

were insignificant. Moreover, the COF exhibited the highest percent contribution followed by E_{22} (E_{33}) and G_{12} (G_{31}) (Table 3.14).

Table 3.14 Significance and percent contributions of the yarn material properties on the frictional energy dissipated under shear loading.

Parameter	Plain	Twill	Satin	Basket
E_{11}	2.5^{*}	1.0^{*}	0.88^{*}	0.52^{*}
E_{22} (E_{33})	24.2^{+}	15.4^{+}	13.2^{+}	14.6^{+}
G_{12} (G_{31})	14.8^{+}	17.7^{+}	20.1^{+}	23.9^{+}
G_{23}	2.4^{*}	3^{*}	2.13^{*}	1.4^{*}
COF (μ)	40.3^{+}	51.7^{+}	52.4^{+}	46.0^{+}

$^{+}$*Significant parameter ($p<0.05$),* **Insignificant parameter ($p>0.05$)*

The main effects of the yarn material properties on the frictional energy outcome are shown in Figure 3.28. All significant yarn material properties had positive effects on the outcome for all weave types. The frictional resistance increases with the increased values (Levels) of E_{22} (E_{33}), G_{12} (G_{31}) and COF. The effect and contribution of the COF to the outcome is clear since it directly affects the energy dissipated due to the contact between the yarns. The effects and contributions of E_{22} (E_{33}) and G_{12} (G_{31}) can be attributed to the yarns' interaction due to yarn-to-yarn contact and pressure developed between the yarns during shear deformation. Increased values of these properties result in higher contact pressures between the yarns, leading to higher frictional resistance (Higher frictional energy dissipation).

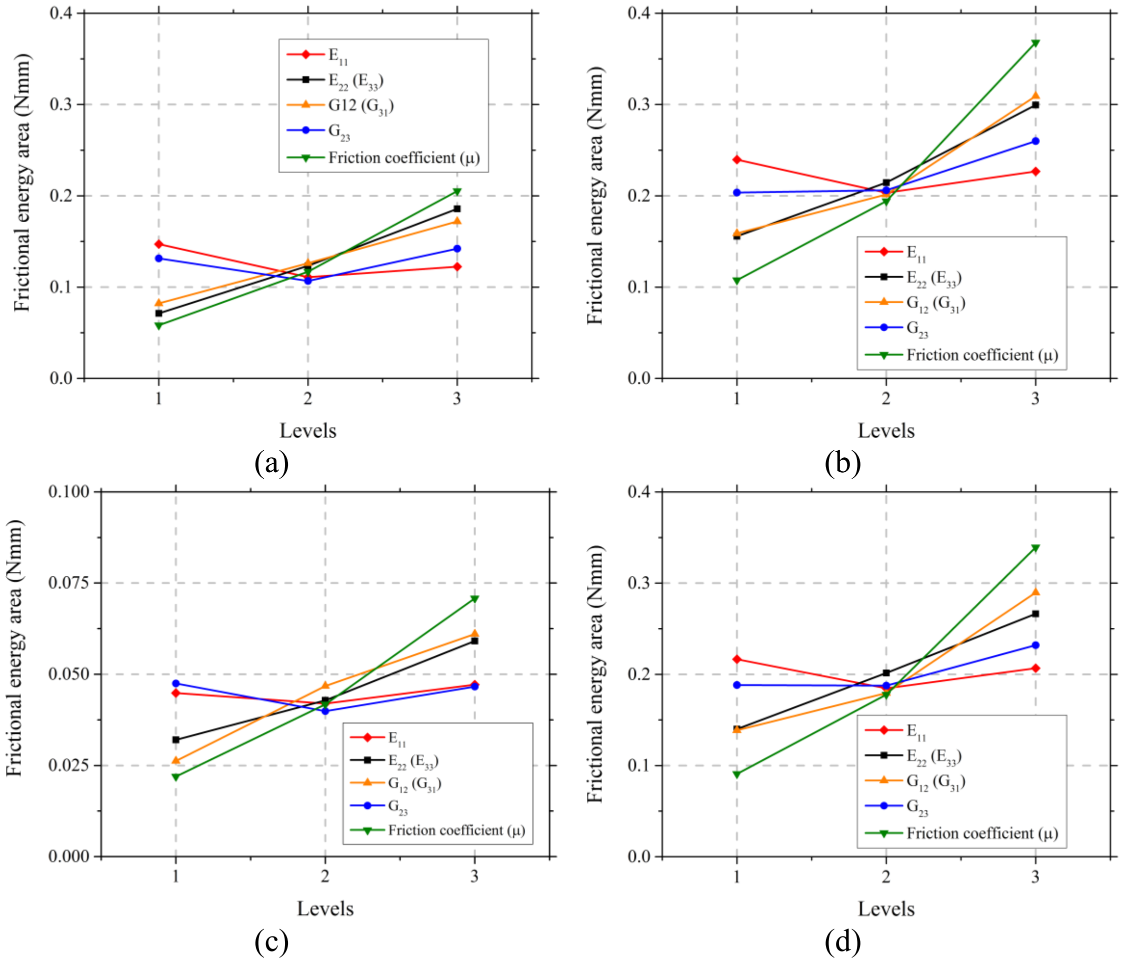

Figure 3.28 Main effects of the yarn material properties on the frictional energy dissipated under shear loading: (a) Plain weave, (b) Twill weave, (c) Basket weave, and (d) Satin weave.

Unit torque - shear angle curves obtained from the simulations were used to investigate the effects of the yarn material properties on the macroscale shear resistance of the woven fabrics with the proposed model. Table 3.15 shows the ANOVA results for the outcome. E_{22} (E_{33}), G_{12} (G_{31}) and COF were found to be significant while E_{11} was determined to be insignificant for all the weave types. The insignificance of E_{11} can be attributed to the periodic boundary conditions imposed on the unit cells to prescribe shear loading. The yarns within the unit cells were not subjected to longitudinal forces due to the definition of the boundary conditions. Hence, the yarns do not undergo uniaxial tensile deformation when the unit cells are subjected to shear loading. Moreover, G_{23} was found to be significant for plain, twill and satin weaves while it was determined to insignificant for basket weave. E_{22} (E_{33}), G_{12} (G_{31}) and COF had the highest contributions while the contributions of E_{11} and G_{23} were relatively small compared to other parameters studied (Table 3.15).

Table 3.15 Significance and percent contributions of the yarn material propertied on the unit torque (Shear resistance) under shear loading.

Parameter	Plain	Twill	Satin	Basket
E_{11}	3.3^*	1.4^*	0.86^*	1.4^*
E_{22} (E_{33})	53.2^+	18.8^+	13.4^+	23.8^+
G_{12} (G_{31})	15.8^+	35.2^+	41^+	9.9^+
G_{23}	6.2^+	12.1^+	5.7^+	0.98^*
COF (μ)	15.8^+	27.5^+	34^+	53.4^+

$^+$*Significant parameter* ($p<0.05$), **Insignificant parameter* ($p>0.05$)

Figure 3.29 shows the relative effects of the yarn material properties on the shear resistance outcome (Area under the unit torque - shear angle curves). All significant material properties had positive effects. As the values (Levels) for these material properties increase, the area under the unit torque - shear angle curve increases, resulting in a higher resistance to shear deformation. During shear deformation, the yarns initially rotate relative to each other. The initial shear resistance of the woven fabric is then governed by the contact between yarns resulting in frictional effects. Hence, COF plays an important role during this initial shear deformation. As the deformation progresses, the yarns start contacting in the transverse direction (22-direction in Figure 3.1). The yarns deform in various ways at these contact locations which result in localized stresses in yarns as shown in Figure 3.27c. Hence, E_{22} (E_{33}) and G_{12} (G_{31}) are important and influence the shear resistance. Moreover, the contributions of the yarn material properties to the outcome highly depend on the weave type (Table 3.15). The difference between the weaves studied can be attributed to their constructions. The weave architecture determines the yarns' structure as well as the deformation mechanisms involved in the mesoscopic length scale (yarn level).

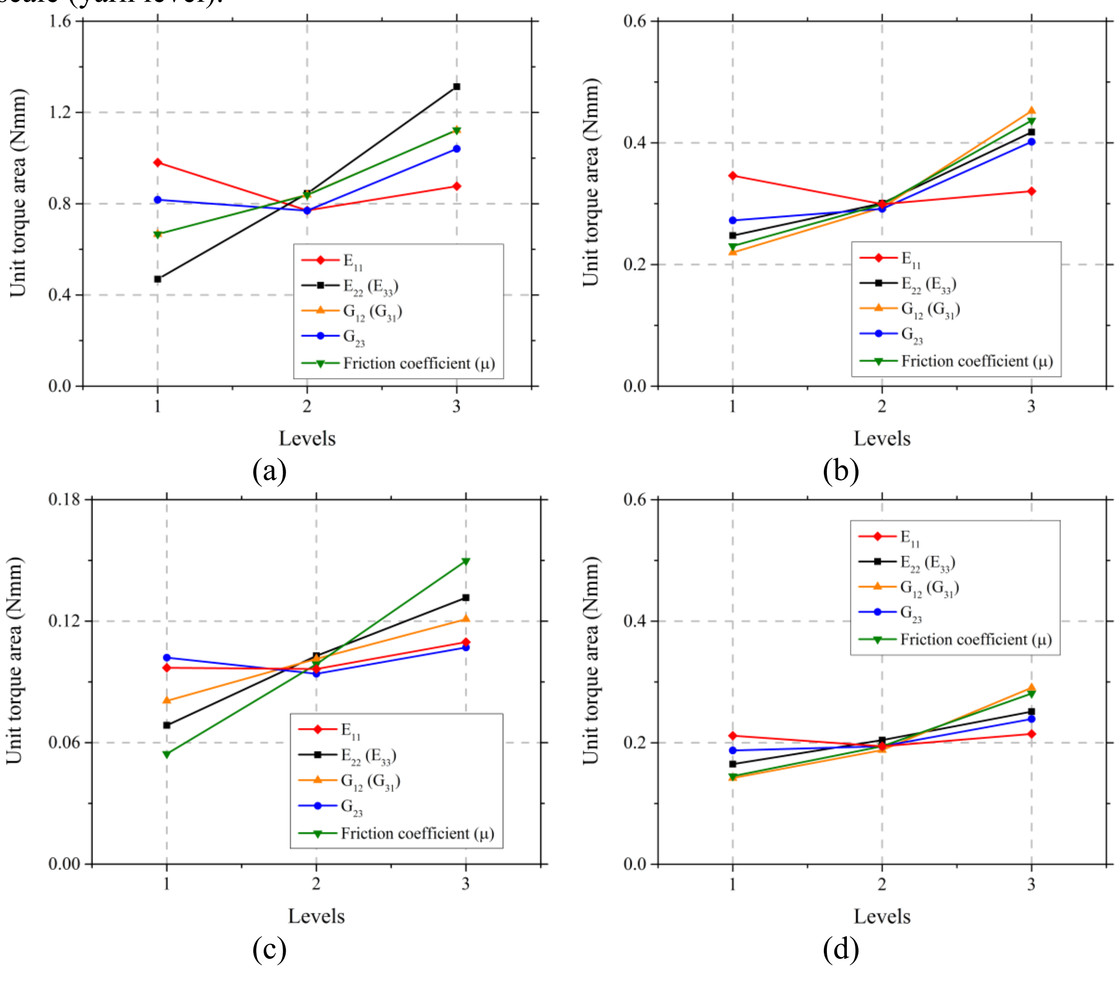

Figure 3.29 Main effects of the yarn material properties on the unit torque (Shear resistance) under shear loading: (a) Plain weave, (b) Twill weave, (c) Basket weave, and (d) Satin weave.

3.4 Summary and Contributions

In the mesoscopic length scale simulations, the yarns within the woven fabrics are modeled explicitly. This modeling approach provides insight into the yarn level deformations and interactions between the yarns under various loading conditions. The current work adopted this length scale modeling to capture/investigate complex deformation mechanisms and associated nonlinear mechanical response involved in woven fabrics. To model woven fabrics, a unit cell finite element modeling approach coupled with periodic boundary conditions was developed. A hyperelastic transversely isotropic yarn material model with transverse material nonlinearity was implemented as a UMAT to model K706 plain weave fabrics. K706 yarn material properties were determined either directly or through an inverse method where simulations and experiments were used. Specifically, the weft and warp yarn longitudinal moduli were determined from the single yarn experiments. The uniaxial tensile test simulations using the unit cell model coupled with the inverse method were carried to determine transverse shear moduli of the yarns. Additionally, unit cell finite elements were simulated under shear loading coupled with the inverse method to determine the transverse moduli of the yarns. Then, the developed yarn model was validated by simulating real uniaxial tensile, bias extension and indentation experiments. The mesoscopic numerical models developed were able to capture the mechanical response observed in these experiments. Currently, there are no single widely accepted yarn material models available in the literature due to difficulties involved in determining yarn material properties. The general approach developed in this work to determine the material properties is to use experimental values together with the proposed inverse method coupled with unit cell level simulations. Most of the mesoscopic numerical models for woven fabrics are limited to unit cell level simulations. The current work extends these methods by coupling the unit cell levels with the fabric level simulations. The developed mesoscopic numerical models in the current work was able to capture both unit cell level deformations and mechanical response as well as the real experiments. Table 3.16 shows the comparison of the developed model to the models available in the literature.

Table 3.16 Comparison of the mesoscopic length scale material model to the available models in the literature.

Work	Material model	Simulations	Validation
Duan et al. [4], [44] Rao et al. [38], [41] Nilakantan et al. [8], [40]	Linear orthotropic Hyperelastic	Fabric level	N/A
Badel et al. [1], [42] Gasser et al. [44] Gatouillat et al. [13]	Transversely isotropic Nonlinear transverse modulus⁺ Hypoelastic	Unit cell	Biaxial Picture frame
Lin et al. [46]	Transversely isotropic Nonlinear transverse modulus⁺ Hypoelastic	Unit cell	Picture frame Compression
Charmetant et al. [48]	Transversely isotropic Nonlinear transverse modulus⁺ Hyperelastic	Unit cell	Uniaxial Biaxial Picture frame
Current work	Transversely isotropic Nonlinear transverse moduli⁺ Hyperelastic	Unit cell Fabric level	Uniaxial Bias extension Indentation $0^o/45^o/90^o$

⁺ *Inverse approach*

Furthermore, the mesoscopic length scale numerical modeling approach was also adopted to study the effects of the yarn material properties and weave architectures on the macroscopic response of the woven fabrics. Unit cell finite element modeling was coupled with a special design-of-experiments technique (Taguchi method) to identify important yarn material properties on macroscale response of various weave architectures. 4 different weave architectures were studied for this purpose: (1) Plain weave, (2) Twill weave, (3) Basket weave, and (4) Satin weave. These architectures were simulated and compared under uniaxial, biaxial and shear loads using the unit cell modeling for the first time. Several macroscale outcomes were defined for each loading case such as fabric modulus before/after decrimping, Poisson's ratio, frictional energy dissipation and shear resistance. The effects of the yarn material properties on these outcomes were studied with the Taguchi method for all the weave architectures.

The results of the study revealed under uniaxial loading the yarn transverse shear moduli (G_{12}=G_{31}) play an important role on the fabric mechanical response before decrimping. It was concluded that the yarns undergo transverse shear deformation while losing their crimp. It was also shown that the response observed during decrimping can be adjusted by changing the transverse shear modulus. Moreover, it was determined that Poisson's ratio for all weave types exhibited a nonlinear form due to the interactions between the yarns and it is highly dependent on the weave architecture and yarn crimp. It was shown that the yarn transverse shear modulus had a negative effect on the Poisson's ratio where lower values resulted in higher Poisson's ratios at a given weave architecture.

The yarn longitudinal modulus (E_{11}), transverse moduli (E_{22} & E_{33}) and transverse shear moduli (G_{12} & G_{31}) are found to be significant for the fabric deformation under biaxial loading. All these yarn material properties have positive influence on the woven fabrics' resistance to biaxial deformation. As the values of these properties increase, the woven fabrics' resistance to deformation under biaxial increases too.

The method developed also revealed the importance of coefficient of friction between the yarns, yarn transverse moduli (E_{22}=E_{33}) and yarn transverse shear moduli (G_{12}=G_{31}) under shear loading. These material properties were found to be important and affect the shear resistance of the woven fabrics studied. It was shown that the frictional energy dissipated during shear can be reduced or increased by changing the yarns' transverse modulus and the friction coefficient. Furthermore, the results revealed that the yarns undergo localized shear deformations at the contact points affecting the resistance of the fabric to shear deformation. Table 3.17 summarizes the results of the developed approach.

Table 3.17 Summary of the important yarn material properties based on the developed approach.

		Important material properties			
Loading	**Outcome**	**Plain weave**	**Twill weave**	**Basket weave**	**Satin weave**
Uniaxial	FMBD	E_{11} G_{12} (G_{31})	E_{11} G_{12} (G_{31})	E_{11} G_{12} (G_{31})	E_{11} G_{12} (G_{31})
	FMAD	E_{11}	E_{11}	E_{11}	E_{11}
	Poisson's ratio	G_{12} (G_{31})	G_{12} (G_{31})	G_{12} (G_{31})	G_{12} (G_{31})
Biaxial	External work	E_{11} E_{22} (E_{33})	E_{11} E_{22} (E_{33})	E_{11} G_{12} (G_{31})	E_{11} G_{12} (G_{31})
Shear	Frictional energy	μ E_{22} (E_{33}) G_{12} (G_{31})	μ E_{22} (E_{33}) G_{12} (G_{31})	μ E_{22} (E_{33}) G_{12} (G_{31})	μ E_{22} (E_{33}) G_{12} (G_{31})
	Unit torque	μ E_{22} (E_{33}) G_{12} (G_{31})	μ E_{22} (E_{33}) G_{12} (G_{31}) G_{23}	μ E_{22} (E_{33}) G_{12} (G_{31})	μ, E_{22} (E_{33}), G_{12} (G_{31}) & G_{23}

Since different weaves were studied using the method, the differences observed in mechanical responses between the architectures were also identified. It was shown that the crimp amount due to the weave design has a significant effect on the mechanical response and deformation kinematics observed under uniaxial tensile loading. Moreover, the results of the study showed that the resistance to shear deformation can be adjusted by changing the weave architecture.

Even though mesoscopic length scale numerical modeling allows studying yarn level deformation mechanisms while providing valuable insights, it is not possible to simulate large scale structures due to prohibitive computational costs associated. Hence, macroscopic length scale models, that are computationally more efficient are necessary to simulate large structures. The following chapters aim to develop macroscopic material models while investigating the trades-off between different length scale modeling approaches.

Chapter 4

MACROSCOPIC LENGTH SCALE COMPUTATIONAL MODELING

4.1 Introduction

Since the thickness of the woven fabric is smaller than the in-plane dimensions, they are considered as 2D materials and they are modeled as non-orthogonal continuums with material non-linearity in macroscopic length scale modeling approaches. The models in this length scale adopt either shell or membrane elements to simulate woven fabrics given their 2D physical nature. Usage of these elements results in computationally efficient and faster simulations. Since the out-of-plane stresses are not included in membrane/shell elements, it is important to determine woven fabrics' in-plane mechanical response under uniaxial, biaxial and shear loads in the macroscopic length scale modeling. Moreover, the discrete nature of the fabric should be homogenized in this length scale because it is assumed that the fabric behave as a continuum.

The main goal of this chapter is to develop macroscopic material models with certain assumptions to demonstrate their ability to capture complex deformation mechanisms and nonlinear mechanical response. Hence, two material models with different complexities are developed. The first material model simplifies the fabric by assuming the yarns lie on the same plane and only considers uniaxial and shear response. This allows computationally efficient and simplified constitutive relations in the expense of losing certain deformation mechanisms. On the other hand, the second model takes into account the 3D structure of the fabric. The model considers uniaxial, biaxial and shear responses involved in woven fabrics. However, consideration of 3D structure of fabrics results in complex constitutive relations and requires additional computational resources compared to the first material model. The chapter also aims to demonstrate the capability of the material model to capture woven fabric response under various loads by comparing them to each other.

4.2 Planar Material Model (PMM)

4.2.1 Model basics and implementation

Woven fabrics have two distinct yarn directions called: (1) weft, and (2) warp due to the weaving process. Different weave architectures can be obtained by alternating each yarn direction over and under the other yarn direction. This construction of woven fabrics also creates a basic unit cell within the fabric as shown in Chapter 3 (Figure 4.1). The first proposed material model is based on a single unit cell and assumes that the crossing yarns lie on the same plane and they are pin-jointed at the crossover point (Figure 4.1). Therefore, the material model is named "Planar Material Model" (PMM). The mechanical response of unit cell is implemented with two components: (1) yarns as trusses for uniaxial response, and (2) rotational crossover spring for shear response (Figure 4.1).

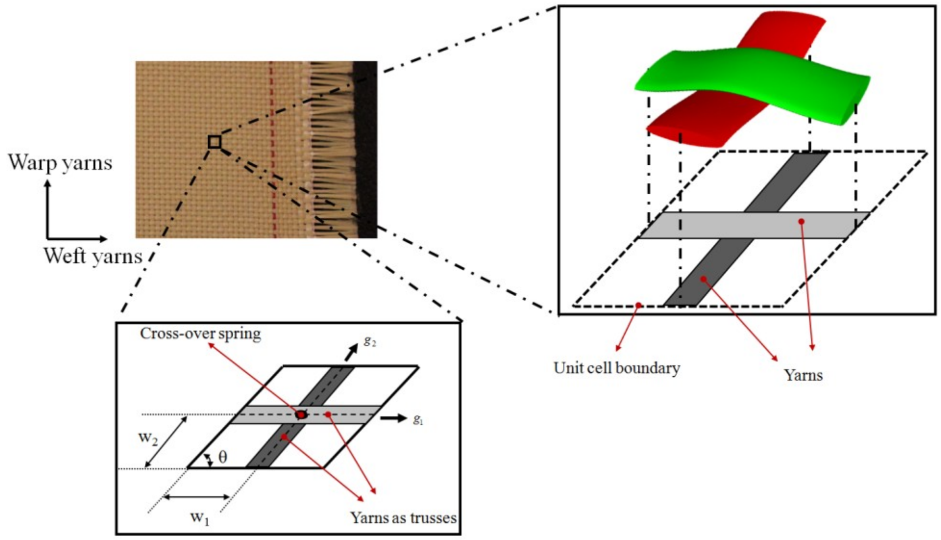

Figure 4.1 Unit cell adopted for PMM and mechanisms used to define mechanical response of the woven fabrics.

The yarns are initially orthogonal to each other when the woven fabric is not deformed. However, they can rotate relative to each to other under shear loading and do not stay orthogonal. Since the yarns are implemented as trusses in the current material model, two unit vectors (g_i) are assigned for each truss to keep track of the yarn orientation as well as the angle between them. These unit vectors form a non-orthogonal reference frame defining the orientation of the unit cell at any given deformation. The orientations of the unit vectors are determined from a co-rotational reference frame (orthogonal) attached to the shell element with basis vectors ($\underline{q}_i$) (Figure 4.2). In LS-DYNA, this co-rotational reference frame is based on the node numbering and it stays orthogonal during any deformation. The unit vectors defining yarn orientations can be related to their initial configurations (g_i^0) by using the deformation gradient ($\underline{F}$) defined in the element co-rotational reference as:

$$\underline{g_i} = \underline{F}\,\underline{g_i^0} \tag{4.1}$$

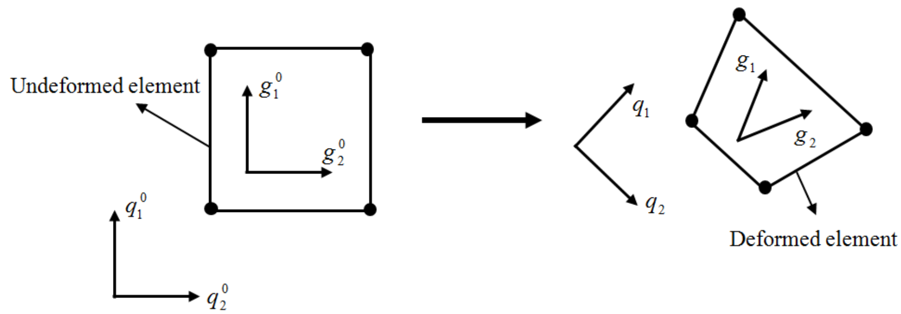

Figure 4.2 Non-orthogonal and co-rotational reference frames used to determine kinematics.

Then, the stretches (λ_i) along the unit vector directions can be calculated as [58, 74]:

$$\lambda_i = \sqrt{\underline{g}_i^0 \underline{C} \underline{g}_i^0} \tag{4.2}$$

where $\underline{C}$ is the Green-Cauchy deformation tensor and defined as:

$$\underline{C} = \underline{F}^T \underline{F} \tag{4.3}$$

The angle between the unit vectors (θ) and shear angle (γ) can be determined from the yarn stretches as:

$$\begin{gathered} \theta = \cos^{-1}\left(\frac{\underline{g}_1^0 \underline{C} \underline{g}_2^0}{\lambda_1 \lambda_2} \right) \\ \gamma = \frac{\pi}{2} - \theta \end{gathered} \tag{4.4}$$

Since the material model assumes that the yarns lie on the same plane, the configuration of unit cell at any given deformation can be determined from the unit cell quarter half lengths (w_i, i=1,2) and the angle between the unit vectors (θ) (Figure 4.1). Hence, the unit cell quarter half lengths can be determined from yarn stretches as:

$$w_i = w_i^0 \lambda_i \tag{4.5}$$

In PMM, yarns are modeled as trusses while a rotational spring is adopted to implement shear behavior of the plain weave fabric as mentioned before. Yarn in woven fabrics exhibit a permanent crimp due to the weaving and they undergo a significant deformation called decrimping when they are subjected to uniaxial tensile loads. During decrimping, the yarns are subjected to transverse shear until they are fully straightened. They initially exhibit a compliant mechanical response until their crimp is removed. After this point, the mechanical response becomes non-compliant since the filaments' longitudinal direction is aligned with the loading direction. To implement this behavior in the material model, the yarns are modeled as truss elements and the tensions developed (T_i) in each truss is defined as:

$$T_i = E_i(\varepsilon_i) A_i \varepsilon_i \tag{4.6}$$

where E_i, A_i and ε_i are yarn longitudinal modulus as a function of yarn strain, yarn cross sectional area and yarn strain, respectively. It is assumed that the yarns' uniaxial behavior is independent from each other. The yarn strain for each direction is determined from the associated yarn stretch:

$$\varepsilon_i = \lambda_i - 1 \tag{4.7}$$

The yarns exhibit a bilinear response when they are subjected to tensile loading. Hence, the yarn longitudinal modulus (E_i) can be implemented in a nonlinear fashion to obtain this bilinear mechanical response:

$$E_i(\varepsilon_i) = \begin{cases} E_i^1 & \varepsilon_i < 0 \\ E_i^1 + \dfrac{E_i^2}{1 + \exp\left[-\beta_i\left(\varepsilon_i - \varepsilon_{i,crimp}\right)\right]} & 0 \le \varepsilon_i \le \varepsilon_{i,trans} \\ E_i^2 & \varepsilon_i > \varepsilon_{i,trans} \end{cases} \tag{4.8}$$

where E_i^1, E_i^2, β_i, $\varepsilon_{i,\mathrm{trans}}$ and $\varepsilon_{i,crimp}$ are yarn modulus before decrimping, yarn modulus after decrimping, shape parameter, transition strain where E_i becomes equal to E_i^2 and decrimping strain, respectively. Eq. 4.8 provides a function with two constant yarn modulus (before and after decrimping) with a smooth transition region between them.

Shear response of woven fabrics is governed by the interactions of the yarns at the mesoscopic length scale. The shear resistance of the woven fabrics comes from different deformation mechanisms. The yarns are initially free to rotate relative to each other and essentially frictional resistance to yarn motion governs the shear response during this rotation. The yarns start to compress themselves in the transverse direction after a certain amount of rotation. The filaments within the yarns start packing and fill the gaps present in the yarns. This results in increased shear resistance. The yarns lock after the gaps are filled by the filaments resulting in a high resistance to shear deformation. All these deformation mechanisms result in a highly nonlinear mechanical response. A rotational spring located at the crossover point is implemented to capture this complex mechanical response. The moment (M_s) generated by the spring is defined as a function of shear angle (γ) [74]:

$$M_s = C_1\left[e^{C_2|\gamma|}\right] - 1 \tag{4.9}$$

where C_1 and C_2 are material parameters. The material model assumes that the tensile and shear behavior is decoupled from each other and implemented with separate constitutive relations. The out-of-plane mechanical response (Transverse shear deformation and bending) is also decoupled from in-plane response and treated independently. The fabric thickness change during deformation is assumed to be negligible while relatively high transverse shear modulus is used for the shell elements to limit the effects of transverse shear on the in-plane response.

The forces and moments/torques generated from the unit cell structural elements (Yarn trusses and rotational crossover spring) can be calculated after the configuration of the unit cell is determined from deformation gradient. These forces/moments are assumed to be balanced by the stresses that exert tractions on the unit cell boundaries (Figure 4.3). Hence, these tractions ($\underline{t}$) can be related to Cauchy stress ($\underline{\sigma}$) as [58]:

$$\underline{t} = \underline{\sigma}\underline{n}dS \tag{4.10}$$

where dS and $\underline{n}$ are small surface element and unit normal of the surface, respectively. Then, the Cauchy stress tensor at a given material point can be expressed in terms of the unit vectors as:

$$\begin{aligned}\underline{\sigma} = &\frac{1}{2w_2 t_f^0 \sin\theta}\left[T_1 - \frac{M_s \cos\theta}{2w_1 \sin\theta}\right]\left(\underline{g}_1 \otimes \underline{g}_1\right) + \frac{1}{2w_1 t_f^0 \sin\theta}\left[T_2 - \frac{M_s \cos\theta}{2w_2 \sin\theta}\right]\left(\underline{g}_2 \otimes \underline{g}_2\right) \\ &+ \frac{M_s}{4w_1 w_2 t_f^0 \sin^2\theta}\left(\underline{g}_1 \otimes \underline{g}_2 + \underline{g}_2 \otimes \underline{g}_1\right)\end{aligned} \tag{4.11}$$

where t_f^0 and $\otimes$ are fabric's initial thickness and dyadic (Tensorial) product.

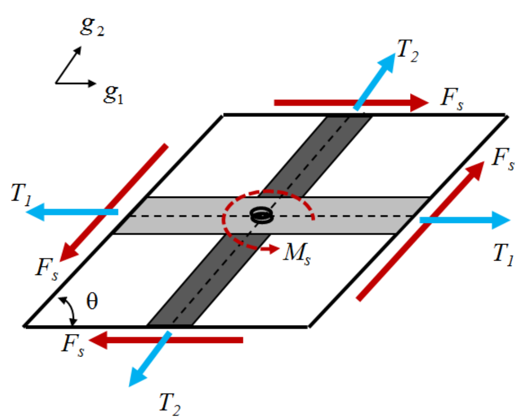

Figure 4.3 Force/moment reflected to the unit cell boundaries for Cauchy stress calculations (F_s is the boundary force balancing the moment generated by the rotational spring.).

Eq. 4.11 can be implemented in an explicit finite element code with standard shell/membrane elements. The constitutive relations developed are implemented in LS-DYNA's double precision vectorized user-defined-material (UMAT) subroutine and the code is complied in Linux Xeon64 environment. Figure 4.4 shows the flow chart of the material model implemented. LS-DYNA sends the incremental strains and deformation gradient in the element co-rotational reference frame at each time step to the material subroutine. The deformation gradient is used to determine the unit vector configurations. Then, the angle between these vectors and yarn strains are calculated from these configurations. Finally, forces/moments developed within the unit cell are used for stress calculations and transformed back to the element coordinate system and returned back to LS-DYNA for the next time step.

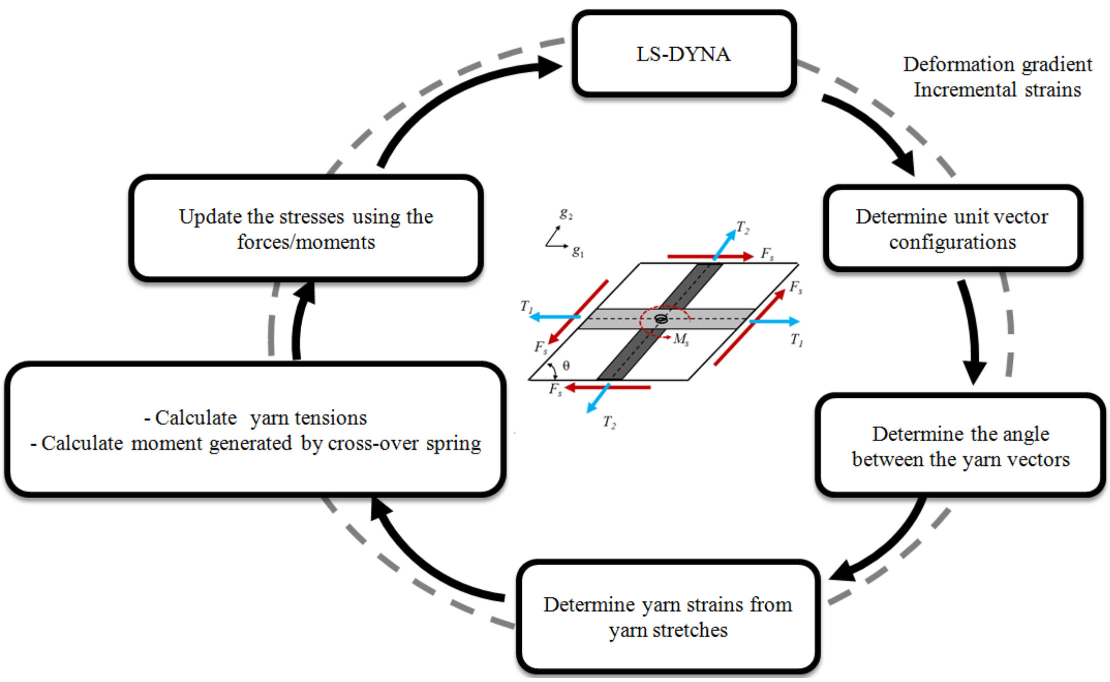

Figure 4.4 Implementation flow chart for PMM within a finite element code.

4.2.2 Validation of the Material Model

To validate the material model under various loads, two different Kevlar fabrics are used: (1) Kevlar 706 (K706), and (2) Kevlar 745 (K745). Both fabric types have plain weave architecture. K706 is tightly woven and lighter with 34 yarns per inch. On the other hand, K745 is a looser and heavier weave compared to K706 and it has 17 yarns per inch.

The yarn material properties and parameters required by the material model are obtained from the experimental stress-strain curves of uniaxial tensile tests on fabrics [9, 74]. Stress-strain curves are converted to stress-strain curves for single yarns by assuming the yarns have elliptical cross sections. Hence, the yarn cross-sectional areas (A_i) are calculated from:

$$A_i = 0.25\pi a_i^1 a_i^2 \tag{4.12}$$

where a_i^1 and a_i^2 are yarn major and minor diameters, respectively. The obtained curves are then used to determine E_i^1, E_i^2, $\varepsilon_{i,trans}$ and $\varepsilon_{i,crimp}$. The yarn modulus change with the applied strain for weft yarns is shown in Figure 4.5a. Moreover, the values of material properties/parameters for Eq. 4.8 are presented in Table 4.1.

Rotational crossover spring parameters (C_1 and C_2) are obtained from bias extension tests. The moment/torque generated by the rotational spring within the unit cell corresponds to the moment/torque required to deform a one crossover point on a woven experimental test specimen. This experimental unit moment/torque (M_{exp}) can be determined from the energy made through the tensile machine to deform the specimen and is given as [66]:

$$M_{\exp}(\gamma) = \frac{1}{(2H-3W)}\left\{\left(\frac{H}{W}-1\right)F\left(\cos\frac{\gamma}{2}-\sin\frac{\gamma}{2}\right)-WM_{\exp}\left(\frac{\gamma}{2}\right)\cos\frac{\gamma}{2}\right\} \tag{4.13}$$

where H, W and F are experimental specimen height and width, and force measured by the tensile machine, respectively. The details of the procedure of obtaining this unit moment/torque is given in Chapter 2. The parameters of Eq. 4.9 are then determined by minimizing the root mean square error (RMSE) between the experimental average unit moment/torque and Eq. 4.9. The values obtained from experimental unit moment/torque for shear parameters are presented in Table 4.1. The upper and lower bounds for the shear spring parameters (C_1 and C_2) were also determined by fitting Eq. 4.9 to the experimental upper (Experimental average + 1 SD) and lower (Experimental average - 1 SD) bounds and presented in Table 4.1. Figure 4.5b shows the curve fits obtained for the experimental average for K706 and K745 fabric styles.

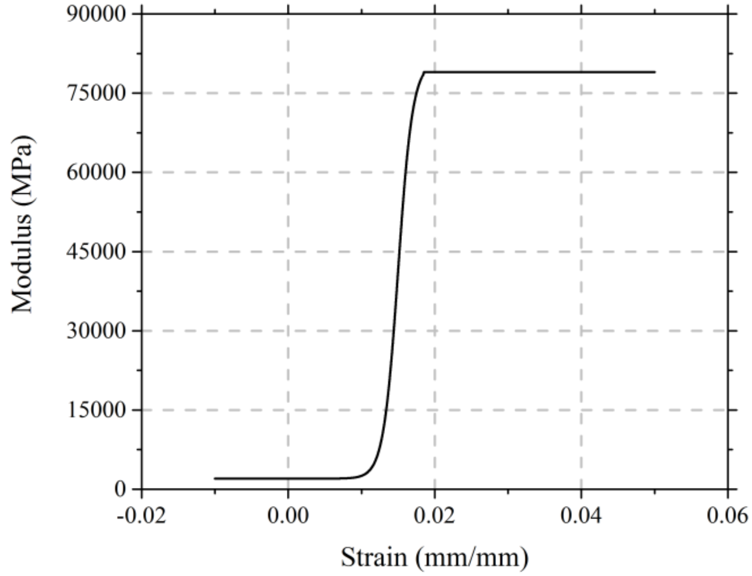

(a)

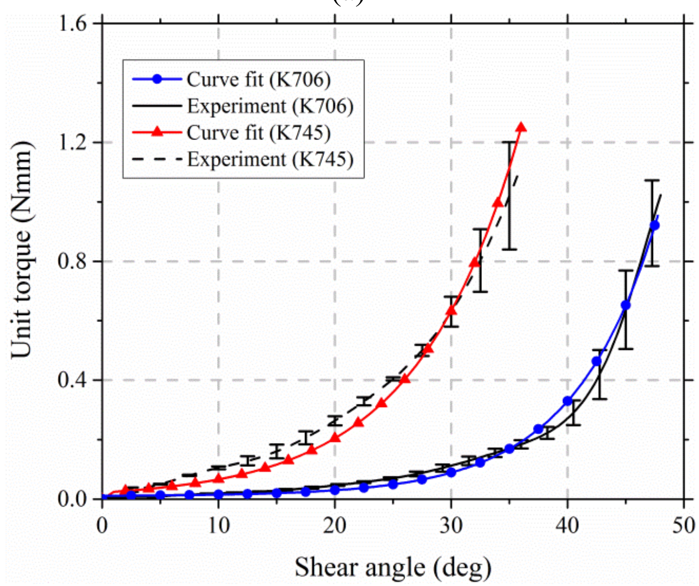

(b)

Figure 4.5 Mechanical response components of the PMM: (a) Yarn nonlinear modulus, and (b) Moment/torque response of the rotational crossover spring.

Table 4.1 Material properties and parameters used for PMM simulations.

Fabric		E_i^1 (MPa)	E_i^2 (MPa)	β_i	$\varepsilon_{i,crimp}$	$\varepsilon_{i,trans}$
K706	Weft ($i=1$)	4000	79000	1000	0.015	0.018
	Warp ($i=2$)	4000	69000		0.025	0.0285
	Shear parameters		C_1 (Nmm)	C_2 (rad^{-1})		
		Average	0.0008	8.47		
		Upper bound	0.001	8.38		
		Lower bound	0.0013	7.59		
	Geometric parameters	w_1^0 (mm)	w_2^0 (mm)	t_f^0 (mm)		
		0.747	0.747	0.293		
K745		E_i^1 (MPa)	E_i^2 (MPa)	β_i	$\varepsilon_{i,crimp}$	$\varepsilon_{i,trans}$
	Weft ($i=1$)	4000	77000	1000	0.02	0.0229
	Warp ($i=2$)	4000	65000		0.035	0.0377
	Shear parameters		C_1 (Nmm)	C_2 (rad^{-1})		
		Average	0.04	5.3		
		Upper bound	*0.034*	5.8		
		Lower bound	0.046	4.74		
	Geometric parameters	w_1^0 (mm)	w_2^0 (mm)	t_f^0 (mm)		
		1.494	1.494	0.61		

To validate the PMM's tensile and shear behavior, two experimental tests were simulated with the developed material model. The uniaxial tensile test simulations were carried out to validate material model's tensile behavior while bias extension test simulations were run for the shear response.

The computational models for the uniaxial tensile test simulations had a width of 25.4 mm and a length of 101.6 mm for both fabric types (K706 and K745). Both yarn directions were simulated by aligning the specific yarn direction with the loading direction. An initial mesh sensitivity analysis with different square element sizes (0.747 mm, 1.05 mm and 1.494 mm) was carried out. The simulation results were not sensitive to the mesh sizes studied. Hence, larger element size (1.494 mm) was used to model the fabrics. Figure 4.6 shows the simulation and experimental (Taken from

Dong et al.'s work [9]) results of uniaxial tensile loading for K706 and K745 style fabrics, respectively. The material model was able to capture the fabrics' experimentally observed bilinear mechanical response under uniaxial loading. It can be seen from Figure 4.6, the fabrics exhibit different mechanical behavior such as the strain level that decrimping occurs. This difference is mainly due to the structure of the fabric types even though they have the same weave architecture. K706 has smaller yarns and tighter weave compared to K745. Hence, K706 has less crimp compared to K745 resulting in smaller decrimping strains for both yarn directions.

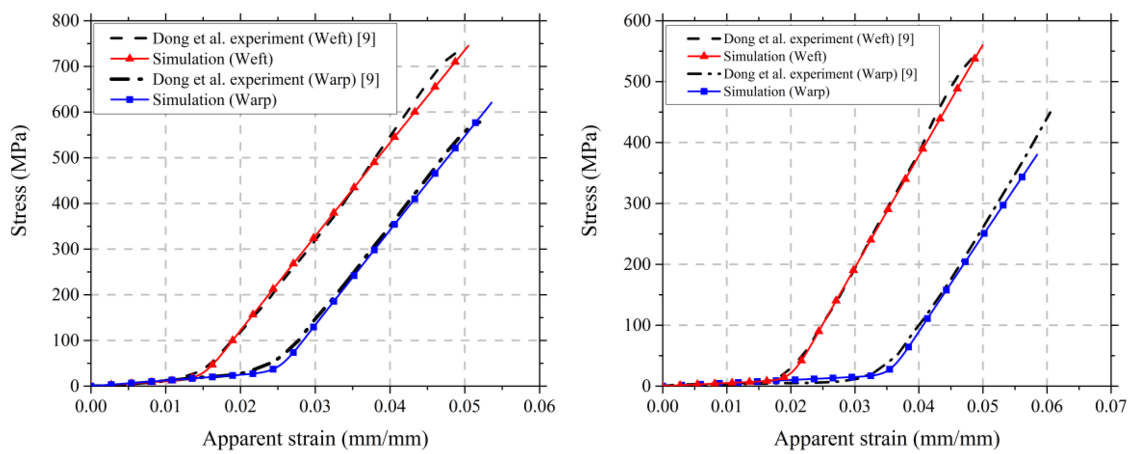

(a) (b)

Figure 4.6 Uniaxial tensile test simulations: (a) K706, and (b) K745 [9].

Bias extension tests were simulated by rotating the yarn directions by 45^{o} with respect to the loading direction within the unit cell. An initial mesh sensitivity was carried out to investigate the mesh density's effect on the results. The Grid Convergence Index (GCI) method is adopted to determine the convergence of the bias extension test simulations [68]. The details of the method are presented in Chapter 3.

To study the convergence of the bias extension test simulations, two outcomes were used: (1) shear angle, and (2) total force at the end of the simulations. The results of the GCI analysis for bias extension test simulations are presented in Table 4.2. The element sizes for both fabric types were based on their fabric spans with a refinement ratio (r) of ~1.4. Based on the GCI analysis, 0.747 mm and 1.494 mm element sizes were chosen for K706 and K745 fabrics, respectively.

Table 4.2 GCI analysis results for bias extension test simulations.

Fabric	Element sizes (mm)		Shear angle		Force	
K706	0.525, 0.747, 1.057	GCI_{12} GCI_{23}	1.38% 1.88%	k=0.999	11.6% 15.4%	k=0.986
K745	1.057, 1.494, 2.1	GCI_{12} GCI_{23}	4.07% 5.02%	k=1.01	9.48% 14.4%	k=0.978

Figure 4.7 shows the results for bias extension test simulations for both fabric types. The force - displacement as well as the shear angle - displacement curves obtained from simulations are compared to the experiments (Figure 4.7). Moreover, shear angle (γ_{ideal}) assuming ideal kinematics (pin-jointed rods with no slippage) is also presented to compare the results. This ideal shear angle is given as:

$$\gamma_{ideal} = \frac{\pi}{2} - 2\cos^{-1}\left[\cos\theta_0 + \frac{\delta}{2(H-W)\cos\theta_0}\right] \tag{4.14}$$

where δ and θ_0 are the cross head displacement of the tensile machine and the initial angle between the yarns and the loading direction (45^{o}), respectively. It can be seen from Figure 4.7a that force - displacement curve of K706 fabric agrees well with the experimental results. The force response slightly deviates from the experimental average around 20 mm cross head displacement. A similar but more distinct trend is observed in force displacement curve of K745 fabric (Figure 4.7c). The force response of the simulation follows the experiment up until ~15 mm displacement. Then, the simulation results start deviating from the experiments and overestimate the shear angle which results in higher force values. Similar behavior is also observed in the shear angle - displacement curves for both fabric types. The model follows the experimental shear angle up to ~20 mm displacement (31^o) fairly well for K706 while this displacement is ~15 mm (25^o) for K745. For both cases, the simulations overestimate the shear angle which results in higher force values. The model's overestimation in both shear angle and force response could be attributed to the assumption of pin-jointed yarns at the crossover point in the unit cell formulation. As observed experimentally, the yarn slippage becomes the prominent deformation mechanisms during the bias extension test experiments. The yarns at the boundaries are clamped at only one end while the other end is free to move. Due to these boundary conditions, these yarn start to slip causing the test specimen to extend without increasing the shear angle. This also results in softer mechanical response. The yarn slippage is highly dependent on the yarns' bending stiffness and the frictional resistance between the yarns.

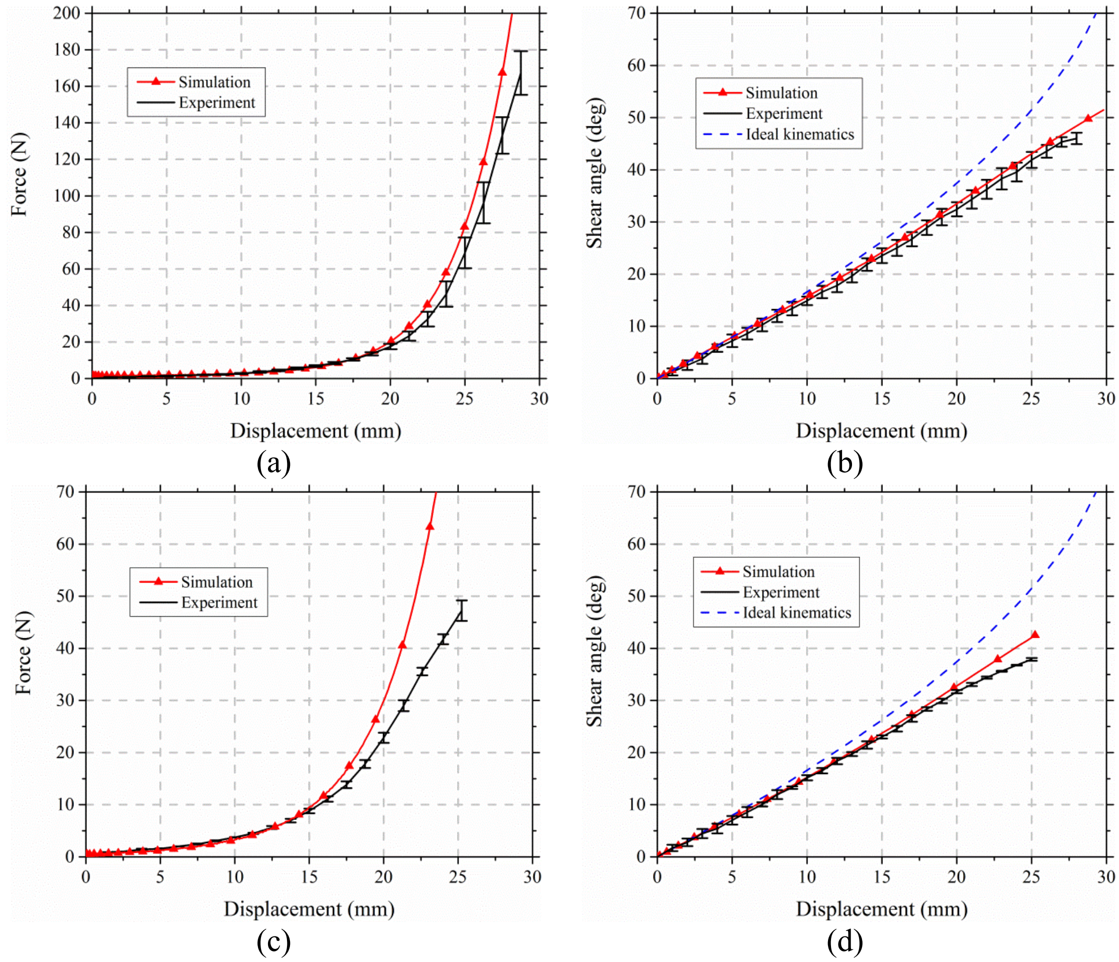

Figure 4.7 Bias extension test simulations: K706: (a) Force - displacement, (b) Shear angle - displacement; K745: (c) Force - displacement, (d) Shear angle - displacement.

From Figures 4.7a and 4.7c, yarn sliding seems to be more prominent in K745 fabric compared to K706. This difference can be attributed to the structure of the fabrics. K745 is a looser weave with less number of yarns per inch compared to K706. Because of this difference, the yarn slippage is more distinct in the experimental results of K745. Since the material model is based on the mesoscale unit cell of the woven fabric, it can determine the stretches of individual yarns (Eq. 4.2). Figure 4.8

shows the yarn stretches for K706 fabric at 20 mm crosshead displacement. It can be seen that the yarns at the boundaries exhibit the highest stretches and these yarn start to slide when they overcome the frictional resistance and yarn bending resistance during the experiments. PMM assumes no yarn slippage occurs at these yarns. Hence, the force response is slightly overestimated during bias extension test simulations.

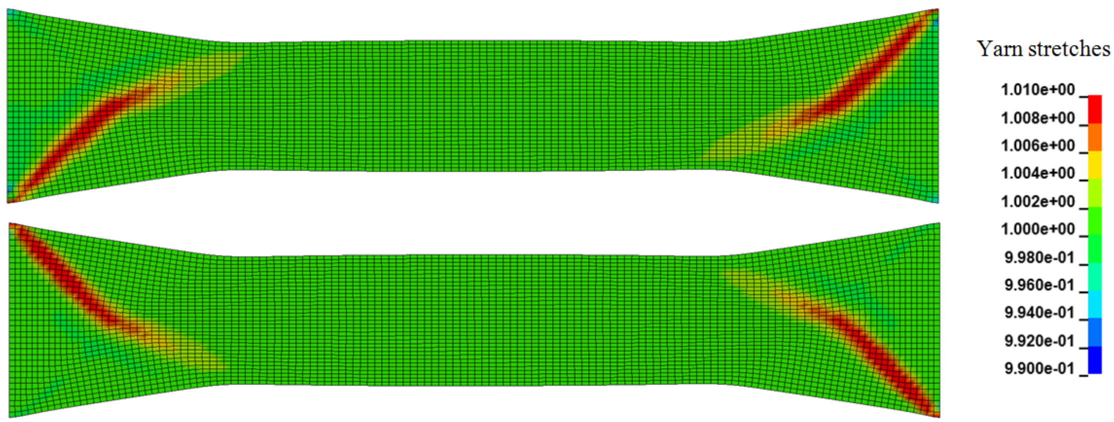

Figure 4.8 Yarn stretches at the boundary yarns for K706 fabric where top and bottom images correspond to weft and warp yarn directions (20 mm crosshead displacement).

Figure 4.9 shows the shear angle comparison across the fabrics between simulations and experiments at 20 mm crosshead displacement. The shear angles measured in the experiments and simulations are fairly close to each other in K706. On the other hand, the values deviate by ~2^o - 3^o for K745 fabric type. This deviation is attributed to the yarn slippage since the start of this deformation mechanism was determined at ~15 mm crosshead displacement for K745 (Figures 4.7c and 4.7d).

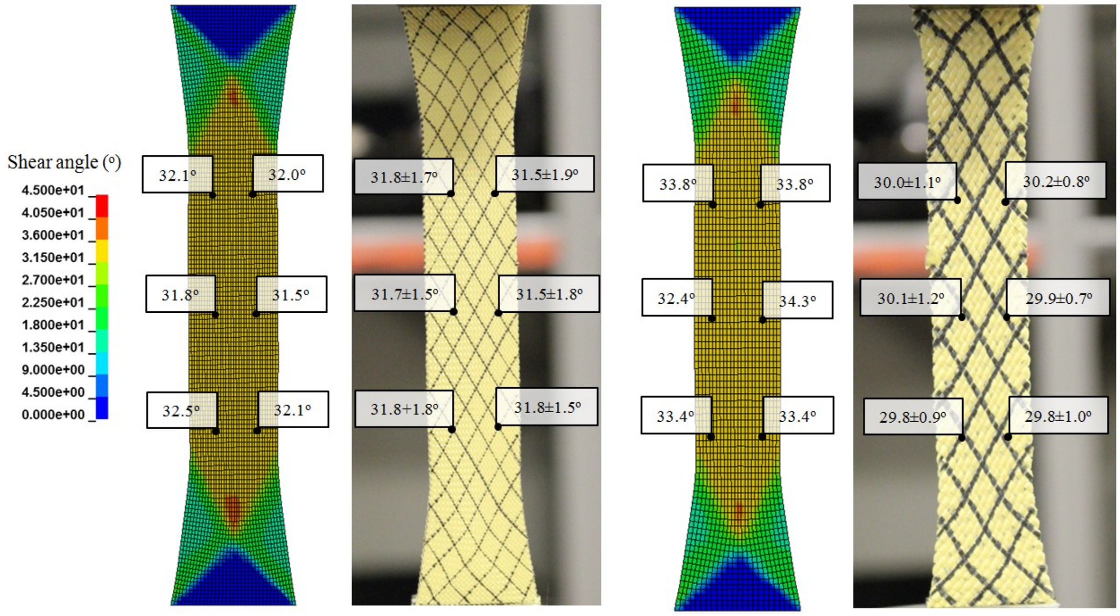

(a) (b)

Figure 4.9 Shear angle distribution for simulations and experiments at 20 mm crosshead displacement: (a) K706, and (b)K745.

To further validate the in-plane behavior of the material model, 30^o off-axis tensile test simulations were carried out. This test is similar to bias extension tests but the yarns are oriented such that they are at 30^o/60^o with respect to the loading direction. Experimental results were adopted from Dong et al.'s work to validate the simulation results [9]. The fabric specimens had dimensions of 101.6 mm x 25.4 mm similar to uniaxial and bias extension test specimens. In the simulations, one of the short edges was constrained while a displacement boundary condition was applied to the other end. Figure 4.10a shows the force - displacement curves for K706 fabric. It can be seen that the PMM is capable of simulating the mechanical response observed in the experiments fairly well. Since the yarn directions are different than the bias extension, the fabric deforms in a different way compared to the bias extension tests (Figure 4.10b).

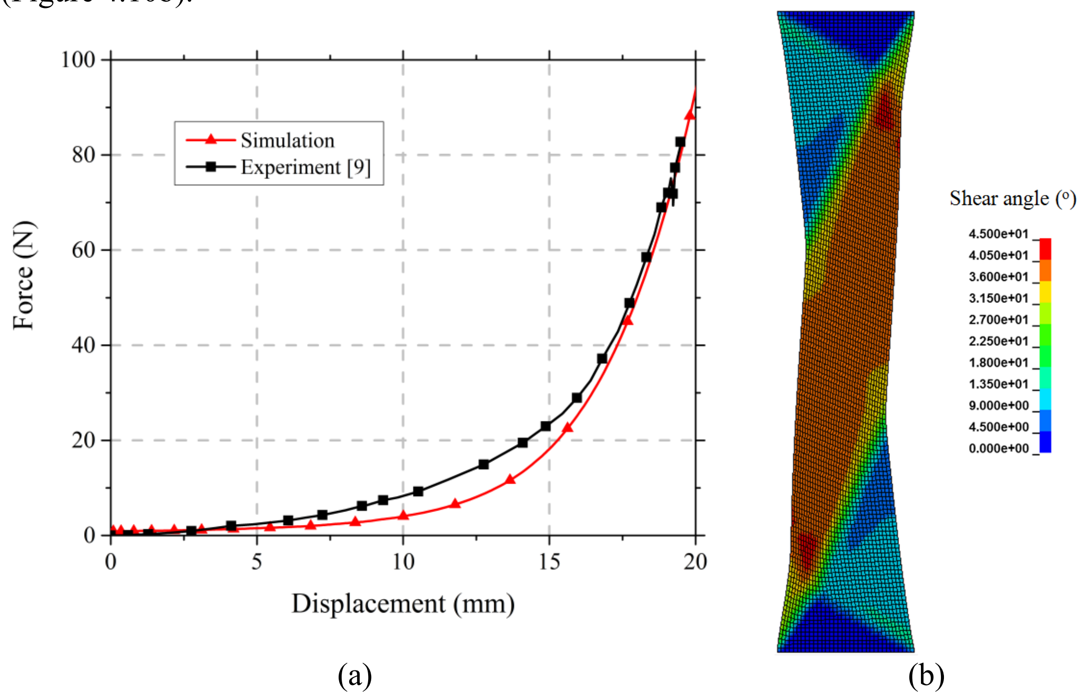

Figure 4.10 30° off-axis tensile test simulation: (a) Force - displacement, and (b) Shear angle distribution at 16 mm crosshead displacement [9].

Out-of-plane behavior of the material model is also studied with indentation tests (Figure 4.11a). Two different test cases were simulated based on the yarns' orientation angles (ψ) with respect to the clamped edges: (1) 0°/90°, and (2) ±45° (Figure 4.11b). The experimental results of 0°/90° case were taken from Manimala et al. while ±45° results were adopted from Dong et al. [9, 49]. The 0°/90° test specimens had dimensions of 51 mm x 40 mm and the indenter had a diameter of 12 mm while the ±45° specimen had a size of 52 mm x 25 mm with a 14 mm diameter indenter. In both test cases, the translational degree-of-freedoms (DOFs) of the short edges were constrained while the rotational DOFs were free to simulate the flexible nature of the woven fabrics studied. The indenter was modeled as halved spheres with shell elements. An isotropic material model with steel material properties was adopted for the indenters. The contact between the fabric and the indenter was defined with a single surface contact algorithm for all simulations (AUTOMATIC SINGLE SURFACE in LS-DYNA). Coulomb friction is defined between the indenter and fabric with a coefficient of friction of 0.2.

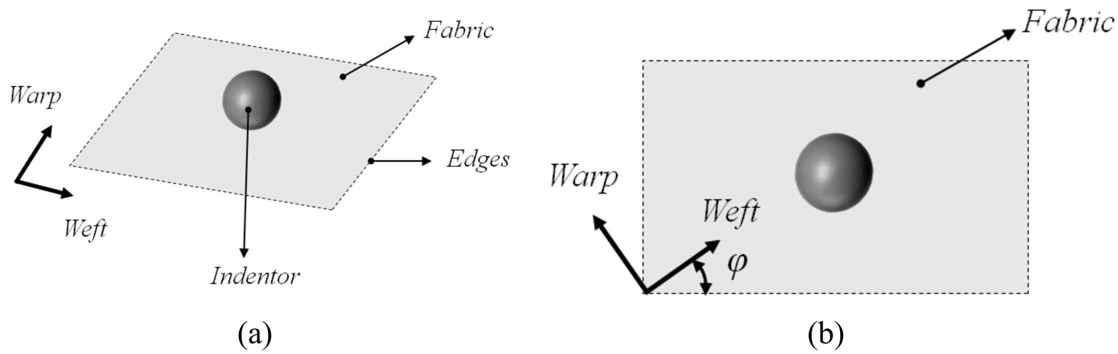

Figure 4.11 Indentation test simulations: (a) Test setup, and (b) Yarn orientation angle [9, 49].

Figure 4.12 shows the force - displacement results for each case studied. The simulation results for 0^o and 90^o cases are shown in Figures 4.12a and 4.12b. The warp yarns were clamped at both ends for 0^o case while weft yarns were constrained in 90^o case. Both simulations and experiments exhibit an initial compliant response followed by a rapid rise in the force response. The mechanical response during the simulations and experiments is mainly governed by the yarns that are located underneath the indenter. These yarns initially undergo decrimping deformation resulting in a very compliant response. A rapid force increase is observed when these yarns lose their crimp completely. Since the crimp amounts are different in weft and warp directions, different mechanical responses are observed during indentation loads.

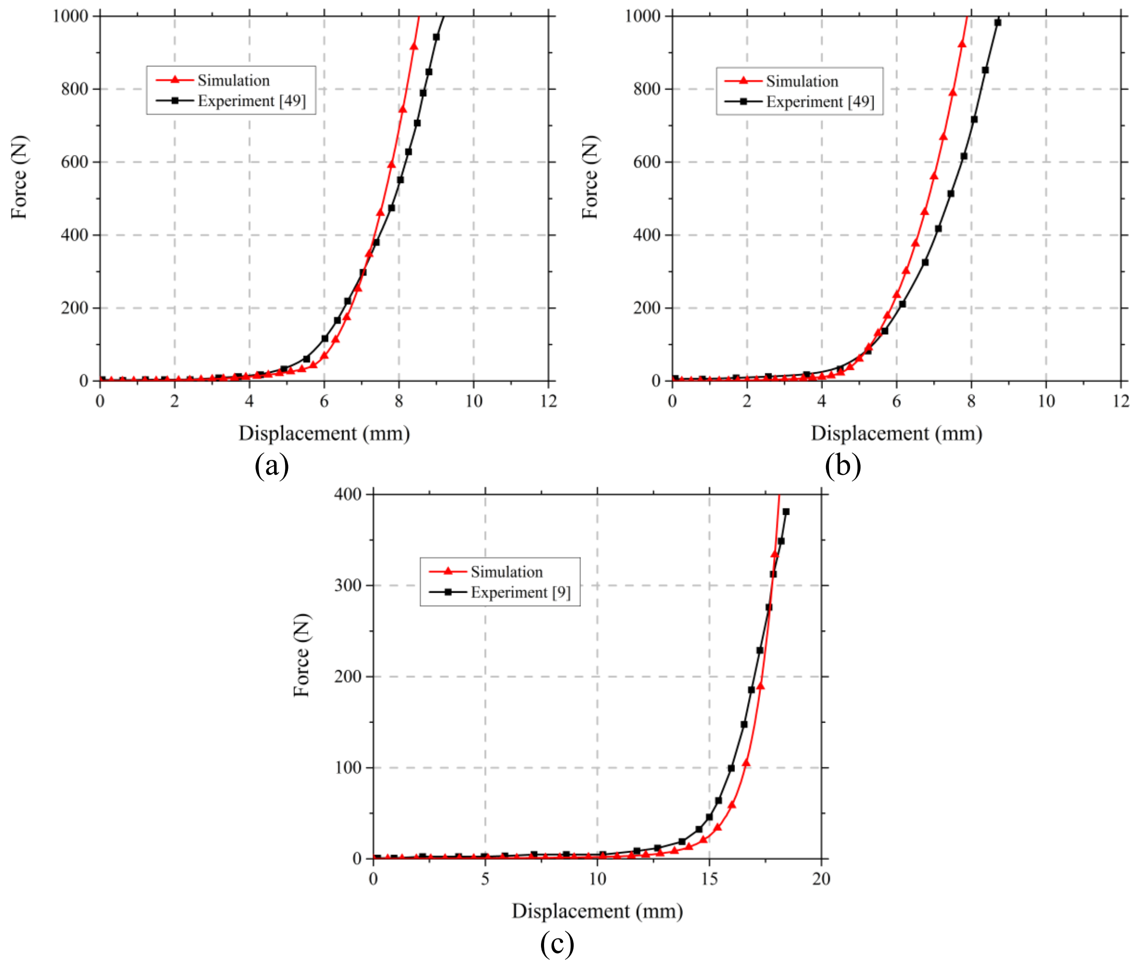

Figure 4.12 Indentation test simulations: (a) 0°, (b) 90°, and (c) ±45° [9, 49].

Figure 4.12c shows the results for ±45° simulations and experiments. Force response of both simulation and experiment are highly nonlinear with an initial complaint response up until ~13 mm displacement. After this displacement, a sudden increase in the force response is observed. This nonlinear behavior can be attributed to the yarn orientations and specimen dimensions. The specimen dimensions used in both experiments and simulations result in an aspect ratio of ~2. This ratio initially allows yarns to freely rotate relative to each other due to the indentation load. Hence, an initial compliant mechanical response is observed. After the locking angle is reached, the yarns cannot rotate further leading to an increased shear stiffness. Moreover, Figure 4.13 shows the simulated shear angle distribution of K706 woven fabric at 13 mm displacement. The shear angles near the indentation location reach up to 35^o while smaller shear angles are observed right underneath the indenter. This difference can be attributed to the contact between the fabric and the indenter. The yarns under the indenter cannot rotate freely due to the friction while nearby yarns are free to rotate.

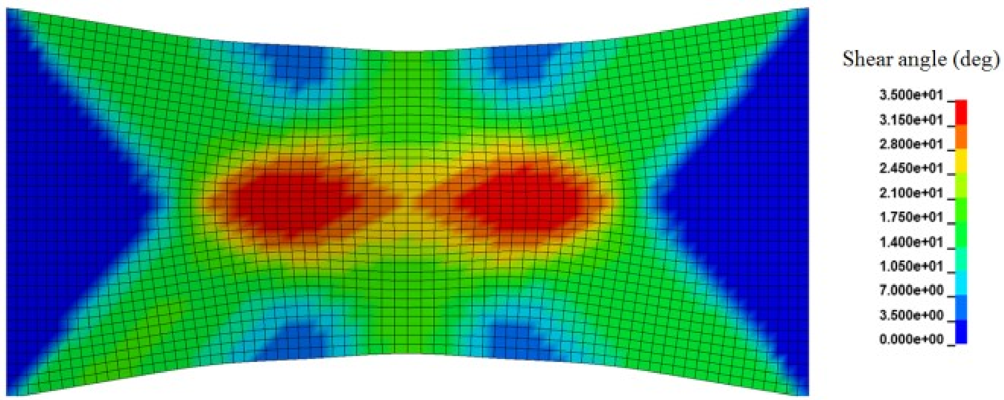

Figure 4.13 Shear angle distribution for K706 at 13 mm displacement.

The material model is further used to numerically compare the mechanical response and deformation mechanisms of the two fabric styles used in this work (K706 and K745). For this purpose, a larger fabric specimen (100 mm x 50 mm) with short edges clamped was modeled with an indenter of diameter 20 mm. The numerical model was simulated using K706 and K745 with a coefficient of friction of 0.2. Figure 4.14a shows the force versus indenter displacement results for both fabric styles. Comparing both Kevlar fabric styles, both fabrics show similar mechanical response, low force response followed by the rapid rise in the force. The main deformation mechanism is again the relative yarn rotations followed by the locking of the yarns in both fabrics. As the deformation progresses, K745 exhibits stiffer response compared to K706. As it can be seen from Figure 4.5b, K745 requires higher effort (moment/torque) to deform a unit cell compared to K706. Therefore, the force required to deform K745 fabric is higher as seen in Figure 4.14a. The shear angle distribution at 30 mm indenter displacement for K706 and K745 are shown in Figures 4.14b and 4.14c, respectively. For both fabric types, the highest shear angles are observed around the indenter. It can be seen from Figure 4.14, K706 has higher shear angles compared to K745. This difference can be attributed to the shear response of the fabric styles. In Chapter 2, the shear response of K706 and K745 fabrics were characterized with bias extension tests and it was shown that K745 had a lower locking angle resulting in higher shear stiffness compared to K706 fabric. Hence, it is easier to deform K706 fabric style which results in higher shear angles across the fabric during indentation simulations.

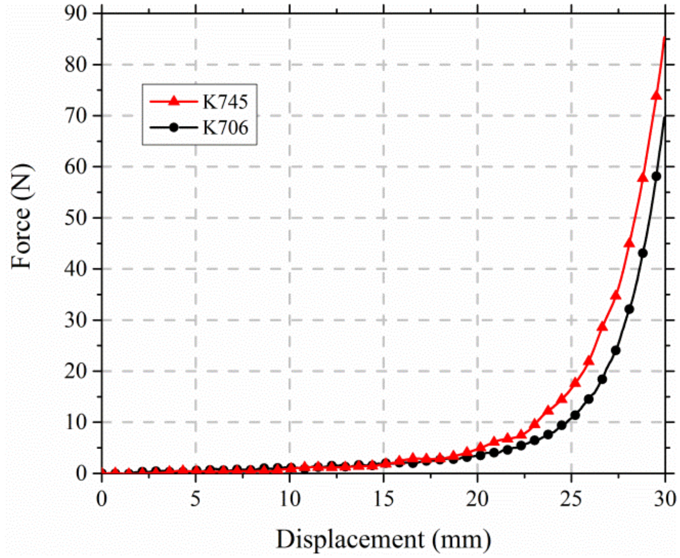

(a)

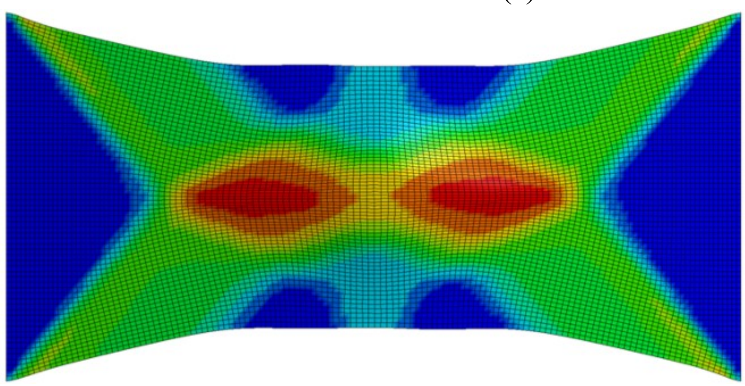

(b)

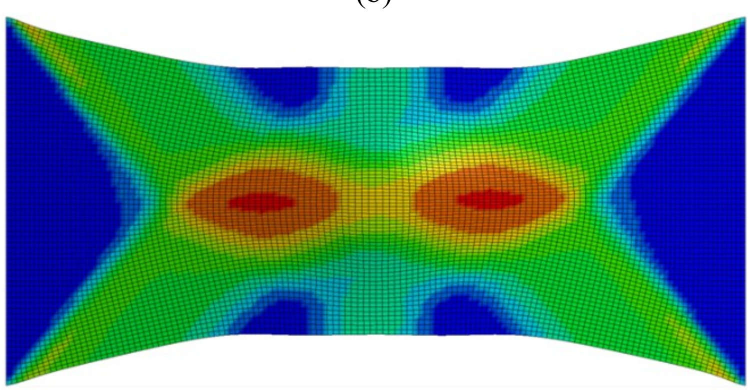

(c)

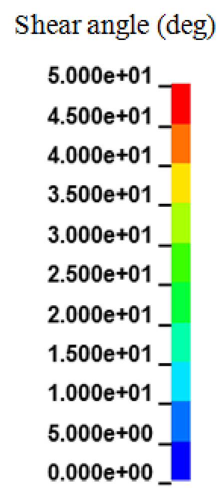

Figure 4.14 Comparison between K706 and K745 fabric styles: (a) Force - displacement curves; Shear angle distribution: (b) K706, and (c) K745.

4.2.3 Sensitivity analysis on material model properties/parameters

To determine the effects of the material model properties/parameters on the mechanical response and to quantify the model's sensitivity to these parameters, a sensitivity analysis was performed on both material models.

For the PMM, the values of E_i^1, E_i^2, β_i, $\varepsilon_{i,crimp}$, C_1 and C_2 are varied ±50% from their experimentally determined values. E_i^1 and E_i^2 represent the yarn longitudinal moduli before and after the decrimping while β_i and $\varepsilon_{i,crimp}$ replicate the decrimping of the yarns. C_1 and C_2 are the rotational spring parameters defining the model's resistance to shear deformation. The values used for the sensitivity analysis for each material property/parameter are presented in Table 4.3. The sensitivity analysis is carried out for uniaxial tensile test simulations included the effects of E_i^1, E_i^2, β_i, and $\varepsilon_{i,crimp}$ while C_1 and C_2 are varied to investigate the sensitivity of shear response (Bias extension). The material properties/parameters E_i^1, E_i^2, β_i, $\varepsilon_{i,crimp}$ affect the uniaxial mechanical response of the woven fabric response. Figure 4.15a shows the effect of the E_i^1. It can be seen that the higher E_i^1 values result in a stiffer response, especially before decrimping. However, the mechanical response after decrimping is not affected by the E_i^1 studied. The effect of E_i^2 is shown in Figure 4.15b. E_i^2 has a significant influence on the mechanical response after decrimping. Stiffer mechanical response is observed as the values of E_i^2 increase. β_i and $\varepsilon_{i,crimp}$ determine the transition region for the yarn from their crimped state to fully straightened state. Figure 4.16a shows the effect of the β_i on the uniaxial mechanical response of the PMM. This material parameter affects the transition region during decrimping. Higher values of β_i result in a sharper transition region for decrimping as shown in Figure 4.16a. Moreover, Figure 4.16b shows the effects of the decrimping strain ($\varepsilon_{i,crimp}$). This material property determines the location of yarn decrimping. Hence, the increased values of $\varepsilon_{i,crimp}$

result in a shift towards higher strain values in the uniaxial force response of the material model as shown in Figure 4.16b.

The C_1 and C_2 material parameters determine the moment/torque output of the rotational crossover spring. C_1 acts as a spring stiffness while C_2 determines the location of the locking angle where the shear response of the woven fabric exhibits a very stiffened response. Figure 4.17a shows the effect of the C_1 on the mechanical response observed during bias extension test simulations with PMM. Increased values of C_1 result in stiffened mechanical response. C_2 has a similar effect on the mechanical response but its effect is more significant compared to C_1's effect. C_1 affects the shear stiffness at given shear angle while C_2 determines the location of the locking phenomenon. Hence, the locking angle of the material model decreases as the C_2 value increases, resulting in an earlier stiffened response.

Table 4.3 Values used for the sensitivity analysis of PMM.

Parameter	Lower level	Middle level	Upper level	Simulation
E_i^1 (MPa)	2000	4000	6000	Uniaxial
E_i^2 (MPa)	39500	79000	118500	Uniaxial
β_i	500	1000	1500	Uniaxial
$\varepsilon_{i,crimp}$	0.0075	0.015	0.0225	Uniaxial
C_1 (Nmm)	0.0004	0.0008	0.012	Bias
C_2 (rad^{-1})	4.235	8.47	12.705	Bias

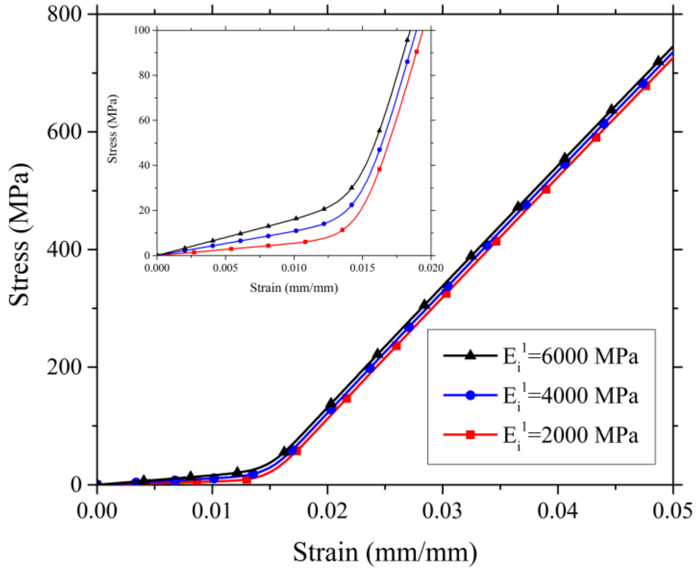

(a)

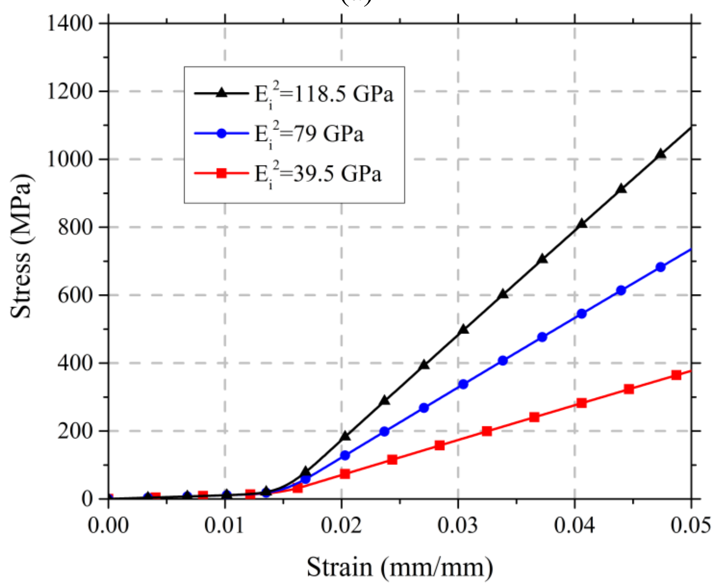

(b)

Figure 4.15 Sensitivity of uniaxial tensile response to model parameters: (a) E_i^1, and (b) E_i^2.

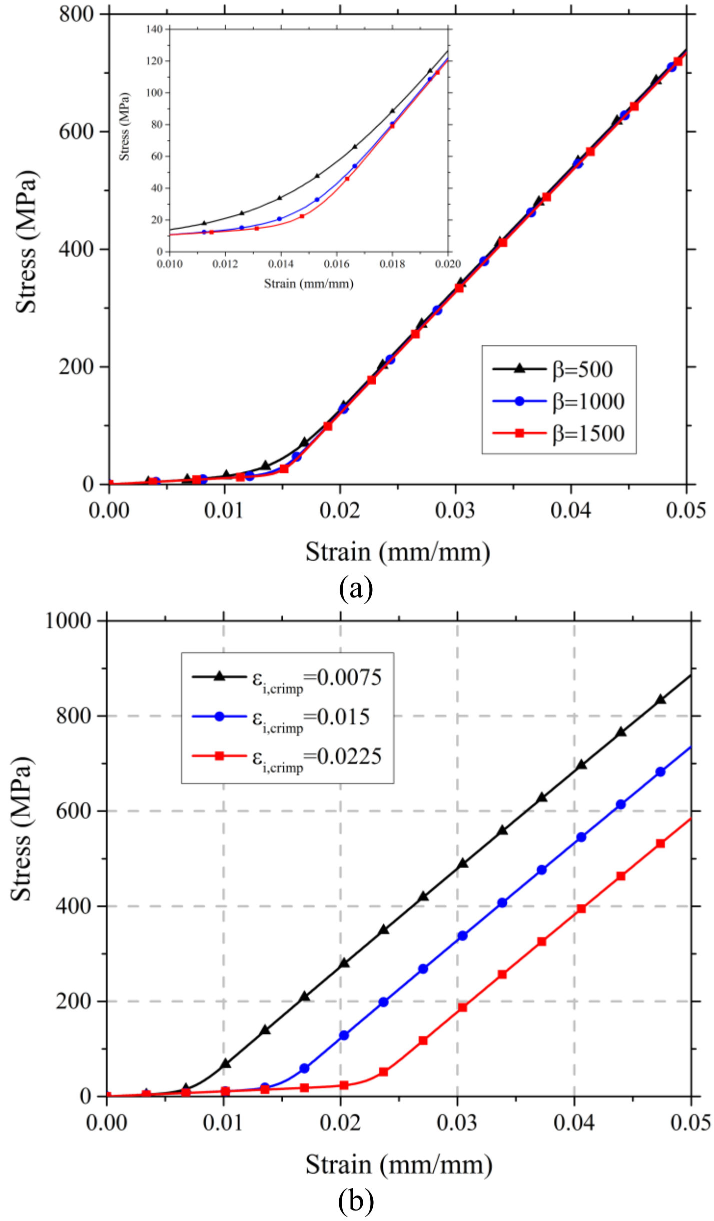

Figure 4.16 Sensitivity of uniaxial tensile response to model parameters: (a) β_i, and (b) $\varepsilon_{i,crimp}$.

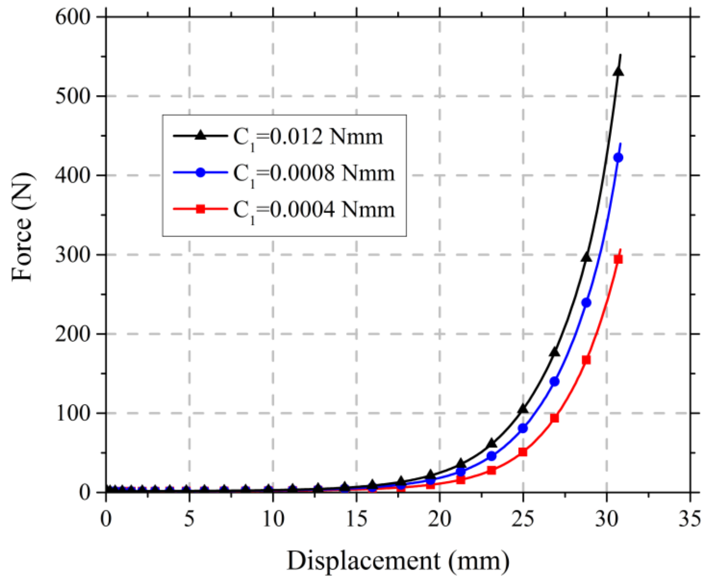

(a)

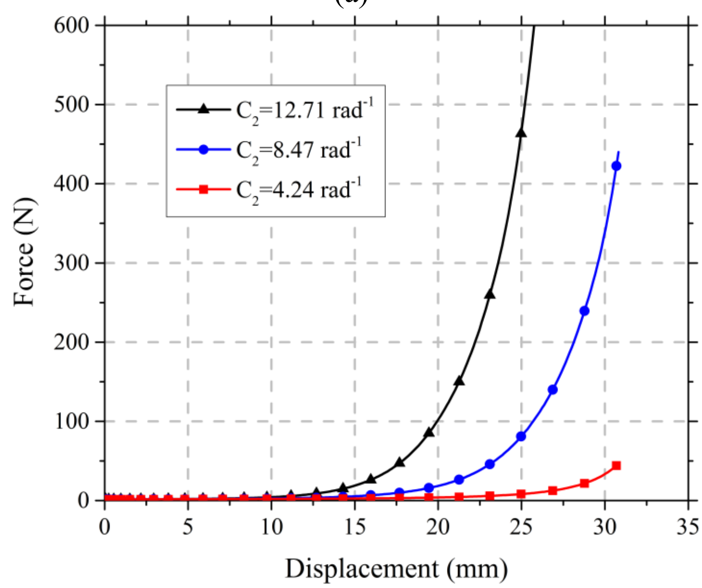

(b)

Figure 4.17 Sensitivity of shear response (Bias extension) to model parameters: (a) C_1, and (b) C_2.

4.3 Sawtooth Material Model (SMM)

In section 4.1, a macroscopic material model named Planar Material Model (PMM) was introduced. The material model simplifies the mesocopic structure of the woven fabrics and assumes that the yarns lie on the same plane. This assumption leads to simplifications in the fabric response resulting in only uniaxial tensile and shear resistances while allowing to develop an easy-to-implement and efficient material model for woven fabrics. It was demonstrated with validation studies that the material model is capable of reproducing experimental mechanical responses under various loading conditions. However, woven fabrics exhibit stiffened mechanical response when both yarns are subjected to tensile loads as shown in Chapter 3 with mesoscopic level simulations. Hence, a more complex macroscopic material model considering the 3D structure of woven fabrics is developed in this section to capture the uniaxial, biaxial and shear resistance at the expense of increased computational resources.

4.3.1 Model basics and implementation

To model a woven fabric's 3D structure within a shell element formulation, the Sawtooth geometry (Figure 4.18) developed by Kawabata et al. is adopted [58, 68]. In this geometry, both yarn directions are approximated with linear elements where they are connected to each other at the crossover location. The model considers the mesoscale unit cell of plain weave fabrics at a single crossover point and it has been adopted by various researchers to study woven fabrics [39, 58, 59]. In the current work, this geometry is adopted to develop a nonlinear material model called Sawtooth material model (SMM) that is capable of reproducing various deformation mechanisms and associated mechanical behavior involving biaxial response.

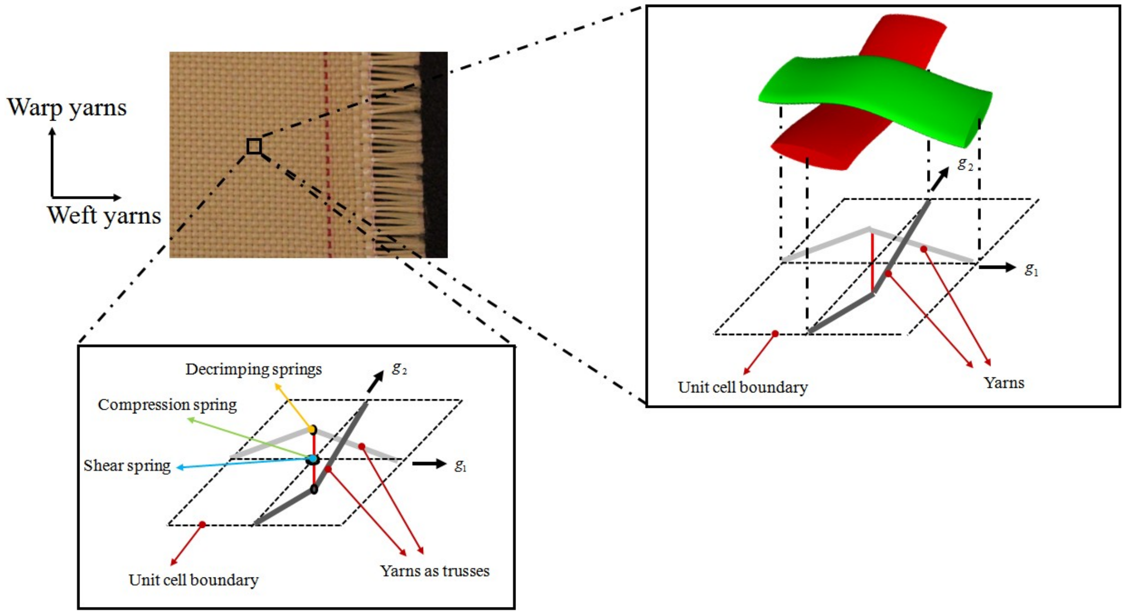

Figure 4.18 Sawtooth material model and unit cell approach.

To obtain the nonlinear mechanical response of woven fabrics with the sawtooth geometry, yarns are modeled as trusses while other deformation mechanisms are implemented with nonlinear springs (Figure 4.19a). The sawtooth geometry of the unit cell at a given configuration is determined from 9 geometric dimensions: (1) Yarn lengths (L_i), (2) Unit cell quarter lengths (w_i), (3) Crimp amplitudes (h_i), (4) Yarn crimp angles (β_i), and (5) the angle between the yarns (θ). These dimensions are shown in Figure 4.19b. Out of 9 variables, only 5 dimensions are independent due to the sawtooth structure used in the material model. The rest of the dimensions can be determined from the independent dimensions. For the current work, unit cell quarter lengths (w_i), crimp amplitudes (h_i) and angle between the yarns (θ) are chosen as the independent variables. Then, the yarn crimp angles (β_i) and yarn lengths (L_i) can be determined from following expressions:

$$L_i = \sqrt{h_i^2 + w_i^2}$$

$$\beta_i = \cos^{-1}\left(\frac{w_i}{L_i}\right) \tag{4.15}$$

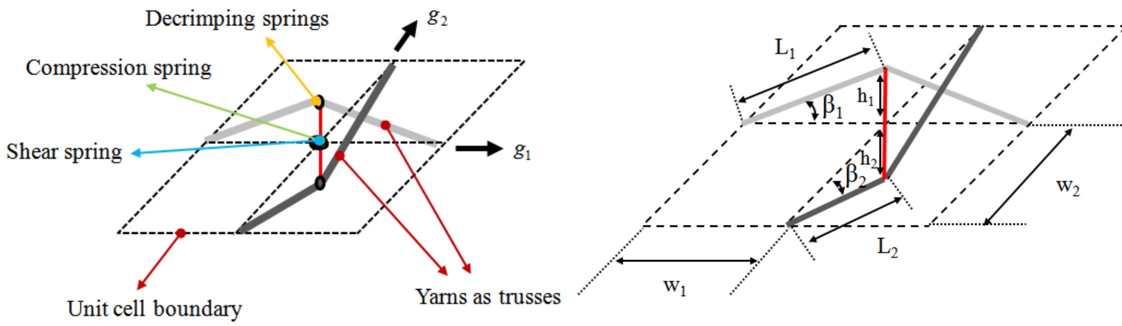

Figure 4.19 Sawtooth material model unit cell: (a) Truss and nonlinear spring locations, and (b) Geometric dimensions.

Two unit vectors are assigned to each yarn direction to keep track of the yarn orientations in a similar way to PMM formulation. Then, the unit cell quarter lengths and angle between the yarns are determined by using Eqs. 4.4 and 4.5 with the help of deformation gradient.

The uniaxial tensile response of the yarns is implemented with truss elements and decrimping springs for each yarn direction. Since the yarns are not on the same plane due to the sawtooth geometry, the angle between yarns and the fabric plane (yarn crimp angle, β_i) can change during deformation replicating the decrimping deformation mechanisms. The tension developed (T_i) within each yarn is defined as [58]:

$$T_i = E_i A_i \frac{\left(L_i - L_i^0\right)}{L_i^0} \tag{4.16}$$

where E_i, A_i, L_i and L_i^0 are yarn modulus, yarn cross-sectional area, current length of the yarn and initial yarn length, respectively. The yarn modulus can be obtained either from the single yarn tensile or fabric level uniaxial tensile tests while the initial yarn length can determined from the microscopy. A rotational yarn decrimping spring is defined to implement the initial stiffness observed during decrimping deformation. The moment generated (M_i^b) by this spring is related to the change in the yarn crimp angle for each yarn direction as [58]:

$$M_i^b = k_i^b\left(\beta_i - \beta_i^0\right) \tag{4.17}$$

where k_i^b, β_i^0 and β_i are decrimping spring stiffness, initial and current yarn crimp angles, respectively. The spring stiffness can be determined from the compliant region of the uniaxial tensile tests conducted on the crimped yarns.

The yarn-to-yarn interactions in the transverse (out-of-plane) direction at the crossover point are implemented with the crossover spring (Figure 4.19a). The force generated (F_i^c) by the spring as a function of the yarn transverse displacement (r_i^z) is defined as [39]:

$$\begin{gathered} F_i^c = \frac{b r_i^z}{a - r_i^z} \\ r_i^z = h_i^0 - h_i \end{gathered} \tag{4.18}$$

where b and a are compression spring constant and upper limit for the transverse compression, respectively. This spring represents the compressible nature of the yarns and the contact between the yarns in the transverse (out-of-plane) direction. Figure 4.20 shows the force generated by the spring as a function of yarn transverse displacement. The spring response exhibits a nonlinear response replicating the rearrangement of the filaments and compaction of the filaments. Since the interaction between each yarn direction is achieved through this spring unlike the PMM, SMM is capable of reproducing the biaxial nature of woven fabrics.

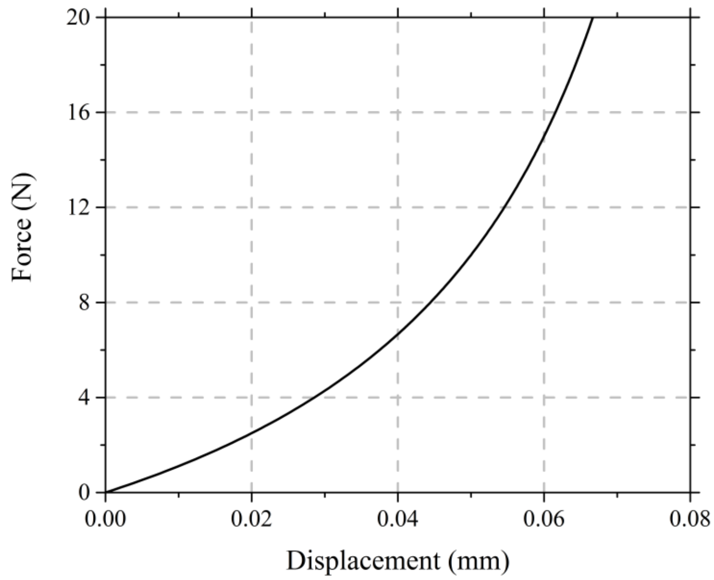

Figure 4.20 Compression spring response.

Shear resistance of woven fabrics is a complex 3D deformation mechanism and governed by the mesoscale interactions between the yarn families. Hence, it is very challenging to model this deformation mechanism at the macroscopic length scale with shell elements. In the material model, the shear resistance is implemented through the crossover shear spring (Figure 4.19a). This is a new implementation of the shear response for macroscale material models based on the sawtooth geometry. The available material models in the literature either do not consider the shear response or use phenomenologically-based interlocking truss elements within their formulation to implement the shear behavior [39, 58]. In this work, the shear deformation and the nonlinear mechanical response is modeled in a similar manner to the PMM for the

SMM. Therefore, the moment/torque response as a function of the shear angle is defined by Eq. 4.9 with two parameters: (1) C_1, and (2) C_2. The determination of the values for the spring parameters can be done using the normalized bias extension tests and minimizing the RMSE between the Eq. 4.9 and the experimental average.

Since the shell elements are adopted to model the woven fabrics in the material, only 3 of the independent geometric dimensions (the angle between the yarns and the unit cell half lengths) can be determined from the deformation gradient. The other 2 independent dimensions (yarn crimp amplitudes, h_i) can take any value. To determine the values of the crimp amplitudes, a two variable Newton-Raphson iterative scheme is adopted [39]. Hence, two conditions for the crossover points are defined: (1) equilibrium of forces due to the yarn-to-yarn contact, and (2) the compatibility condition in the out-of-plane direction. At the crossover point, the forces developed in the out-of-plane direction due to the tensions developed within the yarns should be balanced to satisfy the force equilibrium. These forces (F_i^v) can be determined from the yarn tensions and the geometric dimensions of the unit cell (Figure 4.21):

$$F_i^v = 2T_i \sin(\beta_i) \tag{4.19}$$

where β_i is defined as a function of yarn crimp amplitudes (h_i). Then, the equilibrium condition requires the following expression at the crossover point:

$$F_1^v(h_1) = F_2^v(h_2) \tag{4.20}$$

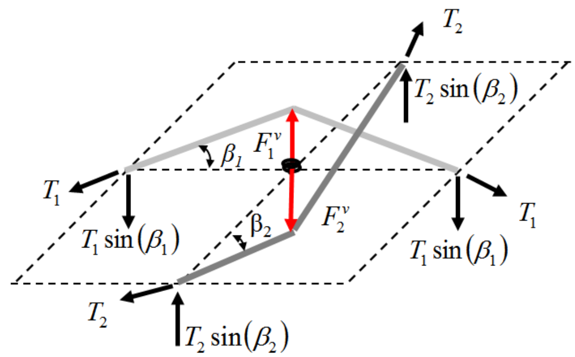

Figure 4.21 Vertical force balance within the unit cell.

Moreover, the compatibility condition relating the current crimp amplitudes to the initial values should also be satisfied at the crossover:

$$h_1 + h_2 = h_1^0 + h_2^0 - r_1^z - r_2^z \tag{4.21}$$

where h_1^0 and h_2^0 are initial yarn heights. To implement the force equilibrium and compatibility at the crossover and determine the current crimp amplitudes (h_i), a Newton-Raphson routine with the following functions is adopted:

$$\begin{aligned} f_1 &= h_1 + h_2 + r_1^z + r_2^z - h_1^0 - h_2^0 \\ f_2 &= F_1^v(h_1) - F_2^v(h_2) \end{aligned} \tag{4.22}$$

Then, the yarn crimp amplitudes can be determined from:

$$\begin{bmatrix} h_1^n \\ h_2^n \end{bmatrix} = \begin{bmatrix} h_1^{n-1} \\ h_2^{n-1} \end{bmatrix} - J^{-1} \begin{bmatrix} \partial f_1 / \partial h_1 & \partial f_1 / \partial h_2 \\ \partial f_2 / \partial h_1 & \partial f_2 / \partial h_2 \end{bmatrix}^{-1} \begin{bmatrix} f_1 \\ f_2 \end{bmatrix} \tag{4.23}$$

where J and n are Jacobian and the current iteration in the Newton-Raphson routine. Moreover, an objective function is defined for the iterations and iterations are terminated based on a pre-defined tolerance. The objective function (f) used for the material model is defined as:

$$f = |f_1| + |f_2| \quad f < tolerance \tag{4.24}$$

After the current yarn amplitudes are determined from Newton-Raphson iterations, other unit cell dimensions are updated. Then, forces and moments generated by the trusses and springs are calculated and Cauchy stresses are calculated in a similar manner to the PMM (Figure 4.22). The Cauchy stress tensor for the material model is given as:

$$\begin{aligned} \bar{\sigma} = & \frac{1}{2w_2 t_f^0 \sin\theta}\left[T_1 \cos\beta_1 - \frac{M_s \cos\theta}{2w_1 \sin\theta} - \frac{M_1^b \sin\beta_1}{L_1}\right](g_1 \otimes g_1) \\ & + \frac{1}{2w_1 t_f^0 \sin\theta}\left[T_2 \cos\beta_2 - \frac{M_s \cos\theta}{2w_2 \sin\theta} - \frac{M_2^b \sin\beta_2}{L_2}\right](g_2 \otimes g_2) \\ & + \frac{M_s}{4w_1 w_2 t_f^0 \sin^2\theta}(g_1 \otimes g_2 + g_2 \otimes g_1) \end{aligned} \tag{4.25}$$

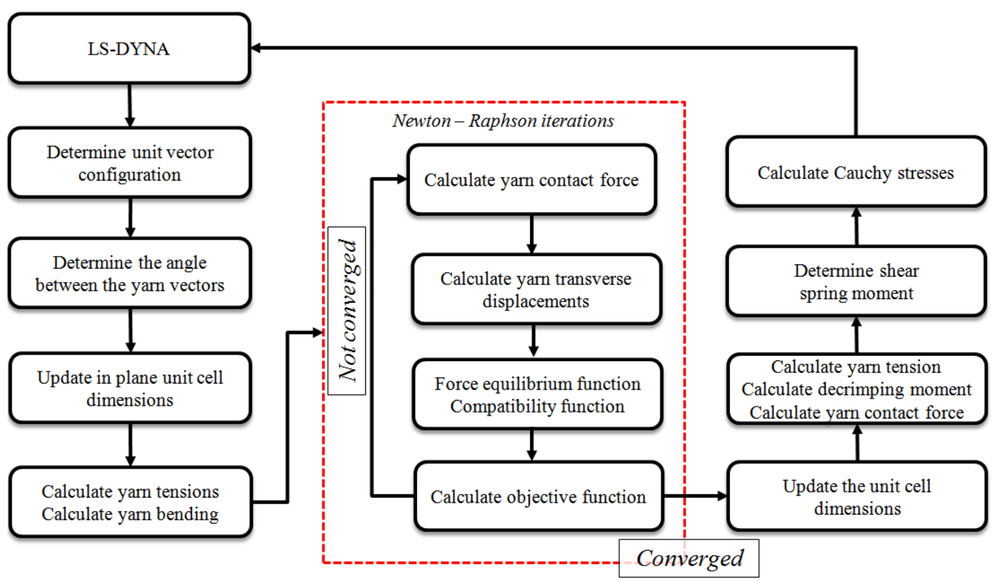

Figure 4.22 Sawtooth material model algorithm steps.

Finally, Table 4.4 shows the material properties/parameters required by the "Sawtooth Material Model", their short explanation and the assessment methods that can be used to obtain the values of these properties/parameters.

Table 4.4 Material properties and parameters required by Sawtooth Material Model (SMM).

Geometric dimensions			
Parameters	**Explanation**	**Assessment**	**Reference**
w_i	Unit cell quarter length	Microscopy (Independent)	[39], [58]
a_i^1	Yarn major diameter	Microscopy (Independent)	
a_i^2	Yarn minor diameter	Microscopy (Independent)	
h_i	Yarn half height	Dependent	
L_i	Yarn length	Dependent	
β_i	Crimp angle	Dependent	
Yarn trusses & decrimping springs			
Parameters	**Explanation**	**Assessment**	
E_i	Yarn modulus	Yarn experiments	[58]
k_i^b	Decrimping stiffness	Yarn/Fabric experiments	
Compressive spring			
Parameters	**Explanation**	**Assessment**	
a	Shape parameter	Biaxial/compression experiments or analytical models	[39]
b	Spring stiffness		
Shear spring			
Parameters	**Explanation**	**Assessment**	
C_1	Shear parameter	Bias extension tests	Unique contribution
C_2	Shear parameter		

4.3.2 Validation of the Material Model

The material model is validated under various loads for K706 fabric type. The independent geometric dimensions shown in Table 4.4 are determined from cross-sectional images of the plain weave K706 fabric [75]. Then, the dependent dimensions are calculated by using the independent dimensions and the geometric relations defined by the sawtooth unit cell structure. Table 4.5 shows the geometric dimensions used for the validation simulations of the SMM.

The yarn material properties including yarn modulus (E_i) and yarn decrimping spring stiffness (k_i^b) are determined from the experimental stress - strain curves of uniaxial tensile tests on fabrics by normalizing the curves per yarn basis (Table 4.5). The compression spring that defines the contact between the two yarn directions requires 2 parameters (*a* and *b)*. To determine the values for the compression spring parameters, biaxial or compression experiments can be adopted. However, an analytical model describing the compressive behavior of plain weave fabrics is adopted due to the unavailability of compression data for K706 [76]. The analytical model relating the compressive force (F_{fabric}) to the fabric thickness reduction (d_c) for a single cross-over point is given as:

$$F_{fabric} = \frac{8E_{yarn}(\pi-2)^2\left[2(\pi-2)t_f^0 + \pi d_c\right]d_c\left(t_f^0 - d_c\right)^5}{3\pi l^2\left[8d_c^3 - 24(\pi-2)\left(t_f^0 - d_c\right)d_c^{\,2} + 5(\pi-2)^3\left(t_f^0 - d_c\right)^3\right]} \tag{4.26}$$

where E_{yarn}, l and t_f^0 are the yarn modulus, fabric span and the initial fabric thickness, respectively. Hence, Eq. 4.26 is used to determine the compression spring parameters. The values obtained from Eq. 4.26 for compression spring parameters are shown in Table 4.5. The shear spring parameters (C_1 and C_2) were determined from the normalized unit torque/moment obtained from bias extension tests by minimizing the RMSE between the experimental average and Eq. 4.9. The values determined for the shear spring are presented in Table 4.5.

Table 4.5 The values used for the material properties/parameters of the SMM.

Geometric dimensions		
Parameters	**Weft value (i=1)**	**Warp value (i=2)**
w_i (mm)	0.3735	0.3735
a_i^1 (mm)	0.57	0.536
a_i^2 (mm)	0.131	0.163
h_i (mm)	0.066	0.082
L_i (mm)	0.379	0.382
β_i (deg)	9.95	12.3
Yarn trusses & decrimping springs		
Parameters	**Weft value (i=1)**	**Warp value (i=2)**
E_i (MPa)	79000	69000
k_i^b (Nmm/rad)	1.5	1.8
Compressive spring		
Parameters	**Value**	
a (N)	0.11	
b (mm)	12.6	
Shear spring		
Parameters	**Value**	
C_1 (Nmm)	0.0008	
C_2 (rad^{-1})	8.47	

Uniaxial tensile test simulations are carried out to validate the SMM's tensile behavior under uniaxial loading. The fabric models have a width of 25.4 mm and a length of 101.6 mm (similar to the simulations of the PMM). The mesh densities used in PMM simulations were those also used in the SMM simulations. The simulation results are validated using Dong et al.'s work on K706 plain weave fabric [9]. Figure 4.23 shows the results of the uniaxial tensile test simulations for weft and warp directions of K706. The material model is able to capture the mechanical response observed during the uniaxial tensile tests where an initial compliant force response is followed by a non-compliant force response. Decrimping and crimp interchange are the most prominent deformation mechanisms observed in woven fabrics under uniaxial loading. The material model is capable of modeling these deformation mechanisms with the compressive spring defined at the crossover point. This spring replicates the yarns' contact and their interactions. Hence, the yarns aligned with the loading direction in the simulations lose their crimp while the yarns in the other direction increase theirs. Figure 4.23b shows the crimp angle change (the angle that a yarn direction makes with the fabric plane) where the warp direction is aligned with the loading direction. The warp direction yarns decrease their crimp angle while the weft yarns increase their crimp. Since the yarns can change their crimp angle (the crimp amount), the woven fabric model can extend its length while contracting in the width direction. This deformation mechanism results in a Poisson's effect. Figure 4.23c shows the Poisson's ratio change with the applied strain under uniaxial loading. The crimp amounts of the yarn directions are different due to the weaving process. This difference directly affects the form of the Poisson's ratio change and the location of the maximum Poisson's ratio attained during the deformation. The weft yarns exhibit less crimp compared to the warp yarns. Hence, the maximum Poisson's ratio is reached at an earlier strain value when the weft yarns are aligned with the loading direction. Moreover, the form and the values of the Poisson's ratios observed during the simulations depend on various material properties/parameters defined in the material model. These properties/parameters include: decrimping spring stiffness for both yarn directions (k_i^b) and compressive spring parameters (a and b).

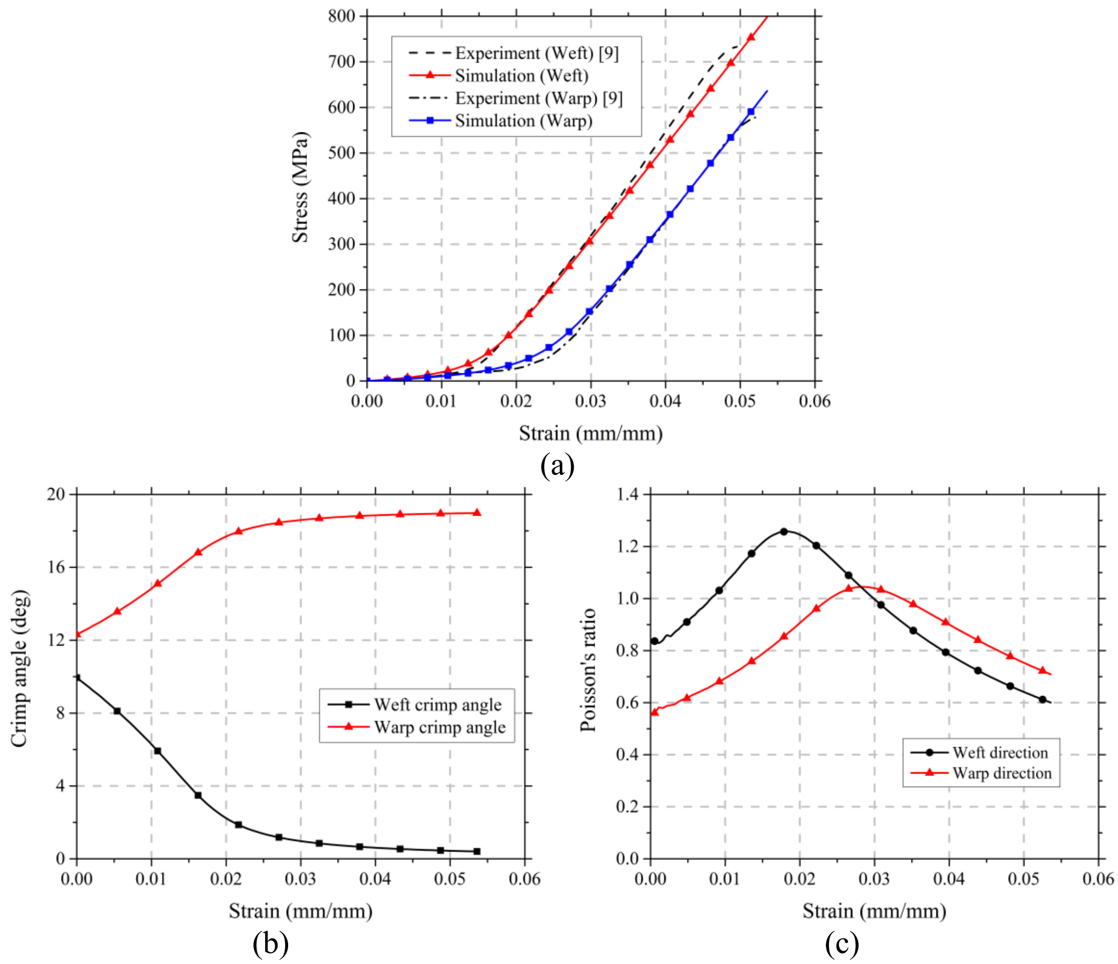

Figure 4.23 Uniaxial tensile test simulations for K706: (a) Stress - strain curves, (b) Crimp angle change with applied strain, and (c) Poisson's ratio change with applied strain [9].

The shear response of the SMM is validated by simulating the bias extension tests. The yarn directions are rotated ±45^{o} with respect to the loading direction. The woven fabric with a 0.747 mm element size is adopted based on the mesh sensitivity study carried out for the PMM. Figure 4.24a shows the force response of the material model during the bias extension test simulation. The material model is able to capture the nonlinear force response observed in the experiments. The simulated force response starts to deviate slightly from experimental average around 20 mm crosshead displacement. This deviation could be attributed to the yarn slippage observed in the experimental bias extension tests. Since the yarns are pin-jointed at the cross-over point (similar to the PMM), the material model is not capable of reproducing this inherent deformation of bias extension tests. Hence, a stiffer mechanical response is observed. Moreover, the kinematics of the material model are also validated by comparing the simulated and experimental shear angles. Figure 4.24b shows the shear angle changes of the simulations and experiments at the middle the specimen. The material model shear angle closely follows the experimental average up to ~18 mm crosshead displacement which corresponds to 29^o shear angle. Then, the SMM's shear angle starts to deviate from the experimental shear angle. Figure 4.24c also shows the comparison of the shear angle distribution at 20 mm crosshead displacement for simulations and experiments. The simulated woven fabric shear angles are slightly higher than the experimental average. This difference can also be attributed to the assumption of pin-jointed yarns where the yarn slippage is not implemented.

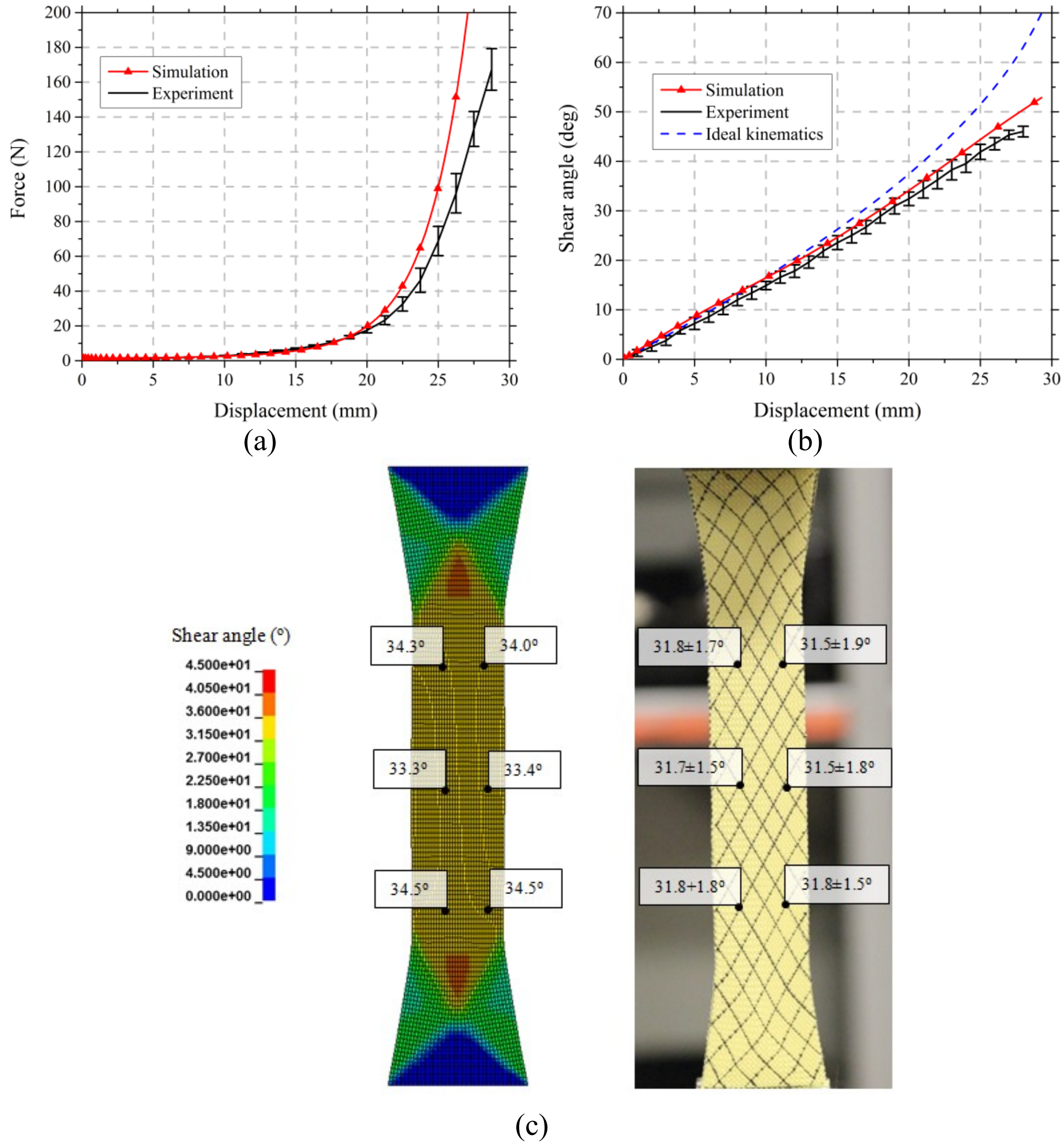

Figure 4.24 Bias extension test simulation results for K706: (a) Force - Displacement, (b) Shear angle - displacement, and (c) Shear angle distribution at 20 mm crosshead displacement.

The mechanical response of the material model is also validated by simulating 30^{o} off-axis tensile tests. In these simulations, the yarns are oriented $30^{o}/60^{o}$ with respect to the loading direction. Figure 4.25 shows the force response of the material model and its comparison to the experimental results taken from Dong et al.'s work [9]. The material model is able to capture the nonlinear mechanical response observed in the experiments fairly well.

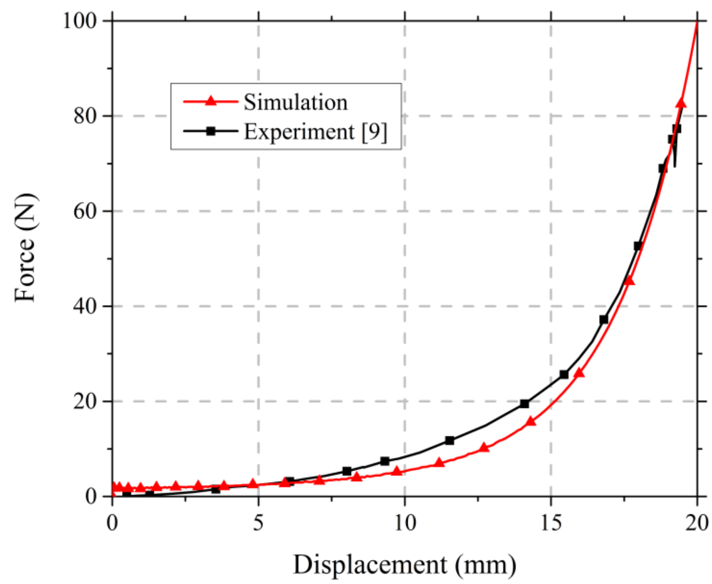

Figure 4.25 30^{o} off-axis tensile test simulation results [9].

Out-of-plane behavior is also validated similar to PMM by carrying out indentation test simulations shown in Figure 4.11. Three different cases are studied with different yarn orientations (0^{o}, 90^{o} and $\pm45^{o}$). Figure 4.26 shows the force - displacement curves for all of the yarn orientation angles studied. The material model is capable of reproducing the nonlinear mechanical responses observed in the experiments. Indentation simulations with 0^{o} and 90^{o} yarn orientations are governed by the yarns underneath the indenter. These yarns undergo decrimping as the indenter force increases since both ends are clamped. Hence, an initial compliant response followed by a rapid force increase is observed. The material model can capture the nonlinear mechanical response observed for both 0^o and 90^o indentation cases. Moreover, the material model is also capable of reproducing the force response observed in $\pm 45^o$ experiments as shown in Figure 4.26c. The force response is highly nonlinear and is governed by the interaction between the yarns themselves and the indenter.

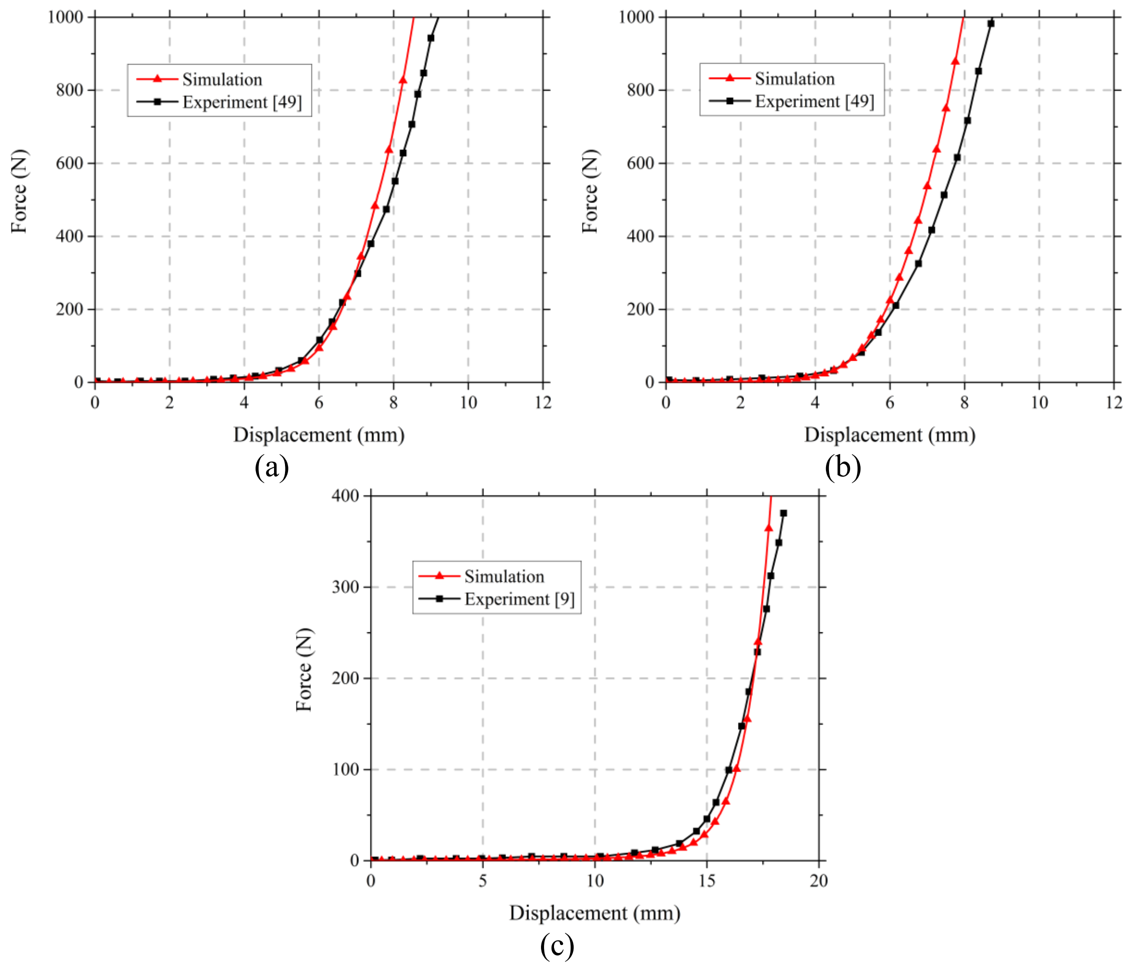

Figure 4.26 Indentation test simulations: (a) 0^o, (b) 90^o, and (c) $\pm 45^o$ [9, 49].

4.3.3 Sensitivity analysis on material model properties/parameters

Continuing the sensitivity analyses now for the SMM, Table 4.6 lists the material properties/parameters studied and associated mechanical response. The sensitivity of these material properties/parameters are studied at three different levels where the middle level corresponds to the values used in the validation simulations. Middle levels are varied ±50% for lower and upper levels.

Table 4.6 Sensitivity of material properties/parameters required by the SMM.

Parameter	Lower level	Middle level	Upper level	Simulation
E_i (MPa)	39500	79000	118500	Uniaxial
k_i^b (Nmm/rad)	0.75	1.5	2.25	Uniaxial
a (mm)	0.055	0.11	0.165	Uniaxial
b (N)	6.3	12.6	18.9	Uniaxial
C_1 (Nmm)	0.0004	0.0008	0.0012	Bias
C_2 (rad^{-1})	4.24	8.47	12.71	Bias

The sensitivity analysis is carried out for uniaxial tensile test simulations including the effects of E_i, and compressive spring parameters (a and b). Figure 4.27 shows the effects of E_i on the mechanical response observed during the uniaxial tensile test simulations. E_i is the young's modulus of the yarn and has a significant influence on the mechanical response after decrimping. A stiffer mechanical response is observed with the increased E_i values as shown in Figure 4.27.

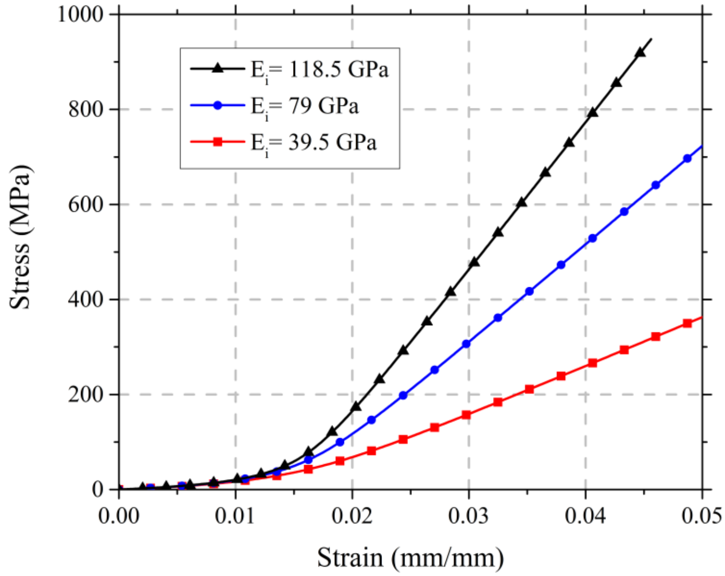

Figure 4.27 Sensitivity of uniaxial tensile test simulations to yarn modulus (E_i).

Figure 4.28 shows the sensitivity of uniaxial tensile test simulations to yarn decrimping spring stiffness (k_i^b). This material property directly affects the mechanical response before decrimping. Increased values of k_i^b result in stiffer mechanical response before decrimping as shown in Figure 4.28a. Moreover, the yarn decrimping springs also influence the Poisson's ratio observed during the uniaxial tensile test simulations. The crimp interchange mechanism is implemented within the material model using the compressive spring. The yarns aligned with the loading direction reduce their crimp while the yarns in the other direction increases their crimp. Increased k_i^b values result in increased resistance to crimp deformation in both yarn directions. Hence, lower Poisson's ratios are observed with the increased k_i^b values as shown in Figure 4.28b. Moreover, the effect of k_i^b is similar to the effect of transverse shear modulus in the mesoscopic length scale finite element models presented in Chapter 3.

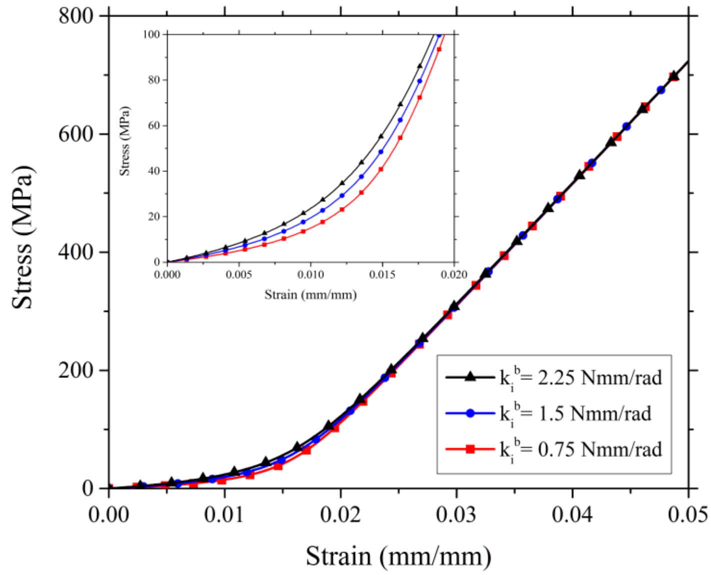

(a)

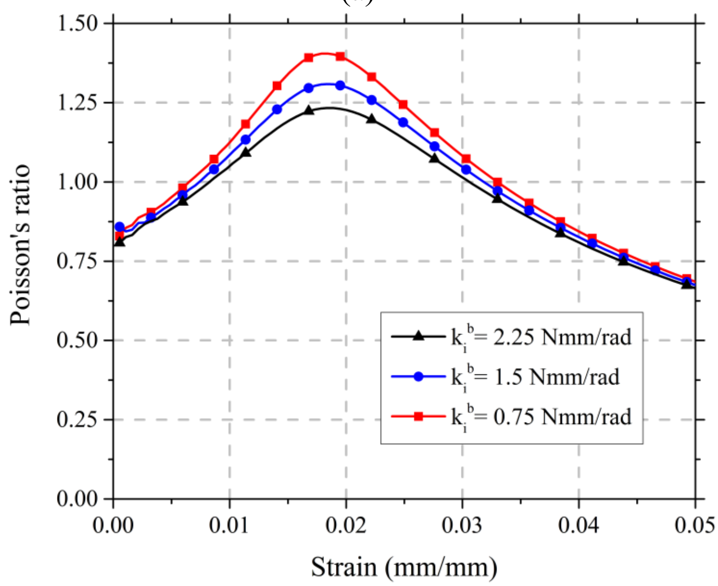

(b)

Figure 4.28 Sensitivity of uniaxial tensile test simulations to k_i^b: (a) Stress -strain, and (b) Poisson's ratio.

Figure 4.29 shows the sensitivity of uniaxial tensile test simulations to the compressive spring parameter *a*. It is determined that this compressive spring parameter does not affect the mechanical response observed during the uniaxial tensile tests. The parameter "a" acts as a limiting displacement where the compressive spring becomes very stiff. Hence, the compressive spring becomes stiffer at earlier spring displacements for lower "a" values as shown in Figure 4.29a. The compressive spring also determines the compressibility of the yarns. The sensitivity study revealed that "a" affects the kinematics of the deformation even though it does not influence the mechanical response. Figure 4.29b shows the Poisson's ratio change at various "a" values. Higher values of "a" result in softer yarn response in the transverse direction. Hence, lower Poisson's ratio values are observed for higher values of "a" since the yarns are more compressible.

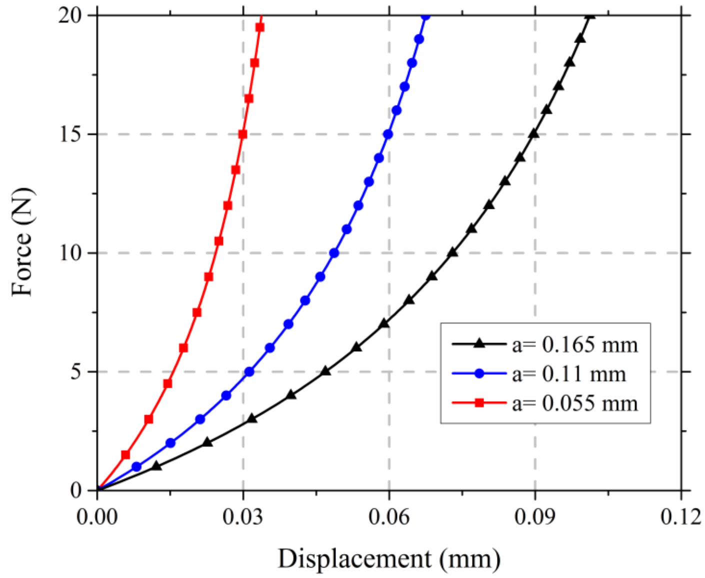

(a)

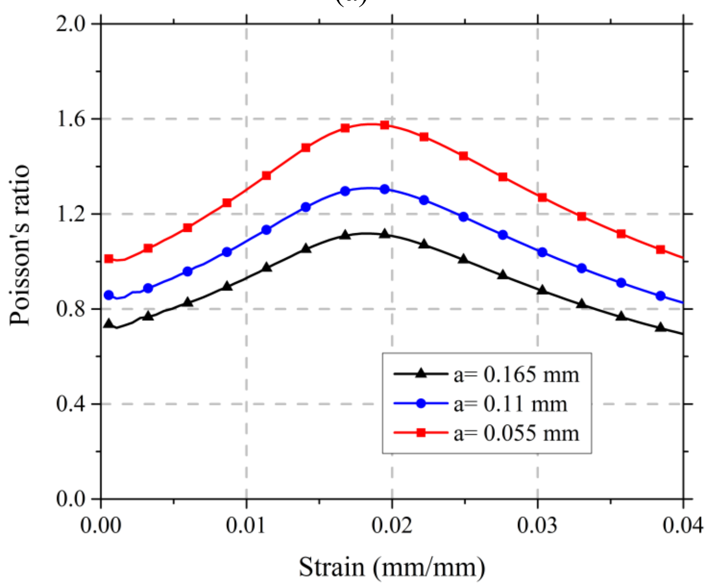

(b)

Figure 4.29 Sensitivity of uniaxial tensile test simulations to compressive spring parameter *a*: (a) Force response of the spring at various *a* values, and (b) Poisson's ratio change.

The second parameter of the compressive spring (*b*) acts as the spring stiffness constant. The higher values of this parameter results in stiffer spring response at a given "*a*" value as shown in Figure 4.30a. In a similar manner, the variation of the parameter does not influence the force response observed in the uniaxial tensile test simulations. However, it affects the deformation kinematics (Poisson's ratio change) as shown in Figure 4.30b. The higher values of *b* result in stiffer spring response resulting in less compressible yarns. Hence, the yarns can interact with each without compressing themselves at the crossover points under uniaxial loads resulting in crimp interchange. Hence, a stiffer compressive spring results in a higher Poisson's ratio since the yarns undergo crimp interchange rather than compressing each other.

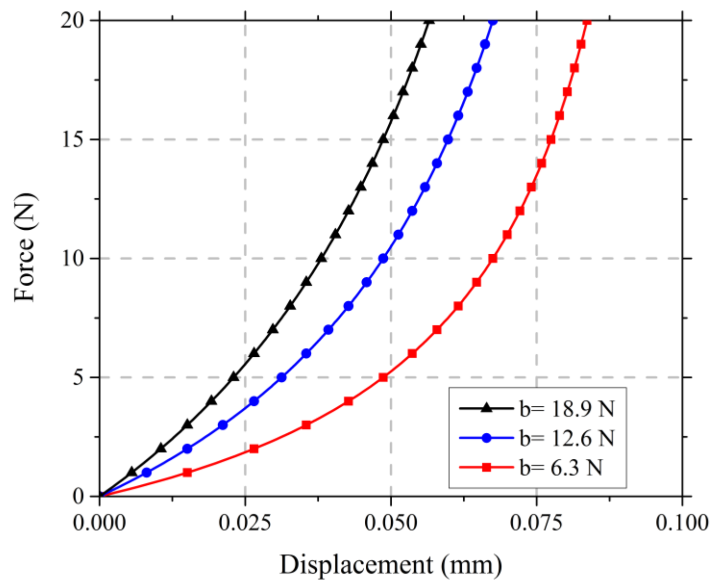

(a)

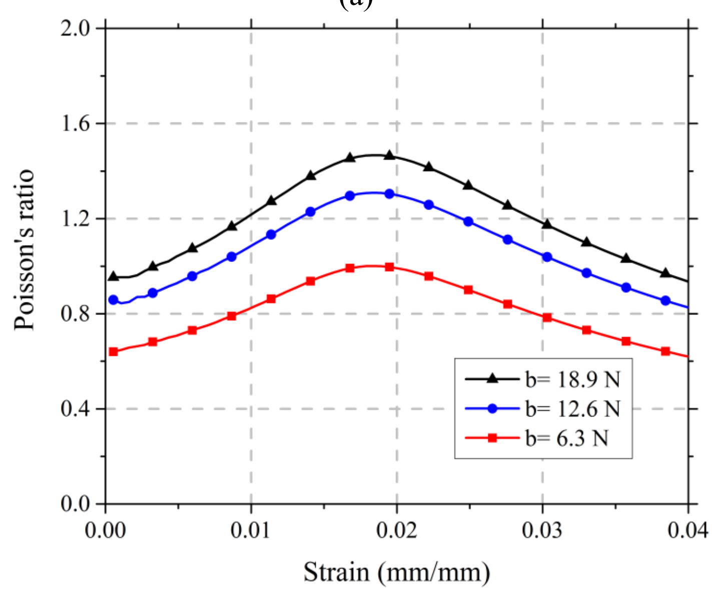

(b)

Figure 4.30 Sensitivity of uniaxial tensile test simulations to compressive spring parameter *b*: (a) Force response of the spring at various *b* values, and (b) Poisson's ratio change.

The sensitivity of bias extension tests to shear spring parameters are also studied with a parametric study. The torque/moment output of the shear spring is determined by two parameters (C_1 and C_2). Hence, these two parameters have an influence on the mechanical response observed during the bias extension test simulations. Figure 4.31a shows the sensitivity of bias extension test simulations to variation of C_1. Figures 4.31b show the sensitivity of the bias extension mechanical for C_2 variation. As C_2 increases, the material model response becomes more compliant and the force response is softer at higher displacements.

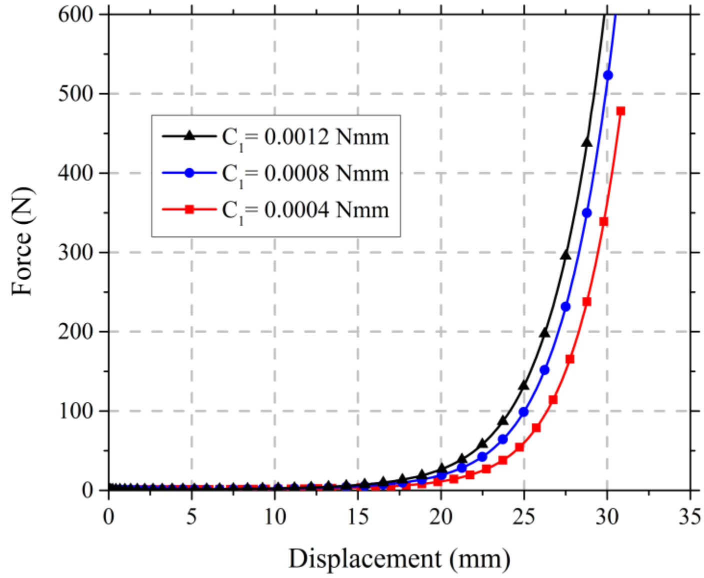

(a)

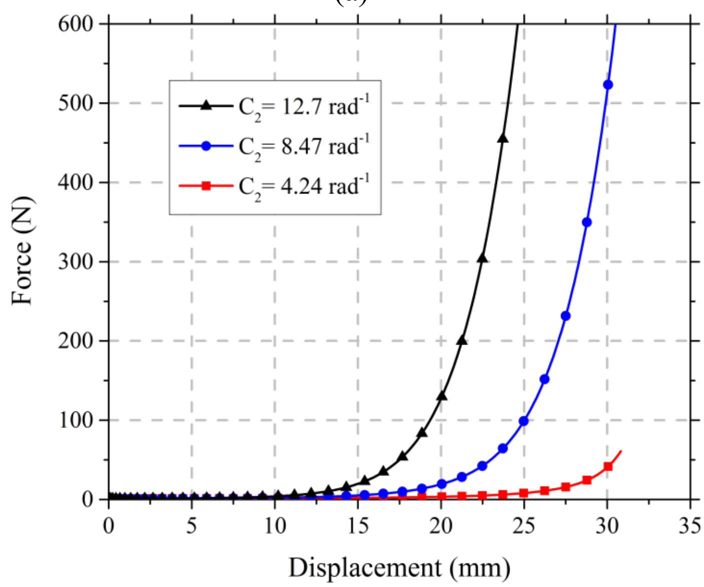

(b)

Figure 4.31 Sensitivity of bias extension test simulations to shear spring parameters: (a) Force response change at different C_1 values, and (b) Force response change at different C_2 values.

4.4 Comparison of Planar and Sawtooth Material Models

Developing shell-element based material models for woven fabrics at the macroscopic length scale requires certain limiting assumptions to simplify the actual material response. The material models developed (the PMM and the SMM) in the current work have limiting assumptions affecting the mechanical response and deformation mechanisms obtained from the material models. The PMM simplifies the fabric response by considering only the uniaxial and shear loads while the SMM considers uniaxial, biaxial and shear responses. Hence, the macroscopic length scale material models developed are initially compared under uniaxial, biaxial and shear loads by simulating standard tests presented in Chapter 2. Then, more complex loading cases where fabrics undergo large distortions are studied with both material models to investigate the limitations of the material models.

Both Planar and Sawtooth material models can reproduce the nonlinear mechanical response observed during the experiments under uniaxial loading as shown in Figure 4.32a. However, the deformation kinematics observed in both materials are different due to the limiting assumption made in the constitutive relations of the PMM. The tensile behavior of the yarns was assumed to be uniaxial and any interactions between the yarns were assumed to be not important. On the other hand, these yarn-to-yarn interactions were implemented with a compressive spring in the SMM formulation. Hence, the SMM can better simulate the deformation kinematics observed under uniaxial tensile loading. Figure 4.32b shows the nonlinear Poisson's ratio change for the SMM during uniaxial tensile test simulations. Since the yarns can interact with each other through the compression spring, the crimp interchange deformation mechanism and Poisson's effects can be simulated with the SMM. Figure 4.32c also shows the transverse displacement of the woven fabric models under uniaxial loading. The simulated woven fabric with the PMM does not change its width due to the limiting assumption while the fabric with the SMM decreases its width as the deformation progresses.

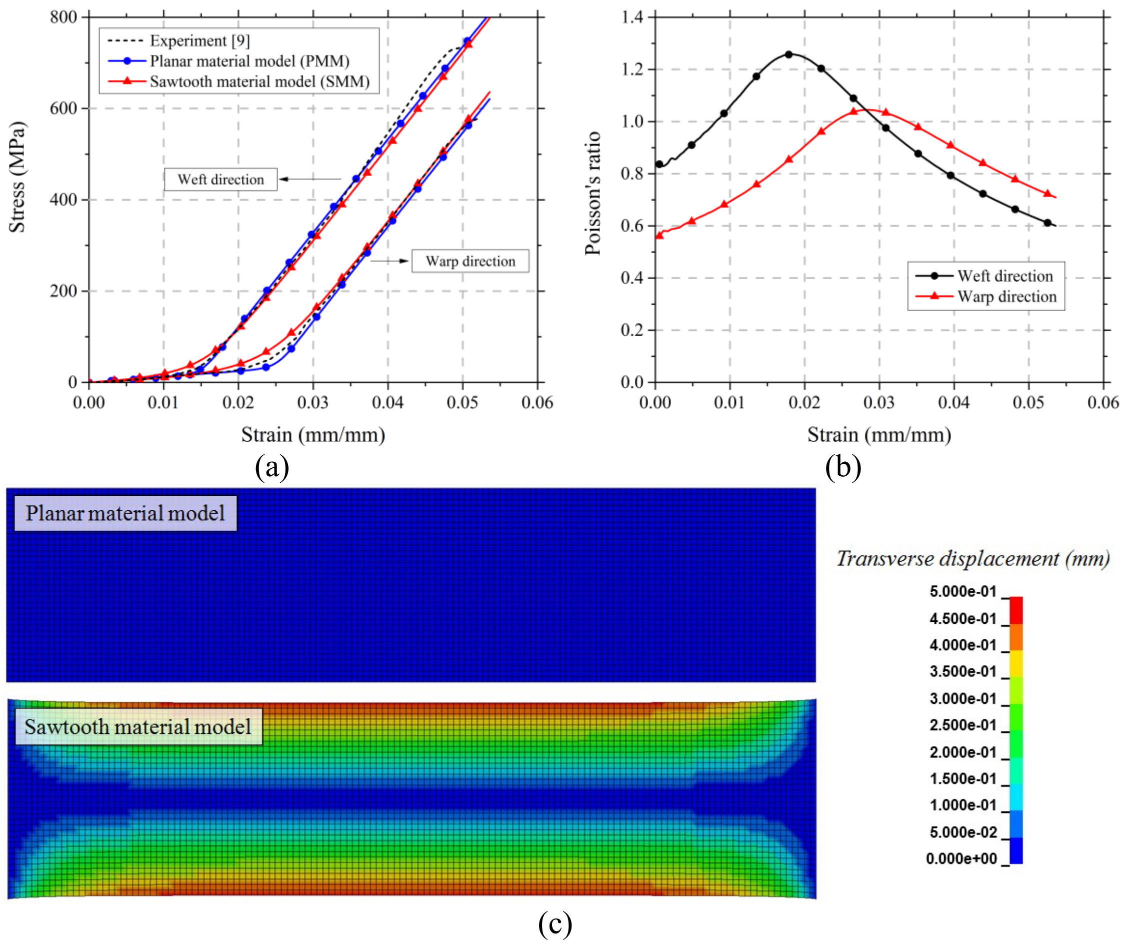

Figure 4.32 Comparison of uniaxial tensile test simulations: (a) Stress-strain curves, (b) Poisson's ratio change of Sawtooth material model (SMM), and (c) Transverse displacement of PMM and SMM simulations under uniaxial loading at 0.04 strain [9].

The limiting assumption made in the tensile response in the PMM also affects the mechanical response under biaxial loading. To investigate the effects of the assumptions, biaxial tensile test simulations were performed with both material models. Figure 4.33a shows the model setup used for the biaxial tensile test simulations. The woven fabric models had a cruciform shape with an outer dimensions of 120 mm. The total effective areas was assigned as 42 mm x 42 mm as shown in Figure 4.33a. Displacement boundary conditions with the varying displacement values were assigned to both edges resulting in strain ratios of 0.5, 1 and 2. Figure 4.33b shows the stress - strain curves obtained from the simulations (strain ratios: 0.5, 1 and 2) with the PMM and the SMM. It can be seen that the SMM exhibits a stiffer response compared to the PMM. During biaxial loading, both yarn are subjected to tensile loads and they start to straighten while compressing each other at the crossover point. Because of the yarns' compression, the mechanical response observed under biaxial loading is stiffer than the uniaxial response of the fabric. Since the PMM does not consider the interactions of the yarns and the tensile behavior is only uniaxial, the biaxial mechanical response is the same as the uniaxial. On the other hand, the SMM exhibits a stiffer response since the compressive spring replicates the crossover compression mechanism.

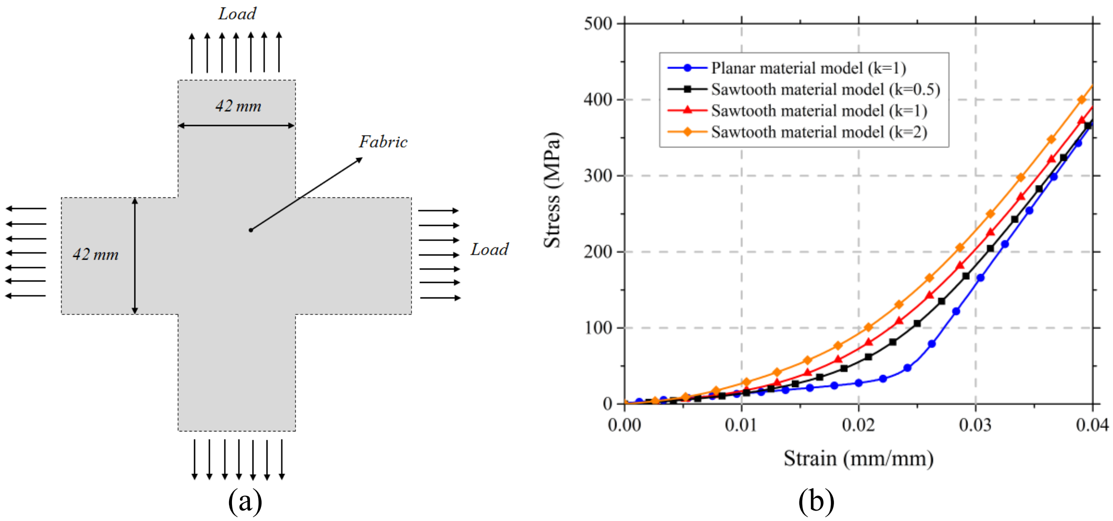

Figure 4.33 Comparison of biaxial tensile test simulations: (a) Setup of the biaxial tensile test simulation, (b) Stress-strain curves.

Figure 4.34 shows the comparison of the PMM and the SMM bias extension test simulations. Both models are capable of reproducing the nonlinear mechanical response observed during the bias extension tests. The difference between the material models with the experiments can be attributed to the yarn slippage deformation mechanism involved in bias extension experiments. Since the yarns are pin-jointed in both material models, this deformation cannot be modeled. Hence, stiffer responses were generated by the material models. Furthermore, the force responses of the PMM and the SMM show a different force profile. The SMM exhibits a stiffer response compared to the PMM. This difference may be attributed to the biaxial effects included in the SMM simulations through the compression spring.

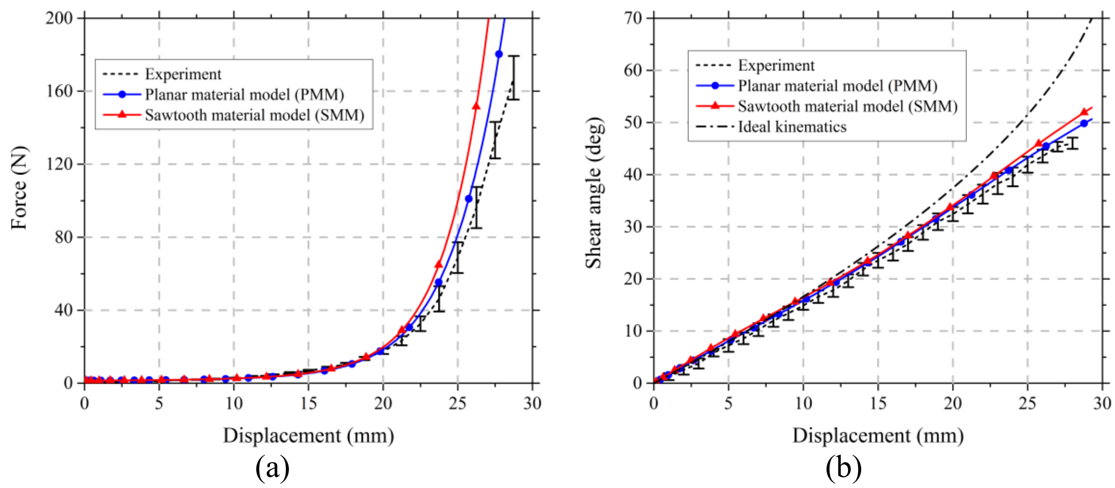

Figure 4.34 Comparison of bias extension test simulations: (a) Force - displacement, and (b) Displacement - shear angle.

The material models' mechanical responses were also compared under the indentation loading. Figure 4.35 shows the results for 0^{o} yarn orientation indentation simulations (51 mm x 40 mm woven fabric with 2 edges clamped). Both models are capable of capturing the mechanical response observed in the experiments. Since there is no biaxial loading involved, both models can generate the force response observed as shown in Figure 4.35.

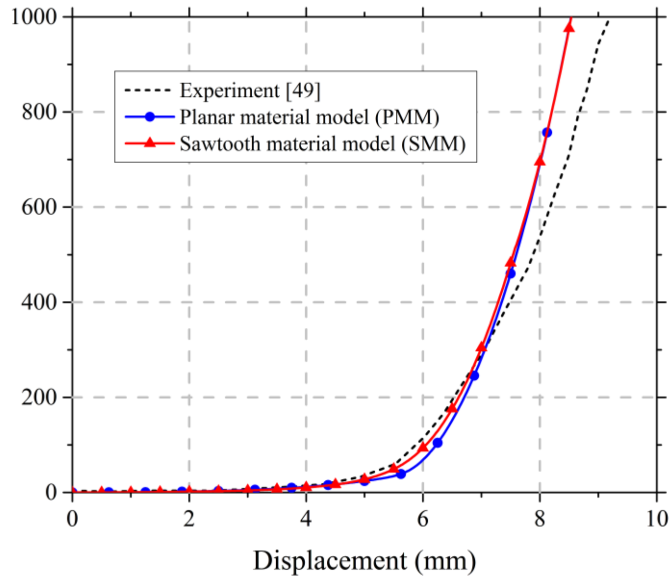

Figure 4.35 Comparison of indentation test simulations with 0^o yarn orientation with two short edges clamped [49].

Figure 4.36a shows the comparison of the material models with the 45^o yarn orientation (51 mm x 25 mm with 2 edges clamped). Both the PMM and the SMM can reproduce the experimentally observed mechanical response. Even though the force responses are the same, the von Misses Stress distribution of the material models are significantly different (Figure 4.36b). Both yarn directions are subjected to tensile forces underneath the indenter while they rotate relative to each other due to shear loading. Since the SMM takes into account of the yarns' interaction with each other (biaxial nature), the stresses are higher where the indenter makes contact with the fabric (Figure 4.36b). This difference might be significant for certain applications such as forming processes for composites manufacturing where the determination of residual stresses are important to obtain better end results.

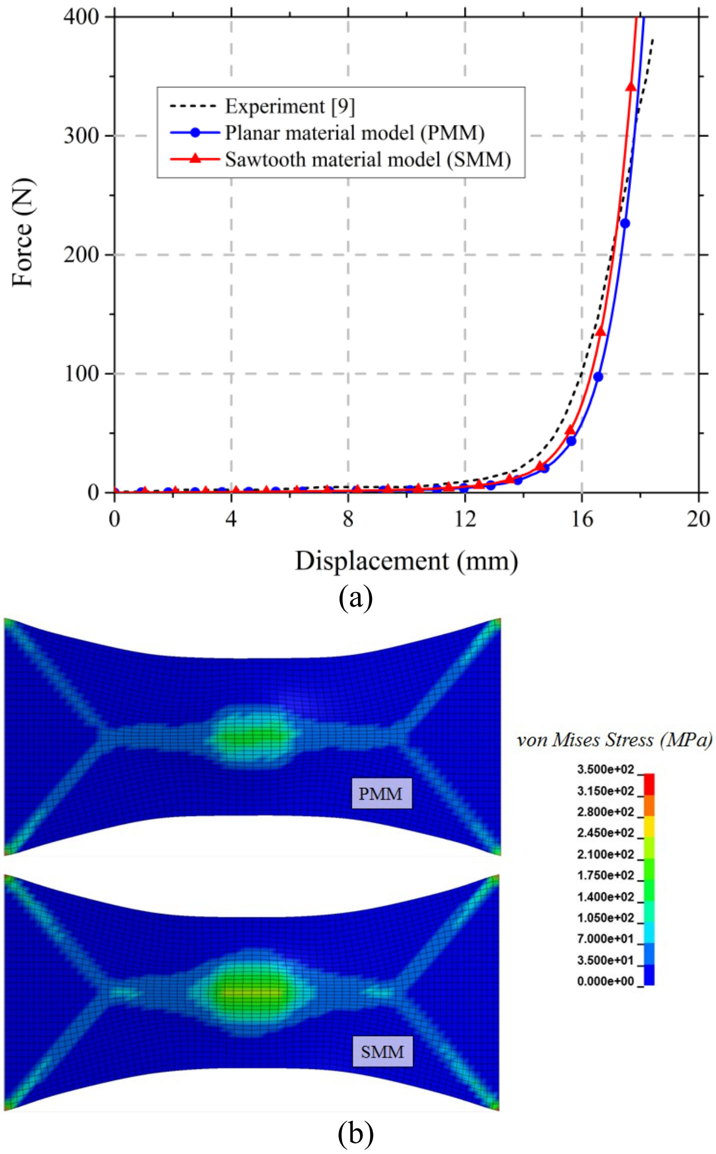

Figure 4.36 45^o yarn orientation indentation test simulations: (a) Force - displacement, and (b) Stress distribution at 16 mm indenter displacement [9].

To further investigate the different between the material models, a numerical study is carried out. A square fabric model with 50 mm x 50 mm dimensions and an indenter of 12 mm were used for the study. Indentation test is chosen to simulate a more complex deformation condition on the fabric. All 4 edges were clamped by restricting only translational DOFs. A displacement of 8 mm was prescribed to the indenter. The orientation of yarns was varied: (1) 0^o, (2) 15^o, (3) 30^o and (d) 45^o. Figures 4.37a and 4.37b show the simulation results for the PMM and the SMM, respectively. It can be seen that the force responses for both models exhibit stiffer response as the yarn orientation angle decreases. This change in the force response can be attributed to the yarns that are located in the vicinity and underneath of the indenter. These yarns are subjected to tensile loads as the indenter moves and they undergo decrimping. The length of these yarns are dependent on the fabric orientation angle. As the fabric orientation angle increases, the length of these yarns also increases. Hence, the yarns are the longest when the orientation angle is 45^o and higher indenter displacements are required to deform these yarns. The SMM exhibits a stiffer response for all the yarn orientations compared to the PMM. This could be attributed to the boundary conditions prescribed in the model where all 4 edges are clamped. Hence, the yarns are subjected to biaxial loads during deformation. Since the PMM does not take into account biaxial response, its mechanical response is softer compared to the SMM. Figure 4.37c shows the comparison of these two material models at 0^o and 45^o yarn orientations.

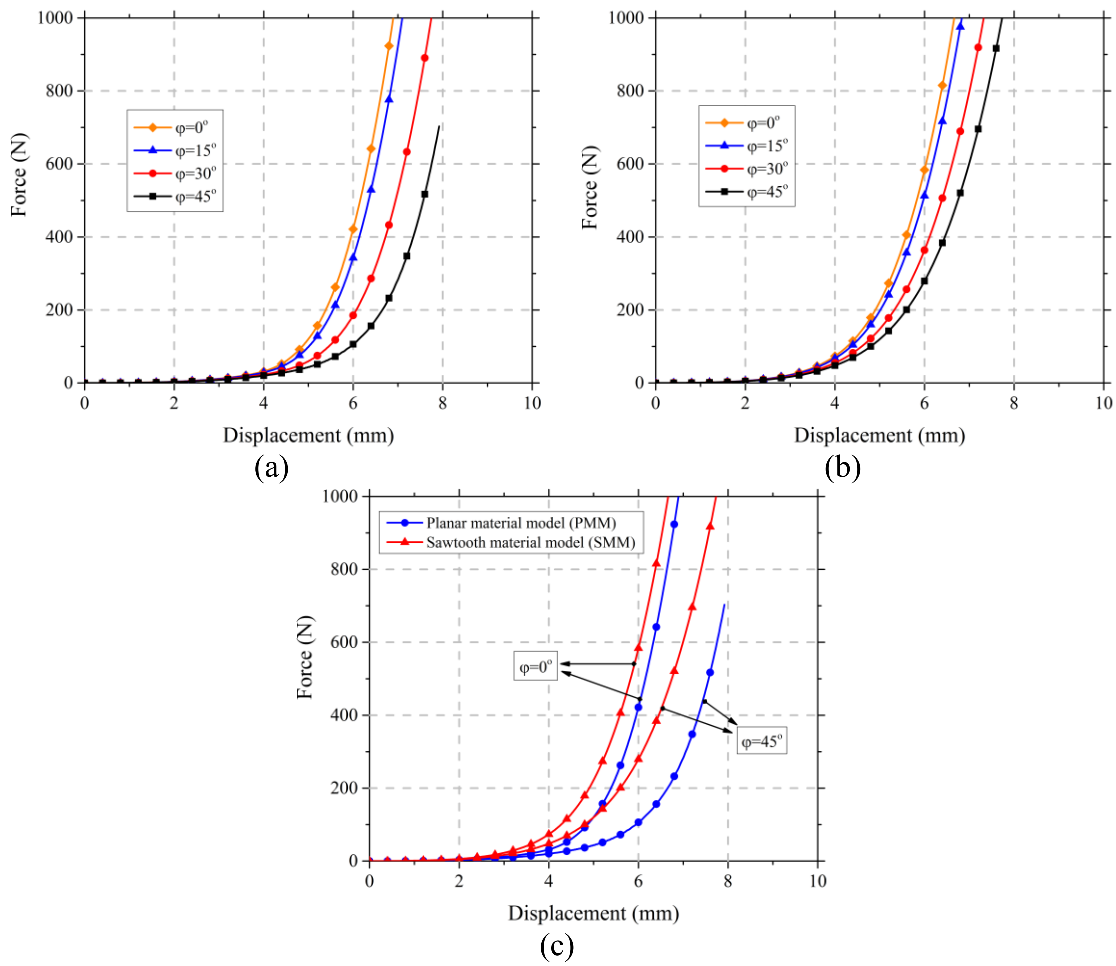

Figure 4.37 Indentation simulations with 4 edges clamped and various yarn orientations: (a) Planar material model results, (b) Sawtooth material model results, and (c) Comparison of Planar and Sawtooth material models.

Figure 4.38 shows the von Mises stress distributions of the PMM and the SMM at various yarn orientations at 6 mm indenter displacement. It should be noted that the stress levels shown in Figure 4.38 include the stresses due to yarn extension and fabric shear for both models. On the other hand, the stresses related to biaxial response is only included for the SMM in Figure 4.38. All simulations exhibit a stress concentration at the middle section of the fabric due to the indenter contact with the fabric model. As the fabric orientation increases, the stress levels decreases which is also consistent with the force - displacement curves shown in Figure 4.37. Since the yarns can interact with each other through the compression spring in the SMM simulations, the stress distributions are higher compared to the PMM.

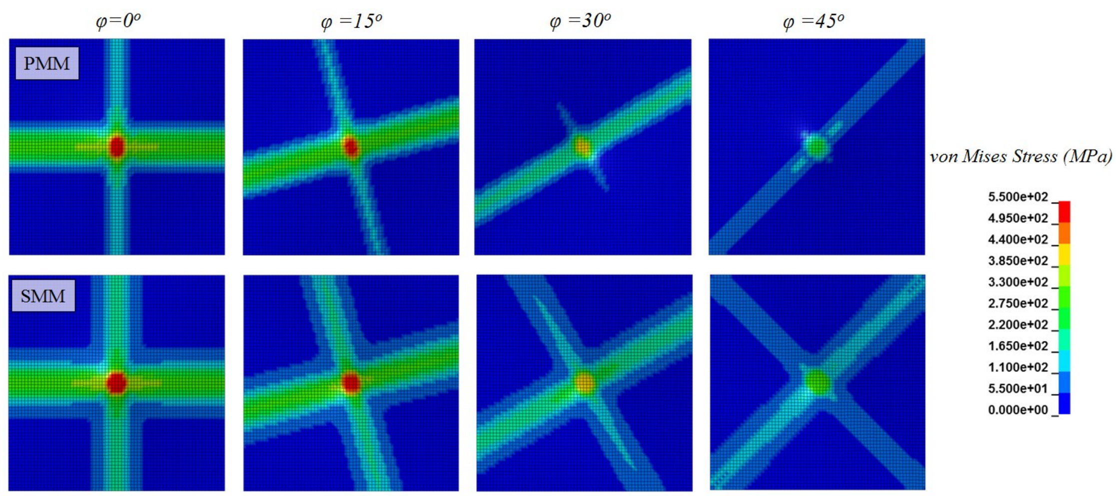

Figure 4.38 von Mises Stress distribution comparison for Planar and Sawtooth material models at 6 mm crosshead displacement.

4.5 Summary and Contributions

A widely acceptable material model for woven fabrics in the macroscopic length scale does not exist because of the complex deformation mechanisms involved in woven fabrics under various loading conditions. The current work introduces two new macroscopic length scale material models for woven fabrics to simulate deformation mechanisms and nonlinear mechanical response of woven fabrics. The first material model developed, the Planar Material Model (PMM) is based on the mesoscopic length scale unit of a plain weave and the yarns are assumed to lie on the same plane. The mechanical response of the unit cell is modeled with yarns as trusses for uniaxial response and a rotational nonlinear crossover spring for shear response. Continuum mechanics are adopted to implement non-orthogonal nature of the woven fabrics. The model assumes that the tensile behavior of the yarns are only uniaxial and all the deformation mechanisms (tensile, shear and out-of-plane) are decoupled from each other. Table 4.7 shows the comparison of the PMM to other material models available in the literature assuming a planar material behavior. All these materials adopt different constitutive relations and formulations to implement fabric behavior. These material models do not consider the mesoscopic structure of the woven fabric and require inverse methods where numerical simulations are carried out to fit material properties/parameters to the experiments (numerically calibrated) [9, 14, 23, 49, 51, 68]. The numerical calibration is time consuming and might become computationally expensive due to the number of runs needed. Moreover, special finite element formulations are also required based on the material model developed to model the woven fabric behavior which introduces additional computational costs [1, 16, 55, 56, 77]. One of the contributions of the PMM is that the material properties/parameters required by the model can be directly obtained from either experiments or mesoscopic level simulations without running any numerical simulations to fit the material model response to experiments. The PMM also does not require any special finite element formulations and can be directly used with available shell element formulations. Moreover, the material model has been validated with various experiments where the woven fabrics are subjected to various loads.

Table 4.7 Comparison of the PMM to similar material models available in the literature.

Material model	Response type & calibration			Validation
	Uniaxial	Biaxial	Shear	
Dong et al. [9]	Nonlinear (NC)	No	Yes (NC)	Uniaxial tensile Bias extension 30^o off-axis Indentation (45^o)
Jauffress et al. [22]	Nonlinear (EC)	No	Yes (EC)	Bias extension Picture frame
Peng et al. [23]	Nonlinear (EC)	No	Yes (EC)	Uniaxial tensile Picture frame
Boisse et al. [20]	Linear (EC)	Yes (NC)	Yes (NC)	Draping
Current work (PMM)	Nonlinear (EC)	No	Yes (EC)	Uniaxial tensile Bias extension 30^o off-axis Indentation ($0^o/90^o/45^o$)

EC: Experimentally calibrated
NC: Numerically calibrated (Simulations required)

The second material model developed, Sawtooth Material Model (SMM) is also based on the mesoscopic length scale unit cell of woven fabrics. The material model adopts a sawtooth geometry where the yarns do not lie on the same plane and can interact with each other at the crossover point. Constitutive relations are used to implement several deformation mechanisms and the associated nonlinear mechanical responses. Yarns are modeled as non-orthogonal trusses along with rotational decrimping springs for uniaxial tensile response. The compressive spring is used to obtain yarn-to-yarn interactions which reproduces the biaxial nature of the woven fabrics. The shear resistance of the fabric due to mesoscopic yarn interactions in the transverse direction is modeled with the nonlinear rotational spring located at the crossover point. Table 4.8 shows the comparison of the SMM to the available material models that are based on the sawtooth geometry. Most of these models were developed for impact problems and were not validated under various loading conditions (especially for shear response) [36, 39, 57, 60]. Since the constitutive relations used to implement material behavior are different, the formulations adopted in these models are different. The material properties/parameters required by the SMM can be directly determined from experiments without carrying out any numerical simulations. The material model was also validated for various loading cases including uniaxial tensile, bias extension, 30^{o} off-axis and indentation.

Table 4.8 Comparison of SMM to similar material models available in the literature.

Material model	Response type & calibration			Validation
	Uniaxial	Biaxial	Shear	
King et al. [58]	Nonlinear (EC)	Yes	Yes (NC)	Uniaxial tensile Bias extension Impact
Shahkarami et al. [39]	Nonlinear (N/A) (No decrimping)	Yes	Yes (N/A)	Uniaxial tensile Impact
Grujicic et al. [36]	Nonlinear (N/A (No decrimping)	Yes	Yes (N/A)	Impact
Current work (SMM)	Nonlinear (EC)	Yes	Yes (EC)	Uniaxial tensile Bias extension 30^{o} off-axis Indentation ($0^{o}/90^{o}/45^{o}$)

EC: Experimentally calibrated
NC: Numerically calibrated (Simulations required)

In the current work, two macroscopic material models were developed and validated by comparing experiments. The first material model (the PMM) simplifies the fabric structure by assuming the yarns lie on the same plane and the tensile response of the yarns are only uniaxial. On the other hand, the second material model (SMM) takes into account the yarns' interaction in the transverse direction resulting in biaxial response by modeling the 3D fabric structure, unlike the PMM. Both the PMM and the SMM were able to capture the mechanical response observed under uniaxial and shear loads. However, the PMM was not able to reproduce the biaxial responses due to assumptions made to simplify the material response. On the other hand, the

SMM was able to simulate the biaxial nature since the yarn interactions were included in the constitutive relations.

The selection of the material models developed for a specific application depends on the desired output from the simulations. The PMM can be used in applications where the woven fabrics are not subjected to high loads, especially biaxial loading. For example, the PMM can be used to analyze the draping of woven fabrics over complex molds for composites manufacturing to determine and identify the shear angle distribution to estimate wrinkling. On the other hand, the SMM can be adopted for applications such as airbags or ballistic impact studies where accurate mechanical response of the woven fabric is desired. It should be noted that the SMM is computationally more expensive compared to the PMM because of the numerical minimization algorithm adopted to determine the unit cell configuration at a given deformation. Moreover, the material properties/parameters required for the uniaxial and shear responses can be obtained from standard tests. However, the compression spring defined in the SMM (the biaxial response) requires additional material properties/parameters. Hence, additional work has to be carried out to determine the inputs required by the SMM.

In this chapter, the material properties/parameters required by the both macroscopic material models were obtained from experiments. Since both of these models are based on the mesoscopic unit cell, the constitutive relations developed provide a unique opportunity to determine the properties/parameters from mesoscopic length scale simulations. This structure of the models also allows the study of woven fabrics in a systematic way at meso and macro length scale while linking them. The following chapter explores this link between meso and macro length scale modeling approaches to develop a systematic design framework for woven fabrics.

Chapter 5

INTEGRATED MULTISCALE DESIGN FRAMEWORK FOR WOVEN FABRICS

5.1 Introduction

Woven fabrics exhibit a complex hierarchy due to the length scales involved in their construction. This complex hierarchy results in a highly nonlinear mechanical response and deformation mechanisms under various loads. Hence, it is important to study the length scale effects involved in woven fabrics. This chapter systematically investigates the mesoscopic and macroscopic length scale models. In this work, mesoscopic length scale models (Chapter 3) are used to develop and determine the material properties/parameters required by the macroscale material models developed (Chapter 4). The models are numerically verified by carrying out simulations using both the mesoscopic and macroscopic length scale models. The models are then compared in terms of their capability of simulating various deformation modes and computational efficiency.

5.2 Integration of Mesoscopic and Macroscopic Length Scale Computational Models

In Chapter 4, two different macroscopic material models based on the mesoscopic structure of woven fabrics were developed. The current chapter investigates the relationships between the mesoscopic numerical models developed in Chapter 3 and the macroscopic material models by linking them in a systematic way.

5.2.1 Linking Planar Material Model (PMM) with mesoscopic length scale simulations

The first macroscopic material model developed in Chapter 4 is called the Planar Material Model (PMM) (Figure 4.1). The material model assumes that the yarns lie on the same plane and their tensile response is only uniaxial. The yarns are modeled as truss elements while shear behavior of the woven fabric due to yarn-to-yarn interactions is modeled with a nonlinear rotational spring located at the crossover location. In Chapter 4, the material properties/parameters required by the material model were obtained from uniaxial tensile tests on yarns/fabrics and bias extension tests. Since the constitutive relations used are based on the mesoscopic unit cell of the woven fabric, the inputs required by the model can also be determined from mesoscopic length scale simulations where each yarn within the fabric is modeled explicitly. To link the meso and macro length scales, unit cell mesoscopic length scale simulations are used to determine the PMM's required material properties/parameters. Figure 5.1 shows the approach adopted to determine the values of PMM inputs from mesoscopic unit cell simulations. Mesoscopic length scale unit cell simulations are used to obtain the values of the PMM material properties/parameters while various simulations including standard tests are carried out with both mesoscopic length scale models as well as the PMM to verify the adopted approach.

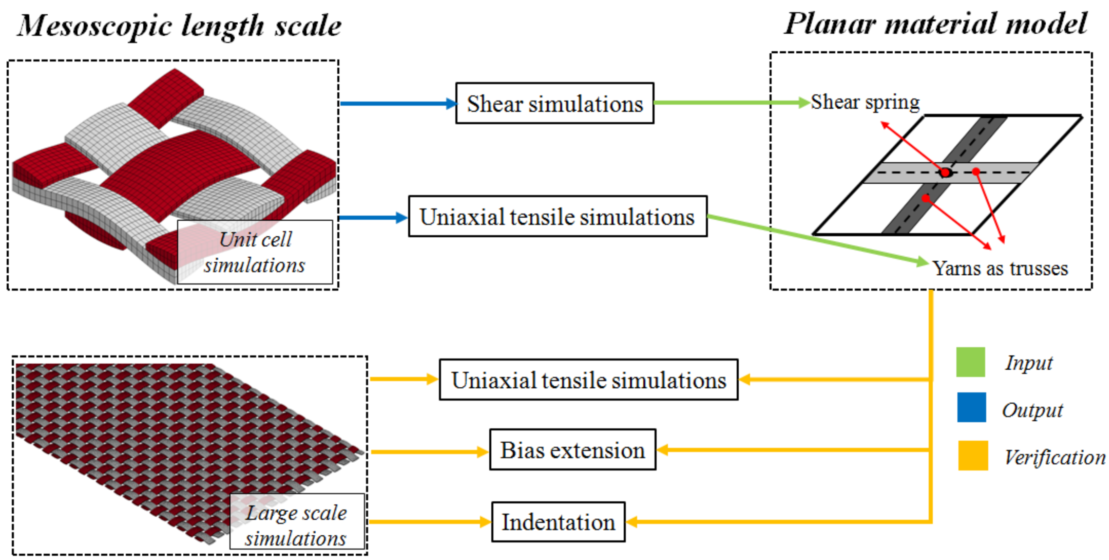

Figure 5.1 Link between the PMM and mesoscopic length scale simulations.

The PMM requires several material properties/parameters as inputs to reproduce the mechanical response observed under uniaxial and shear loads. The material properties/parameters used in the material model are presented in Table 5.1 (The details of these material parameters can be found in Chapter 4).

Table 5.1 Material properties/parameter required by Planar Material Model (PMM).

Response type	Parameter	Definition
Uniaxial tensile	E_i^1	Modulus before decrimping
	E_i^2	Modulus after decrimping
	β_i	Shape parameter
	$\varepsilon_{i,crimp}$	Decrimping strain
	$\varepsilon_{i,trans}$	Transition strain
Shear	C_1	Shear parameter
	C_2	Shear parameter

The material properties/parameters for the uniaxial tensile response of the model were obtained from uniaxial tensile experiments in Chapter 4. In current chapter, mesoscopic unit cell simulations under uniaxial tensile loads are adopted to determine the values of these parameters. Therefore, mesoscopic unit cell simulations under uniaxial loads are used to generate stress-strain curves for single yarns. Then, the yarn modulus before and after decrimping (E_i^1 and E_i^2) are calculated from the stress-strain curve generated as shown in Figure 5.2a. The decrimping and transition strains ($\varepsilon_{i,crimp}$ and $\varepsilon_{i,trans}$) are also determined from the intersection of the compliant and non-compliant parts of the stress-strain curves. On the other hand, the shape parameter (β_i) controlling the transition region during decrimping is determined based on the stability of the simulations to avoid any sudden changes. Furthermore, mesoscopic unit cell simulations under shear loading are carried out to determine the shear response of the PMM. The unit torque/moment required as a function of shear angle is extracted from mesoscopic simulations using the external work done on the unit cell (The details of unit torque/moment from external work done on a unit cell is presented in Chapter 3) Then, the PMM's shear spring parameters (C_1 and C_2) are varied while minimizing the RMSE between the mesoscopic unit torque/moment and shear spring moment. The adopted approach linking the meso and macro length scales for shear response is shown in Figure 5.2b.

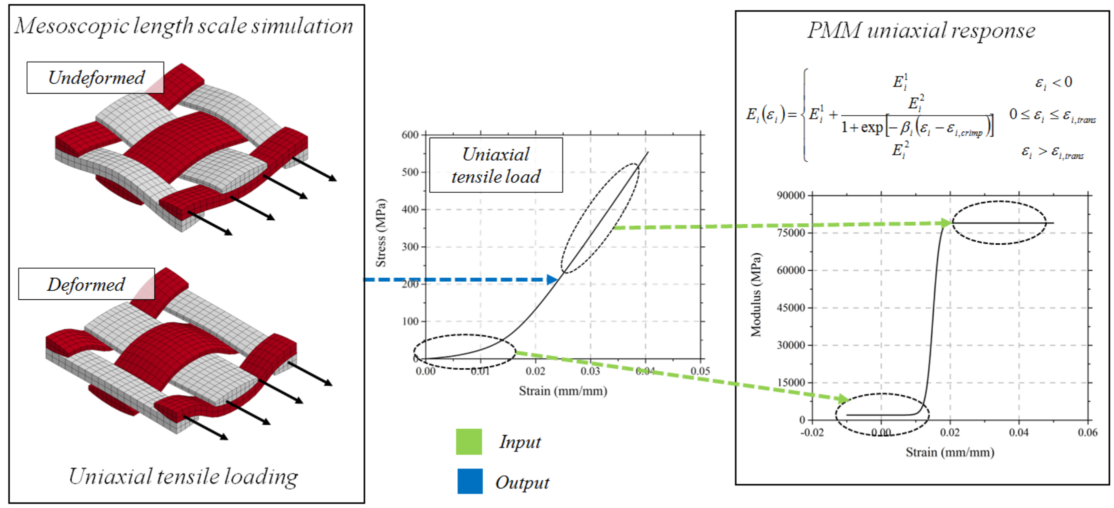

(a)

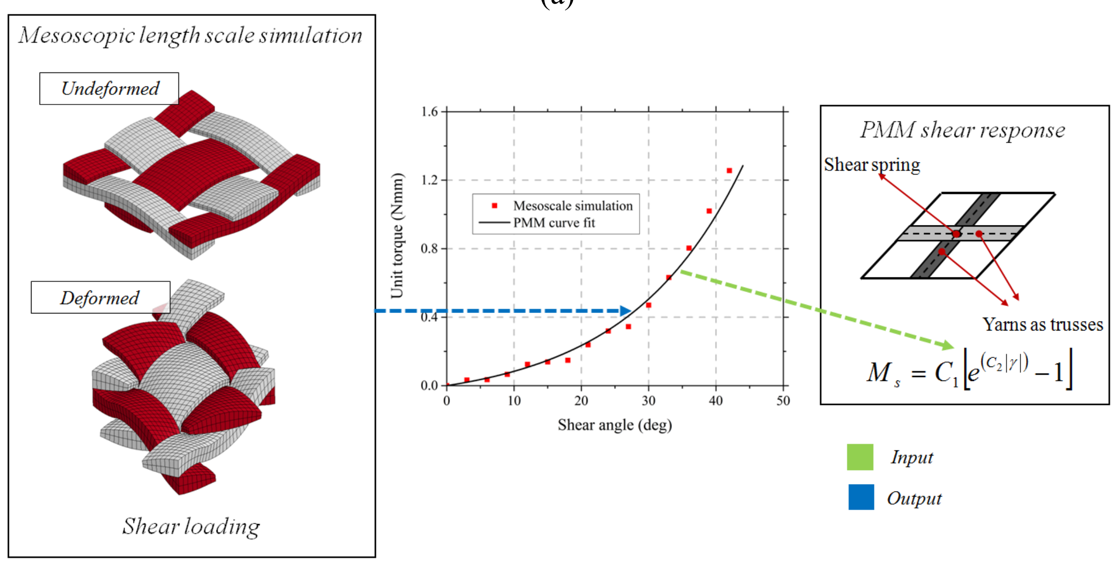

(b)

Figure 5.2 Determination of PMM material properties/parameters from mesoscopic length scale simulations: (a) Uniaxial tensile response, and (b) Shear response.

To demonstrate the approach developed in Figure 5.2, mesoscopic length scale unit cell simulation for K706 were carried out under uniaxial tensile and shear loads using the same geometric dimensions and material properties used in Chapter 3. Then, the approach shown in Figure 5.2 is carried out to determine the values of the PMM inputs presented in Table 5.1. Figure 5.3 shows the curve fit obtained for the PMM's shear spring from the mesoscopic unit cell simulations under shear loading. It can be seen that the both mesoscopic and shear spring unit torque/moments are similar.

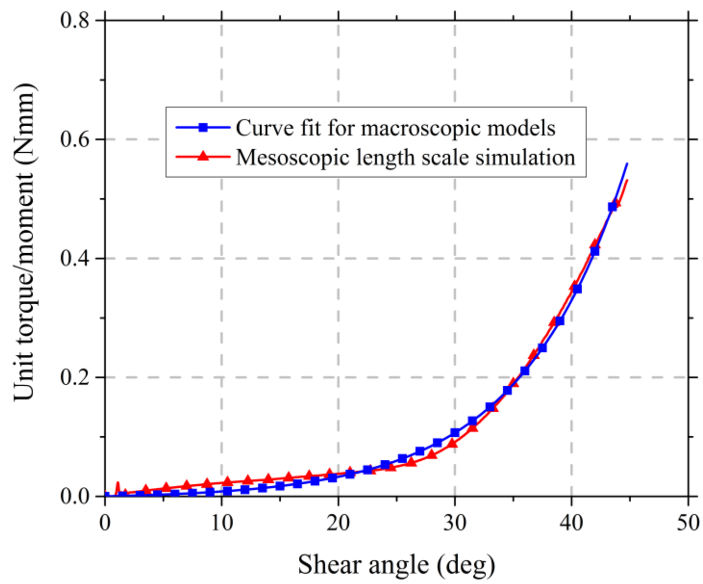

Figure 5.3 PMM shear spring moment with spring parameters determined from mesoscopic unit cell shear simulations.

Table 5.2 shows the PMM's material properties/parameters obtained from mesoscopic unit cell simulations under uniaxial tensile and shear loads. It should be noted that the values presented for material properties/parameters in Table 5.2 are different than the values presented in Table 4.2. This difference is mainly due to the method used to determine the values of the parameters. In Table 4.2, the values were obtained from experiments. On the other hand, the values presented in Table 5.2 are all based on the mesoscopic length scale unit cell simulations with the goal of linking meso and macro length scales. Hence, the values presented in these tables are different from each other.

Table 5.2 The PMM input values determined from unit cell mesoscopic length scale simulations.

Response type	Parameter	Weft direction	Warp direction
Uniaxial tensile	E_i^1 (MPa)	2006.8	1254.6
	E_i^2 (MPa)	79000	69000
	β_i	100	100
	$\varepsilon_{i,crimp}$	0.015	0.025
	$\varepsilon_{i,trans}$	0.018	0.028
Shear	C_1 (Nmm)	0.0041	
	C_2 (rad^{-1})	6.31	

5.2.2 Linking Sawtooth Material Model (SMM) with mesoscopic length scale simulations

The Sawtooth material model (SMM) is the second macroscopic material model developed in the current work. The details of the material models and its experimental validation are presented in Chapter 4. The developed material model is based on the sawtooth geometry developed by Kawabata et al. and is capable of modeling uniaxial, biaxial and shear mechanical responses [78]. The unit cell adopted is based on the mesoscopic structure of plain weave fabrics similar to the PMM. Therefore, the material inputs of the SMM can be determined from mesoscopic length scale simulations in a similar manner to the PMM. Figure 5.4 shows the developed approach for the SMM to determine these material properties/parameters as well as the verification simulations carried out to verify the method developed.

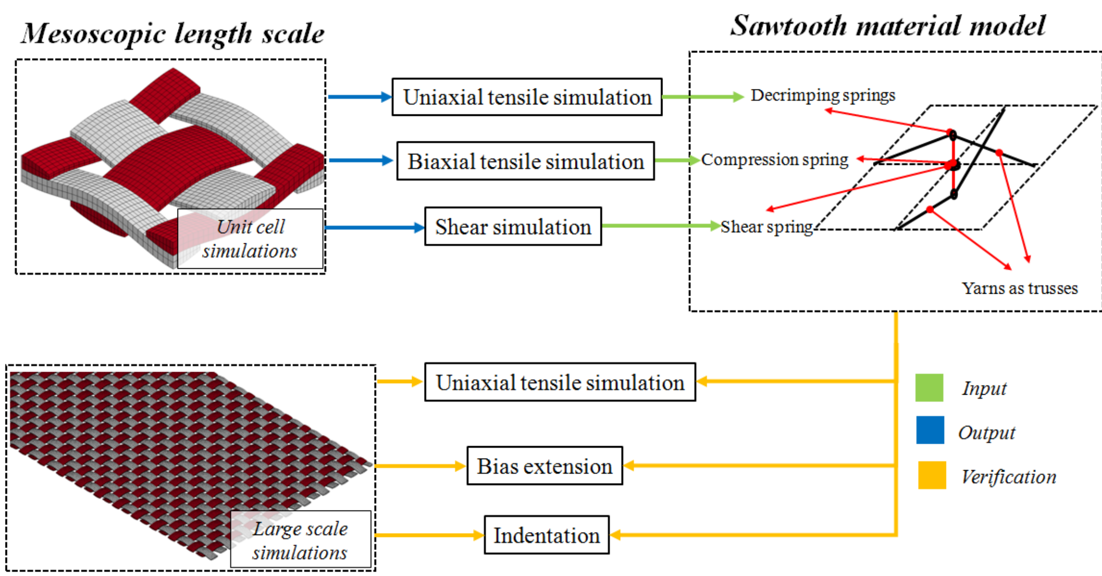

Figure 5.4 Link between the SMM and mesoscopic length scale simulations.

As explained before, the SMM is capable of modeling mechanical responses under uniaxial, biaxial and shear loads. This capability is achieved through several truss elements and springs defined using the constitutive relations. Hence, the material model requires material properties/parameters for each mechanical response modeled. These parameters and their definitions based on the mechanical response modeled are presented in Table 5.3.

Table 5.3 Material properties/parameters required by Sawtooth material model (SMM).

Response type	Parameter	Definition
Uniaxial tensile	E_i k_i^b	Yarn modulus Yarn decrimping spring stiffness
Biaxial	a b	Compression spring parameters
Shear	C_1 C_2	Crossover spring parameters

The uniaxial mechanical response of the SMM requires two material properties as shown in Table 5.3: (1) yarn modulus (E_i), and (2) yarn decrimping spring stiffness (k_i^b) for each yarn direction. To determine these material properties, mesoscopic length scale simulations under uniaxial loading for each direction are carried out. Then, stress-strain curves for single yarns are generated using the nodal forces and effective yarn areas. The yarn decrimping spring directly affects the mechanical response before decrimping while yarn modulus affects the post decrimping behavior under uniaxial tensile loads as shown in Chapter 3 for the SMM. Hence, the yarn decrimping spring stiffness is determined from the initial portion of the stress-strain curves (before decrimping) as shown in Figure 5.5. For this purpose, the crimp angles for each yarn direction are determined from the mesoscopic unit cell simulations by assuming a sawtooth geometry. Then, the forces developed in each yarn are used along with the unit cell dimensions at a given strain to calculate the yarn decrimping spring stiffnesses. On the other hand, the yarn modulus is determined from the non-compliant portion of the stress-strain curve (Figure 5.5).

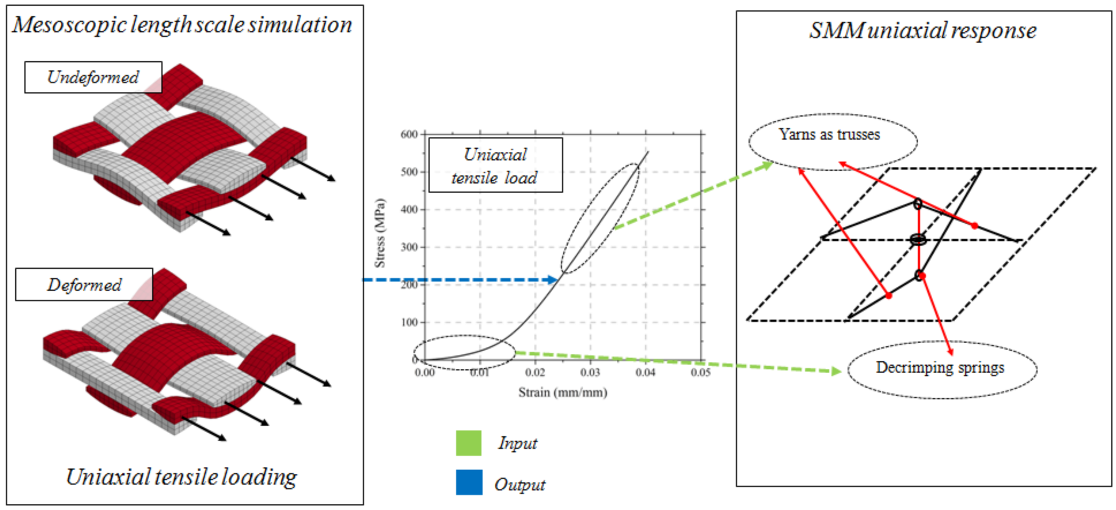

Figure 5.5 Determination of uniaxial tensile response material properties/parameters for the SMM.

The compressive spring defined at the crossover point for the SMM replicates the yarns' interaction between them (Figure 5.4). Since the yarns are capable of interacting with each other through the compression spring, the SMM is capable of reproducing the biaxial mechanical response of woven fabrics. To determine the parameters required by the compressive spring, the mesoscopic unit cell simulations under biaxial loading can be carried out. Figure 5.6a shows the approach adopted for this purpose. Unit cell simulations are carried out where the same displacement boundary conditions are imposed on the unit cell boundaries. Initially, the nodal forces developed between the yarns at the crossover point as a function of applied strain are recorded and then the force developed within the spring is curve fit while minimizing the RMSE (Figure 5.6b).

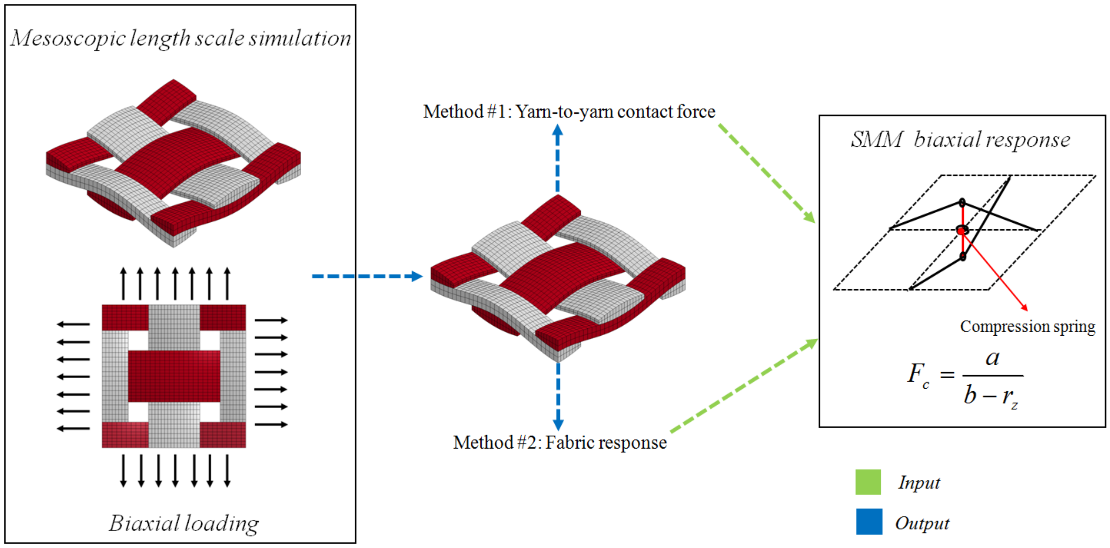

(a)

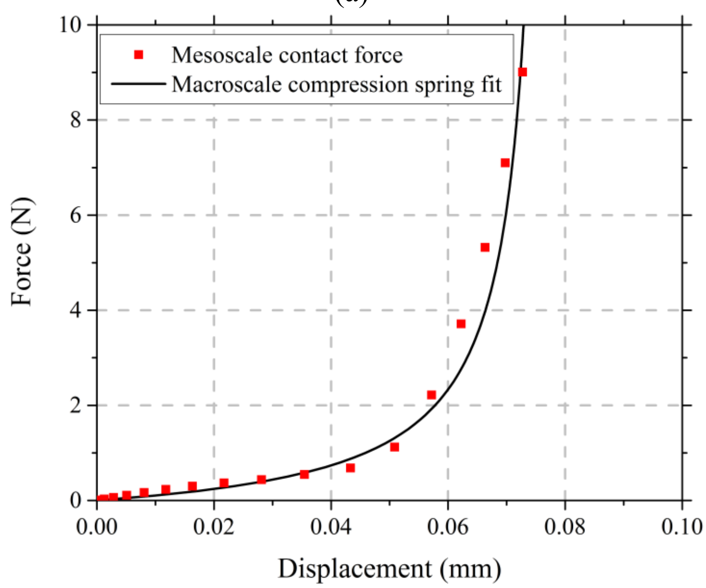

(b)

Figure 5.6 Determination of biaxial response material properties/parameters for the SMM: (a) Methods adopted to determine compressive spring parameters, and (b) Determination of SMM compressive spring parameters from mesoscale contact force.

Initial biaxial tensile test simulations were carried out and compared to the unit cell level simulations for verification purposes. Figure 5.7a shows the SMM's mechanical response under biaxial loading and its comparison to the mesoscopic length scale simulations (mesoscopic length scale uniaxial simulation results are shown as the baseline for comparison purposes). It can be seen that the SMM is stiffer compared to the uniaxial tensile case. However, the material model was not able to reproduce the mechanical response observed in mesoscopic unit cell subjected to biaxial loading. This difference was attributed to the determination of spring parameters from yarn-to-yarn contact force (Method #1 in Figure 5.6a). The contact force extracted from the mesoscopic finite element simulations only represent the contact pressure developed between the yarns and does not include the yarn material response in the transverse direction. Hence, the compressive spring parameters determined from the contact force are too low and acts as the lower limit for the compressive spring. To obtain a more accurate biaxial mechanical response, Method #2 shown in Figure 5.6a is adopted. In this method, the compressive spring parameters were varied while minimizing the RMSE between stress-strain values of the SMM and mesoscopic unit cell simulations. Figure 5.7b shows the SMM mechanical response under biaxial loading with the adjusted compressive spring parameters. It can be seen that SMM can reproduce the mechanical response observed in the mesoscopic unit cell subjected to biaxial loading.

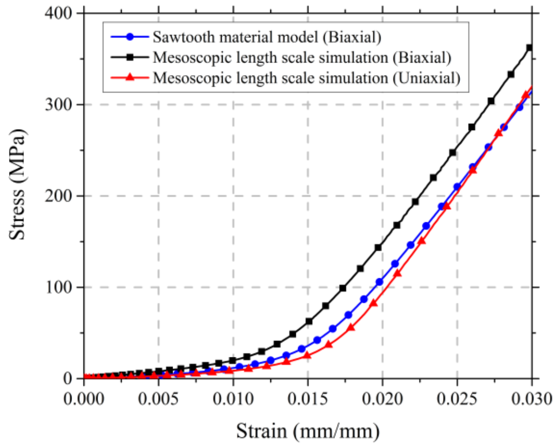

(a)

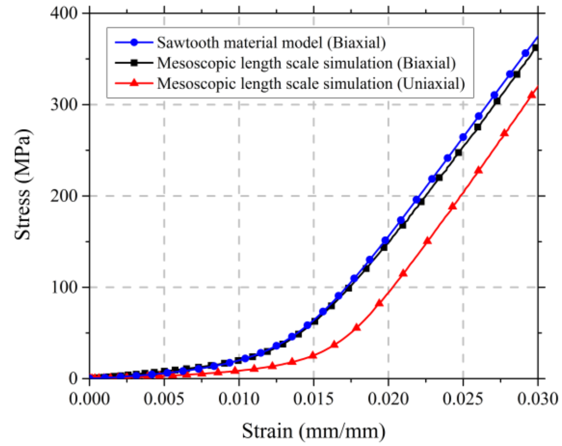

(b)

Figure 5.7 Comparison of SMM biaxial mechanical response to unit cell mesoscopic simulations: (a) Compressive spring parameters determined from contact forces (Method #1), and (b) Compressive spring parameters determined from fabric response (Method #2).

The SMM's shear response of the woven fabric is implemented with a rotational nonlinear spring in a similar manner to PMM by using Eq. 4.9. Hence, the method adopted to determine the PMM's shear spring parameters is also used for the SMM's shear spring. The unit torque/moment obtained from mesoscopic unit cell simulations is used to determine shear spring parameters (C_1 and C_2) by minimizing the RMSE between Eq. 4.9 and mesoscopic unit torque/moment (Figure 5.3). Table 5.4 shows the material properties/parameters of the SMM determined from mesoscopic unit cell simulations outlined in Figure 5.4. It should be noted the values presented in Table 5.4 are different than the values presented in Table 4.5. Experiments were used to determine the values in Table 4.5 values while the current chapter adopted mesoscopic length scale unit cell simulations to determine these values.

Table 5.4 SMM material properties/parameters determined from mesoscopic unit cell simulations.

Response type	Parameter	Weft direction	Warp direction
Uniaxial tensile	E_i (MPa)	79000	69000
	k_i^b (Nmm/rad)	1.1	1.2
Biaxial	a (N)	0.02	
	b (mm)	0.7	
Shear	C_1 (Nmm)	0.0041	
	C_2 (rad^{-1})	6.31	

5.3 Verification of the PMM, SMM and Mesoscopic Length Scale Simulations

To establish a link between meso and macro length scales, the inputs required by the macroscopic material models are obtained from mesoscopic unit cell level simulations under uniaxial, biaxial and shear loads based on the approach developed in the previous section. To further verify the approaches developed and determine the limitations of the modeling approaches, several large scale simulations are carried out with the PMM, the SMM and mesoscopic length scale numerical models. These simulations include uniaxial, biaxial, bias extension and indentations tests. For this purpose, the values presented in Tables 5.2 and 5.4 are used for the PMM and the SMM in the simulations, respectively.

First, uniaxial tensile tests are simulated with the developed numerical models. For all modeling approaches, the fabric model had a length of 101.6 mm and a width of 25.4 mm. Figure 5.8 shows the comparison of the mechanical response obtained from the models. It can be seen that all numerical models are capable of reproducing the bilinear mechanical response observed in woven fabrics.

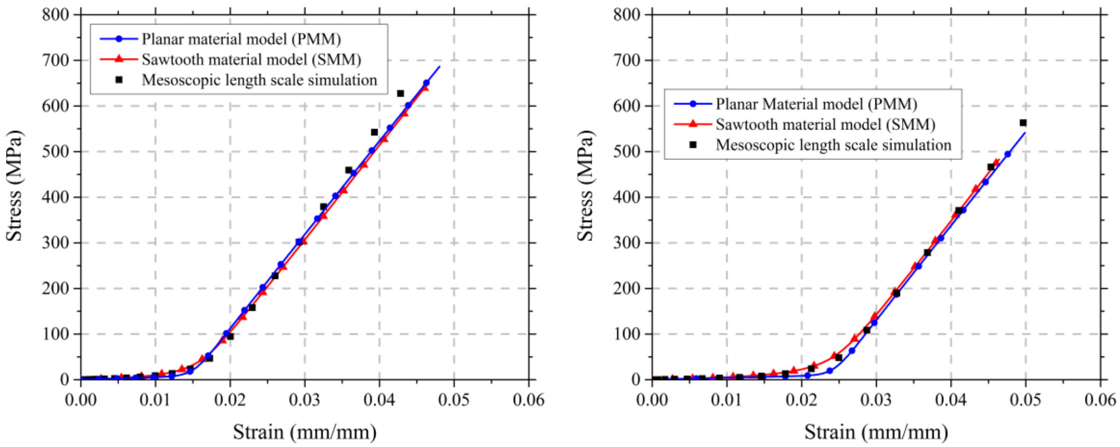

(a) (b)

Figure 5.8 Comparison of uniaxial tensile test simulations: (a) Weft direction, (b) Warp direction.

Even though all of the numerical models are able to capture mechanical response under uniaxial loading, the PMM can't generate certain deformation kinematics due to limiting assumptions made to define the constitutive relations. One of these deformation kinematics is the crimp interchange resulting in the width change of fabric under uniaxial loading. Figure 5.9a shows the transverse displacement of the numerical models at 3% longitudinal strain. Since the yarns are explicitly modeled in mesoscopic length scale models, the mesoscopic numerical model can capture the transverse displacement of the fabric specimen. The SMM is also able to capture this deformation kinematic since the yarn-to-yarn interactions are implemented through the compression spring at the crossover point. Hence, both SMM and mesoscopic model can reduce the specimen width while PMM cannot as shown in Figure 5.9a. Moreover, SMM and mesoscopic model are able to simulate Poisson's effects since they can capture the yarn crimp interchange deformation mechanism. Figures 5.9b and 5.9c show the Poisson's ratio change with the applied strain for the SMM and mesoscopic length scale numerical model respectively.

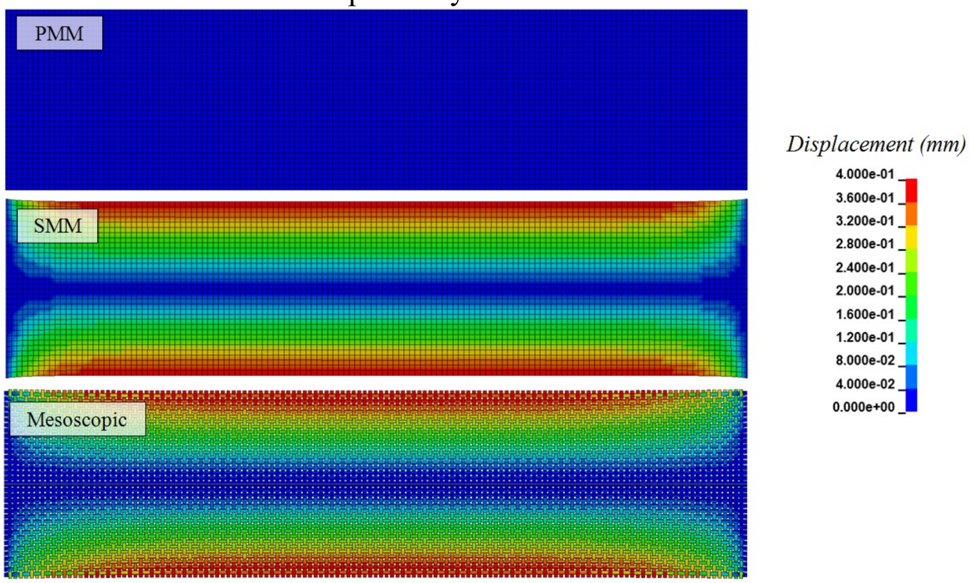

(a)

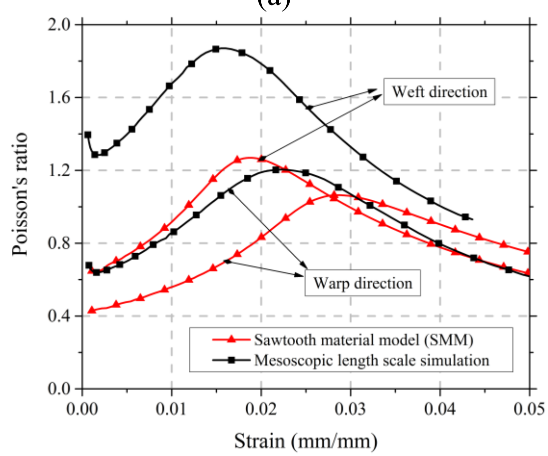

(b)

Figure 5.9 Woven fabric deformation kinematics under uniaxial tensile loads with the developed material models: (a) Transverse displacement at 3% strain, (b) Poisson's ratio change comparison for the SMM and mesoscopic length scale simulations.

Both models can capture the nonlinear behavior of Poisson's ratio. However, the values of the Poisson's ratios attained in the SMM simulations are fairly lower than the mesoscopic numerical model simulations. The difference can be attributed to the assumptions made in the SMM. The SMM is based on the sawtooth geometry and the yarns' interaction with each other in the transverse direction is simplified with a compressive spring. However, the yarn-to-yarn interactions are 3D and fairly complex.

Bias extension tests are also simulated with the developed numerical models. The simulated specimens had a length of 101.6 mm and a width of 25.4 mm similar to the uniaxial tensile test simulations. One of the short edges was clamped while a displacement boundary condition (~25 mm) was applied to the other end. Figure 5.10 shows the simulation results obtained from the numerical models developed. It can be seen that both macroscopic material models exhibit a stiffer response compared to the mesoscopic length scale simulations. Mesoscopic length scale simulations are able to capture the inherent yarn slippage deformation observed during bias extension tests since the yarn is explicitly modeled. On the other hand, both macroscopic material models assume the yarns are pin-jointed so that the yarn slippage is not possible. Hence, stiffer responses are observed in macroscopic simulations compared to the mesoscopic ones.

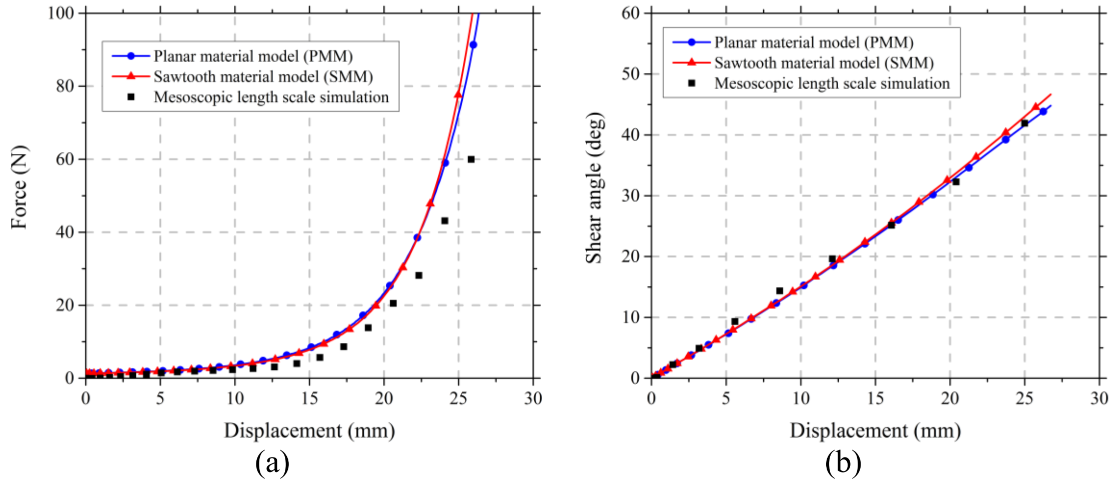

Figure 5.10 Bias extension test simulations: (a) Force - displacement, and (b) Shear angle - displacement,

Furthermore, the deformation kinematics of the numerical models developed during bias extension are also compared. Figure 5.11 shows the overall shape of simulated deformed specimens for all of the numerical models at 20 mm crosshead displacement. It can be seen that all numerical models were able to capture the three distinct deformation regions. However, the macroscopic material models were not able to capture the yarn raveling observed at the clamped edges.

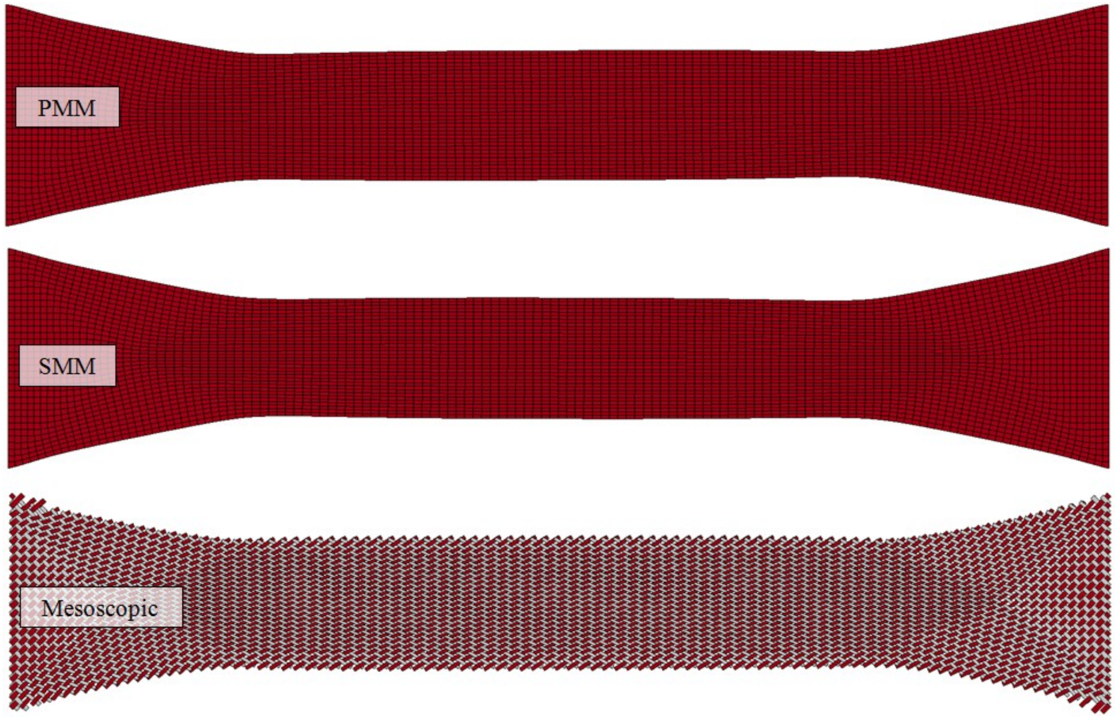

Figure 5.11 Bias extension test simulation deformation patterns at 20 mm crosshead displacement.

The numerical models' ability to capture the biaxial nature of woven fabrics is also investigated by simulating the biaxial tensile tests. Both the PMM and the SMM were simulated with the biaxial tensile test setup shown in Figure 4.33a. The mechanical responses of the macroscopic material models were verified with the mesoscopic unit cell simulations under biaxial loading. Since the mesoscopic unit cell can capture the overall fabric response, the verification of the macroscopic material models with unit cell models was carried out with only unit cell simulations.

Figure 5.12a shows the comparison of the mechanical responses obtained from the numerical models developed in the current work. Since the PMM assumes that the yarns tensile behavior is only uniaxial, the PMM mechanical response is the same with the uniaxial tensile response. On the other hand, the SMM is able to capture the biaxial mechanical response through the compressive spring replicating the interactions between the yarns. Moreover, the mesoscopic simulations are able to capture the biaxial nature without any special formulations since the yarns are explicitly modeled and their interactions are determined through the contact defined between them. Figure 5.12b shows the comparison of the von Mises Stress distributions of the PMM and the SMM simulations. It can be seen that the stress levels are higher in SMM compared to the PMM. This difference can again be attributed to the limiting assumptions made in the tensile behavior of the PMM.

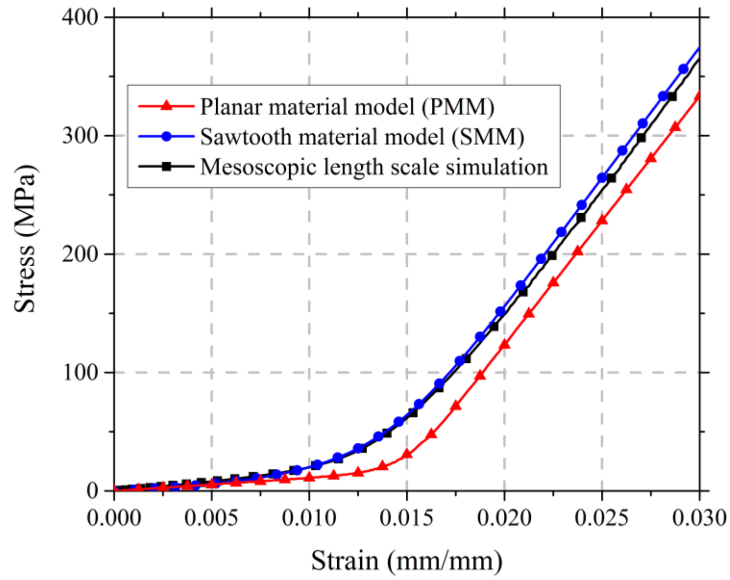

(a)

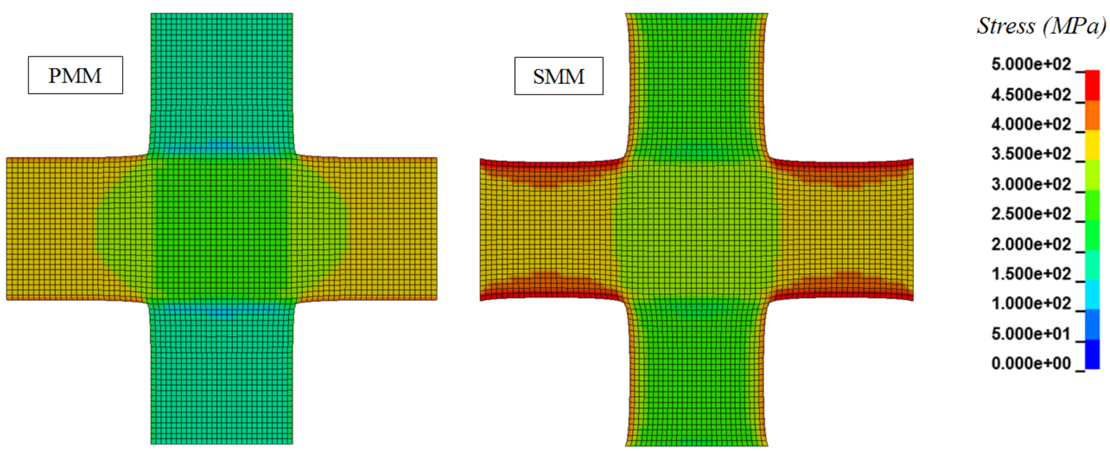

(b)

Figure 5.12 Comparison of numerical model mechanical responses under biaxial loading: (a) Stress-strain curves, and (b) von Mises Stress distribution comparison of the PMM and SMM simulations.

Further verification studies are carried out with indentation tests with different yarn orientation angles (Figure 4.11). Similar to the previous simulations presented in Chapters 3 and 4, 0° and 90° yarn orientation fabric models had dimensions of 51 mm x 40 mm with an indenter of 12 mm diameter. The short edges were clamped by constraining the translational DOFs while the longer edges were free to move for all of the numerical simulations. Figure 5.13 shows the force responses obtained from the numerical models. It can be seen that all force responses obtained from the numerical models are similar to each other and the models are able to capture nonlinear mechanical response. Since only one yarn direction is clamped in the numerical models, the biaxial effects are not significant in the simulations. Hence, all of the numerical models can capture the mechanical response.

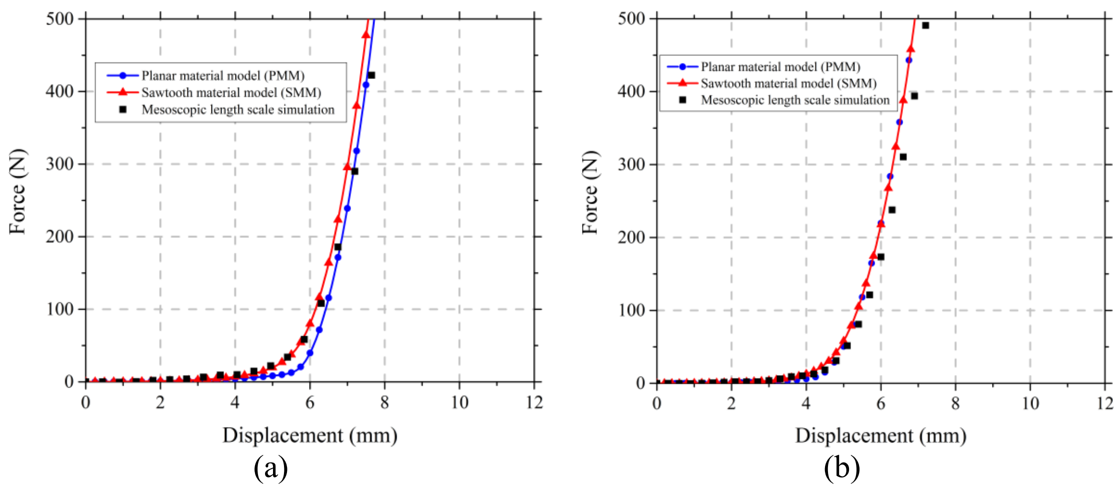

Figure 5.13 Comparison of indentation test simulations: (a) 0^o direction clamped, and (b) 90^o direction clamped.

Figure 5.14 shows the fabric deformation at 6 mm indenter displacement for 0^o and 90^o yarn orientations. The fabric deformation patterns are similar to each other for all the numerical models. The patterns exhibit an elliptical shape due to the rectangular fabric shape used in the simulations.

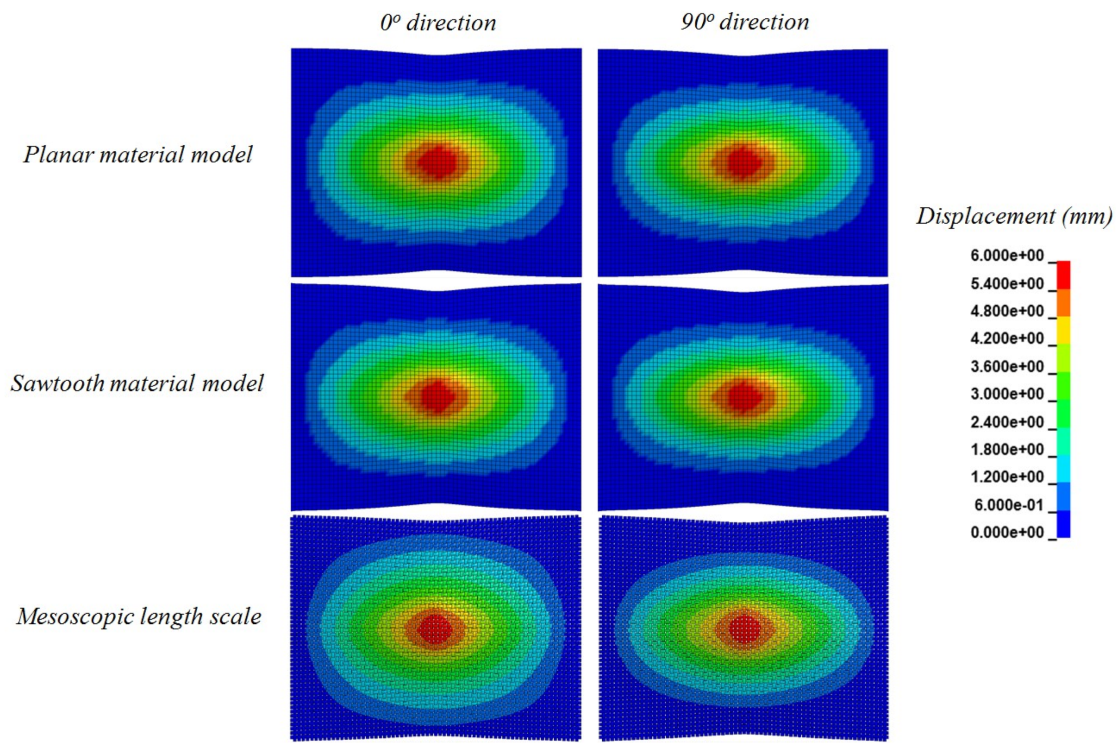

Figure 5.14 Comparison of woven fabric deformation at 6 mm indenter displacement.

Moreover, the stress distributions of the numerical models at 6 mm indenter displacement are shown in Figure 5.15 for comparison purposes. It can be seen that the yarns that are clamped at both ends and underneath the indenter are stretched more compared to the other yarns for all the numerical models used. These yarns undergo decrimping deformation mechanism due to the interactions between the fabric and indenter and the applied boundary conditions at the clamped ends. Therefore, localized stresses are observed along the longer side of the fabric. It should be noted that the legends showing the stress distributions in Figure 5.15 are different. This difference is due to the length scale modeled in the simulations. In the mesoscopic length scale models, the yarn level stresses can be extracted from the simulations. On the other hand, the stresses shown in Figure 5.15 for the macroscopic models are based on the repeating unit cell rather than individual yarns. These stresses include yarn tension as well as the shear resistance of the unit cell.

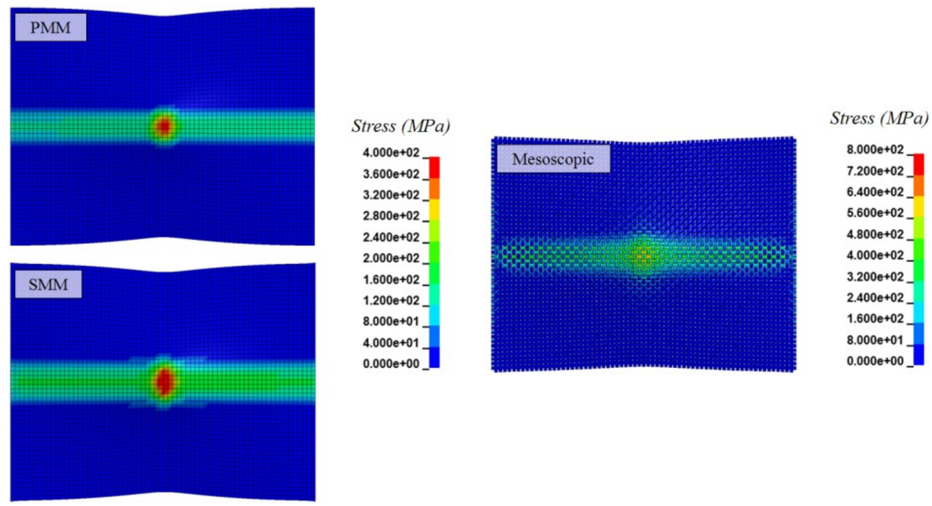

(a)

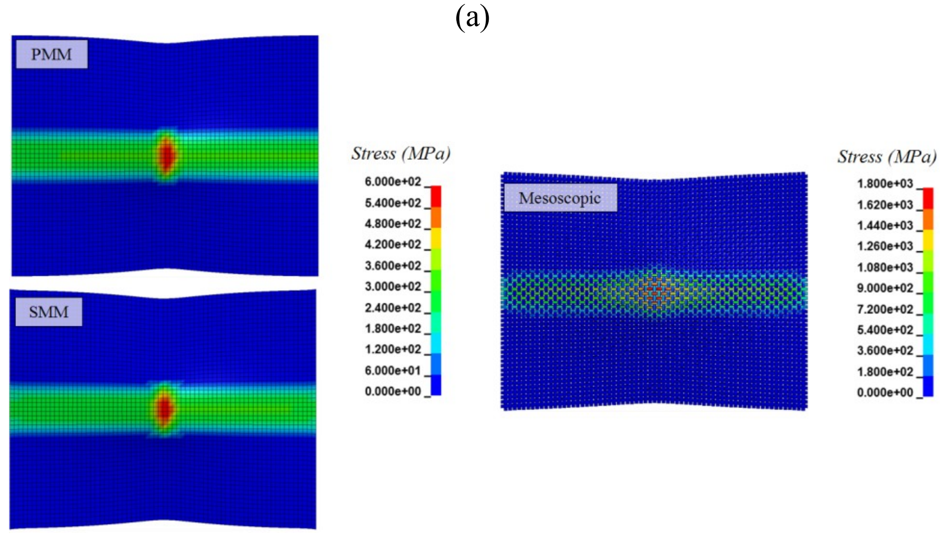

(b)

Figure 5.15 Stress distribution at 6 mm indenter displacement: (a) 0^{o} direction clamped, and (b) 90^{o} direction clamped.

Another indentation test simulation is carried out where the yarns are oriented at ±45^{o} with respect to the clamped edges to verify the numerical models. The simulation setup is shown in Figure 3.17a. In these simulations the fabric numerical models had dimensions of 51 mm x 25 mm with a 12 mm diameter indenter where both short edges were clamped. Figure 5.16 shows the comparison of the force response obtained from the mesoscopic and macroscopic material models. It can be seen that all numerical models exhibit similar force responses with a highly nonlinear profile.

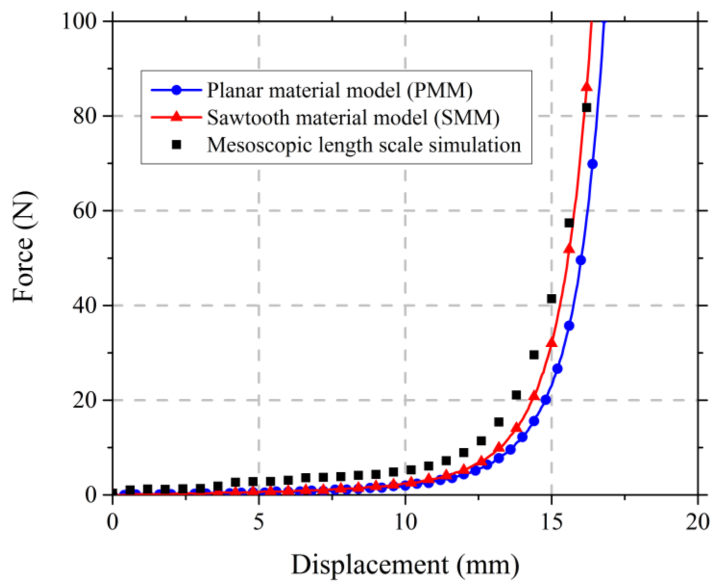

Figure 5.16 Mechanical response observed during ±45^{o} indentation.

The deformation of the fabric with this specific configuration under indentation load is also compared to verify the simulations. Figure 5.17 shows the comparison of the transverse displacement of the fabric models at 16 mm indenter displacement. It can be seen that the deformation patterns for all numerical models exhibit distinct regions similar to each other with the largest transverse deformation observed where the indenter contacts with the fabric.

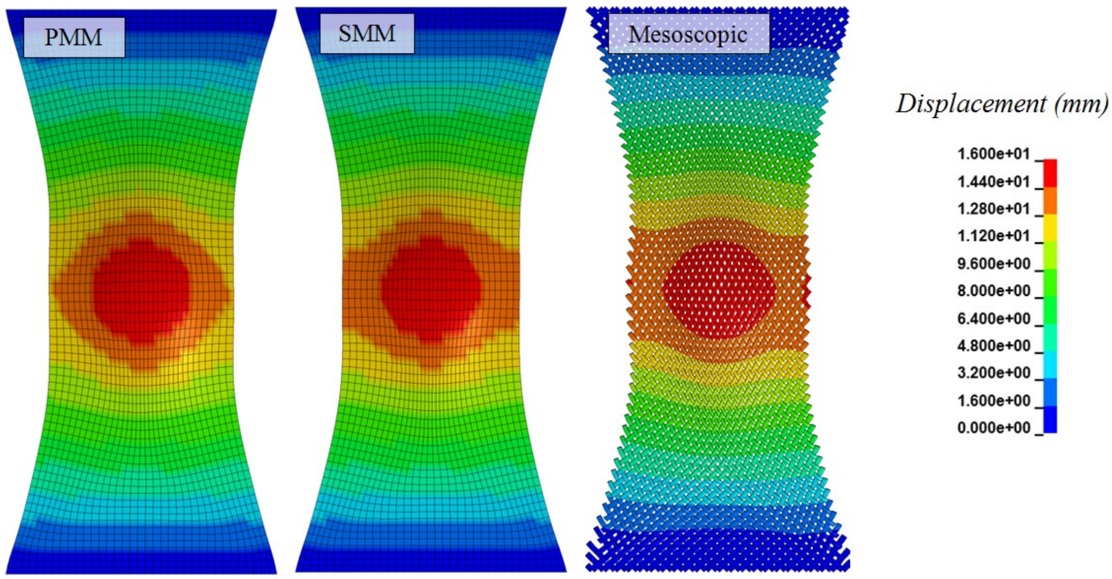

Figure 5.17 Comparison of woven fabric deformation for ±45^{o} indentation case at 16 mm indenter displacement.

Figure 5.18 shows the von Mises stress distributions across the fabric models at 16 mm indenter displacement. Different stress scales were used for both macroscopic and mesoscopic simulations due to the different length scales modeled. The stress levels shown in macroscopic length scale simulations include the tensile deformation of the yarns as well as the shear deformation. On the other hand, the stresses shown for mesoscopic model are based on the localized yarn deformation. Therefore, two different stress scales were used to compare the models. It can be seen that the highest stresses are observed at indenter contact locations and the boundary yarns which are subjected to tensile loading. The shape of the stressed areas are different between the macroscopic and mesoscopic simulations. The macroscopic models exhibit an elliptical shape while the mesoscopic simulation has a circular stress distribution where the indenter contacts the fabric. This difference can be attributed to the difference between the contact mechanics that can be modeled at different length scale. Since the contact of the yarns with each other and with the indenter can be modeled explicitly in mesoscopic simulations, the stress distribution profiles can be simulated more accurately compared to the macroscopic material models.

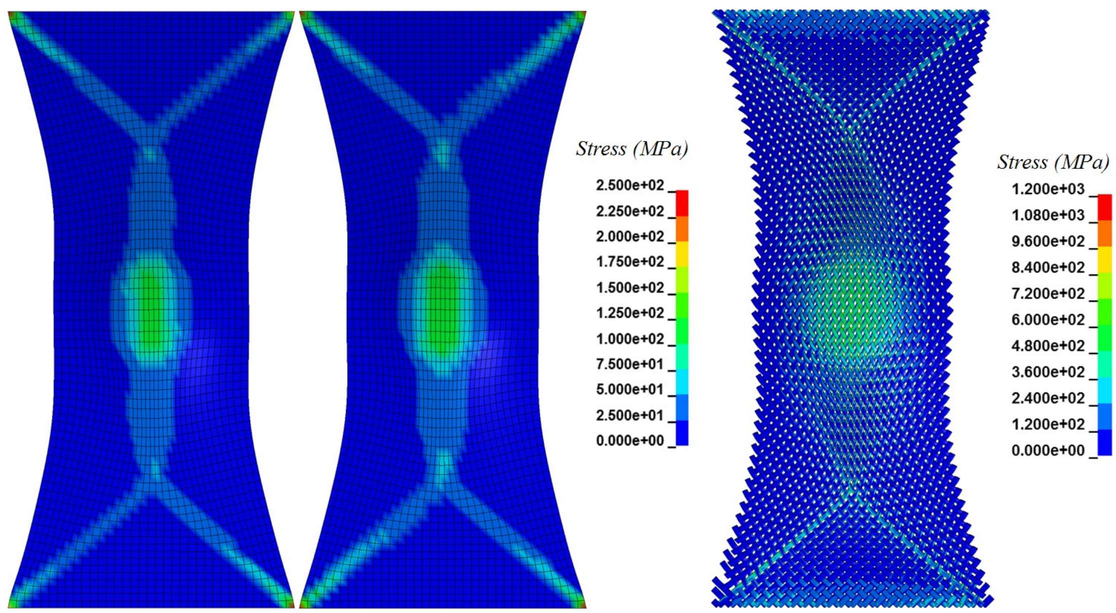

Figure 5.18 Stress distribution for ±45^{o} indentation case at 16 mm indenter displacement.

The developed numerical models are also compared with an indentation test where all 4 edges are clamped. A 50 mm x 50 mm fabric is modeled with the material models developed. The indentation loading is imposed on the fabric with a 12 mm diameter indenter. All 4 edges are clamped by constraining the translational DOFs of the nodes located at the fabric boundaries. Figure 5.19 shows the comparison of the mechanical responses obtained from the numerical models developed. It can be seen that the force response of PMM is more compliant compared to the SMM and mesoscopic length scale's responses. Since all of the 4 edges are clamped, both yarn directions underneath the indenter are subjected tensile loads. These yarn interact with each other in the transverse direction and stiffen the mechanical response due to the biaxial nature of the woven fabrics. Hence, the SMM and mesoscopic length scale simulations exhibit a stiffer mechanical response compared to the PMM. The yarns are explicitly modeled in the mesoscopic length scale and the biaxial effects are included directly in the woven fabric response. On the other hand, constitutive relations are defined (compressive spring) in the SMM to implement the biaxial response of the woven fabric. However, the yarns tensile behavior is assumed to be uniaxial in the PMM where biaxial effects are not considered.

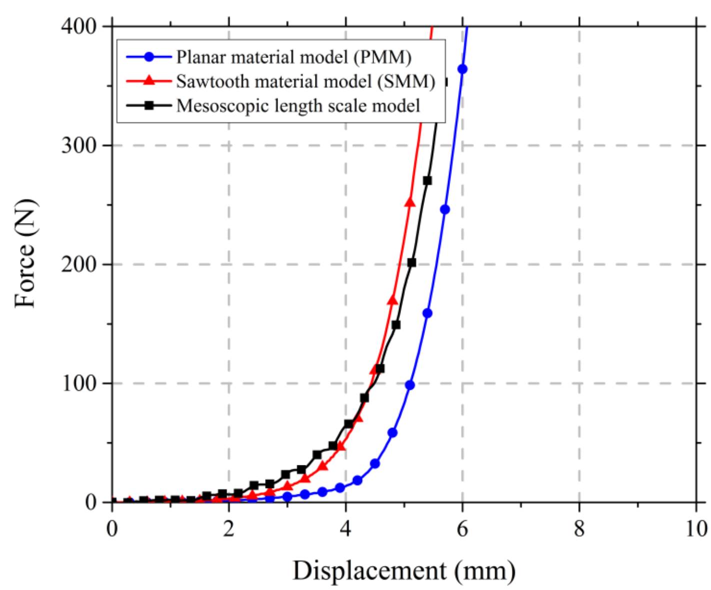

Figure 5.19 Comparison of force-displacement results for 50 mm x 50 mm fabric with 4 edges clamped.

Figure 5.20 shows the deformation patterns at 6 mm indenter displacement. All of the numerical models used exhibit similar deformation patterns. The highest displacements are observed where the indenter contacts the fabric. The transverse displacement of the fabric models reduces towards to the clamped edges by showing stages shaped as a 2D diamond.

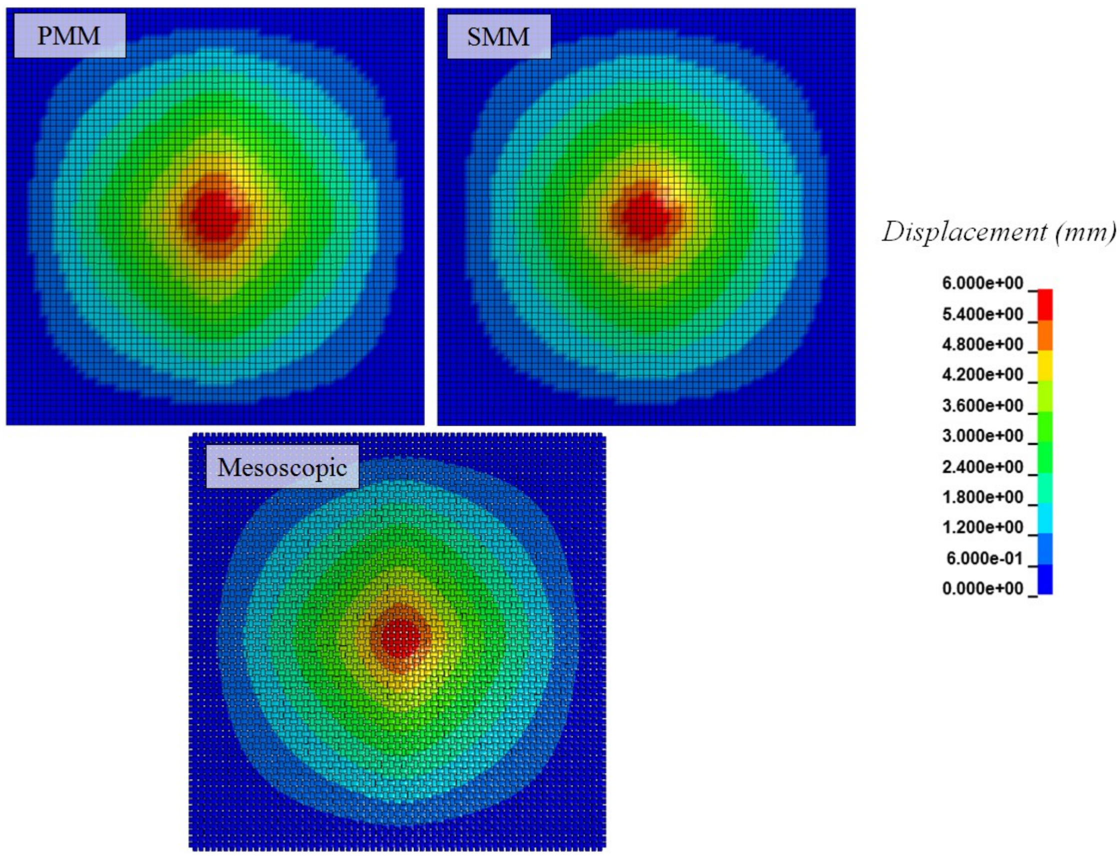

Figure 5.20 Indentation of 50 mm x 50 mm fabric with 4 edges clamped: Transverse displacement contours at 6 mm crosshead displacement.

Figure 5.21 shows the comparison of the von Mises stress distributions across the fabric numerical models. It can be seen that both yarn directions are subjected to axial loads due to the indenter for all the numerical models. This loading results in stresses along both yarn directions since all of the edges are clamped. Since the biaxial nature of the woven fabrics is implemented in both the SMM and mesoscopic length scale numerical models higher stresses are observed compared to the PMM. It should be noted that the stresses shown in Figure 5.21 for the macroscopic length scale models are different than the mesoscopic length scale similar to the previous simulation cases. The stresses shown for mesoscopic length scale simulations are based on the individual yarns while the stress levels shown for macroscopic numerical models are based on the unit cell modeled which includes yarns' tensile response as well as the shear deformation of the unit cell.

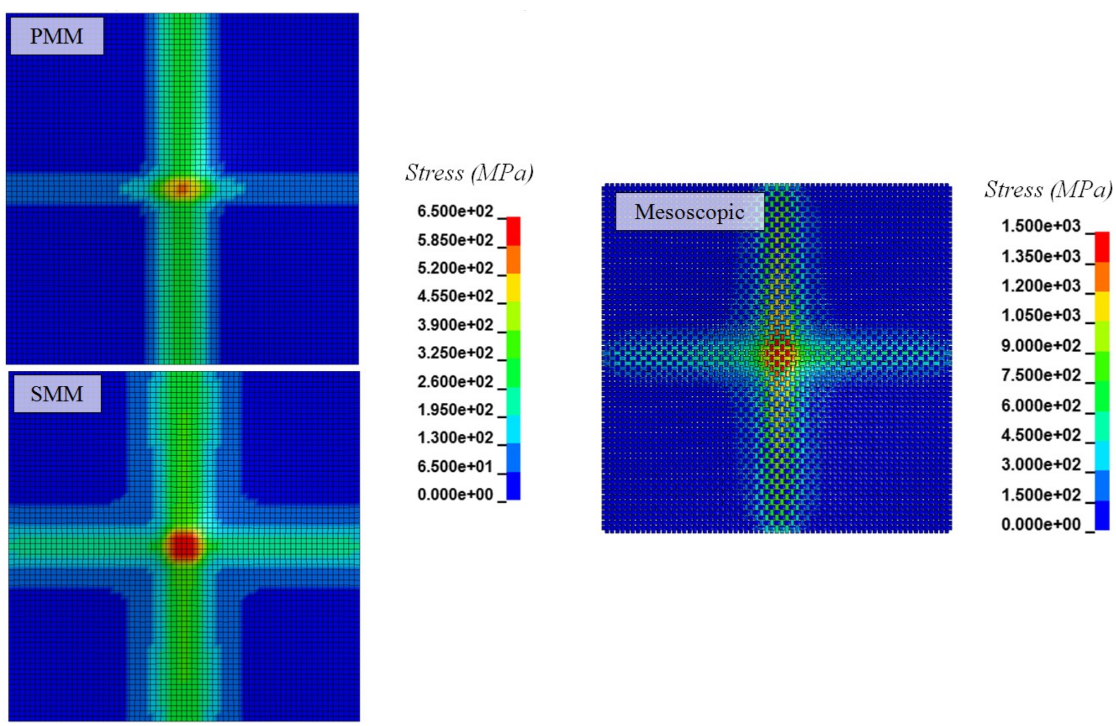

Figure 5.21 Indentation of 50 mm x 50 mm fabric with 4 edges clamped: Stress distribution at 6 mm crosshead displacement.

5.4 Comparison of PMM, SMM and Mesoscopic Length Scale Simulations

Numerical models developed in the current work can capture different deformation mechanisms and associated nonlinear mechanical response based on the length scale used and the constitutive relations used. The capabilities of the developed numerical models in terms of modeling the mechanical responses are compared in Table 5.5. The comparison presented is based on the simulations carried out under various loading conditions. The macroscopic and mesoscopic material models developed are able to reproduce the uniaxial and shear responses. However, the PMM cannot capture the biaxial response due to assumptions made in yarns' tensile behavior.

Table 5.5 Comparison of the numerical model capabilities in terms of generating certain mechanical responses and number of inputs requires

	Model		
Mechanical response	**PMM**	**SMM**	**Mesoscopic**
Uniaxial	Yes	Yes	Yes
Biaxial	No	Yes	Yes
Shear	Yes	Yes	Yes
# of inputs	15	14	10

Table 5.6 compares the numerical models developed based on their ability to reproduce the deformation kinematics under uniaxial, biaxial and shear loads. Since the yarns are explicitly modeled and the fibrous nature of the yarns is taken into account in the mesoscopic length scale models, this modeling approach can model various deformations under different loading conditions. The mesoscopic numerical models are able to capture the yarn decrimping, crimp interchange and yarn transverse compression under uniaxial and biaxial tensile loads. Yarn rotations, compaction, locking and slippage deformations under shear loads can be modeled directly. For

example, the yarn raveling at the fabric edges for bias extensions tests can be captured as shown in Figure 5.11 with the mesoscopic length scale models.

Table 5.6 Comparison of the numerical models developed in the current work in terms of their capability of modeling deformation mechanisms involved in woven fabrics.

Loading	Deformation mechanism	PMM	SMM	Mesoscopic
Uniaxial	Yarn decrimping	No	Yes	Yes
	Crimp interchange	No	Yes	Yes
Biaxial	Yarn transverse compression	No	Yes	Yes
Shear	Relative yarn rotation	Yes	Yes	Yes
	Yarn locking	No	No	Yes
	Yarn compaction	No	No	Yes
	Yarn slippage	No	No	Yes

On the other hand, the assumptions made in the macroscopic material models to simplify the fabric behavior do not allow modeling of certain deformations that result in nonlinear mechanical behavior. Even though the PMM can generate the mechanical response under uniaxial loading, it cannot model the deformation kinematics observed such as yarn decrimping and crimp interchange. The mechanical response under biaxial loading cannot be modeled with the PMM since the fabric's tensile response is assumed to be only uniaxial. The model's inability to capture the biaxial mechanical response is demonstrated with both biaxial tensile tests and indentation simulations where 4 edges were clamped (Figures 5.12 and 5.19) The model tends to underestimate the stresses and deformations in certain applications where biaxial loading is significant and care should be taken with the model. The nonlinear shear response of the PMM is implemented with a nonlinear rotational spring. It is assumed that the yarns are pin-jointed at the crossover point and relative yarn rotations are determined using continuum mechanics. Since the shear behavior is simplified with the nonlinear shear spring, certain deformations cannot be modeled such as yarn locking and compaction even though the mechanical response can be reproduced. Moreover, yarn slippage cannot be modeled with the PMM due to the assumption of pin-jointed yarns.

The SMM can model both the mechanical response and deformation mechanisms observed under uniaxial tensile loads. This is achieved with the sawtooth geometry and compressive spring defining the interactions of the yarns with each other. Since the yarns can interact with each other based on the sawtooth geometry, the yarn decrimping and crimp interchange deformation mechanisms can be modeled using the SMM (Figures 5.9). The compressive spring defined in the SMM also allows modeling of biaxial mechanical response (Figure 5.12). The shear response is implemented in a similar manner to PMM with a rotational spring located at the crossover point. Hence, the material model can model the shear mechanical response as well as the relative yarn rotations. However, it's not capable of modeling yarn locking, compaction and slippage.

Each numerical model developed in this work is capable of modeling certain mechanics of woven fabrics. Mesoscopic length scale models are capable of modeling most of the deformation mechanisms involved compared to macroscopic models. On the other hand, macroscopic length scale material models can capture a limited amount of deformation mechanisms and mechanical responses based on the assumptions made. It should be noted that the PMM only requires uniaxial tensile and shear experiments/simulations to determine the necessary material properties/parameters. The SMM requires additional experiments/simulations to obtain the material properties/parameters for the biaxial response.

Macroscopic models are more computationally efficient compared to the mesoscopic length scale models since membrane/shell elements are used to model the fabrics (Table 5.7). On the other hand, computationally expensive solid elements are used to model individual yarns in the mesoscopic numerical models. This makes modeling of woven fabrics computationally prohibitive with mesoscopic numerical models. Table 5.7 also compares the number of calculations carried out within the user-defined-material subroutine at a given time step for a single element. The PMM has the lowest number of computations followed by mesoscopic model. The SMM has the highest number of computations. However, this number can increase based on the convergence of the numerical minimization algorithm adopted to determine the unit cell configuration at a given deformation state.

Table 5.7 Comparison of numerical models in terms of elements and number of computations per time step.

Model	Element type	# of calculation/time step
PMM	Shell	66
SMM	Shell	<109
Mesoscopic	Solid	73

Table 5.8 shows the number of elements used with each numerical model used for various simulations carried out. Since the same mesh densities were used for both the PMM and the SMM, they have the same number of shell elements. It can be seen that there is a large difference between the number of elements used for macroscopic and mesoscopic length scale models. This is mainly due to the complexity involved in mesoscopic numerical models where all the yarns within the fabric are modeled individually.

Table 5.8 Number of elements used in each simulation with the material models developed.

	Number of elements				
Model	**Uniaxial**	**Bias**	**0 deg**	**45 deg**	**4 EC**
PMM & SMM	4624	4624	3904	2882	5134
Mesoscopic	1.33×10^6	1.45×10^6	1.06×10^6	0.72×10^6	1.09×10^6

Figure 5.22 shows the comparison of normalized simulation times for various loading cases. It can be seen that mesoscopic length scale simulations had the highest run times compared to the macroscopic material models for all the loading cases studied. This can be attributed to the large number of solid elements used to model all the yarns individually. Both macroscopic material models have shorter simulation times compared to the mesoscopic simulations. Moreover, the PMM simulations are faster than the SMM simulations. It should be noted that the mesh densities for all the simulations carried out with the PMM and the SMM had the same mesh densities. The number of computations required by the PMM and the SMM at each time step are also shown in Table 5.7. The SMM can model the biaxial mechanical response because of the unit cell geometry adopted. However, this mechanical response requires additional computations every time step to determine the unit cell configuration using the minimization algorithm. As a result, the SMM simulations require longer simulation times compared to the PMM simulations as shown in Figure 5.22.

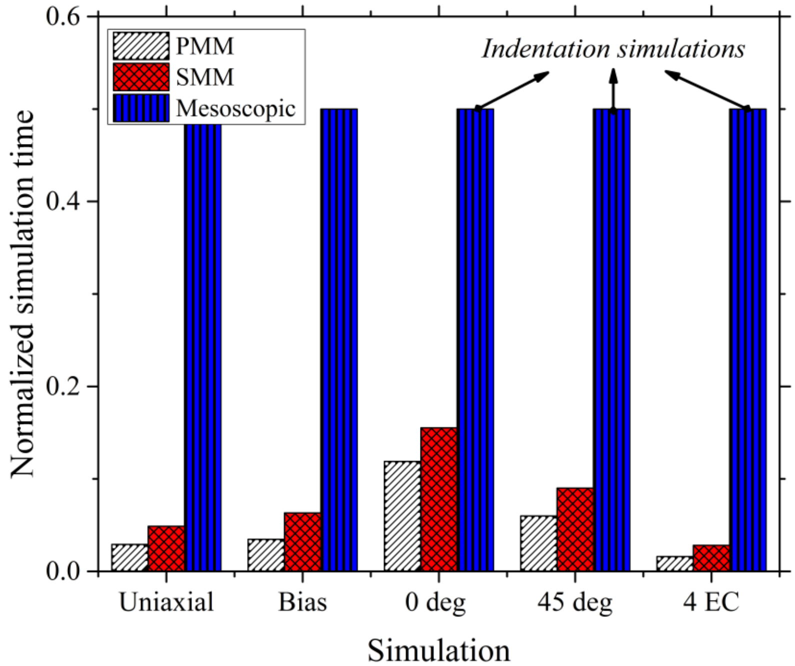

Figure 5.22 Comparison of normalized simulation times for the numerical models studied (Mesoscopic length scale normalize simulation times are scaled by 0.5 for visibility).

Figure 5.23 shows the percent CPU utilizations for the numerical models under uniaxial tensile loading. The element processing had the highest percentage of CPU utilization for all of the numerical models. Mesoscopic numerical models also requires a contact definition to define the yarns' contact and their interaction. This results in additional computational expenses as well as longer simulation times.

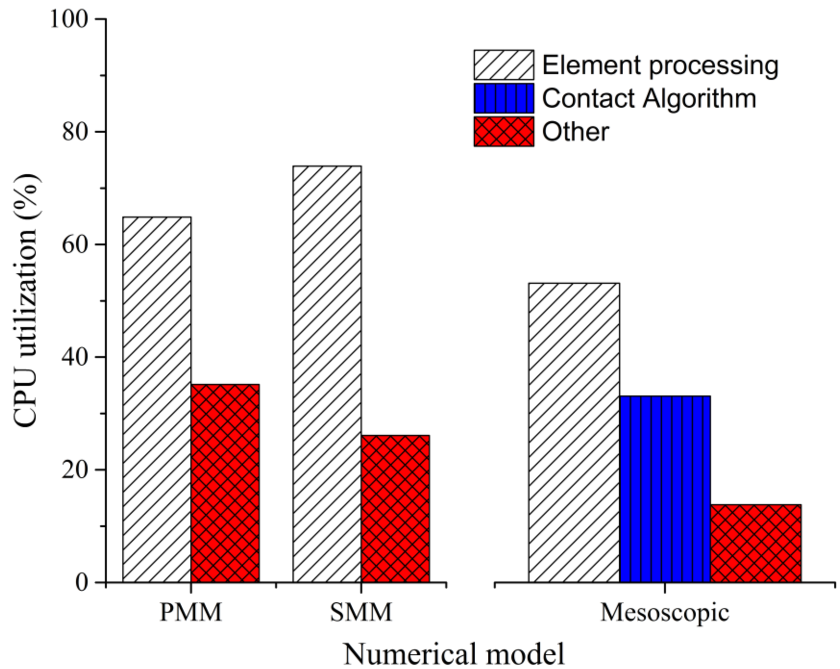

Figure 5.23 Comparison of percent CPU utilizations for the numerical models studied.

5.5 Summary and Contributions

In the current work, the macroscopic material models developed are based on mesoscopic unit cell of woven fabrics. The nonlinear mechanical response involved in these models are implemented with mesoscopic level components such as trusses and springs using constitutive relations. The mechanical response and deformation of these components were determined from experiments in Chapter 4. The current chapter focuses on developing novel method to determine the material properties/parameters required by these macroscopic material models using mesoscopic length scale simulations rather than using experimental results. For this purpose, two different approaches are developed for each macroscopic material model. For both material models, the properties/parameters are obtained from mesoscopic unit cell numerical models that are subjected to uniaxial, biaxial and shear loads. Then, both macroscopic material models are verified by simulating several tests and comparing the results to the mesoscopic length scale simulations. The simulated tests included uniaxial tensile, biaxial, bias extension and indentation tests. Another contribution of the current chapter is the identification of the developed material model capabilities in terms of simulating different mechanical responses as well as deformation mechanisms. The models are also compared in terms of the computational resources required to run the models. It is shown that mesoscopic length scale models are capable of simulating most of the loading conditions accurately in the expense of computational resources. The PMM is also able to capture certain mechanical responses under uniaxial and shear loads. However, it cannot capture the deformation kinematics under uniaxial loading and biaxial mechanical response due to the assumptions made during the development of the material model. The SMM is capable of uniaxial, biaxial and shear responses as well as the deformation mechanisms involved expect yarn slippage. However, it requires longer simulation times compared to the PMM due to the minimization algorithm adopted to determine the unit cell configuration. Both macroscopic material models are more computationally efficient compared to the mesoscopic length scale modeling since shell elements are used to model woven fabrics. However, it should be noted that the SMM requires additional material properties/parameters and processes to determine the biaxial response while requiring additional computational resources (simulation time). Therefore, the selection of macroscopic material model can be based on the application in which the PMM can be adopted as a preliminary design/analysis tool while the SMM can be used to obtain more accurate results if desired.

Chapter 6

CONCLUSIONS, UNIQUE CONTRIBUTIONS AND FUTURE WORK

6.1 Conclusions

Woven fabrics have been used in various engineering application including personal protective systems, airbags, functional rehabilitation garments, medical scaffolds and as reinforcements in composite materials. Their complex multiscale construction provides certain advantages over conventional material for these applications which require specific directional material properties, mechanical responses and flexibility. Because of their complex nature, the integration of woven materials in engineering systems requires accurate and computationally efficient modeling tools coupled with experiments to simulate the behavior of woven fabrics within the system designed. The current work focused on developing an experimentally validated systematic numerical modeling framework considering mesoscopic and macroscopic length scales.

6.1.1 Mesoscopic length scale modeling approach

A mesoscopic numerical modeling approach was developed to capture the yarn level deformation mechanisms and associated nonlinear mechanical response of woven fabrics. A hyperelastic transversely isotropic yarn material model with transverse material nonlinearity was developed. The material properties/parameters were obtained from experiments through an inverse method. Then, the material model developed was validated by simulating the uniaxial, bias extension and indentation test experiments. The material model was able to capture the nonlinear mechanical response of the experiments and the yarn level deformation mechanisms. Furthermore, mesoscopic unit cell finite element modeling was coupled with the Taguchi method to investigate the relative effects of yarn material properties on the macroscale response of woven fabrics under uniaxial, biaxial and shear loads. Architectural design effects were also studied with 4 different weaves: (1) Plain, (2) Twill, (3) Basket, and (4) Satin weave. The results of the study revealed that the yarn longitudinal and transverse shear modulus play an important role on fabric modulus before and after decrimping as well as fabric's Poisson's ratio under uniaxial loading. It was also shown that yarn longitudinal, transverse modulus and transverse shear modulus have positive influence woven fabrics' resistance to biaxial deformation. Moreover, it is shown that coefficient of friction, yarn transverse and transverse shear moduli have significant influence on the shear resistance.

6.1.2 Macroscopic length scale modeling approach

To simulate woven fabrics using macroscopic models, two new models with different mechanical response capabilities were developed in the current work. Both material models are based on mesoscopic unit cell of woven fabrics. The first material model developed (PMM) assumes the yarns lie on the same plane while the second one (SMM) adopts the 3D sawtooth geometry. The PMM only considers the uniaxial and shear response while the SMM includes uniaxial, shear and biaxial mechanical responses. Continuum mechanics was adopted to implement the non-orthogonal nature of woven fabrics. The material properties/parameters required by the models were determined directly from standard experiments without running any simulations to fit model response. The models were validated under various loading conditions. It was shown that both models are able to capture the experimental mechanical responses. However, it was demonstrated that both models cannot capture the inherent yarn slippage deformation mechanism of bias extension tests. Moreover, both material models were compared to each other to investigate the difference. It was shown that even though both material models could capture mechanical response, modeling certain deformation mechanisms such as Poisson's effects are not possible with the PMM. Moreover, the results of the study also revealed that the localized stresses were higher in the SMM simulations. These difference were attributed to the SMM's capability of simulating biaxial mechanical response.

6.1.3 Link between the mesoscopic and macroscopic length scale models

Finally, a systematic link was proposed between the mesoscopic and macroscopic length scale numerical modeling approaches to develop a robust multiscale design framework for woven fabrics. The material properties/parameters required by the macrscopic material models were obtained using mesoscopic simulations. Then, the material models were validated/verified with experiments and mesoscopic length scale simulations. The material models were compared to each other to determine whether they can model certain mechanical responses. It was shown that mesoscopic numerical models were able to capture most of the deformation mechanisms as well as the mechanical responses observed. On the other hand, PMM was only able to capture uniaxial and shear responses and failed to reproduce biaxial tensile response while the SMM was able to capture all these mechanical responses. The models were also compared in terms of computational efficiency. It was shown that macroscopic material models can be adopted to simulate woven fabrics within certain accuracy limits and computational efficiency based on the requirements of the application.

6.2 Unique contributions

Some of the key contributions of this dissertation work are presented below.

- A new transversely isotropic yarn material model with transverse material nonlinearity was developed as a user-defined-material model. An exponential form for the transverse nonlinearity was adopted to avoid possible oscillatory behavior in the material response due to the commonly adopted polynomial functions. Moreover, a hyperelastic formulation, where Green strains are related to 2nd Piola-Kirchoff stresses (different than the available models which are based on hypoelastic/hyperelastic), was coupled with the material model to determine the stress state at a given deformation and handle large displacements and rotations.
- A novel method combining unit cell finite element modeling and design-of-experiments method was developed to investigate the relative effects of yarn material properties and weave architecture on the macroscopic length scale response of woven fabrics.
- The effect of yarn transverse shear moduli (G_{12} & G_{31}) on the fabric modulus and Poisson's ratio under uniaxial loading was identified for different weave architectures. It was also shown that the yarn transverse moduli (E_{22} & E_{33}) and transverse shear moduli (G_{12} & G_{31}) significantly affect both tensile and shear responses for the weave types studied.
- Poisson's ratio of different woven fabric architectures are parametrically studied using mesoscopic length scale models for the first time.

- The mechanical response of plain, twill, basket and satin weaves were compared under uniaxial, biaxial and shear loads. It was shown that the crimp amount due to weaving architecture has an influence on mechanical response under uniaxial and biaxial loads and this influence was quantified with the developed method. Moreover, the satin weave was determined to have the least shear resistance while the plain weave has the highest.
- Two macroscopic material models with different mechanical response capabilities based on the plain weave mesoscopic unit cell were developed and implemented within an explicit finite element code. Both material models were experimentally validated. The unique contribution is that the formulations of the developed material models allow material properties/parameters to be directly obtained from either experiments, or mesoscopic length scale simulations without running any simulations.
- An integrated multiscale design framework considering mesosopic and macroscopic length scales was developed for woven fabrics and it was demonstrated for plain weave fabrics. The mesoscopic and macroscopic length scale material models were linked through a systematic approach where the material properties/parameters of macroscopic material models were determined from mesoscopic unit cell simulations. The trade-offs between the material models based on mechanical response, deformation kinematics and computational efficiency were studied under various loading conditions.

6.3 Future work

Future works can be suggested to improve the material models and the multiscale design framework based on the work presented in this dissertation.

It was shown that mesoscopic length scale simulations where the yarns are modeled with solid elements require high computational resources and simulation times to simulate real fabric structures. The computational resource requirements of this length scale might be improved by modeling the yarns as shell elements coupled with a nonlinear yarn material for woven fabrics (Figure 6.1). Comparison of the model's capability to capture woven fabric mechanical response as well as deformation mechanisms to both mesoscopic simulations with solid elements and macroscopic length scale can be beneficial to extend the framework proposed in this research work.

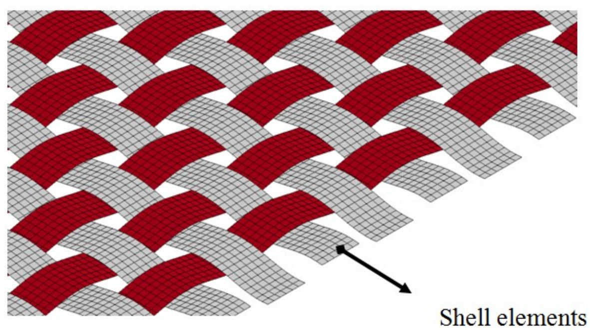

Figure 6.1 Woven fabric modeling with shell elements to improve computational efficiency.

In the current work, the link between the mesoscopic and macroscopic length scale approaches was demonstrated with plain weave fabrics. The work can be extended to include other weave architectures such as twill, basket and satin. A new unit cell definition might be required with additional structural components to develop macroscopic material models. Figure 6.2a shows an example of an unit cell for a basket weave. Moreover, this approach can also be extended to other fabric structures such as knitted fabrics as shown in Figure 6.2b where mesoscopic and macroscopic length scale approaches can be used together to model fabric structures.

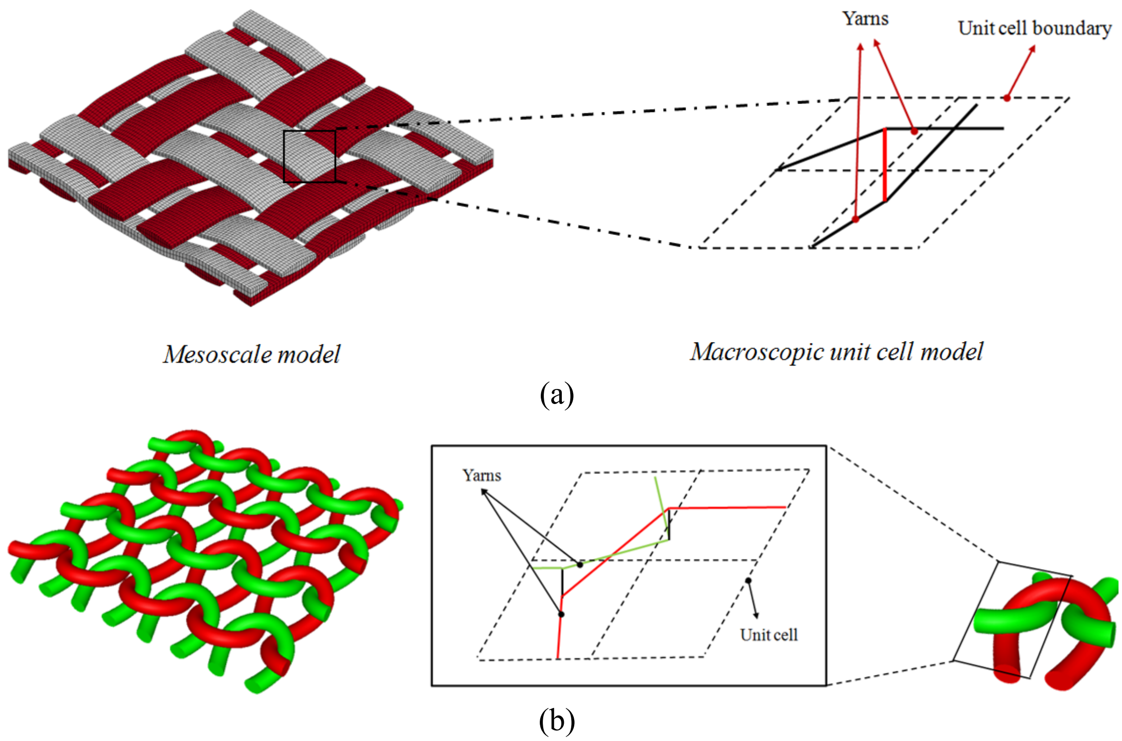

Figure 6.2 Extension of the integrated design framework to other fabric architectures: (a) Basket weave, (b) Knitted fabrics.

Only macroscopic and mesoscopic length scales were considered in this research work. However, the yarns within the woven fabrics are made out of hundreds of filaments. Another length scale is involved in woven fabrics called microscopic length scale because of the filaments and their interaction with each other. Numerical modeling of this length scale allows studying various deformation mechanisms at the filament level that might affect the mesoscopic and/or macroscopic mechanical response of woven fabrics. Hence, integration of microscopic length into the developed design framework can provide additional insight and help aid the design process (Figure 6.3). Addition of the microscopic length scale modeling will require determination of packing of filaments within a yarn as well as filament material properties. Since there are multiple filaments (400 filaments within a K706 yarn), the modeling approach would be limited to single crossover due to the requirement of high computational resources. The yarn material properties/parameters in the mesoscopic modeling can be determined from microscopic length scale simulations while understanding how the filaments/yarns deform in a more detailed way.

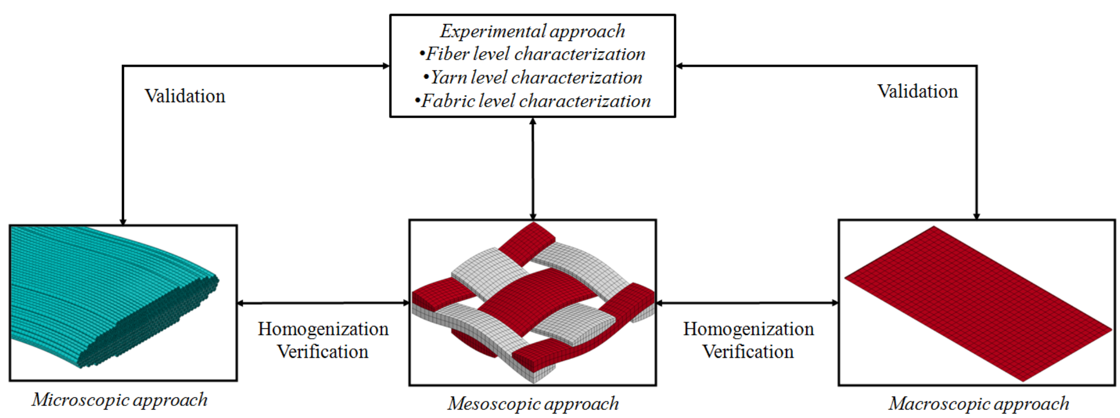

Figure 6.3 Extension of the integrated design framework to include microscopic length scale approach.

Even though the numerical models developed in the current work were used to simulate quasi-static loading, they can be improved by including different failure models and criteria to study more complex loading schemes such as ballistic loads. Finally, the developed framework in this dissertation can be used to design functional garments by linking the finite element simulations at the macroscopic length scales to biomechanical simulations as shown in Figure 6.4. Since macroscopic finite element models are more computationally efficient compared to mesoscopic length scale models, they can be used to simulate real-life structures such as functional garments. By simulating these special garments such as sleeves as shown in Figure 6.4, several outcomes can be extracted from the finite element simulations with the fabric sleeve such as the joint torques and pressure on the dummy arm. These outcomes can then be fed into the biomechanical simulations to determine the effort needed to carry out a given task. Hence, different architectures and materials for woven fabrics can be designed and simulated virtually to determine the optimized set of materials as well as the architectures for a given task.

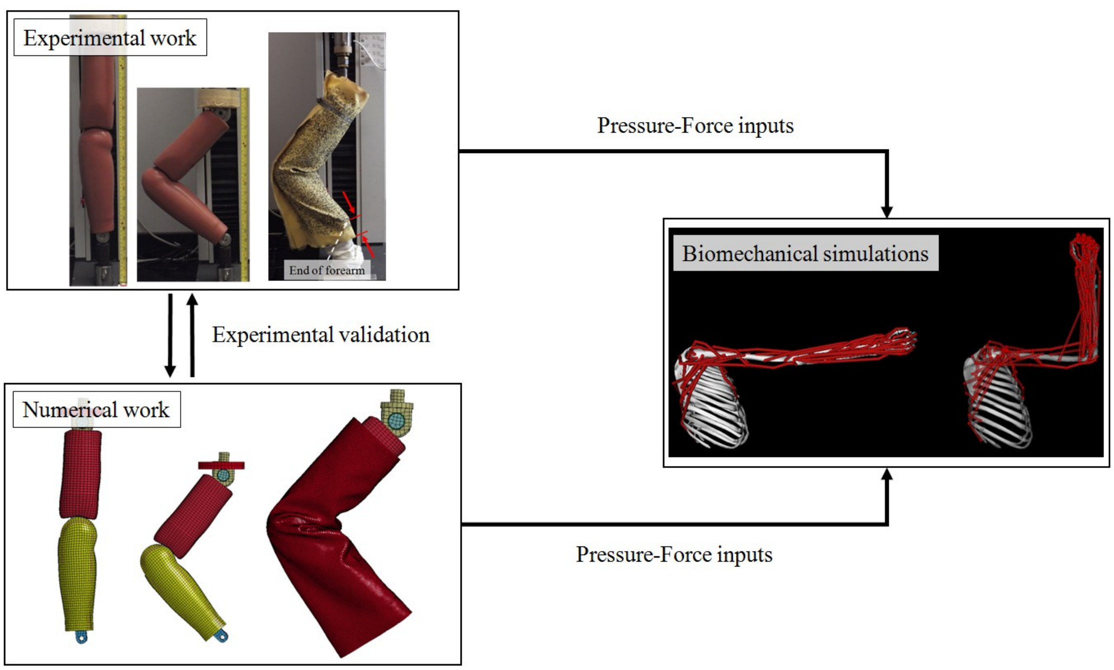

Figure 6.4 Designing functional garments with the developed integrated design framework for woven fabrics and biomechanical simulations.

REFERENCES

[1] P. Badel, S. Gauthier, E. Vidal-Sallé, and P. Boisse, "Rate constitutive equations for computational analyses of textile composite reinforcement mechanical behaviour during forming," *Compos. Part A Appl. Sci. Manuf.*, vol. 40, no. 8, pp. 997–1007, 2009.

[2] R. Barauskas and A. Abraitiene, "Computational analysis of impact of a bullet against the multilayer fabrics in LS-DYNA," *Int. J. Impact Eng.*, vol. 34, no. 7, pp. 1286–1305, 2007.

[3] P. Boisse, B. Zouari, and A. Gasser, "A mesoscopic approach for the simulation of woven fibre composite forming," *Compos. Sci. Technol.*, vol. 65, no. 3–4, pp. 429–436, 2005.

[4] Y. Duan, M. Keefe, T. A. Bogetti, and B. A. Cheeseman, "Modeling the role of friction during ballistic impact of a high-strength plain-weave fabric," *Compos. Struct.*, vol. 68, no. 3, pp. 331–337, 2005.

[5] Y. Duan, M. Keefe, T. A. Bogetti, and B. A. Cheeseman, "Modeling friction effects on the ballistic impact behavior of a single-ply high-strength fabric," *Int. J. Impact Eng.*, vol. 31, no. 8, pp. 996–1012, 2005.

[6] N. Hamila and P. Boisse, "A meso-macro three node finite element for draping of textile composite preforms," *Appl. Compos. Mater.*, vol. 14, no. 4, pp. 235–250, 2007.

[7] G. Nilakantan, M. Keefe, J. W. Gillespie Jr, E. D. Wetzel, T. A. Bogetti, and R. Adkinson, "An experimental and numerical study of the impact response (V50) of flexible plain weave fabrics: Accounting for statistical distributions of yarn strength," *1st Jt. Am. Int. Conf. Compos. 24th Annu. ASC Tech. Conf. Univ. Delaware, Newark, 19711, USA*, pp. 15–17, 2009.

[8] G. Nilakantan, M. Keefe, E. D. Wetzel, T. A. Bogetti, and J. W. Gillespie, "Computational modeling of the probabilistic impact response of flexible fabrics," *Compos. Struct.*, vol. 93, no. 12, pp. 3163–3174, 2011.

[9] Z. Dong, J. Manimala, and C. T. Sun, "Mechanical behavior of silica nanoparticle-impregnated kevlar fabrics," *J. Mech. Mater. Struct.*, vol. 5, no. 4, pp. 529–548, 2010.

[10] Z. Dong and C. T. Sun, "Testing and modeling of yarn pull-out in plain woven Kevlar fabrics," *Compos. Part A Appl. Sci. Manuf.*, vol. 40, no. 12, pp. 1863–1869, 2009.

[11] M. Cheng, W. Chen, and T. Weerasooriya, "Mechanical Properties of Kevlar® KM2 Single Fiber," *J. Eng. Mater. Technol.*, vol. 127, no. 2, p. 197, 2005.

[12] D. Zhu, B. Mobasher, J. Erni, S. Bansal, and S. D. Rajan, "Strain rate and gage

length effects on tensile behavior of Kevlar 49 single yarn," *Compos. Part A Appl. Sci. Manuf.*, vol. 43, no. 11, pp. 2021–2029, 2012.
[13] S. Gatouillat, A. Bareggi, E. Vidal-Sallé, and P. Boisse, "Meso modelling for composite preform shaping - Simulation of the loss of cohesion of the woven fibre network," *Compos. Part A Appl. Sci. Manuf.*, vol. 54, pp. 135–144, 2013.
[14] X. Q. Peng and J. Cao, "A continuum mechanics-based non-orthogonal constitutive model for woven composite fabrics," *Compos. Part A Appl. Sci. Manuf.*, vol. 36, no. 6, pp. 859–874, 2005.
[15] M. N. Raftenberg and T. J. Mulkern, "Quasi-Static Uniaxial Tension Characteristics of Plain-Woven Kevlar KM2 Fabric," no. December, 2002.
[16] P. Boisse, A. Gasser, and G. Hivet, "Analyses of fabric tensile behaviour: Determination of the biaxial tension-strain surfaces and their use in forming simulations," *Compos. - Part A Appl. Sci. Manuf.*, vol. 32, no. 10, pp. 1395–1414, 2001.
[17] V. Carvelli, J. Pazmino, S. V. Lomov, and I. Verpoest, "Deformability of a non-crimp 3D orthogonal weave E-glass composite reinforcement," *Compos. Sci. Technol.*, vol. 73, no. 1, pp. 9–18, 2012.
[18] A. Willems, S. V. Lomov, I. Verpoest, and D. Vandepitte, "Optical strain fields in shear and tensile testing of textile reinforcements," *Compos. Sci. Technol.*, vol. 68, no. 3–4, pp. 807–819, 2008.
[19] D. Zhu, B. Mobasher, A. Vaidya, and S. D. Rajan, "Mechanical behaviors of Kevlar 49 fabric subjected to uniaxial, biaxial tension and in-plane large shear deformation," *Compos. Sci. Technol.*, vol. 74, pp. 121–130, 2013.
[20] P. Boisse, B. Zouari, and J. L. Daniel, "Importance of in-plane shear rigidity in finite element analyses of woven fabric composite preforming," *Compos. Part A Appl. Sci. Manuf.*, vol. 37, no. 12, pp. 2201–2212, 2006.
[21] J. K. Lin, L. S. Shook, J. S. Ware, and J. V Welch, "Flexible Material Systems Testing," *NASA Tech. Rep.*, vol. NASA/CR-20, no. October, 2010.
[22] D. Jauffrès, J. A. Sherwood, C. D. Morris, and J. Chen, "Discrete mesoscopic modeling for the simulation of woven-fabric reinforcement forming," *Int. J. Mater. Form.*, vol. 3, no. SUPPL. 2, pp. 1205–1216, 2010.
[23] X. Peng, Z. Guo, T. Du, and W. R. Yu, "A simple anisotropic hyperelastic constitutive model for textile fabrics with application to forming simulation," *Compos. Part B Eng.*, vol. 52, pp. 275–281, 2013.
[24] J. Cao *et al.*, "Characterization of mechanical behavior of woven fabrics: Experimental methods and benchmark results," *Compos. Part A Appl. Sci. Manuf.*, vol. 39, no. 6, pp. 1037–1053, 2008.
[25] L. Li, Y. Zhao, H. gia nam Vuong, Y. Chen, J. Yang, and Y. Duan, "In-plane shear investigation of biaxial carbon non-crimp fabrics with experimental tests and finite element modeling," *Mater. Des.*, vol. 63, pp. 757–765, 2014.
[26] P. Harrison, M. J. Clifford, and A. C. Long, "Shear characterisation of viscous woven textile composites: A comparison between picture frame and bias extension experiments," *Compos. Sci. Technol.*, vol. 64, no. 10–11, pp. 1453–

1465, 2004.

[27] P. Harrison, F. Abdiwi, Z. Guo, P. Potluri, and W. R. Yu, "Characterising the shear-tension coupling and wrinkling behaviour of woven engineering fabrics," *Compos. Part A Appl. Sci. Manuf.*, vol. 43, no. 6, pp. 903–914, 2012.

[28] P. Harrison, M. K. Tan, and a C. Long, "Kinematics of Intra-Ply Slip in Textile Composites during Bias Extension Tests," *8th Int. ESAFORM Conf. Mater. Form.*, pp. 2–5, 2005.

[29] a. G. Prodromou and J. Chen, "On the relationship between shear angle and wrinkling of textile composite preforms," *Compos. Part A Appl. Sci. Manuf.*, vol. 28, pp. 491–503, 1997.

[30] I. Taha, Y. Abdin, and S. Ebeid, "Comparison of picture frame and Bias-Extension tests for the characterization of shear behaviour in natural fibre woven fabrics," *Fibers Polym.*, vol. 14, no. 2, pp. 338–344, 2013.

[31] O. Döbrich, T. Gereke, and C. Cherif, "Modelling of textile composite reinforcements on the micro-scale," *Autex Res. J.*, vol. 14, no. 1, pp. 28–33, 2014.

[32] D. Durville, "Finite element simulation of the mechanical behaviour of textile composites at the mesoscopic scale of individual fibers," *Text. Compos. Inflatable Struct. II, Comput. Methods Appl. Sci.*, pp. 15–34, 2008.

[33] G. Nilakantan, "Filament-level modeling of Kevlar KM2 yarns for ballistic impact studies," *Compos. Struct.*, vol. 104, pp. 1–13, 2013.

[34] S. Sockalingam, J. W. Gillespie, and M. Keefe, "Modeling the fiber length-scale response of Kevlar KM2 yarn during transverse impact," *Text. Res. J.*, 2016.

[35] Y. Wang, Y. Miao, D. Swenson, B. A. Cheeseman, C. F. Yen, and B. LaMattina, "Digital element approach for simulating impact and penetration of textiles," *Int. J. Impact Eng.*, vol. 37, no. 5, pp. 552–560, 2010.

[36] M. Grujicic, W. C. Bell, T. He, and B. A. Cheeseman, "Development and verification of a meso-scale based dynamic material model for plain-woven single-ply ballistic fabric," *J. Mater. Sci.*, vol. 43, no. 18, pp. 6301–6323, 2008.

[37] G. Nilakantan, E. D. Wetzel, T. A. Bogetti, and J. W. Gillespie, "Finite element analysis of projectile size and shape effects on the probabilistic penetration response of high strength fabrics," *Compos. Struct.*, vol. 94, no. 5, pp. 1846–1854, 2012.

[38] M. P. Rao, Y. Duan, M. Keefe, B. M. Powers, and T. A. Bogetti, "Modeling the effects of yarn material properties and friction on the ballistic impact of a plain-weave fabric," *Compos. Struct.*, vol. 89, no. 4, pp. 556–566, 2009.

[39] A. Shahkarami and R. Vaziri, "A continuum shell finite element model for impact simulation of woven fabrics," *Int. J. Impact Eng.*, vol. 34, no. 1, pp. 104–119, 2007.

[40] G. Nilakantan, M. Keefe, T. A. Bogetti, R. Adkinson, and J. W. Gillespie, "On the finite element analysis of woven fabric impact using multiscale modeling techniques," *Int. J. Solids Struct.*, vol. 47, no. 17, pp. 2300–2315, 2010.

[41] M. P. Rao, G. Nilakantan, M. Keefe, B. M. Powers, and T. a. Bogetti, "Global/Local Modeling of Ballistic Impact onto Woven Fabrics," *J. Compos. Mater.*, vol. 43, no. 5, pp. 445–467, 2009.
[42] P. Badel, E. Maire, E. Vidal-Sallé, and P. Boisse, "Computational determination of the mechanical behavior of textile composite reinforcement. Validation with x-ray tomography," *Int. J. Mater. Form.*, vol. 1, no. SUPPL. 1, pp. 823–826, 2008.
[43] A. B. Ilyani Akmar, T. Lahmer, S. P. A. Bordas, L. A. A. Beex, and T. Rabczuk, "Uncertainty quantification of dry woven fabrics: A sensitivity analysis on material properties," *Compos. Struct.*, vol. 116, no. 1, pp. 1–17, 2014.
[44] A. Gasser, P. Boisse, and S. Hanklar, "Mechanical behaviour of dry fabric reinforcements. 3D simulations versus biaxial tests," *Comput. Mater. Sci.*, vol. 17, no. 1, pp. 7–20, 2000.
[45] M. Komeili and A. S. Milani, "The effect of meso-level uncertainties on the mechanical response of woven fabric composites under axial loading," *Comput. Struct.*, vol. 90–91, no. 1, pp. 163–171, 2012.
[46] H. Lin, M. Clifford, A. C. Long, and M. Sherburn, "Finite element modelling of fabric shear," *Model. Simul. Mater. Sci. Eng.*, vol. 17, no. 1, p. 15008, 2008.
[47] P. Badel, E. Vidal-Sallé, and P. Boisse, "Computational determination of in-plane shear mechanical behaviour of textile composite reinforcements," *Comput. Mater. Sci.*, vol. 40, no. 4, pp. 439–448, 2007.
[48] A. Charmetant, E. Vidal-Sallé, and P. Boisse, "Hyperelastic modelling for mesoscopic analyses of composite reinforcements," *Compos. Sci. Technol.*, vol. 71, no. 14, pp. 1623–1631, 2011.
[49] J. M. Manimala and C. T. Sun, "Investigation of failure in Kevlar fabric under transverse indentation using a homogenized continuum constitutive model," *Text. Res. J.*, vol. 84, no. 4, pp. 388–398, 2014.
[50] X. Peng and F. Ding, "Validation of a non-orthogonal constitutive model for woven composite fabrics via hemispherical stamping simulation," *Compos. Part A Appl. Sci. Manuf.*, vol. 42, no. 4, pp. 400–407, 2011.
[51] P. Xue, X. Peng, and J. Cao, "A non-orthogonal constitutive model for characterizing woven composites," *Compos. Part A Appl. Sci. Manuf.*, vol. 34, no. 2, pp. 183–193, 2003.
[52] Y. Aimene, E. Vidal-Salle, B. Hagege, F. Sidoroff, and P. Boisse, "A Hyperelastic Approach for Composite Reinforcement Large Deformation Analysis," *J. Compos. Mater.*, vol. 44, no. 1, pp. 5–26, 2010.
[53] S. Dridi, A. Dogui, and P. Boisse, "Finite element analysis of bias extension test using an orthotropic hyperelastic continuum model for woven fabric," *J. Text. Inst.*, vol. 102, no. 9, pp. 781–789, 2011.
[54] L. M. Dangora, C. J. Mitchell, and J. A. Sherwood, "Predictive model for the detection of out-of-plane defects formed during textile-composite manufacture," *Compos. Part A Appl. Sci. Manuf.*, vol. 78, pp. 102–112, 2015.

[55] N. Hamila, P. Boisse, and S. Chatel, "Semi-discrete shell finite elements for textile composite forming simulation," *Int. J. Mater. Form.*, vol. 2, no. SUPPL. 1, pp. 169–172, 2009.
[56] N. Hamila and P. Boisse, "Simulations of textile composite reinforcement draping using a new semi-discrete three node finite element," *Compos. Part B Eng.*, vol. 39, no. 6, pp. 999–1010, 2008.
[57] I. Ivanov and A. Tabiei, "Loosely woven fabric model with viscoelastic crimped fibres for ballistic impact simulations," *Int. J. Numer. Methods Eng.*, vol. 61, no. 10, pp. 1565–1583, 2004.
[58] M. J. J. King, P. Jearanaisilawong, and S. Socrate, "A continuum constitutive model for the mechanical behavior of woven fabrics," *Int. J. Solids Struct.*, vol. 42, no. 13, pp. 3867–3896, 2005.
[59] E. M. Parsons, M. J. King, and S. Socrate, "Modeling yarn slip in woven fabric at the continuum level: Simulations of ballistic impact," *J. Mech. Phys. Solids*, vol. 61, no. 1, pp. 265–292, 2013.
[60] a Tabiei and I. Ivanov, "Computational micro-mechanical model of flexible woven fabric for finite element impact simulation," *Int. J. Numer. Methods Eng.*, vol. 53, no. 1, pp. 1259–1276, 2002.
[61] P. Harrison, "Modelling the forming mechanics of engineering fabrics using a mutually constrained pantographic beam and membrane mesh," *Compos. Part A Appl. Sci. Manuf.*, vol. 81, pp. 145–157, 2016.
[62] E. M. Parsons, T. Weerasooriya, S. Sarva, and S. Socrate, "Impact of woven fabric: Experiments and mesostructure-based continuum-level simulations," *J. Mech. Phys. Solids*, vol. 58, no. 11, pp. 1995–2021, 2010.
[63] "Manufacturer's datasheet, JPS Composite Materials."
[64] G. Lebrun, M. N. Bureau, and J. Denault, "Evaluation of bias-extension and picture-frame test methods for the measurement of intraply shear properties of PP/glass commingled fabrics," *Compos. Struct.*, vol. 61, no. 4, pp. 341–352, 2003.
[65] J. Launay, G. Hivet, A. V. Duong, and P. Boisse, "Experimental analysis of the influence of tensions on in plane shear behaviour of woven composite reinforcements," *Compos. Sci. Technol.*, vol. 68, no. 2, pp. 506–515, 2008.
[66] F. Härtel and P. Harrison, "Evaluation of normalisation methods for uniaxial bias extension tests on engineering fabrics," *Compos. Part A*, vol. 67, pp. 61–69, 2014.
[67] H. JO, "LS-DYNA Theory Manual." Livermore Software Technology Corporation, 2006.
[68] Z. Stahlecker, B. Mobasher, S. D. Rajan, and J. M. Pereira, "Development of reliable modeling methodologies for engine fan blade out containment analysis. Part II: Finite element analysis," *Int. J. Impact Eng.*, vol. 36, no. 3, pp. 447–459, 2009.
[69] Q. T. Nguyen *et al.*, "Mesoscopic scale analyses of textile composite reinforcement compaction," *Compos. Part B Eng.*, vol. 44, no. 1, pp. 231–241,

2013.
[70] R. Lochner and J. Mater, *Designing for quality: An introduction to the best of Taguchi and Western methods of statistical experimental design*. New York, NY: Quality Resources, 1990.
[71] R. Mason, R. Gunst, and J. Hess, *Statistical design and analysis of experiments with applications to engineering and science*. Hoboken, NJ: Wiley, 2003.
[72] R. Roy, *A primer on the Taguchi method*. Dearborn, MI: Society of Manufacturing Engineers.
[73] G. Taguchi, S. Chowdhury, and Y. Wu, *Taguchi's quality engineering handbook*. Hoboken, NJ: Wiley, 2005.
[74] O. Erol, B. Powers, and M. Keefe, "Development of a non-orthogonal macroscale material model for advanced woven fabrics based on mesoscale structure," *Compos. Part B*, vol. 110, pp. 497–510, 2017.
[75] G. Nilakantan, R. L. Merrill, M. Keefe, J. W. Gillespie, and E. D. Wetzel, "Composites : Part B Experimental investigation of the role of frictional yarn pull-out and windowing on the probabilistic impact response of kevlar fabrics," *Compos. PART B*, vol. 68, pp. 215–229, 2015.
[76] B. Chen and T. W. Chou, "Compaction of woven-fabric preforms in liquid composite molding processes: Single-layer deformation," *Compos. Sci. Technol.*, vol. 59, no. 10, pp. 1519–1526, 1999.
[77] P. Boisse, A. Gasser, B. Hagege, and J.-L. Billoet, "Analysis of the mechanical behavior of woven fibrous material using virtual tests at the unit cell level," *J. Mater. Sci.*, vol. 40, pp. 5955–5962, 2005.
[78] M. N. and H. K. S. Kawabata, "The Finite-Deformation Theory of Plain-Weave Fabrics. Part I: The Biaxial-Deformation Theory," *Text. Inst. Ind.*, vol. 64, no. 1, pp. 21–46, 1973.

Appendix A

REPRINT PERMISSION LETTERS

FIGURE 1.1a - COPYRIGHT AGREEMENT

This Agreement between Galip Ozan Erol ("You") and Elsevier ("Elsevier") consists of your license details and the terms and conditions provided by Elsevier and Copyright Clearance Center.

Your confirmation email will contain your order number for future reference.

Printable details.

License Number	4120940654257
License date	Jun 02, 2017
Licensed Content Publisher	Elsevier
Licensed Content Publication	Composites Part A: Applied Science and Manufacturing
Licensed Content Title	Shear behaviour of architectural fabrics subjected to biaxial tensile loads
Licensed Content Author	A.G. Colman,B.N. Bridgens,P.D. Gosling,G.-T. Jou,X.-Y. Hsu
Licensed Content Date	Nov 1, 2014
Licensed Content Volume	66
Licensed Content Issue	n/a
Licensed Content Pages	12
Type of Use	reuse in a thesis/dissertation
Portion	figures/tables/illustrations
Number of figures/tables/illustrations	1
Format	both print and electronic
Are you the author of this Elsevier article?	No
Will you be translating?	No
Order reference number	
Original figure numbers	Figure 1
Title of your thesis/dissertation	MULTI LENGTH SCALE FINITE ELEMENT DESIGN FRAMEWORK FOR ADVANCED WOVEN FABRICS
Expected completion date	Aug 2017
Estimated size (number of pages)	280
Elsevier VAT number	GB 494 6272 12
Requestor Location	Galip Ozan Erol 130 Spencer Lab NEWARK, DE 19716 United States Attn: Galip Ozan Erol
Publisher Tax ID	98-0397604
Total	0.00 USD

FIGURE 1.1b - COPYRIGHT AGREEMENT

Order Completed

Thank you for your order.

This Agreement between Galip Ozan Erol ("You") and Elsevier ("Elsevier") consists of your license details and the terms and conditions provided by Elsevier and Copyright Clearance Center.

Your confirmation email will contain your order number for future reference.

Printable details.

License Number	4120921438864
License date	Jun 02, 2017
Licensed Content Publisher	Elsevier
Licensed Content Publication	International Journal of Impact Engineering
Licensed Content Title	Development of reliable modeling methodologies for fan blade out containment analysis – Part I: Experimental studies
Licensed Content Author	D. Naik,S. Sankaran,B. Mobasher,S.D. Rajan,J.M. Pereira
Licensed Content Date	Jan 1, 2009
Licensed Content Volume	36
Licensed Content Issue	1
Licensed Content Pages	11
Type of Use	reuse in a thesis/dissertation
Portion	figures/tables/illustrations
Number of figures/tables/illustrations	1
Format	both print and electronic
Are you the author of this Elsevier article?	No
Will you be translating?	No
Order reference number	
Original figure numbers	Figure 19
Title of your thesis/dissertation	MULTI LENGTH SCALE FINITE ELEMENT DESIGN FRAMEWORK FOR ADVANCED WOVEN FABRICS
Expected completion date	Aug 2017
Estimated size (number of pages)	280
Elsevier VAT number	GB 494 6272 12
Requestor Location	Galip Ozan Erol 130 Spencer Lab NEWARK, DE 19716 United States Attn: Galip Ozan Erol
Publisher Tax ID	98-0397604
Total	0.00 USD

FIGURE 1.1c - COPYRIGHT AGREEMENT

This Agreement between Galip Ozan Erol ("You") and Elsevier ("Elsevier") consists of your license details and the terms and conditions provided by Elsevier and Copyright Clearance Center.

Your confirmation email will contain your order number for future reference.

Printable details.

License Number	4120931433289
License date	Jun 02, 2017
Licensed Content Publisher	Elsevier
Licensed Content Publication	Acta Astronautica
Licensed Content Title	Entry descent and landing systems for small planetary missions: Parametric comparison of parachutes and inflatable systems for the proposed Vanguard Mars mission
Licensed Content Author	E. Allouis,A. Ellery,C.S. Welch
Licensed Content Date	October–December 2006
Licensed Content Volume	59
Licensed Content Issue	8-11
Licensed Content Pages	12
Type of Use	reuse in a thesis/dissertation
Portion	figures/tables/illustrations
Number of figures/tables/illustrations	1
Format	both print and electronic
Are you the author of this Elsevier article?	No
Will you be translating?	No
Order reference number	
Original figure numbers	Figure 7
Title of your thesis/dissertation	MULTI LENGTH SCALE FINITE ELEMENT DESIGN FRAMEWORK FOR ADVANCED WOVEN FABRICS
Expected completion date	Aug 2017
Estimated size (number of pages)	280
Elsevier VAT number	GB 494 6272 12
Requestor Location	Galip Ozan Erol 130 Spencer Lab NEWARK, DE 19716 United States Attn: Galip Ozan Erol
Publisher Tax ID	98-0397604
Total	0.00 USD

FIGURE 1.10 - COPYRIGHT AGREEMENT

This Agreement between Galip Ozan Erol ("You") and Elsevier ("Elsevier") consists of your license details and the terms and conditions provided by Elsevier and Copyright Clearance Center.

Your confirmation email will contain your order number for future reference.

Printable details.

License Number	4105071331231
License date	May 09, 2017
Licensed Content Publisher	Elsevier
Licensed Content Publication	International Journal of Impact Engineering
Licensed Content Title	Digital element approach for simulating impact and penetration of textiles
Licensed Content Author	Youqi Wang,Yuyang Miao,Daniel Swenson,Bryan A. Cheeseman,Chian-Feng Yen,Bruce LaMattina
Licensed Content Date	May 2010
Licensed Content Volume	37
Licensed Content Issue	5
Licensed Content Pages	9
Type of Use	reuse in a thesis/dissertation
Portion	figures/tables/illustrations
Number of figures/tables/illustrations	1
Format	both print and electronic
Are you the author of this Elsevier article?	No
Will you be translating?	No
Order reference number	
Original figure numbers	Figure 7
Title of your thesis/dissertation	MULTI LENGTH SCALE FINITE ELEMENT DESIGN FRAMEWORK FOR ADVANCED WOVEN FABRICS
Expected completion date	Aug 2017
Estimated size (number of pages)	280
Elsevier VAT number	GB 494 6272 12
Requestor Location	Galip Ozan Erol 130 Spencer Lab NEWARK, DE 19716 United States Attn: Galip Ozan Erol
Publisher Tax ID	98-0397604
Total	0.00 USD

FIGURE 1.11 - COPYRIGHT AGREEMENT

This Agreement between Galip Ozan Erol ("You") and Elsevier ("Elsevier") consists of your license details and the terms and conditions provided by Elsevier and Copyright Clearance Center.

Your confirmation email will contain your order number for future reference.

Printable details.

License Number	4105390848889
License date	May 10, 2017
Licensed Content Publisher	Elsevier
Licensed Content Publication	Composite Structures
Licensed Content Title	Filament-level modeling of Kevlar KM2 yarns for ballistic impact studies
Licensed Content Author	Gaurav Nilakantan
Licensed Content Date	October 2013
Licensed Content Volume	104
Licensed Content Issue	n/a
Licensed Content Pages	13
Type of Use	reuse in a thesis/dissertation
Portion	figures/tables/illustrations
Number of figures/tables/illustrations	1
Format	both print and electronic
Are you the author of this Elsevier article?	No
Will you be translating?	No
Order reference number	
Original figure numbers	Figure 9
Title of your thesis/dissertation	MULTI LENGTH SCALE FINITE ELEMENT DESIGN FRAMEWORK FOR ADVANCED WOVEN FABRICS
Expected completion date	Aug 2017
Estimated size (number of pages)	280
Elsevier VAT number	GB 494 6272 12
Requestor Location	Galip Ozan Erol 130 Spencer Lab NEWARK, DE 19716 United States Attn: Galip Ozan Erol
Publisher Tax ID	98-0397604
Total	0.00 USD

This Agreement between Galip Ozan Erol ("You") and Elsevier ("Elsevier") consists of your license details and the terms and conditions provided by Elsevier and Copyright Clearance Center.

Your confirmation email will contain your order number for future reference.

Printable details.

License Number	4151890261686
License date	Jul 18, 2017
Licensed Content Publisher	Elsevier
Licensed Content Publication	Composites Part B: Engineering
Licensed Content Title	Development of a non-orthogonal macroscale material model for advanced woven fabrics based on mesoscale structure
Licensed Content Author	Ozan Erol,Brian Powers,Michael Keefe
Licensed Content Date	Feb 1, 2017
Licensed Content Volume	110
Licensed Content Issue	n/a
Licensed Content Pages	14
Type of Use	reuse in a thesis/dissertation
Portion	full article
Format	both print and electronic
Are you the author of this Elsevier article?	Yes
Will you be translating?	No
Order reference number	
Title of your thesis/dissertation	MULTI LENGTH SCALE FINITE ELEMENT DESIGN FRAMEWORK FOR ADVANCED WOVEN FABRICS
Expected completion date	Aug 2017
Estimated size (number of pages)	280
Elsevier VAT number	GB 494 6272 12
Requestor Location	Galip Ozan Erol 130 Spencer Lab NEWARK, DE 19716 United States Attn: Galip Ozan Erol
Publisher Tax ID	98-0397604
Total	0.00 USD